Stony Brook University

Thermal and near-infrared analyses for understanding Martian surface mineralogy through orbital measurements, laboratory studies and statistical models

A Dissertation Presented

by

Cong Pan

to

The Graduate School

in Partial Fulfillment of the

Requirements

for the Degree of

Doctor of Philosophy

in

Geosciences

Stony Brook University

May 2016

Stony Brook University

The Graduate School

Cong Pan

We, the dissertation committee for the above candidate for the

Doctor of Philosophy degree, hereby recommend

acceptance of this dissertation.

Dr. Deanne Rogers – Dissertation Advisor
Assistant Professor, Geosciences

Dr. Timothy Glotch - Chairperson of Defense
Associate Professor, Geosciences

Dr. Hanna Nekvasil
Professor, Geosciences

Dr. Scott Mclennan
Professor, Geosciences

Dr. Joseph Michalski
Research Scientist
Planetary Science Institute

This dissertation is accepted by the Graduate School

Charles Taber
Dean of the Graduate School

Abstract of the Dissertation

Thermal and near-infrared analyses for understanding Martian surface mineralogy through orbital measurements, laboratory studies and statistic models

by

Cong Pan

Doctor of Philosophy

in

Geosciences

Stony Brook University

2016

Understanding the geologic evolution of Mars requires a detailed characterization of Martian surface compositions and their geologic settings. Because much of the Martian surface is covered with regolith or unconsolidated materials, in this work I focused on key locations in which to characterize Martian crustal materials as well as assess the degree of influence from physical sorting processes on measured surface compositions from orbit.

In Chapter 2, I identified and characterized 26 crater central peaks with distinctive spectral signatures from surrounding plains with thermal infrared and visible/near-infrared data, based on a global survey of Martian impact craters between 10-200 km diameter. Some degree of regional clustering is observed, suggesting that subsurface diversity in crust-forming compositions, physical properties or alteration environments are present. The western Noachis Terra area is the only region where multiple THEMIS-defined spectral units are present in individual central peaks, suggesting crustal stratigraphies of igneous units or ejected crustal materials or impact melt from the Argyre Basin.

In Chapter 3, I assessed the degree and occurrence of thermophysical and compositional heterogeneity for 42 dune fields on Mars. Among these, only four exhibit spatial heterogeneity in spectral properties and composition. Two of the four sites show a strong positive relationship between particle size and olivine abundance. The rarity of compositional heterogeneity within dune fields may indicate phenocryst-poor source rocks; alternatively sorting within individual bedforms may be present but is below the resolution of available instruments.

Discoveries of extensive sedimentary rock units on Mars call for a critical assessment of the ability to quantify mineral abundance from lithified sedimentary materials using infrared spectroscopy. In Chapter 4, I characterized the TIR spectral properties of compacted, very fine-grained mineral mixtures and assessed the linearity of spectral combination using non-negative linear least squares minimization. Non-linear relationships between known and modeled abundance are observed. However, using a partial least squares method, accurate mineral abundances can be recovered from TIR spectra of very fine-grained rocks (within +/- 10% of known abundance for 78-90% of mixtures). This method could potentially be applied to landed or orbital TIR observations.

Dedication Page

To Apollo Chen and Yu Chen for love

Table of Contents

List of Figures

List of Tables

Acknowledgments

I would like to thank

My advisor, Deanne Rogers for her thoughtful advice during my time at Stony Brook. Her patience and encouragement have helped me through the whole doctoral study, especially for some of the difficult time.

My committee members: Scott McLennan, Hanna Nekvasil, Timothy Glotch and Joseph Michalski for reviewing this work.

The people in the department of Geosciences for their help, especially the research group members and my friends: Michael Thorpe, Marcella Yant, Joseph Tamborski, Xianyin Chen, Xuebing Wang, Shengnan Wang, Xintong Qi, Yuanyuan Liu, Congcong Che.

And finally my husband, my son and my parents who always support and encourage me.

Chapter 1: Introduction and Overview

1.1 Introduction

Minerals preserved in rocks and sediments on the surface of terrestrial bodies record a significant part of a planet's history. Furthermore, minerals can be used to understand the nature surface-atmosphere interactions, crustal formation and evolution, and the potential role of water for habitable environments(e.g. [*Clancy et al.*, 1995; *Farquhar et al.*, 1998; *Knauth et al.*, 2005; *Mustard et al.*, 2005; *Mangold et al.*, 2007; *S Murchie et al.*, 2009a; *Michalski and Niles*, 2010; *Ehlmann et al.*, 2011a]). The species, abundance, and geologic context of minerals identified in various geologic settings may provide information about the igneous history and the ancient and modern environmental conditions of Mars [e.g., [*Mustard et al.*, 2008; *Tornabene et al.*, 2008; *Ehlmann et al.*, 2011]. For example, abundant olivine suggests mantle-derived basaltic magmas with minimal fractionation during ascent and lava emplacement (e.g. [*McSween et al.*, 2006; *Peslier*, 2010; *Filiberto and Dasgupta*, 2011]). More importantly, due to the relatively rapid weathering rate of olivine in common aqueous conditions, it can serve as a useful indicator of environmental conditions following when the rock was emplaced (e.g. [*Hurowitz et al.*, 2006; *Zolotov and Mironenko*, 2007; *Hausrath et al.*, 2008]). One example way to study ancient Mars is through analyses of crustal materials exposed by impact craters. Central uplifts of impact craters are a natural probe to the subsurface, which may reveal information about early geological conditions (e.g. [*Pieters and Tompkins*, 1999; *Tompkins and Pieters*, 1999; *Rogers and Fergason*, 2011a; *J R Skok et al.*, 2012b]). On the other hand, because many sand dunes are active on the Martian surface, the sediments within sand dunes provide information on modern environmental condition [*Fenton et al.*, 2003; *Mangold et al.*, 2008; *Matthew Chojnacki et al.*, 2011].

The infrared spectroscopic instruments from orbiters, landers and rovers have mapped the surface globally with various spatial and spectral resolutions (e.g. [*Christensen et al.*, 2001; *Christensen et al.*, 2004; *Bibring et al.*, 2006; *S Murchie et al.*, 2009a]). Laboratory spectroscopy, which provides data similar to that acquired by orbiters, landers and rovers, is a powerful tool to help interpret remote sensing data (e.g. [*Ramsey and Christensen*, 1998; *Shepherd and Walsh*, 2002; *Michalski et al.*, 2006b]). The aim of this dissertation is to understand aspects of Mars' crustal evolution and modification through a detailed infrared spectroscopic study of minerals. In particular, in this work I investigated the mineralogy of central uplifts in impact craters in order to better understand the compositional properties and heterogeneity of the crust. Next, I examined the heterogeneity of composition and thermophysical properties within sand dunes to enhance our knowledge on aeolian processes and physical sorting on Martian sediments. Lastly, I characterized the thermal infrared spectral properties of synthetic mineral mixtures, applying statistical models to enhance our abilities to extract quantitative compositional information from infrared spectra of sedimentary rocks.

1.1.1 Major characteristics of the martian surface as observed from orbit and some open questions

Over the past 15 years, many instruments have successfully explored the Martian surface, including CTX (Context Camera), HiRISE (High Resolution Imaging Science Experiment), CRISM (Compact Reconnaissance Imaging Spectrometer for Mars), OMEGA (Observatoire pour la Mine´ralogie, l'Eau, les Glaces et l'Activite), TES (Thermal Emission Spectrometer) and THEMIS (Thermal Emission Imaging System). This section focuses on the mineral composition and physical properties of the Martian surface provided by spectrometers covering visible and near infrared (VNIR) to thermal infrared (TIR) wavelengths.

1.1.1.1 Composition

VNIR and TIR spectroscopy have identified and mapped the primary igneous minerals (including plagioclase feldspar, pyroxene and olivine) and secondary altered minerals (including phyllosilicates, sulfates, carbonate, hematite, chlorite and chlorate) in low dust cover areas globally. The igneous and basaltic nature of Martian crust is confirmed by the detection of primary igneous minerals. The diversity in volcanic rock compositions from olivine-rich basalts to basalts, combined with the rare identifications of dacitic [e.g. *Christensen et al*., 2005], granitic [*Bandfield et al.,* 2004] and possibly anorthositic [*Carter and Poulet*, 2013] rocks, displays a wide distribution of various minerals in distinct areas, indicating that Martian surface is heterogeneous and has undergone diverse igneous processes. The first global mineral maps produced from TES showed that there are two major types of spectral units dominating the surface [*Bandfield et al.,* 2000b]: "Surface Type 1", which was found mainly in the southern highlands and is spectrally consistent with terrestrial flood basalt; and "Surface Type 2", which was found primarily in the northern lowlands and some portions in the highlands, and interpreted as basaltic andesite or weathered basalt [*Wyatt and McSween*, 2002]. In follow-up studies, the surfaces were further classified into four units using an improved spectral library and longer wavelength range [*Rogers and Christensen*, 2007a], and ten distinct classes combining observations from TES, GRS and CRISM [*Rogers and Hamilton*, 2015], showing variations in basaltic mineral assemblage or chemistry that correspond with major crustal provinces or age. The identification of mafic minerals (olivine, low-calcium pyroxene (LCP), and high-calcium pyroxene (HCP)) from the VNIR spectrometer OMEGA extended the observations from thermal infrared measurements [*Mustard et al.*, 2005; *Bibring et al.*, 2006]: LCP is enriched in the ancient Noachian crust, HCP is found in more recent lava flows and olivine is detected in pyroxene-bearing areas or localized crater floors and rims

where olivine is dominant. The lack of mafic mineral detections on younger surfaces of younger surface indicates that it has been altered or covered by dust.

Chemical weathering interacting with primary igneous minerals and physical weathering provoking mechanical breakdown are suggestive of various alterations environments on the surface of Mars that are varying spatially and temporally throughout its geological history. It has been proposed that phyllosilicates formed during early Martian history; while sulfates formed in a second mineralogical era characterized by an acidic environment; and lastly anhydrous ferric oxides formed in the most recent era with slow superficial weathering [*Bibring et al.*, 2006]. The global widespread occurrence of phyllosilicates in the ancient Noachian terrains of Mars [*Bibring et al.*, 2005; *Poulet et al.*, 2005; *Mustard et al.*, 2008; *Ehlmann et al.*, 2009; *S Murchie et al.*, 2009a; *Ehlmann et al.*, 2011a; *J Carter et al.*, 2013] suggests subsurface formation by hydrothermal groundwater circulation and potentially cold, arid conditions on surface for over 4 billion years. Hydrated sulfates associated with hematite were found in Hesperian sedimentary rocks indicating groundwater upwelling to form the shallow lakes [*Grotzinger et al.*, 2005]. Carbonate-bearing rocks have been found in west of the Isidis basin and some impact craters in southern highlands [*Ehlmann et al.*, 2008; *Niles et al.*, 2013]. The lack of widespread carbonate phases may indicate deep burial, destruction by acid alteration, or a lack of a thick CO_2 atmosphere throughout Martian history (e.g.,[*Bullock and Moore*, 2007; *Ehlmann et al.*, 2011a; *Edwards and Ehlmann*, 2015]). Hydrated salts with VNIR spectral features consistent with magnesium perchlorate, magnesium chlorate, and sodium perchlorate were found associated with recurring slope lineae in Palikir crater, Horowitz crater, Hale crater, and Coprates Chasma suggesting the possible role of liquid in the formation of the lineae [*Ojha et al.*, 2015].

1.1.1.2 Physical properties

Thermal inertia is a physical property that incorporates subsurface heat conduction and heat storage capacity of the surface layer, controlling the diurnal and seasonal temperature cycle in surface temperature. It is an indicator of material property including composition, particle size, porosity, density, soil temperature, heterogeneity of the bulk soil, and distribution of particle size. The global maps of thermal inertia derived from TES data observations covering 3 Mars years shows broad regions with diurnal and seasonal differences at mid-latitudes and greater differences in the polar regions, indicating horizontal and vertical heterogeneity affecting the change of apparent thermal inertia with the time of day and season [*Putzig and Mellon*, 2007]. Unlike elsewhere on the planet where thermal inertia represents any mixtures of loose grains, rocks, and consolidated materials, dune fields composed of well-sorted unconsolidated particles are ideal sites for particle size estimates [*Fenton and Mellon*, 2006].

Albedo, which is the fraction of sunlight reflected, is a function of both particle size and composition. At a global scale, Mars' albedo is largely indicative of dust cover. The low albedo (<0.2) regions defined by the broadband visible to near infrared lambert albedo values are consistent with relatively dust-free surfaces [*Ruff and Christensen,* 2002], with spectroscopy studies focusing on these dark regions (e.g. [*Bandfield et al.*, 2000b; *Rogers and Christensen*, 2007a]). With the comparisons of TES with Viking and Mariner 9 images, it suggested that the surface of Mars has changed dramatically during the three decades, with more than one third of the surface area becoming brightened or darkened by at least 10%, resulting from aeolian erosion [*Geissler*, 2005]. In a study of albedo of the Martian surface using the 2004-2010 Omega data, it showed that the surface albedo changed most dramatically during the 2007 global dust storm and the following year [*Vincendon et al.*, 2015].

1.1.2 Open questions

Despite the extensive body of knowledge the exists about Mars surface and crust, there are many questions remaining. These include: 1. How do subsurface compositions differ from those of the Martian surface layer? 2. What is the spatial and vertical variability of the bulk composition of the upper Martian crust, on a global scale? 3. How does the bulk composition vary between phyllosilicate-bearing and non-phyllosilicate-bearing impact materials and can this reveal information about the origin of crater-hosted phyllosilicate minerals? 4. What is the role of aeolian processes in affecting Martian surface compositions measured from orbit? As described in **Section 1.2**, two of my chapters address these questions.

1.1.3 Quantitative mineral abundance determination

Discoveries of various rock units on the Martian surface call for a critical assessment of the ability to quantify mineral abundance in order to constrain the geological and climatic evolution of the Martian history. The confounding effects with minerals, particle size, surface physical properties, and matrix effects are major factors influencing the quantitative estimation of mineral abundance.

The assumption of linear mixing of end-member radiant energy at the thermal emission spectra allows the application of a linear deconvolution algorithm to determine the mineral abundance from thermal infrared spectra, and enables mineral percentage prediction within 5% on average, with residual errors less than 0.1% [*Ramsey and Christensen*, 1998]. The linear deconvolution algorithm has been applied to derive mineral composition of a suite of igneous and metamorphic rocks using thermal infrared emission spectra [*Feely and Christensen*, 1999]. A similar method is now widely used to determine mineral abundance from thermal infrared spectra orbiting the Martian surface such as TES and THEMIS (e.g. [*Bandfield et al.*, 2000b; *Rogers and Christensen*, 2007b; *Rogers and Hamilton*, 2015]).

These statistic models can provide useful information regarding quantitative estimation of mineral abundances, and have been applied to surface composition on Mars. However, what is currently not well understood is linearity of mixing within sedimentary rocks. Sedimentary rocks may contain a range of crystal sizes and fine-grained minerals, thus it is not clear how well bulk rock abundance may be modeled by a linear deconvolution algorithm and a library with coarse-grained minerals. Assessing the linearity of spectral combination of fine-grained minerals and our ability to determine their abundances have great importance for spectral interpretation of sedimentary materials. This is the focus of one of my chapters, described in **Section 1.2**.

1.2 Overview of Chapters

There are five chapters in this dissertation, including the introduction chapter. The subsequent three chapters each focus on a different aspect of application of near and thermal infrared spectroscopy, emphasizing the observation of mineral detection from orbital data and model building to quantitatively estimate the mineral abundance.

In Chapter 1, the Section 1.1 described the objectives of the chosen study topics for this dissertation. The Section 1.2 outlines the structure of the dissertation and overviews data and methods and using to solve the problems discussing in Chapter 2 to Chapter 4 and their major results.

In Chapter 2, I first conducted a systematic global survey of previously-catalogued crater central peaks located in low-dust regions of Mars, to locate spectrally distinct materials associated with central peaks. In order to identify which craters within this subset exhibit spectrally distinct materials in the central peak, ejecta, walls or floor, THEMIS decorrelation stretched (DCS) radiance browse images were examined for each crater. It was determined that only 26 central peaks contained spectrally distinct materials in THEMIS images. The final set of 26 spectrally

distinct central peaks was further analyzed using the following data sets: (1) THEMIS thermal infrared images; (2) CRISM multispectral and targeted images; (3) TES hyperspectral data (where available); and (4) high-resolution visible imagery from THEMIS and CTX. A cubic polynomial fit is used to determine the emissivity minimum of each THEMIS spectrum. The global distribution of spectrally distinct central peaks shows some degree of regional clustering, with a distribution similar to that presented by *Skok et al.* [2012], and are mostly restricted to low latitudes. Most of the spectrally distinct central peaks are found in western Noachis Terra, Tyrrhena Terra, and within the northern rim of Hellas Basin; two are located in the northern lowlands. The western Noachis Terra area is the only region in this study where multiple THEMIS-defined spectral units are present in individual central peaks. These units may represent crustal stratigraphies of igneous units or ejected crustal materials or impact melt from the Argyre Basin. A manuscript based on this work was published at Journal of Geophysical Research-Planets.

In Chapter 3, forty-two (42) dune fields or sand deposits within impact craters located between 0°N and -14.3°N, 43°E to 195°E were initially included as candidate areas for detailed study. First, each site was closely inspected with high-resolution visible imagery from the THEMIS and CTX to assess the degree of sand cover continuity within the sand deposit or dune field. Only six were found to exhibit contiguous sand cover. Next, each potential dune field was independently examined for spectral or thermophysical heterogeneity using THEMIS. Data from the THEMIS instrument was used to assess thermal inertia variations within each field and determine effective particle sizes. Analysis of compositional heterogeneity was carried out using THEMIS and CRISM images. Of the 42 sites, only four were found to exhibit spatial heterogeneity in spectral properties. All four of those sites are among the six contiguous-coverage dune fields described above, and also exhibit thermophysical heterogeneity. Among the four spectrally heterogeneous dune fields,

two show a strong positive relationship between olivine and particle size, similar to trends described for Gale crater [*Lapotre et al.*, 2015] and El Dorado [*Sullivan et al.*, 2008], but notably, opposite the trend described for basaltic sediments in Iceland [*Mangold et al.*, 2011]. A manuscript based on this work is being prepared.

In Chapter 4, I characterize the spectral properties of compacted, very fine-grained (<10-25 μm) mineral mixtures of oligoclase, augite, calcite, gypsum and montmorillonite to assess spectral mixing behavior of very fine-grained (<~10-25 um) materials. To assess linearity of spectral combination in compacted fine-grained mixtures, non-negative linear least squares minimization (NNLS) using spectra of pellets and powders of the end-member minerals was used to model mineral abundance of mixtures over the 350-1650 cm^{-1} spectral range. For the first time, we also apply a partial least squares (PLS) method to model mineral abundance from thermal emission spectra and provide an assessment of the applicability of PLS to fine-grained rocks. The results indicates that thermal infrared spectra from very fine-grained (<10 μm) rocks cannot be modeled reliably with NNLS. But, PLS can be used to recover abundances from very fine-grained rocks to within +/- 10% (absolute) from TIR datasets, provided a suitable training set is available. A manuscript based on this work is under revision at Journal of Geophysical Research-Planets.

In Chapter 5, I summarize the major findings and conclusion for the preceding chapters and point out the possible improvement for this work.

Reference

Bandfield, J. L., V. E. Hamilton, and P. R. Christensen (2000), A global view of Martian surface compositions from MGS-TES, *Science*, *287*(5458), 1626-1630.

Barlow, N. G., and C. B. Perez (2003), Martian impact crater ejecta morphologies as indicators of the distribution of subsurface volatiles, *J. Geophys. Res.-Planets*, *108*(E8), doi:10.1029/2002je002036.

Bibring, J. P., et al. (2005), Mars surface diversity as revealed by the OMEGA/Mars Express observations, *Science*, *307*(5715), 1576-1581, doi:10.1126/science.1108806.

Bibring, J. P., et al. (2006), Global mineralogical and aqueous mars history derived from OMEGA/Mars express data, *Science*, *312*(5772), 400-404, doi:10.1126/science.1122659.

Bridges, N. T., P. E. Geissler, A. S. McEwen, B. J. Thomson, F. C. Chuang, K. E. Herkenhoff, L. P. Keszthelyi, and S. Martinez-Alonso (2007), Windy Mars: A dynamic planet as seen by the HiRISE camera, *Geophysical Research Letters*, *34*(23), doi:10.1029/2007gl031445.

Bullock, M. A., and J. M. Moore (2007), Atmospheric conditions on early Mars and the missing layered carbonates, *Geophysical Research Letters*, *34*(19), doi:10.1029/2007gl030688.

Carr, M. H., and J. W. Head, III (2010), Geologic history of Mars, *Earth and Planetary Science Letters*, *294*(3-4), 185-203, doi:10.1016/j.epsl.2009.06.042.

Carter, J., F. Poulet, J. P. Bibring, N. Mangold, and S. Murchie (2013), Hydrous minerals on Mars as seen by the CRISM and OMEGA imaging spectrometers: Updated global view, *J. Geophys. Res.-Planets*, *118*(4), 831-858, doi:10.1029/2012je004145.

Chojnacki, M., D. M. Burr, J. E. Moersch, and T. I. Michaels (2011), Orbital observations of contemporary dune activity in Endeavor crater, Meridiani Planum, Mars, *J. Geophys. Res.-Planets*, *116*, doi:10.1029/2010je003675.

Christensen, P. R., et al. (2001), Mars Global Surveyor Thermal Emission Spectrometer experiment: Investigation description and surface science results, *J. Geophys. Res.-Planets*, *106*(E10), 23823-23871, doi:10.1029/2000JE001370.

Christensen, P. R., et al. (2004), The Thermal Emission Imaging System (THEMIS) for the Mars 2001 Odyssey Mission, *Space Sci. Rev.*, *110*(1-2), 85-130, doi:10.1023/b:spac.0000021008.16305.94.

Clancy, R. T., S. W. Lee, G. R. Gladstone, W. W. McMillan, and T. Rousch (1995), A NEW MODEL FOR MARS ATMOSPHERIC DUST BASED UPON ANALYSIS OF ULTRAVIOLET THROUGH INFRARED OBSERVATIONS FROM MARINER-9, VIKING, AND PHOBOS, *J. Geophys. Res.-Planets*, *100*(E3), 5251-5263, doi:10.1029/94je01885.

Clark, R. N., and T. L. Roush (1984), REFLECTANCE SPECTROSCOPY - QUANTITATIVE-ANALYSIS TECHNIQUES FOR REMOTE-SENSING APPLICATIONS, *Journal of Geophysical Research*, *89*(NB7), 6329-6340, doi:10.1029/JB089iB07p06329.

Clegg, S. M., E. Sklute, M. D. Dyar, J. E. Barefield, and R. C. Wiens (2009), Multivariate analysis of remote laser-induced breakdown spectroscopy spectra using partial least squares, principal component analysis, and related techniques, *Spectrochimica Acta Part B-Atomic Spectroscopy*, *64*(1), 79-88, doi:10.1016/j.sab.2008.10.045.

Cornwall, C., J. L. Bandfield, T. N. Titus, B. C. Schreiber, and D. R. Montgomery (2015), Physical abrasion of mafic minerals and basalt grains: Application to martian aeolian deposits, *Icarus*, *256*, 13-21, doi:10.1016/j.icarus.2015.04.020.

Cudahy, T. J., R. Hewson, J. F. Huntington, M. A. Quigley, P. S. Barry, and I. Ieee (2001), *The performance of the satellite-borne Hyperion hyperspectral VNIR-SWIR imaging system for mineral mapping at Mount Fitton, South Australia*, 314-316 pp.

Diniega, S., S. Byrne, N. T. Bridges, C. M. Dundas, and A. S. McEwen (2010), Seasonality of present-day Martian dune-gully activity, *Geology*, *38*(11), 1047-1050, doi:10.1130/g31287.1.

Dyar, M. D., M. L. Carmosino, E. A. Breves, M. V. Ozanne, S. M. Clegg, and R. C. Wiens (2012),

Comparison of partial least squares and lasso regression techniques as applied to laser-induced breakdown spectroscopy of geological samples, *Spectrochimica Acta Part B-Atomic Spectroscopy*, *70*, 51-67, doi:10.1016/j.sab.2012.04.011.

Edwards, C. S., and B. L. Ehlmann (2015), Carbon sequestration on Mars, *Geology*, *43*(10), 863-866, doi:10.1130/g36983.1.

Ehlmann, B. L., J. F. Mustard, S. L. Murchie, J.-P. Bibring, A. Meunier, A. A. Fraeman, and Y. Langevin (2011), Subsurface water and clay mineral formation during the early history of Mars, *Nature*, *479*(7371), 53-60, doi:10.1038/nature10582.

Ehlmann, B. L., et al. (2008), Orbital Identification of Carbonate-Bearing Rocks on Mars, *Science*, *322*(5909), 1828-1832, doi:10.1126/science.1164759.

Ehlmann, B. L., et al. (2009), Identification of hydrated silicate minerals on Mars using MRO-CRISM: Geologic context near Nili Fossae and implications for aqueous alteration, *J. Geophys. Res.-Planets*, *114*, doi:10.1029/2009je003339.

Farquhar, J., M. H. Thiemens, and T. Jackson (1998), Atmosphere-surface interactions on Mars: Delta O-17 measurements of carbonate from ALH 84001, *Science*, *280*(5369), 1580-1582, doi:10.1126/science.280.5369.1580.

Feely, K. C., and P. R. Christensen (1999), Quantitative compositional analysis using thermal emission spectroscopy: Application to igneous and metamorphic rocks, *J. Geophys. Res.-Planets*, *104*(E10), 24195-24210, doi:10.1029/1999je001034.

Fenton, L. K., J. L. Bandfield, and A. W. Ward (2003), Aeolian processes in Proctor Crater on Mars: Sedimentary history as analyzed from multiple data sets, *J. Geophys. Res.-Planets*, *108*(E12), doi:10.1029/2002je002015.

Fenton, L. K., and R. K. Hayward (2010), Southern high latitude dune fields on Mars: Morphology, aeolian inactivity, and climate change, *Geomorphology*, *121*(1-2), 98-121, doi:10.1016/j.geomorph.2009.11.006.

Fenton, L. K., and M. T. Mellon (2006), Thermal properties of sand from Thermal Emission Spectrometer (TES) and Thermal Emission Imaging System (THEMIS): Spatial variations within the Proctor Crater dune field on Mars, *J. Geophys. Res.-Planets*, *111*(E6), doi:10.1029/2004je002363.

Filiberto, J., and R. Dasgupta (2011), Fe2+-Mg partitioning between olivine and basaltic melts: Applications to genesis of olivine-phyric shergottites and conditions of melting in the Martian interior, *Earth and Planetary Science Letters*, *304*(3-4), 527-537, doi:10.1016/j.epsl.2011.02.029.

Gardin, E., P. Allemand, C. Quantin, S. Silvestro, and C. Delacourt (2012), Dune fields on Mars: Recorders of a climate change?, *Planetary and Space Science*, *60*(1), 314-321, doi:10.1016/j.pss.2011.10.004.

Geissler, P. E. (2005), Three decades of Martian surface changes, *J. Geophys. Res.-Planets*, *110*(E2), 23, doi:10.1029/2004je002345.

Grotzinger, J. P., et al. (2005), Stratigraphy and sedimentology of a dry to wet eolian depositional system, Burns formation, Meridiani Planum, Mars, *Earth and Planetary Science Letters*, *240*(1), 11-72, doi:10.1016/j.epsl.2005.09.039.

Grotzinger, J. P., and R. E. Milliken (2012), THE SEDIMENTARY ROCK RECORD OF MARS: DISTRIBUTION, ORIGINS, AND GLOBAL STRATIGRAPHY, in *Sedimentary Geology of Mars*, edited by J. P. Grotzinger and R. E. Milliken, pp. 1-48, S E P M - Soc Sedimentary Geology, Tulsa.

Hapke, B. (1981), BIDIRECTIONAL REFLECTANCE SPECTROSCOPY .1. THEORY, *Journal of Geophysical Research*, *86*(NB4), 3039-3054, doi:10.1029/JB086iB04p03039.

Hausrath, E. M., A. K. Navarre-Sitchler, P. B. Sak, C. I. Steefel, and S. L. Brantley (2008), Basalt weathering rates on Earth and the duration of liquid water on the plains of Gusev Crater, Mars, *Geology*, *36*(1), 67-70, doi:10.1130/g24238a.1.

Hayward, R. K., L. K. Fenton, and T. N. Titus (2014), Mars Global Digital Dune Database (MGD(3)): Global dune distribution and wind pattern observations, *Icarus*, *230*, 38-46,

doi:10.1016/j.icarus.2013.04.011.
Hayward, R. K., K. F. Mullins, L. K. Fenton, T. M. Hare, T. N. Titus, M. C. Bourke, A. Colaprete, and P. R. Christensen (2007), Mars global digital dune database and initial science results, *J. Geophys. Res.-Planets*, *112*(E11), doi:10.1029/2007je002943.
Hecker, C., J. H. Dilles, M. van der Meijde, and F. D. van der Meer (2012), Thermal infrared spectroscopy and partial least squares regression to determine mineral modes of granitoid rocks, *Geochemistry Geophysics Geosystems*, *13*, doi:10.1029/2011gc004004.
Hurowitz, J. A., S. M. McLennan, N. J. Tosca, R. E. Arvidson, J. R. Michalski, D. W. Ming, C. Schroder, and S. W. Squyres (2006), In situ and experimental evidence for acidic weathering of rocks and soils on Mars, *J. Geophys. Res.-Planets*, *111*(E2), doi:10.1029/2005je002515.
Jaumann, R., et al. (2005), Interior channels in Martian valleys: Constraints on fluvial erosion by measurements of the Mars Express High Resolution Stereo Camera, *Geophysical Research Letters*, *32*(16), doi:10.1029/2005gl023415.
Knauth, L. P., D. M. Burt, and K. H. Wohletz (2005), Impact origin of sediments at the opportunity landing site on Mars, *Nature*, *438*(7071), 1123-1128, doi:10.1038/nature04383.
Lapotre, M., B. Ehlmann, F. Ayoub, S. Minson, N. Bridges, A. Fraeman, R. Arvidson, J. Eigenbrode, R. Ewing, and J. Johnson (2015), The Bagnold Dunes at Gale Crater---A Key to Reading the Geologic Record of Mount Sharp, paper presented at Lunar and Planetary Science Conference.
Mangold, N. (2012), Fluvial landforms on fresh impact ejecta on Mars, *Planetary and Space Science*, *62*(1), 69-85, doi:10.1016/j.pss.2011.12.009.
Mangold, N., D. Baratoux, O. Arnalds, J. M. Bardintzeff, B. Platevoet, M. Gregoire, and P. Pinet (2011), Segregation of olivine grains in volcanic sands in Iceland and implications for Mars, *Earth and Planetary Science Letters*, *310*(3-4), 233-243, doi:10.1016/j.epsl.2011.07.025.
Mangold, N., A. Gendrin, B. Gondet, S. LeMouelic, C. Quantin, V. Ansan, J.-P. Bibring, Y. Langevin, P. Masson, and G. Neukum (2008), Spectral and geological study of the sulfate-rich region of West Candor Chasma, Mars, *Icarus*, *194*(2), 519-543, doi:10.1016/j.icarus.2007.10.021.
Mangold, N., et al. (2007), Mineralogy of the Nili Fossae region with OMEGA/Mars Express data: 2. Aqueous alteration of the crust, *J. Geophys. Res.-Planets*, *112*(E8), doi:10.1029/2006je002835.
McSween, H. Y., et al. (2006), Characterization and petrologic interpretation of olivine-rich basalts at Gusev Crater, Mars, *J. Geophys. Res.-Planets*, *111*(E2), doi:10.1029/2005je002477.
Michalski, J. R., M. D. Kraft, T. G. Sharp, L. B. Williams, and P. R. Christensen (2006), Emission spectroscopy of clay minerals and evidence for poorly crystalline aluminosilicates on Mars from Thermal Emission Spectrometer data, *J. Geophys. Res.-Planets*, *111*(E3), doi:10.1029/2005je002438.
Michalski, J. R., and P. B. Niles (2010), Deep crustal carbonate rocks exposed by meteor impact on Mars, *Nature Geoscience*, *3*(11), 751-755, doi:10.1038/ngeo971.
Murchie, S., et al. (2009), Evidence for the origin of layered deposits in Candor Chasma, Mars, from mineral composition and hydrologic modeling, *J. Geophys. Res.-Planets*, *114*, doi:10.1029/2009je003343.
Mustard, J. F., et al. (2008), Hydrated silicate minerals on mars observed by the Mars reconnaissance orbiter CRISM instrument, *Nature*, *454*(7202), 305-309, doi:10.1038/nature07097.
Mustard, J. F., and C. M. Pieters (1987), QUANTITATIVE ABUNDANCE ESTIMATES FROM BIDIRECTIONAL REFLECTANCE MEASUREMENTS, *Journal of Geophysical Research-Solid Earth and Planets*, *92*(B4), E617-E626, doi:10.1029/JB092iB04p0E617.
Mustard, J. F., F. Poulet, A. Gendrin, J. P. Bibring, Y. Langevin, B. Gondet, N. Mangold, G. Bellucci, and F. Altieri (2005), Olivine and pyroxene, diversity in the crust of Mars, *Science*, *307*(5715), 1594-1597, doi:10.1126/science.1109098.
Niles, P. B., D. C. Catling, G. Berger, E. Chassefiere, B. L. Ehlmann, J. R. Michalski, R. Morris, S. W. Ruff, and B. Sutter (2013), Geochemistry of Carbonates on Mars: Implications for Climate History and Nature of Aqueous Environments, *Space Sci. Rev.*, *174*(1-4), 301-328, doi:10.1007/s11214-012-9940-y.

Ojha, L., M. B. Wilhelm, S. L. Murchie, A. S. McEwen, J. J. Wray, J. Hanley, M. Massé, and M. Chojnacki (2015), Spectral evidence for hydrated salts in recurring slope lineae on Mars, *Nature Geoscience*.

Peslier, A. H. (2010), A review of water contents of nominally anhydrous natural minerals in the mantles of Earth, Mars and the Moon, *J. Volcanol. Geotherm. Res.*, *197*(1-4), 239-258, doi:10.1016/j.jvolgeores.2009.10.006.

Pettijjohn, F. J., P. E. Potter, and R. Siever (1987), *Sand and Sandstone*, Springer Science & Business Media, New York,US.

Pieters, C. M., and S. Tompkins (1999), Tsiolkovsky crater: A window into crustal processes on the lunar farside, *J. Geophys. Res.-Planets*, *104*(E9), 21935-21949, doi:10.1029/1998je001010.

Poulet, F., J. P. Bibring, J. F. Mustard, A. Gendrin, N. Mangold, Y. Langevin, R. E. Arvidson, B. Gondet, C. Gomez, and T. Omega (2005), Phyllosilicates on Mars and implications for early martian climate, *Nature*, *438*(7068), 623-627, doi:10.1038/nature04274.

Poulet, F., and S. Erard (2004), Nonlinear spectral mixing: Quantitative analysis of laboratory mineral mixtures, *J. Geophys. Res.-Planets*, *109*(E2), 12, doi:10.1029/2003je002179.

Poulet, F., N. Mangold, D. Loizeau, J. P. Bibring, Y. Langevin, J. Michalski, and B. Gondet (2008), Abundance of minerals in the phyllosilicate-rich units on Mars, *Astronomy & Astrophysics*, *487*(2), L41-U193, doi:10.1051/0004-6361:200810150.

Putzig, N. E., and M. T. Mellon (2007), Apparent thermal inertia and the surface heterogeneity of Mars, *Icarus*, *191*(1), 68-94, doi:10.1016/j.icarus.2007.05.013.

Ramsey, M. S., and P. R. Christensen (1998), Mineral abundance determination: Quantitative deconvolution of thermal emission spectra, *Journal of Geophysical Research-Solid Earth*, *103*(B1), 577-596.

Robbins, S. J., and B. M. Hynek (2012), A new global database of Mars impact craters≥ 1 km: 1. Database creation, properties, and parameters, *Journal of Geophysical Research*, *117*(E5), E05004.

Rogers, A. D., and P. R. Christensen (2007), Surface mineralogy of Martian low-albedo regions from MGS-TES data: Implications for upper crustal evolution and surface alteration, *J. Geophys. Res.-Planets*, *112*(E1), doi:10.1029/2006je002727.

Rogers, A. D., and R. L. Fergason (2011), Regional-scale stratigraphy of surface units in Tyrrhena and Iapygia Terrae, Mars: Insights into highland crustal evolution and alteration history, *J. Geophys. Res.-Planets*, *116*, doi:10.1029/2010je003772.

Rogers, A. D., and V. E. Hamilton (2015), Compositional provinces of Mars from statistical analyses of TES, GRS, OMEGA and CRISM data, *J. Geophys. Res.-Planets*, *120*(1), 62-91, doi:10.1002/2014je004690.

Ruff, S. W., and P. R. Christensen (2002), Bright and dark regions on Mars: Particle size and mineralogical characteristics based on Thermal Emission Spectrometer data, *J. Geophys. Res.-Planets*, *107*(E12), 22, doi:10.1029/2001je001580.

Shepherd, K. D., and M. G. Walsh (2002), Development of reflectance spectral libraries for characterization of soil properties, *Soil Science Society of America Journal*, *66*(3), 988-998.

Skok, J. R., J. F. Mustard, L. L. Tornabene, C. Pan, D. Rogers, and S. L. Murchie (2012), A spectroscopic analysis of Martian crater central peaks: Formation of the ancient crust, *J. Geophys. Res.-Planets*, *117*, doi:10.1029/2012je004148.

Sullivan, R., et al. (2008), Wind-driven particle mobility on mars: Insights from Mars Exploration Rover observations at "El Dorado" and surroundings at Gusev Crater, *J. Geophys. Res.-Planets*, *113*(E6), doi:10.1029/2008je003101.

Thorpe, M. T., A. D. Rogers, T. F. Bristow, and C. Pan (2015), Quantitative compositional analysis of sedimentary materials using thermal emission spectroscopy: 1. Application to sedimentary rocks, *Journal of Geophysical Research: Planets*, *120*(11), 1956-1983, doi:10.1002/2015JE004863.

Tompkins, S., and C. M. Pieters (1999), Mineralogy of the lunar crust: Results from Clementine, *Meteoritics & Planetary Science*, *34*(1), 25-41.

Tornabene, L. L., J. E. Moersch, H. Y. McSween Jr, V. E. Hamilton, J. L. Piatek, and P. R. Christensen (2008), Surface and crater-exposed lithologic units of the Isidis Basin as mapped by coanalysis of THEMIS and TES derived data products, *Journal of Geophysical Research*, *113*(E10), E10001.

Vincendon, M., J. Audouard, F. Altieri, and A. Ody (2015), Mars Express measurements of surface albedo changes over 2004-2010, *Icarus*, *251*, 145-163, doi:10.1016/j.icarus.2014.10.029.

Wyatt, M. B., and H. Y. McSween (2002), Spectral evidence for weathered basalt as an alternative to andesite in the northern lowlands of Mars, *Nature*, *417*(6886), 263-266, doi:10.1038/417263a.

Wyrick, D., D. A. Ferrill, A. P. Morris, S. L. Colton, and D. W. Sims (2004), Distribution, morphology, and origins of Martian pit crater chains, *J. Geophys. Res.-Planets*, *109*(E6), doi:10.1029/2004je002240.

Zolotov, M. Y., and M. V. Mironenko (2007), Timing of acid weathering on Mars: A kinetic-thermodynamic assessment, *J. Geophys. Res.-Planets*, *112*(E7), 20, doi:10.1029/2006je002882.

Chapter 2: Thermal and Near-Infrared Analyses of Central Peaks of Martian Impact Craters: Evidence for a Heterogeneous Martian Crust

This chapter is a manuscript that was published at Journal of Geophysical Research-Planets with the same name.

Pan, C., A. D. Rogers, and J. R. Michalski (2015), Thermal and near-infrared analyses of central peaks of Martian impact craters: Evidence for a heterogeneous Martian crust, Journal of Geophysical Research-Planets, 120(4), 662-688, doi:10.1002/2014je004676.

Abstract

Central peaks of impact craters contain materials exhumed from depth and therefore, investigation of these materials provide clues to subsurface geology and mineralogy. A global spectral survey of central peaks of Martian impact craters between 10-200 km diameter was completed using Mars Odyssey Thermal Emission Imaging System (THEMIS) data. Twenty-six central peaks with distinctive spectral signatures from surrounding plains were identified and characterized with thermal infrared and visible/near-infrared data. The distribution of spectrally distinct central peaks (SDCPs) shows some degree of regional clustering, with most craters found in western Noachis Terra, Tyrrhena Terra, within the northern rim of Hellas Basin, and fewer in the northern lowlands. With the exception of four craters in western Noachis Terra, SDCPs contain only one spectrally distinct unit at THEMIS resolution (100 m/pixel). The maximum number of spectrally distinct units observed was three, in Jones and Ostrov craters. The western Noachis Terra SDCPs may expose crustal stratigraphies of multiple igneous compositions or impact materials from Argyre. In the highlands, most SDCP units are consistent with enrichments in olivine or pyroxene relative to surrounding plains, suggesting olivine- and pyroxene-basaltic lithologies; few are olivine- and pyroxene-poor. No spatial trend in spectrally-derived

compositions of SDCPs was observed. Three SDCPs contain THEMIS signatures consistent with high abundances of phyllosilicates, which may contain the most phyllosilicate-rich lithologies found in central peak-associated materials globally.

2.1 Introduction

Constraining the compositions of Martian crustal materials is critical to understanding the processes through which the crust formed and evolved. Remote sensing provides a quantitative method for assessing the mineralogical composition of a planetary surface; and, using a number of sensors and techniques, it has been shown that the mineralogy of the Martian surface is diverse and heterogeneous at global, regional and local scales (e.g. [*Bandfield et al.*, 2000; *Christensen et al.*, 2005; *Poulet et al.*, 2007; *Rogers and Christensen*, 2007; *Bell III*, 2008; *Murchie et al.*, 2009b; *Baratoux et al.*, 2011; *Rogers and Fergason*, 2011; *Ody et al.*, 2013; *Sautter et al.*, 2014] and references therein). However, to date, very little is known about compositions at depth.

Exploring the geology of the Martian subsurface is important for several reasons. First, the bulk crustal composition might not be represented in the composition of mobile surface regolith that composes most of the geologic surfaces on Mars [*Christensen and Moore*, 1992]; and, the crust could exhibit compositional stratification with depth [*Baratoux et al.*, 2014]. Second, some of the most well understood Martian materials are the suite of Martian meteorites and, though the precise geographical origin of these stones remains elusive, it is generally accepted that they formed in the subsurface of Mars. Exploring the Martian subsurface is important for connecting petrological histories determined from Martian meteorites to crustal compositions measured remotely. Third, some fraction of the alteration phases detected on Mars likely formed in the subsurface [*Carter et al.*, 2013; *Ehlmann et al.*, 2011; *Loizeau et al.*, 2012; *Michalski and Niles*, 2010]. Characterizing

both altered and unaltered mineral assemblages exhumed from depth is key to understanding the habitability of the Martian subsurface [*Michalski et al.*, 2013].

A promising way to access deeper crustal compositions is through analysis of subsurface materials that have been exposed by natural geologic processes such as faulting or impacts. Both theoretical models and stratigraphic constraints observed in the field have shown that impact craters exhume materials from a depth that roughly equates to 1/10 of the final diameter of the crater. This relationship has been used in numerous studies to explore the subsurface geology and petrology of planetary crusts at depth [*Pinet et al.*, 1993; *Pieters et al.*, 1997; *Tompkins and Pieters*, 1999; *Tornabene et al.*, 2005; *Baratoux et al.*, 2007; *Tornabene et al.*, 2008b; *Barnhart and Nimmo*, 2011; *Caudill et al.*, 2012; *Wulf et al.*, 2012].

Because central peaks experience a variety of syn- and post-impact degradation, alteration and/or obscuration processes (e.g., [*Baratoux et al.*, 2007; *Osinski et al.*, 2013; *Tornabene et al.*, 2013; *Tornabene et al.*, 2014]), there are challenges associated with using the remotely-measured morphology and spectral characteristics of central peak materials to infer subsurface properties. For example, impact-generated hydrothermal alteration can occur in central peaks, resulting in formation of a variety of phases including K-feldspar, carbonates, silica, phyllosilicate and zeolite minerals [*Osinski et al.*, 2013; *Tornabene et al.*, 2013]. In addition, bedrock uplifted during impact can be subsequently obscured by impact melt. The spectral properties of impact melt is difficult to predict, because it can range from glassy to fully crystalline (e.g.[*French*, 1998]), and also may be altered [*Tornabene et al.*, 2013] and/or contain lithic clasts from the target [*Cannon et al.*, 2014; *Wohler et al.*, 2014]. Impact melts may in some cases be inferred from morphological and textural properties (e.g.[*McEwen et al.*, 2007; *Morris et al.*, 2010; *Tornabene et al.*, 2012]), but this requires high-resolution imagery with adequate spatial coverage, which is not always available. Last,

uplifted bedrock may be partially or fully obscured by regionally-derived surface materials [e.g. *Tornabene et al.*, 2014], either from shallower crustal units, or transported to the peak by wind or other impacts.

Central peaks that contain materials that are spectrally distinguishable from surrounding materials are not likely to be fully obscured by regionally derived materials, because otherwise they would not be spectrally distinct from those materials. However, it must be recognized that the spectral properties presented in this work are likely not accurate representations of subsurface mineralogy in many cases, and could be influenced by regionally derived regolith material or impact melt. Despite these complications, useful inferences about crustal heterogeneity, subsurface alteration, and global variability in peak modification processes may be made, as shown below.

In this work, we conducted a systematic global survey of previously-catalogued crater central peaks [*Barlow et al.*, 2000] located in low-dust regions of Mars, to locate spectrally distinct materials associated with central peaks. To date, compositional analyses of Martian crater central peaks have largely only utilized near-infrared reflectance data [*Tornabene et al.*, 2008a; *J Carter et al.*, 2010; *Marzo et al.*, 2010; *Michalski and Niles*, 2010; *Ehlmann et al.*, 2011; *Quantin et al.*, 2012; *Skok et al.*, 2012; *Sun and Milliken*, 2014] (note that Skok et al. analyzed thermal infrared data for two of their craters), which are sensitive to Fe-bearing and hydrated minerals, even in low abundances. However, thermal infrared data provide a complementary perspective, as they are more sensitive to the bulk composition of materials. Here, we utilized data from both spectral regions to provide a comprehensive picture of primary (including feldspar and mafic minerals) and secondary minerals.

Thermal infrared data in this study are from the Mars Odyssey Thermal Emission Imaging System (THEMIS), which is a multispectral imager with ~100 m/pixel spatial resolution, and the TES instrument, a Michelson interferometer with ~3 x 8 km nominal spatial resolution and 10 cm^{-1} spacing between ~200-1650 cm^{-1} range. The spatial resolution of THEMIS is higher than that of the Mars Express Observatoire pour la Minéralogie, l'Eau, les Glaces et l'Activité (OMEGA, 0.3 to 4 km/pixel) and lower than the Mars Reconnaissance Orbiter Compact Reconnaissance Imaging Spectrometer for Mars (CRISM, ~18 m/pixel for targeted image mode and ~100 m/pixel for global, multispectral survey mode). Though the THEMIS spatial resolution is lower than that of CRISM, we show that many central peaks are resolved and contain spectrally distinct materials from their surroundings in this data set.

Below, we describe the methodology that was used to identify spectrally distinct central peaks. We present the global distribution of spectrally distinct peak materials and characterize their mineralogical compositions with TIR and NIR data sets. We compare our results with that of complementary NIR-based studies [*Salvatore et al.,* 2010; *Quantin et al.,* 2012; *Skok et al.,* 2012] and conclude with a discussion of the implications for crustal heterogeneity and degree of alteration based on our results at global and regional scales.

2.2 Data and Methods

2.2.1 Crater down-selection and prioritization

A crater database created by *Barlow et al.* [2000] was first queried for all craters containing central peaks on Mars (designated "PK" in their database). Next, we further limited our analyses to craters with diameters between 10-200 km. The minimum diameter was constrained by the spatial resolution of the THEMIS thermal imager (100 m/pixel) and the simple-complex crater transition range. The simple-complex crater transition diameter generally ranges between 5-11 km,

depending on terrain type[*Robbins and Hynek*, 2012b], and the largest simple crater on Mars is ~12 km[*Boyce and Garbeil*, 2007]. Also, central peaks in complex craters smaller than 10 km have a tendency to be too small for distinction of spectral units in THEMIS data. The maximum diameter was constrained by the substantial degradation of central peaks associated with most craters above 200 km diameter. After constraining for diameter, 866 craters remained for further analysis (**Figure 2.1)**.

In order to identify which craters within this subset exhibit spectrally distinct materials in the central peak, ejecta, walls or floor, THEMIS decorrelation stretched (DCS) [*Gillespie et al.*, 1986] radiance browse images were examined for each crater (explained in detail below). A priority system was devised in which craters were ranked between zero (no spectral distinction from surroundings) and five (strong spectral distinction from surroundings). The primary criterion for determining a crater's priority rank was whether or not a strong color difference between crater materials and surroundings was observed in THEMIS decorrelation stretched radiance images. Strong color differences between the central peak and the crater floor, or between the crater wall and the rest of the crater, resulted in a higher ranking. In this process, care was taken to ensure that a crater did not receive a high rating arising from radiance saturation or other image artifacts (e.g. [*Bandfield et al.*, 2004]) . Another criterion was the availability of, and spectral detections found in CRISM summary product browse images. A site that showed a spectrally distinct central peak unit in CRISM images received a higher ranking. Finally, the availability of HiRISE and CTX images for the crater factored into a slightly higher rank. Craters in the lower priority ranks (ranked one to three) included those with central peaks with only subtle hue differences from surroundings, as well as craters with spectrally distinct material in floor materials only (e.g. dune fields, crater fill).

Because the criteria for assigning the craters to priority ranks are largely subjective, there may be some variation within the priority ranks. Thus, the central peaks of all craters within the top three priority ranks (158 craters of total 336 craters in one to five priority ranks) were examined in detail with both THEMIS and CRISM (where available) data. The boundary of the central peak was estimated using a combination of MOLA topography and visible images. After comparisons of spectral averages from each central peak and surrounding plains for these highest ranked craters, it was determined that only 26 central peaks contained spectrally distinct materials in THEMIS images (**Figure 2.1**). Peak units were considered spectrally distinct from surroundings if the emissivity values within one standard deviation of the mean for each surface did not overlap, for at least one THEMIS channel. The low number (26) of spectrally distinct peak units compared to the number that were initially flagged as potentially distinct based on the THEMIS DCS images (336) arises from the fact that spectral differences can appear exaggerated in DCS radiance images if there is little true spectral variability in the scene. In addition, color intensity differences can be observed in DCS radiance images that arise from temperature variations (because radiance is a function of emissivity and temperature). **Figure 2.2** shows one example of a crater ranked in priority bin four and which contains a central peak that appears light blue relative to crater surroundings. However, after the conversion to emissivity, and removal of atmospheric contributions, it was found that the spectra from the peak and surroundings (once normalized to the same spectral contrast) are statistically indistinguishable. This strategy of using priority ranking based on DCS radiance images, followed by detailed spectral comparisons to eliminate false positives, is a conservative approach to ensuring that spectrally distinct units within the *Barlow* [2000] population of crater interior morphologies marked "PK" (866) were not missed.

It is important to note that though this global survey was conducted systematically and relatively exhaustively, there are likely to be some spectrally distinct peaks that were missed, due to the diameter constraint and/or the way the crater was flagged in the original database. For example, Ritchey Crater, a 79-km diameter crater near 28.8°S, -51°E, exhibits a spectrally distinct central peak in both CRISM data [*Sun and Milliken*, 2014] and THEMIS data. However, because it was not marked as "PK" in the database of *Barlow et al.* [2000], it was removed from the list of potential craters in the very first down-selection step. We note that the choice to exclude central pits or complex peaks, and only focus on "central peak" crater interior morphologies, may present a bias in the final distribution of spectrally distinct uplifted materials due to the tendency of these different interior morphologies to be associated with differing target properties (e.g., [*Melosh,* 1989; *Robbins and Hynek,* 2012a]).

The final set of 26 spectrally distinct central peaks (SDCPs) (**Figure 2.1**) was further analyzed using the following data sets: (1) THEMIS thermal infrared images; (2) CRISM multispectral and targeted images; (3) TES hyperspectral data (where available); and (4) high-resolution visible imagery from THEMIS and CTX. Results are based on these 26 craters.

2.2.2 THEMIS

THEMIS (Thermal Emission Imaging System) on Mars Odyssey is a multispectral instrument consisting of a 10-band infrared imager with ~100 m/pixel spatial resolution covering ~6.8 to 14.9 μm and a 5-band visible/near-infrared imager with ~18 m/pixel spatial sampling covering 0.425 to 0.86 μm. A detailed description of THEMIS and its calibration is given by [*Christensen et al.*, 2004].

For each THEMIS image, spectral variations arising from time-dependent focal plane array temperature changes and emitted atmospheric radiance were corrected using the methods of [*Bandfield et al.*, 2004]. Radiance was then converted to apparent emissivity using the emissivity normalization method [*Gillespie*, 1986; *Realmuto*, 1990]. Spectral contributions from atmospheric dust and water ice transmission are determined by dividing the average emissivity from a spectrally uniform region by the TES derived surface emissivity from the same area. Those contributions are then removed from the THEMIS scene, leaving only surface emissivity [*Bandfield et al.*, 2004]. Because this method assumes that the atmosphere is invariant between the "known" surface (from TES-derived emissivity) and the region of interest, the training surface used to derive the "known" emissivity was limited to regions within 1000 m altitude and 150 km distance from the area of interest. Spatially variable water ice, if present, is removed using a linear least squares minimization routine [*Bandfield et al.*, 2004].

Decorrelation stretched (DCS) [*Gillespie*, 1986] and principal component analysis (PCA) [*Pearson*, 1901] emissivity images are used to identify spectrally distinct end-members in central peaks. Average spectra from representative regions of each unit are extracted to assess the spectral character of each unit as well as utilize them as scene end-members in a spectral image unmixing algorithm. The purpose of the image unmixing step is twofold: to quantitatively map the distributions of each THEMIS spectral unit [*Bandfield et al.*, 2004] and to provide a check that the spectral unit corresponds with a spatially contiguous surface component rather than an instrumental artifact. Surface emissivity of the whole THEMIS scene is analyzed on a pixel-by-pixel basis with full spectral range and minimized atmospheric and temperature effects. In this work, a synthetic negative spectral slope was included as an end-member to account for sloped emissivity spectra arising from non-isothermalities in pixels containing diverse surface aspect

angles, which were commonly observed on crater rims and other high-relief surfaces. Inclusion of synthetic slope spectra in spectral models to account for the apparent sloping continuum present in some rock/surface spectra arising from disparate temperatures in the field of view has been previously applied successfully by [*Ruff et al.*, 2006; *Stockstill-Cahill et al.*, 2008].

As a means to simply but quantitatively compare THEMIS measurements of surface composition between craters, we used a cubic polynomial curve fitting procedure to determine the wavelength of the emissivity minimum of the Si-O stretching absorption in each unit. Silicate minerals are characterized by broad emissivity minimums in the 8 to 12 μm region due to different Si-O bonding structures. The minimum emissivity in this region shifts to shorter wavelengths as silica content increases [*Coblentz,* 1906; *Vincent and Thomson*, 1972]. High abundance of sulfate minerals will also shift the minimum to shorter wavelengths [*Baldridge and Christensen*, 2009]. Therefore, the emissivity minima are indicators for compositional differences between surfaces. A Gaussian function has been used to determine this relationship between systematic shift in the minima of silicon and oxygen stretching and igneous rock composition [*Gillespie*, 1986] and applied to Thermal Infrared Multispectral Scanner (TIMS) [*Sabine et al.*, 1994] and Advanced Spaceborne Thermal Emission and Reflectance Radiometer (ASTER) data [*Hook et al.*, 2005]. Others have used a "center-of-gravity" technique [*Vincent and Thomson*, 1972] to map the silica content from THEMIS spectra [*Smith et al.*, 2013]. Here, we applied both Gaussian fits and cubic polynomial fits to the THEMIS spectra, but found that cubic polynomial fits were more representative of the spectral shapes from surface units and yield better fits for more than 90% spectra according to root mean square error (RMSE). **Figure 2.3** shows one example comparing Gaussian and cubic polynomial fits, and shows typical cubic polynomial fits to different rock types.

The cubic polynomial fit is used to determine the emissivity minimum of each spectrum here. It fits a nonlinear relationship between the value of x (THEMIS wavelength) and the corresponding conditional mean of y (emissivity):

$$y = p_1x^3 + p_2x^2 + p_3x + p_4 \quad (1)$$

An iterative non-linear least-squares algorithm was used to determine the parameters and minimum of the curve for each average unit spectrum.

2.2.3 CRISM

CRISM (the Compact Reconnaissance Imaging Spectrometers for Mars) on Mars Reconnaissance Orbiter (MRO) is a hyperspectral imaging spectrometer with 544 channels covering the visible to near-infrared spectral region from 0.4 to 4.0μm [*Murchie et al.*, 2007]. There are two investigation modes: (1) a global, multispectral survey mode with ~72 channels at 100~200 m/pixel; (2) a targeted image mode with 544 channels providing ~10×10-20 km images at 15-38 m/pixel. CRISM global mafic mineralogy and hydroxylated silicate indices (also known as "summary parameters") were first used to identify regions of interest for extraction of spectra and detailed analyses. The following summary parameters for both multispectral and targeted images were analyzed: OLINDEX, OLINDEX2, LCPINDEX, HCPINDEX, BD1900 and BD2300. These parameters were designed to capture diagnostic spectral features related to a specific mineralogy [*Pelkey et al.*, 2007], and may be used to infer the presence of olivine, low-calcium pyroxene, high-calcium pyroxene, and hydrated minerals (particularly phyllosilicates) [*Pelkey et al.*, 2007; *Murchie et al.*, 2009a]. However, the indices may be subject to false detection due to a number of factors beyond abundance, for example frosts, aerosols, albedo, spectral slopes, fine-grained coatings, grain size and mineral mixtures (eg.[*Pelkey et al.*, 2007; *Poulet et al.*, 2007; *Clenet et al.*, 2011]). Conversely, omissions can also occur, due to a variety of factors such as

spectral slopes or the presence of other minerals in the mixture (e.g. [*Salvatore et al.*, 2010; *Clenet et al.*, 2013; *Horgan et al.*, 2014]). To confirm mineral detections suggested by the CRISM summary parameters, spectral averages from locations of interest were compared with laboratory spectra from the CRISM spectral library. However, we note that false detections are still possible even with visual inspection, particularly in the case of some mineral mixtures (e.g. *Horgan et al.* [2014]); thus we can *infer* mineral species but not identify them uniquely. Prior to comparison with laboratory spectra, the CRISM spectra were ratioed to reference surfaces, to help further minimize atmospheric influence and accentuate spectral features. Wherever possible, a spectrally neutral reference surface was used, but in some cases, no such surface was available in the scene. These cases are described individually as they are presented.

2.2.4 TES

TES (Thermal Emission Spectrometer) is one of the five instruments on Mars Global Surveyor (MGS) which was launched on 7 November 1996. It consisted of a Fourier-transform Michelson infrared interferometric spectrometer, and visible/near-infrared (0.3-2.9μm) and thermal infrared (5.1-100μm) coaligned radiometers. The spectrometer measured spectral radiance between 5.8 to 50 μm with a selectable sampling interval of 5 or 10 cm^{-1}. The spatial resolution is about 3×~8km from the MGS mapping phase altitude of ~378 km. A detailed description of the TES instrument and summary of its primary mission results is given in [*Christensen et al.*, 1992; *Christensen et al.*, 2001].

For THEMIS-derived spectral units that are large enough to be isolated in TES data, TES spectra were analyzed from those units. A linear deconvolution method with nonnegative least square minimization was used to remove atmospheric components using a library of atmosphere, mineral and blackbody spectra to obtain the best fit emissivity spectrum [*Ramsey and Christensen*,

1998; *Rogers and Aharonson*, 2008]. TES data selection constraints are from [*Rogers and Christensen*, 2007] and a spectral library similar to [*Rogers and Fergason*, 2011] was used. Mineral abundances were grouped according to their structural/chemical class: feldspars, low-Ca pyroxenes (orthopyroxene and pigeonite), high-Ca clinopyroxene (augite and diopside), olivine, and ”high-silica” (combined modeled abundance of phyllosilicates, glasses, opals, zeolites, and amorphous silica). Other mineral groups, such as carbonate, sulfate, and quartz were not found above the general TES detection limits (10%) and are thus not reported here.

2. 3 Results

2.3.1 General characteristics of THEMIS spectra from SDCPs

Using THEMIS data, spectrally distinct materials were identified in 26 central peaks (**Figure 2.1**). In most cases, only a small portion of the peak area was spectrally distinct from surrounding materials in THEMIS data. However, in some cases, the majority of the peak area appears spectrally distinct. For some craters, multiple spectrally distinct units are present, in association with the central peak.

The thermal infrared spectral properties of the SDCPs were compared with one another through both visual comparison of spectra and through calculating the minimum position of the cubic polynomial fit to each peak spectral unit (**Section 2.2**). The cubic fit minima from all spectral units, laboratory spectra of common rocks from **Figure 2.3b**, and TES Surface Type 1 and Surface Type 2 are plotted in **Figure 2.4**. Generally, the shift in emissivity minimum from the longest wavelength to the shortest wavelength likely indicates a shift from more mafic mineralogy to less mafic (e.g. **Figure 2.3b**). The spectral units with strong ~11μm absorption features are consistent with an olivine-enriched composition. Spectral units which are characterized by a minimum near ~9.5-10μm are consistent with an olivine-poor composition; pyroxene-enriched compositions are

possible. Spectral units characterized by a stronger ~9μm absorption are consistent with lithologies that are poor in both pyroxene and olivine, and may indicate significant abundances of phyllosilicates, high silica glasses (volcanic or impact-generated), quartz, opaline silica or sulfate minerals. Additional spectral bands and wider wavelength ranges are required for detailed discrimination of compositional units. CRISM-derived compositional characteristics for each spectral unit associated with the central peaks are described in subsequent sections. Except where specified, all of the CRISM spectral averages are chosen from areas within the THEMIS-defined spectral units.

2.3.2 Global distribution of SDCPs

Locations of spectrally distinct central peaks (SDCPs) are shown in **Figure 2.1**. Though the small number of SDCPs preclude strong conclusions about the global distribution, some degree of geographical clustering is apparent. We attribute this clustering to genuine geological differences considering that all of the regions contain similar quantities of data covering similar numbers of craters in similar detail. The clustering likely reflects regional variation in 1) subsurface composition (including pre-impact alteration) or target properties (**Section 2.1**); 2) surface alteration processes; 3) impact-related alteration and/or 4) degree of exposure or regional sediment mantling (**Section 2.1**). However, we note that the clustering is remarkably similar to that observed by *Skok et al.* [2012], who limited their analyses to central peaks that clearly contained crater-exposed bedrock in HiRISE imagery (using the "Crater-Exposed Bedrock" database created by *Tornabene et al*. [2010]). Thus we suggest that the geographical clustering is less likely to be influenced by regional variation in sediment mantling. Last, SDCPs are apparently not restricted to a particular elevation or diameter range, spanning -5000m to 2000 m elevations and 15 to 143 km diameters (**Table 2.1**).

Figure 2.6 shows the global distribution of THEMIS-derived cubic fit minima (**Section 2.2**) for the 26 SDCPs. There is no apparent association between minimum positions and spatial distribution. However, each geographical region does exhibit some similarities between craters. For example, in THEMIS data, the western Noachis Terra region is the only location where multiple spectrally distinct units are associated with the peak, possibly indicating a higher degree of vertical heterogeneity in this region compared to other, similarly-aged terrains. Possible origins for these units are described in **Section 4.2.1**. The Tyrrhena Terra region is the only area where phyllosilicate-bearing units in central peaks show thermal infrared spectral characteristics consistent with phyllosilicates in THEMIS data, likely indicating a higher abundance of phyllosilicate minerals in these craters. This is described further in **Section 4.2.3**.

For ease of discussion, below we divide the craters into five groups according to their regional locations, and present results within each region. The "western Noachis Terra" group contains SDCPs within Mare Erythraeum, a low albedo region found north of Argyre basin, as well as one located on the northern rim of Argyre. The "northern lowlands" group contains one crater within Acidalia Planitia and one in the Cerberus plains. The "Tyrrhena Terra" group contains central peaks in the cratered terrains between Syrtis Major and Hellas Basin, and includes one crater just to the east of Hesperia Planum. The "northern Hellas" group contains central peaks found generally within the outer ring of the northern portion of Hellas Basin. As will be shown, craters within each of these regions tend to show distinct characteristics from those in other regions, and exhibit shared characteristics within each region. There are three craters that are spatially distant from these regions, and therefore are grouped to "other".

2.3.3 Spectral and geologic characteristics of central peaks by region

2.3.3.1 Western Noachis Terra

There are six craters in the west Noachis Terra region and all of them are found in Noachian-aged terrain (Npl1) [*Scott and Tanaka*, 1986] (**Figure 2.7**). It should also be noted that Hale is located on the rim of Argyre Basin. Four craters (Craters Jones (-19.1°N,-19.7°E, diameter 90km), Alga (-24.3°S, -26.7°E, diameter 20km), Ostrov (-26.5°S, -28.1°E, diameter 76km) and C305 (-30.3°S, -33.6°E, diameter 85km)) contain more than one spectrally distinct unit in the central peaks, which is unique among all of the study regions. Spectral units in this region exhibit cubic fit minima positions from ~11.0 μm to ~9.3μm (**Table 2.1**), nearly covering the full range of minima observed within the full set of 26 craters (**Figure 2.4**). Thermal and near infrared spectral analyses of these craters are described below.

Jones Crater, a 90 km diameter well -preserved crater located at -19.1°N, -19.7°E (**Figure 2.8**) contains a central peak which is bordered by a dune field to the southeast. Based on crater counts on Jones' ejecta as well as cross-cutting relationships with fluvial valleys, *Mangold et al* [2012] suggest that Jones crater formed during the Late Hesperian period. Jones has three distinct THEMIS spectral units with cubic fit minimum positions near ~10.3μm (Unit A), ~9.62μm (Unit C) and ~9.57 μm (Unit B) (**Figure 2.8A-B**). The three units are spatially adjacent to one another and, together, span nearly the entire peak (**Figure 2.8**). Using the average unit spectra from **Figure 2.8B** to linearly unmix the emissivity image (**Figure 2.9A-C**), it can be seen that Jones unit A is found in the low lying, central portion of the peak. Jones Unit B has high concentration in the western part of the peak as well as the dune field abutting the south and eastern margins of the peak. Jones Unit C covers the eastern portion of the peak. From CRISM data (**Figure 2.8**), unit A has a strong 1.2 μm absorption, consistent with olivine, unit B lacks absorption features, and unit C's strong 1.8 μm absorption suggests a dominance of low-Ca pyroxene (**Figure 2.8C-E**). TES data were available only for Unit C, and fully isolate the unit as observed in THEMIS (**Figure**

2.9A-C). **Figure 2.S 9D-I** show geomorphologic characteristics of areas mapped with high concentrations of Unit A to Unit C respectively. High concentrations of Unit A are associated with light-toned buttes that contain intersecting linear raised ridges, which may be dikes. Unit B exhibits high concentrations along the large, light-toned ridge that forms the western portion of the peak, as well as in smaller, low-lying buttes and ridges nearby the larger ridge. It is also present in darker-toned material found on the side and base of the large ridge. Similar to the other two units, Unit C exhibits highest concentrations in the light-toned buttes. These buttes exhibit significant mantling by darker-toned material in many areas; these areas tend to exhibit lower concentrations of Unit C. The TES linear deconvolution model indicates ~40% pyroxene, ~30% feldspar, and ~5% olivine (**Figure 2.10**), consistent with a pyroxene basaltic composition (note that intrusive vs. extrusive origins cannot be distinguished spectrally. The TES spectrum of Jones unit C, convolved with THEMIS bandpasses, is consistent with the average THEMIS spectrum of the same unit (derived from different TES orbits), corroborating the TES-derived spectrum. The THEMIS spectral unit distribution of Unit C is somewhat diffuse (C and I in **Figure 2.9**), likely indicating variable spectral contrast or compositions within the TES field of view, but the spatially dominant composition is Unit C. Combining VNIR and TIR spectral analyses, the three units associated with Jones' peak may be described as follows: unit A is olivine-enriched and feldspar-poor, unit B is olivine- and pyroxene-poor, and unit C is pyroxene basaltic with little to no olivine.

Another large crater, Ostrov (-26.5°S, -28.1°E diameter 76km), also contains three distinct units, with emissivity minimum positions at ~10.85 μm, ~10.16 μm and ~9.57 μm. CRISM shows that the unit with minimum position at ~10.85 μm is olivine–bearing and the other two units are pyroxene-bearing. The THEMIS and CRISM spectral characteristics of Ostrov were described in detail in previous work [*Skok et al.*, 2012], but can also be viewed in **Figure 2.S2**.

Alga crater (-24.3°S, -26.7°E, diameter 20km), located between Jones and Ostrov, has two distinct units with minimum positions at 10.60 μm (Unit 1) and 9.99 μm (Unit 2) respectively. CRISM data show that Unit 1 is olivine-bearing, and the Unit 2 is pyroxene-bearing [*Skok et al.*, 2012](**Figure 2.S1**).

Crater C305 (-30.3°S, -33.6°E, diameter 85km, **Figure 2.S8**), located between Ostrov and Hale crater (**Figure 2.7**), exhibits two statistically distinct spectral units in the central peak; with minimum positions at 11.0 μm and 10.53 μm. The CRISM olivine index stretch map suggests olivine in the peak Unit 1, however, it is difficult to confirm this detection due to the overall noise level in the spectra. Unit 2 of C305 is clearly pyroxene-bearing.

Crater C324 (-28.9°S, -46.2°E, diameter 26km, **Figure 2.S9**), located to the west of the other craters, contains only one spectrally distinct unit in its central peak with a minimum position at 10.56 μm The spectrally distinct unit is also associated with isolated knobs around the margin of the crater floor. CRISM data do not cover the spectrally distinct area of the peak, however there is coverage over the spectrally distinct knobs around the floor. The spectra are consistent with olivine enrichment.

Hale crater (-36°S, -36.2°E, diameter 143km) has a large, central peak that contains large areas that are distinct from the floor materials and surroundings. Its minimum position of cubic fit is at 10.09 μm. In this crater, a spectrally neutral reference surface was not available in CRISM. However, the peak unit likely contains pyroxene based on the broad ~2.0μm absorption feature in the unratioed spectrum. (**Figure 2.S7**).

2.3.3.2 Northern lowlands

There are two craters in the northern lowlands; one of them is located in Chryse/Acidalia and the other one is located in the Cerberus plains. Unlike the western Noachis Terra region, each central peak only exhibits one unit that is spectrally distinct in THEMIS from the surrounding plains or crater floor. In the Cerberus plains (crater C29), the central peak unit was characterized as minimum position at 10.42 μm, indicating increased olivine content relative to surroundings; the crater in Chryse/Acidalia has minimum position at 9.80 μm, indicating olivine-poor materials.

Details for the Cerberus crater (C29, 9.48°N, 150°E, diameter 53km) are shown in **Figure 2.11**. A large dune field covers the crater floor south of the peak. The central peak and the dune field both have an ~11 μm absorption, consistent with olivine enrichment, but the sand dune has a stronger ~11 μm absorption and deeper band depth (**Figure 2.11**). The spectral contrast differences may arise for a number of reasons, such as differences in particle size, concentration, and/or dust cover; the overall similarity in spectral shape suggests that the dunes might have been at least partially sourced from the central peak. CRISM spectra from the dune field are consistent with pyroxene enrichment, and possibly also olivine; the olivine contribution is difficult to assess given the overall positive slope imposed on the ratio spectrum. However, both TES (not shown) and THEMIS data indicate enrichments of olivine and pyroxene. Most of the central peak has no CRISM coverage, including the area identified as spectrally distinct in THEMIS. The small area of the peak that is covered by CRISM is spectrally bland. Though a variety of glassy materials, including impact melts, can have muted spectral features in the NIR, the lower spectral contrast of this area in the TIR points to increased dust cover [*Horgan and Bell*, 2012].

For Crater Kunowsky (56.93°S, -9.71°E, diameter 66km, **Figure 2.S23**), found in Acidalia, CRISM parameter images suggest mafic minerals in a few isolated exposures in the central peak that are ~500m across. Interpretation of CRISM spectra from these areas is somewhat complicated

by the lack of a suitable reference spectrum (the reference surfaces exhibit strong negative slopes towards longer wavelengths, which is typical of the northern plains [e.g. *Poulet et al*., 2007; *Salvatore et al*. 2010]). However, the ratioed spectrum, despite the imposed slope, suggests a mixture of olivine and pyroxene. Olivine is clearly detected in the floor, wall and ejecta of Kunowsky from CRISM data. These observations are interpreted in **Section 4.2.2**. Finally, though phyllosilicate minerals have been detected in some northern plains craters[*J Carter et al.*, 2010], the craters presented here were not among those identified as phyllosilicate-bearing by Carter et al.

2.3.3.3 Tyrrhena Terra and cratered terrain bordering eastern Hesperia Planum

Five SDCPs are found in the Tyrrhena Terra region. The cubic fit minimum positions are from 11.16 μm to 9.58 μm covering almost the whole range of all the spectrally distinct units (**Figure 2.12**). Among the five craters, two craters (C791 (-3.39°S, 97.91°E, diameter 56km) and C910 (-6.08°S, 58.8°E, diameter 43km)) have no mineral detections in CRISM spectral parameter browse images (though coverage does exist). The remaining three craters contain both olivine and hydroxylated silicate absorptions (**Figure 2.13**). For the hydroxylated silicate detections, the extracted spectra all show bands at ~1.4μm, ~1.9μm, and near 2.28-2.3μm, which are consistent with Fe/Mg phyllosilicates (eg. [*Clark*, 1999]). The spectra from crater C811 (-13.4°S, 93.78°E, diameter 20km) also show absorption near ~2.5μm. Paired absorptions at ~ 2.3 μm and ~2.5 μm are consistent with overtones and combination tones of C-O stretching and bending fundamental vibration (e.g. [*Gaffey et al.*, 1993]), possibly indicating carbonates mixed with the phyllosilicates. Alternatively, a mixture of phyllosilicates and zeolites could give rise to these absorptions [e.g. *Tornabene et al.,* 2013]. Zeolites exhibit a metal-OH plus hydration combination tone near ~2.5 μm [*Cloutis et al.,* 2002], (**Figure 2.13**). Carbonate minerals also exhibit absorptions near ~3.4

and 3.9 µm. From our data, it is not clear whether these absorptions are present or not (**Figure 2.15**);interpretation of this spectral region is particularly complex due to contributions from both solar reflectance and thermal emission [*Ehlmann et al.*, 2008].

The THEMIS spectral character of units with 2.3 µm absorptions is variable, ranging from a very strong ~9.6µm absorption in C784 (**Figure 2.14**) to very strong ~11 µm absorption in C811 (-13.4°N, 93.78°E , diameter 20km). In both of these cases, phyllosilicate absorptions are stronger and cover a larger area than the mafic mineral absorptions in CRISM summary parameter images (**Figure 2.16C-D**). On the basis of similar CRISM spectra, we conclude that similar species of phyllosilicate (similar to an Fe-bearing chlorite-group mineral) are found in both craters. However, only C784 exhibits THEMIS spectral character consistent with strong phyllosilicate abundance. Combined with the CRISM data, these observations suggest that the phyllosilicate abundance or particle size is much higher in C784 than in C811.

2.3.3.4 Northern Hellas

There are 10 SDCPs in the northern Hellas region (**Figure 2.17**). As in the northern lowlands and Tyrrhena Terra regions, each crater in the northern Hellas region has only one spectrally distinct unit associated with the central peak, in THEMIS data. The cubic fit minimum positions are from 10.50 µm to 9.65 µm, with no association between composition and spatial distribution or elevation. CRISM spectral parameters suggest that olivine and/or pyroxene are present in all central peaks (except for one crater without CRISM data coverage, C904 (-22.2°S, 66.94°E, diameter 83km). Some craters contain only olivine-bearing materials, with no detectable pyroxene (C881, -31.6°S, 81.67°E, diameter 20km;C906, -22.1°S, 73.18°E, diameter 84km; C862, -24.6°S, 87.56°E, diameter 29km; C870, 36.7°S, 86.66°E, diameter 31km; Crater1_1(-27°S, 76.04°E,

diameter 41km). Two craters contain units whose CRISM spectra are consistent with mixtures of olivine and pyroxene (C17,-23.4°S, 74.36°E, diameter 67km; C151,-18.9°S, 62.81°E, diameter 52km) (**Table 2.1 and also Supplementary figures**). Craters 398 (-21.8°S, 44.78°E, diameter 40km) and 399(-24.5°S, 43.43°E, diameter 23km) contain multiple distinct units in CRISM. Crater 398 contains one olivine-bearing unit, one pyroxene-bearing unit and one unit with a strong ~1.3 μm feature. Crater 399 contains one pyroxene-bearing unit and one unit with a strong ~1.3μm feature. The ~1.3 μm feature has been attributed to feldspar-dominated lithologies such as granitic and/or anorthositic material [*J Carter and Poulet*, 2013; *Wray et al.*, 2013]. THEMIS spectra of C398 and C399 are consistent with anorthosite or basalt, but not with pure granite (**Figure 2.S26**).

Here, we focus on a cluster of three craters centered at -26.95°N, 76.04°E (**Figure 2.18**). Two distinct spectral units (Unit A and Unit B) are associated with the central peak, crater wall and ejecta of these adjacent craters. The two units with cubic fit minimum positions at 10.23 μm and 10.70 μm appear purple and bluish magenta in a THEMIS 8-7-5 DCS mosaic (**Figure 2.18**). They primarily differ by the strength and shape of their THEMIS absorption near ~12μm. Unit A is associated with the central peak and wall of Crater1_1, and with the peak of Crater1_2. Unit B is found in the ejecta of Crater1_1 and Crater1_3 (Crater1_3 is the smallest crater). TES spectral data covering the central peak of the largest of the three craters suggest an olivine abundance of >30% [*Rogers and Fergason*, 2011]. CRISM data also show a spectral distinction between the two units that may arise from differences in olivine composition and/or particle size [e.g. *Ody et al.*, 2012]. If the two spectrally distinct units in these adjacent craters have similar degree of influence from syn- and post-impact degradation processes, they may represent vertical variations present in the subsurface, where Unit A represents the lower of the two units with a maximum depth of ~3km [*Melosh and Ivanov*, 1999].

2.3.3.5 Other

Three isolated craters were also observed to have spectrally distinct materials associated with their central peaks: crater C80 (-30.5°S, 160°E, diameter 84km), located in Mare Sirenum with cubic fit minimum position at 10.06 μm. There, two CRISM spectral units are found in the peak, with one olivine-bearing and the other pyroxene-bearing. Crater C378 (-6.32°S, 19.38°E, diameter 22km), located in Sinus Meridiani with a fit minimum at 9.80 μm contains olivine and pyroxene bearing units in CRISM data. Crater C107 (-32.3°S, 140.8°E, diameter 67km), located in Cimmeria Terra, exhibits a cubic fit minimum at 10.53 μm. Hydroxylated silicates are observed in one crater, C107, located in Cimmeria Terra (**Figure 2.19** and **Figure 2.S5**). Other than the Tyrrhena region, C107 contains the only SDCP where hydrated minerals are observed. The spectral character of the C107 detection, with a lack of a 2.29-2.30 μm absorption, and the presence of a 2.39 μm absorption, suggests phyllosilicate (a mixture of pumpellyite / prehnite and zeolite). This is different than the Fe/Mg-smectites found in the Tyrrhena region. This phyllosilicate unit is mixed with olivine ,and olivine is dominant at THEMIS resolution (with a fit minimum at 10.53 μm).

2.4 Discussion

2.4.1 Implications from global distribution of SDCPs

At THEMIS spatial resolution, SDCPs are generally restricted to latitudes equatorward of 45° (**Figure 2.1**). The lack of SDCPs at high-latitudes suggest that latitude-dependent degradation processes, such as periglacial activity, may have obscured or altered peak units such that they are indistinguishable from surrounding units. From neutron spectroscopy data, near-surface ice is present continuously at latitudes >60° [*Feldman et al.*, 2002]. At latitudes between 30-60°, a discontinuous mantle of “dissected” terrain, interpreted as devolatilized, formerly ice-cemented soils is also present [*Mustard et al.*, 2001]. In addition, global, low-resolution spectral mapping of

martian surface materials has shown a relationship between surface alteration and latitude, which may relate to fluvial or glacial activity [*Pinet and Chevrel*, 1990; *Wyatt et al.*, 2004; *Rogers and Christensen*, 2007]. As described for the global distribution of bedrock exposures by previous work [*Edwards et al.*, 2009], near-surface ice could have led to mechanical breakdown and/or burial of central peak materials, causing enhanced homogenization with surrounding units. Chemical alteration associated with mechanical breakdown of materials could have also occurred, resulting in a lack of strong primary mineral signatures in the northern lowland central peaks.

Some regions in the highlands have a much larger proportion of SDCPs than others. Tyrrhena Terra and western Noachis Terra are similar in age and surface units to Terra Cimmeria, Terra Sirenum, and central Noachis Terra [*Scott and Tanaka*, 1986; *Greeley and Guest*, 1987], yet they have a larger percentage of spectrally distinct craters per unit area. Given that SDCPs are mainly observed within ±30° latitude, this might suggest that the regional differences in peak spectral characteristics within this band are not dominantly due to differences in surficial chemical or mechanical alteration. Rather, subsurface differences in igneous, crust-forming compositions, physical properties or alteration environments may contribute to the regional clustering observed. However, it is difficult to rule out spatial variability in degradation processes. In addition, because the crater interior morphology (e.g. central peak, summit pit, floor pit, complex uplift) is somewhat controlled by the target properties [*Melosh*, 1987], the exclusive focus on central peaks in this study may also exert some control on the global distribution observed in **Figure 2.6**.

Most of the SDCPs exhibit enrichments in pyroxene and/or olivine, which could be consistent with a variety of intrusive or extrusive igneous lithologies. It is difficult to distinguish intrusive and extrusive origins, in that textures (e.g. crystal size), which are critical for distinguishing these origins, are discernable from orbit. It is likely that the crust is composed of

buried volcanics and fragmented regolith that might have been intruded by plutonic rocks and/or dikes at depth, but those scenarios cannot be resolved from spectral data alone.

2.4.2 Characteristics of central peaks in each region

2.4.2.1 Western Noachis Terra

The western Noachis Terra region is distinctive in that multiple spectral units are present in individual central peaks. In a similar study of impact craters using only CRISM data [*Skok et al.*, 2012], which has a much higher spatial resolution than THEMIS, multiple spectral units were found in other regions besides western Noachis Terra. One likely reason for the difference in findings is the scale of the outcrops—for reasons unknown, the individual multiple units are large enough in this region to be distinguished in THEMIS data, but smaller in other locations. An alternative explanation is that perhaps this area has experienced a substantially different erosional history, resulting in better exposure of units.

The spectral character associated with western Noachis Terra SDCPs range from olivine rich basaltic, pyroxene and/or olivine basaltic, and TES Surface Type 2-like (which likely has variable composition, and could include pyroxenite). There are also two units (Ostrov unit 3 and Jones unit B) which are not common in other regions. “Basaltic” designates composition only, and does not distinguish between extrusive, plutonic, or impact melt origins. In both THEMIS and CRISM data, the unit found in Jones crater with minimum at 9.62 μm is consistent with an olivine and pyroxene poor lithology; and the lack of evidence for hydration in CRISM points to a lack of contribution from hydrated silica or sulfates. Thus, this unit may represent a silicic lithology, such as rhyolite, siliceous tuff, or granite, or may have a strong contribution from an anhydrous sulfate such as anhydrite.

Similar to the results of *Quantin et al.* [2012] and *Skok et al*. [2012] for craters in an around this region, low-Ca pyroxene is the dominant pyroxene observed for these craters. As nearly all of these impacted into Noachian crust, these observations support a previously observed trend that Noachian crust is dominated by low-Ca pyroxene (rather than high-Ca pyroxene) (e.g. [*Mustard et al.*, 2005]). Finally, in contrast with the interpretations of previous work in this region [*Skok et al.*, 2012], we do not find evidence for monomineralic olivine-bearing units (e.g. dunites). This may be due to lack of sensitivity to plagioclase in the VNIR, or to the difference in spatial resolution between CRISM and THEMIS, where THEMIS pixels may include greater contribution from regionally derived, non-distinct materials.

It is not clear whether some of these olivine- and pyroxene-basaltic spectral units associated with multiple peaks represent the same stratigraphic units or not. Limited data coverage with high spectral resolution, uncertainties in THEMIS atmospheric correction, and influence from impact-related alteration (shock and/or impact melt) or post-impact degradation processes all contribute to the difficulty in assigning common genetic origin to spatially isolated units separated by hundreds of kilometers. Furthermore, real variations in primary mineral abundance within stratigraphic units could be present, which could be confused as separate stratigraphic units from remote measurements. Nevertheless, below we assess the possibility that some units share a common origin.

For Hale, there is *a priori* evidence that any subsurface materials exposed by this crater may have experienced a distinctly different geologic history than the other craters in the region. Hale crater is located on the rim of Argyre Basin, a much larger impact basin that likely exposed deep crustal material (e.g. [*Ody et al.*, 2013]). Thus we do not consider its units to have a strong likelihood of linkage to the other five craters.

Alga crater, because it has impacted the floor materials of a much larger crater in this region ("Chekalin"), may also not have impacted into similar target materials. Crater depth/diameter relationships for Martian complex craters in the southern highlands [*Robbins and Hynek*, 2012a] indicate that Chekalin likely had a depth of about ~3.8km when it initially formed (though depth/diameter relationships do vary as a function of latitude and terrain type [*Robbins and Hynek*, 2012a]). The current rim-to-floor depth of Chekalin crater is ~800m, suggesting ~3.0 km of fill in Chekalin crater. Though this is an upper limit for fill depth because it does not account for degradation of the crater rim height; these relationships suggest that it is possible that Alga crater (20 km diameter) only exposed Chekalin's crater fill materials, using approximate excavation depths of ~0.03 to~0.10 of the crater diameter [*Maxwell*, 1977; *Croft*, 1985; *Sharpton*, 2014]. However, the lowermost portion of Chekalin's fill materials may be comprised of deposits originating from the melt and breccia lining of the transient cavity, and thus Alga could be sampling some of the same units as nearby Ostrov.

The five remaining craters (including Alga), which range in diameter from ~20-90 km, all exhibit olivine-basaltic or olivine- and pyroxene-basaltic lithologies associated with their central peaks. Alga, Ostrov, and C324 also exhibit olivine-bearing units in the crater walls or in isolated knobs near the margins of the crater floor. Olivine-poor, pyroxene basaltic units are exposed only by Jones, Ostrov, and Alga, which range in diameter from ~20-90 km. Because neither the olivine-basaltic or olivine-poor, pyroxene basaltic compositions are restricted to a given diameter range, a continuous subsurface stratigraphy of only a single olivine-bearing and single pyroxene-bearing basaltic unit is not possible. Rather, the data suggest that these units exist at variable depths or that multiple olivine-bearing units are present in the crustal stratigraphy. To the north, in Ares Valles, multiple olivine-bearing units separated by olivine-poor units are clearly present

in exposed stratigraphy [*Rogers et al.*, 2005; *J H Wilson and Mustard*, 2013]; units exposed in western Noachis Terra SDCPs may be analogous to this. A second possibility, consistent with the variable depths of exposure, is that the peaks expose impact ejecta blocks or impact melt from the Argyre Basin impact event. This giant impact basin would have likely excavated lower crust or mantle materials, which would have been enriched in olivine and pyroxene. Indeed, a high-Ca pyroxene- bearing unit was mapped out with CRISM data within a ring graben around Argyre as well as in nearby knobs interpreted as overturned ejecta from the Argyre impact [*Buczkowski et al*., 2010]. Though most of the units here exhibit absorptions more consistent with LCP than HCP, the possibility that these central peak units access Argyre impact ejecta still exists. Alternatively, thick sheets of impact melt could have differentiated into multiple units prior to complete crystallization. Later impacts into the ejecta would have exposed these materials.

Smaller regions of continuous subsurface stratigraphy might be shared among some of the craters in this region, however. One test for continuous subsurface stratigraphy is that the shallowest units should also be exposed in deep channels in the region. Indeed, there are strong olivine signatures found in Ladon Valles [*Kraft et al.*, 2014], a 2 km-deep channel located ~100km northwest of Alga and Ostrov; however, preliminary analysis of THEMIS and CRISM data shows that there are no similar olivine detections in Samara Valles or Himera Valles, which are ~1 km deep and located ~ 300 km northeast of Alga and Ostrov craters. The small craters in this region (Alga, 20km in diameter) may expose rocks that were originally ~2 km below the pre-impact surface. Thus, it is possible that olivine-bearing units in Ladon Valles and olivine units in some of the western Noachis Terra central peaks are exposing the same subsurface stratigraphy. But an uncommon origin is difficult to rule out.

Jones crater contains an olivine- and pyroxene-poor unit that lacks hydration or hydroxylation features in CRISM data. The combined THEMIS and CRISM signatures of the Jones unit are consistent with siliceous materials, or an anhydrous sulfate-bearing composition. Distinguishing between these compositional possibilities is difficult given the available data. Among the three units present in Jones' central peak, this mafic-poor unit is also dominant in the sand deposits found on the eastern side of the crater floor, suggesting an easily eroded material; and, CTX imagery shows a partially mantled peak unit that has a friable appearance (**Figure 2.9**). Previous work [*Bandfield et al.*, 2013] suggested that, on the basis of thermophysical and morphological observations of highland units exposed in crater and canyon walls, poorly-consolidated materials of likely volcaniclastic origin may dominate the upper few kilometers of some of the Noachian aged surfaces. It is possible that the olivine- and pyroxene-poor unit exposed in this fresh crater may represent a better-preserved, less altered version of such a volcaniclastic unit.

2.4.2.2 Northern lowland central peaks

Surface materials in the northern lowlands are spectrally consistent with glassy or altered materials, either by acid leaching, isochemical surface weathering, silica deposition or oxidative weathering (e.g. [*Bandfield*, 2002; *Kraft et al.*, 2003; *Michalski et al.*, 2006; *Minitti et al.*, 2007; *Salvatore et al.*, 2010; *Horgan and Bell*, 2012]). However, in dune fields found in the floors of large-diameter (>40 km) craters in the northern lowlands [*Rogers and Christensen*, 2007; *Ody et al.*, 2013], olivine-bearing or apparently unaltered basaltic materials have been detected, and small exposures of olivine have been reported in some (but not all) crater ejecta, rims, walls and central peaks in Acidalia and Chryse Planitiae [*Salvatore et al.*, 2010]. These authors argued that the distinctive mafic compositions in these crater-related units represent excavation of Hesperian basaltic material. As most of the olivine-bearing ejecta in Chryse and Acidalia Planitia are found

in small diameter (5-20 km) craters, [*Ody et al.*, 2013] suggested that olivine bearing units are restricted to shallow depths. Our work supports this hypothesis, in that the one central peak (crater >10 km diameter) that was found to be spectrally distinct in Acidalia and Chryse Planitiae (Kunowsky crater), exhibits only very small spots with *weak* olivine absorptions in CRISM data and a minimum at 9.80 μm (olivine-poor) signature in THEMIS data. However, the crater floors, walls and ejecta of this crater is olivine-enriched in both datasets. Thus the subsurface could be olivine-enriched at shallow depth about 0.5-2 km, which is exposed by ejecta only, and the deeper subsurface (>2km) could be olivine-poor, and exposed in central peaks. An alternative explanation is that the ejecta and central peaks may have expose similar compositions but the peaks are obscured compared to the ejecta.

Last, the one SDCP in the northern lowlands that does exhibit THEMIS spectral character consistent with olivine is found in the plains of Cerberus Palus. These plains exhibit morphologies consistent with lava and have been widely interpreted as young volcanic plains [*Plescia,* 1990; *Keszthelyi et al.,* 2006; *Jaeger et al.*, 2007; *Keszthelyi et al.,* 2010; *Ryan and Christensen*, 2012]. The weak olivine signatures found in the central peak of this crater supports this interpretation.

2.4.2.3 Tyrrhena Terra central peaks

A distinguishing characteristic of the Tyrrhena Terra region is that three of the five SDCPs contain both olivine and phyllosilicate minerals in near infrared data (this work, also *Loizeau et al.,* [2012]). For one of these peaks (C811), olivine dominates the THEMIS spectrum over a portion of the phyllosilicate-bearing region of the peak (**Figure 2.16**). The remainder of the phyllosilicate-bearing area of the peak is not spectrally distinct in THEMIS data, suggesting that the abundance of phyllosilicate minerals is low across the peak. However, for craters C784 and

C810, the THEMIS spectrum from the spectrally distinct portion of the peak is consistent with high abundance of phyllosilicates. In fact, this is the only location where phyllosilicate-bearing units associated with central peaks show spectral character consistent with phyllosilicate minerals in THEMIS data, indicating a higher abundance of phyllosilicate minerals in these craters. The Tyrrhena Terra region as whole exhibits a higher than average number of phyllosilicate detections [*J Carter et al.,* 2013];this study adds additional information that there is a higher than usual phyllosilicate *abundance* associated with crater central peaks in this region compared to other regions globally. If the phyllosilicate minerals associated with Tyrrhena peaks formed through non-impact related processes, this could point to a unique subsurface environment in this region.

2.4.2.4 Northern Hellas

The Hellas Basin likely brought mantle materials near the surface, and provides an opportunity to sample very deep materials in superposed crater central peaks along the basin rim. Though many central peaks found within the northern outer ring of Hellas Basin contain spectrally distinct materials, enriched in olivine or pyroxene, we do not observe a clear association between THEMIS cubic fit minimum positions and geographical location, diameter or elevation within the basin rim. This is not surprising, given that the craters sample different depths and that the impact very likely would not bring mantle lithologies up uniformly in depth. Furthermore, the Hellas Basin shows evidence for intense resurfacing and sedimentation [*Tanaka and Leonard*, 1995; *Malin and Edgett*, 2000; *Leonard and Tanaka*, 2001; *Moore and Wilhelms*, 2001; *Korteniemi et al.*, 2005; *Mest and Crown*, 2005; *Moore and Howard*, 2005; *S A Wilson et al.*, 2007; *L M Carter*

et al., 2009; *Williams et al.*, 2009; *Williams et al.*, 2010]; thus alteration, particularly mechanical weathering, may have played a role in modifying the original peak compositions.

Despite the lack of trends on a large scale, some evidence for local-scale stratification in lithology is observed. In **Figure 2.18**, a location with three adjacent craters containing two distinct olivine-bearing compositions is shown. There, two olivine-bearing units are found in locations with self-consistent crater-exposed depths between the three craters. The stratigraphy may represent layers of ejecta brought up from the formation of Hellas basin, or very large scale (~20 km) stratigraphy in the wall rock of the basin. Considering that no other central peaks expose a similar local-scale stratigraphy, it may be a particularly well preserved area within the Northern Hellas region.

2.5 Conclusions

Through detailed analyses of THEMIS, CRISM and TES data, we have made the following major observations and conclusions:

1. Of the 866 craters central peaks and with diameter between 10-200 km, globally, 26 crater central peaks were found to contain materials that are spectrally distinct from surrounding plains in THEMIS data. Central summit pits, floor pits, and complex peaks were not examined in this study.
2. The global distribution of spectrally distinct central peaks (SDCPs) shows some degree of regional clustering, with a distribution similar to that presented by *Skok et al.* [2012], and are mostly restricted to low latitudes. Most SDCPs are found in western Noachis Terra, Tyrrhena Terra, and within the northern rim of Hellas Basin; two are located in the northern lowlands. Though spatial variability in degradational processes are a likely factor, subsurface differences in igneous, crust-forming compositions, physical properties or alteration environments

probably also contribute to the regional differences observed. The lack of SDCPs at high-latitudes (>45°) suggest that latitude-dependent alteration processes have obscured or altered peak units such that they are indistinguishable from surrounding units.

3. Globally, no spatial trend in composition of central peak-associated materials is observed.
4. The western Noachis Terra area is the only region in this study where multiple THEMIS-defined spectral units are present in individual central peaks. These units may represent crustal stratigraphies of igneous units or ejected crustal materials or impact melt from the Argyre Basin.
5. One central peak was found to be spectrally distinct in Acidalia and Chryse Planitiae, and exhibits weak olivine signatures in areally small locations in the peak. Though the peaks do not exhibit strong mafic mineral contributions, the crater floors, walls and ejecta are olivine enriched. The likely explanation, as proposed by *Salvatore et al.* [2010] and *Ody et al*. [2012], is that materials at shallow depths are olivine-bearing, whereas units at deeper levels (>~ 2 km) are olivine poor. Alternatively, peak materials may be less well exposed than wall and ejecta materials.
6. One central peak was observed to contain olivine-bearing material in Cerberus Palus, which has been widely interpreted as young volcanic plains [e.g. *Plescia*, 1990; *Keszthelyi et al.*, 2010].
7. Though numerous central peaks on Mars exhibit strong phyllosilicate signatures in visible/near-infrared data sets [e.g. *Ehlmann et al.*, 2011; *Loizeau et al.*, 2012; *Carter et al.*, 2013], central peaks with THEMIS spectral character consistent with phyllosilicate minerals are rare (among craters with diameter 10-200km, the range examined in this study). Spatial resolution differences likely contribute to many of these discrepancies, but not all of them.

Some central peaks with areally large detections of phyllosilicate-bearing materials lack spectral distinction in THEMIS data, suggesting that the abundance of phyllosilicate minerals may be low. However, in this study, we did identify two central peaks that exhibit strong phyllosilicate absorptions in CRISM data, and that also exhibit thermal infrared spectral character consistent with high abundance of phyllosilicates. If the phyllosilicates formed in the subsurface, rather than through impact-related processes, these craters may indicate regions with unique subsurface environments conducive to formation of abundant phyllosilicate minerals.

8. Along the rim of Hellas Basin, crater central peak-associated materials exhibit a variety of olivine and pyroxene-bearing compositions, and likely sample very deep (possibly mantle) materials brought up by the Hellas impact. Local-scale stratification in lithology is inferred in one location, where two olivine-bearing units are found in locations with self-consistent crater-exposed depths between the three craters.

Acknowledgements

The data for this paper is available at NASA Planetary Data System Archive (http://pds.nasa.gov/). Dataset name: CRISM, THEMIS, TES and OMEGA. Data explorer: http://ode.rsl.wustl.edu/mars/indexproductsearch.aspx. We thank Jacob Gardner for assistance with the global spectral survey, and J.R. Skok for useful discussions. We are grateful to B. N. Horgan, Patrick Pinet and L. L. Tornabene for thorough and constructive reviews, which greatly improved this manuscript. This work was supported by the NASA Earth and Space Science Fellowship program (grant number NNX11AQ92H to C. Pan), the NASA Mars Data Analysis Program (grant number NNX11AI84G to J. Michalski), and the Mars Odyssey Project.

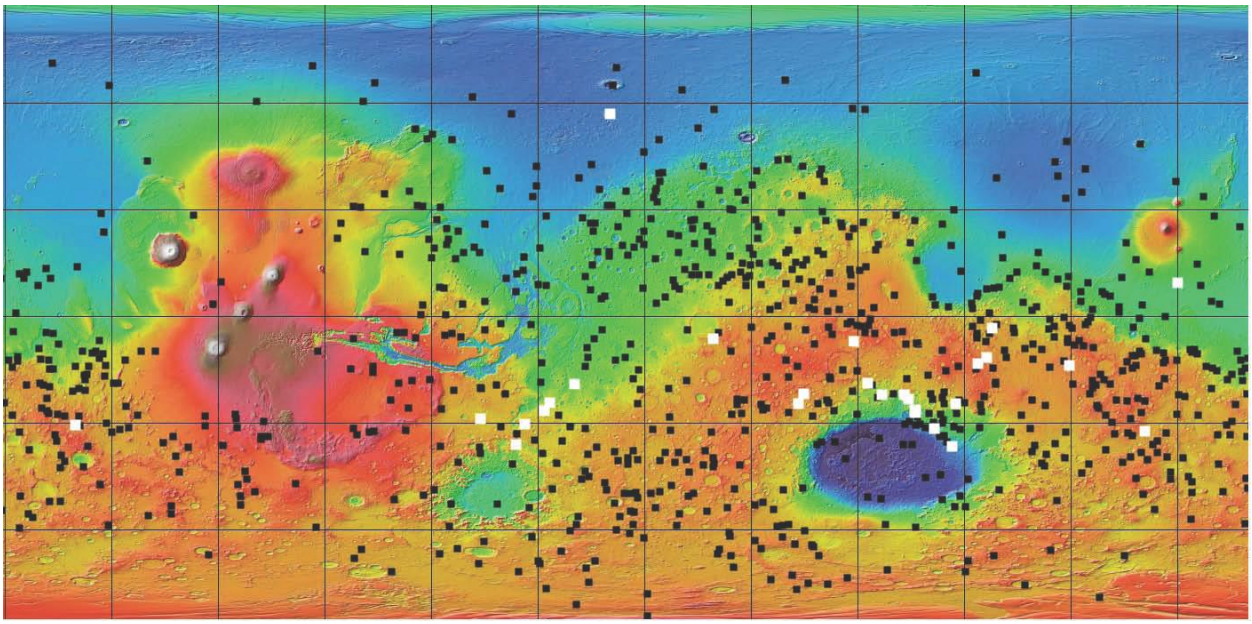

Figure 2.1 Distribution of impact craters with diameters between 10-200 km, and with crater interior morphologies marked “PK” (“peak”) from Barlow’s crater database [*Barlow et al.*, 2000]. Black squares: 840 craters with central peaks that are not spectrally distinct in THEMIS. Color squares: 26 impact craters with well exposed and spectrally distinct central peaks (SDCPs).

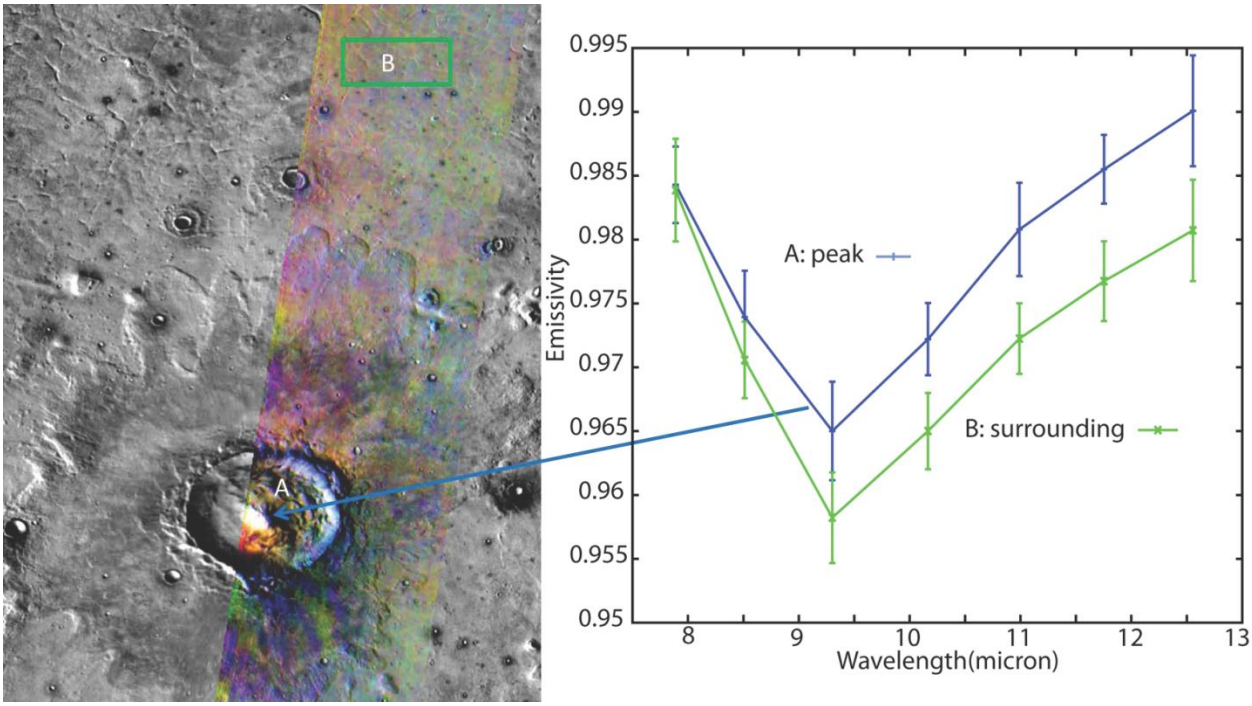

Figure 2.2 Example of a crater that was initially ranked in a high priority bin but was eventually removed after detailed spectral analysis. The crater displays color distinction in the peak (blue) in the THEMIS radiance DCS 8-7-5 image. A. Selection of regions of central peak (the blue spots in the peak) and surrounding area in B. B. Spectra of central peak and surrounding area from A. However, the peak and surrounding spectra have similar spectral characteristics after normalizing to the same spectral contrast.

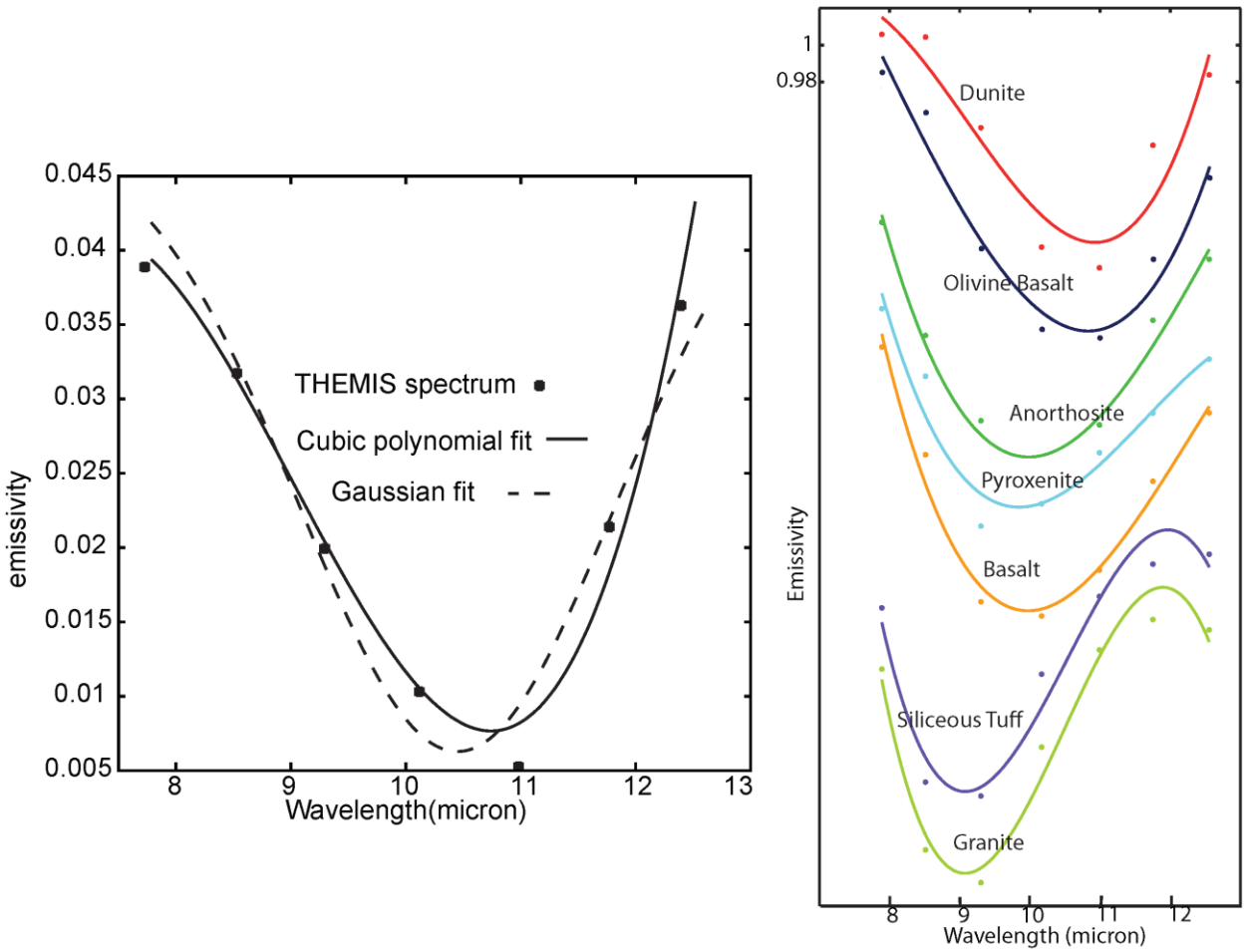

Figure 2.3 Comparison of Gaussian and cubic polynomial fits to THEMIS spectra (a) and cubic polynomial fits to spectra of a variety of rock types at THEMIS resolution (b). The curve minimum of the cubic polynomial fit more closely matches the data minimum than the curve minimum of the Gaussian fit. Curves are offset for clarity.

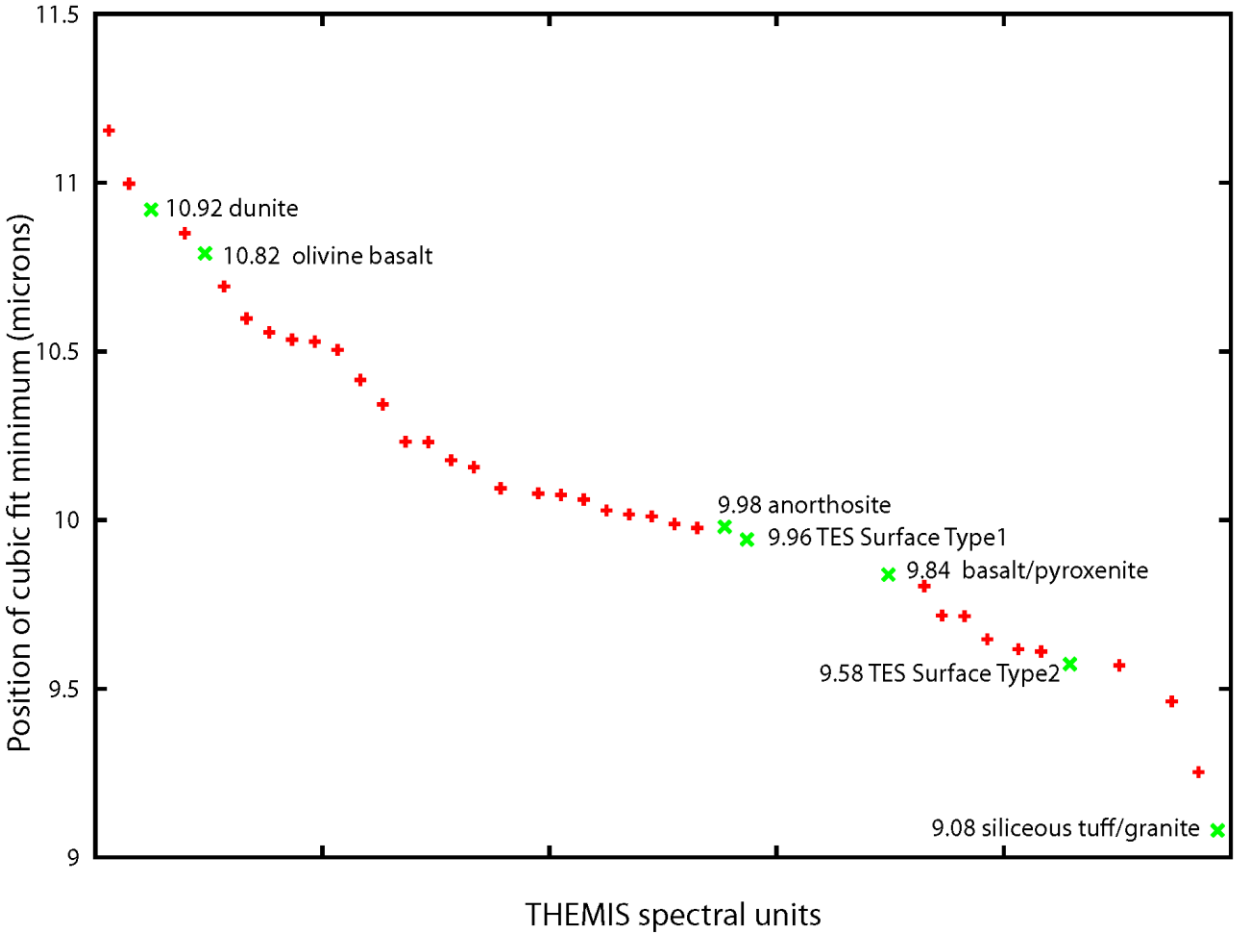

Figure 2.4 Sorted plot of minimum position of cubic polynomial fit of THEMIS-derived spectral units found in central peaks (red crosses) and laboratory spectra of rocks at THEMIS resolution (green crosses). The positions of TES Surface Types 1 and 2 are also shown. The numbers and texts next to green crosses are minimum positions of cubic polynomial fit and names of the rocks.

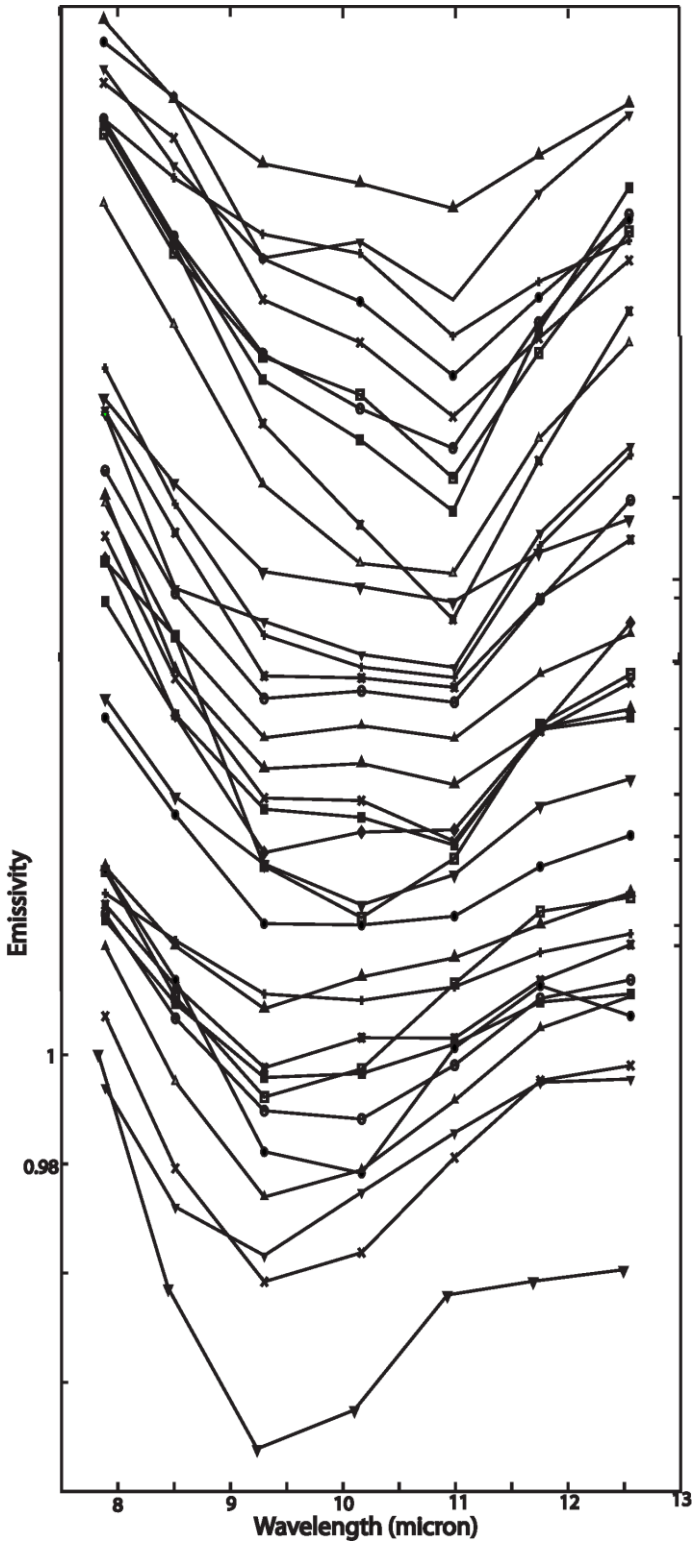

Figure 2.5 Average THEMIS surface emissivity from all spectrally distinct units in central peaks. Spectra are offset for clarity.

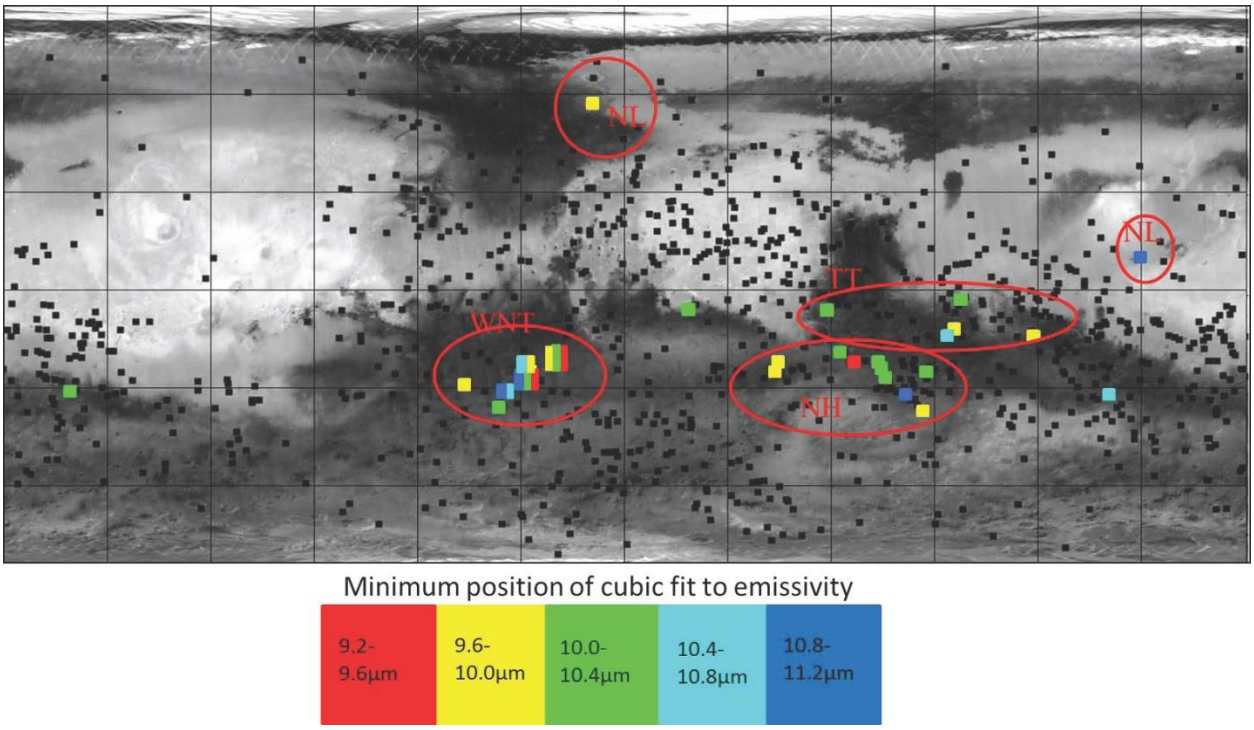

Figure 2.6 Distribution of impact craters with diameters between 10-200 km and with crater interior morphologies marked "PK" ("peak") from Barlow's crater database [*Barlow et al.*, 2000]. Black squares: 840 craters with central peaks that are not spectrally distinct in THEMIS. Color squares: 26 impact craters with well exposed and spectrally distinct central peaks (SDCPs). Some regional clustering of SDCPs is observed. For ease of discussion in the text, SDCPs were divided by region (red ovals): northern Hellas (NH), northern lowland(NL), western Noachis Terra (WNT) and Tyrrhena Terra (TT) (Section 2.3.0). For display proposes, all the spectrally distinct units are divided equally to five categories of colors based on the minimum position of cubic polynomial fits for emissivity, with interval 0.4μm (see legend).

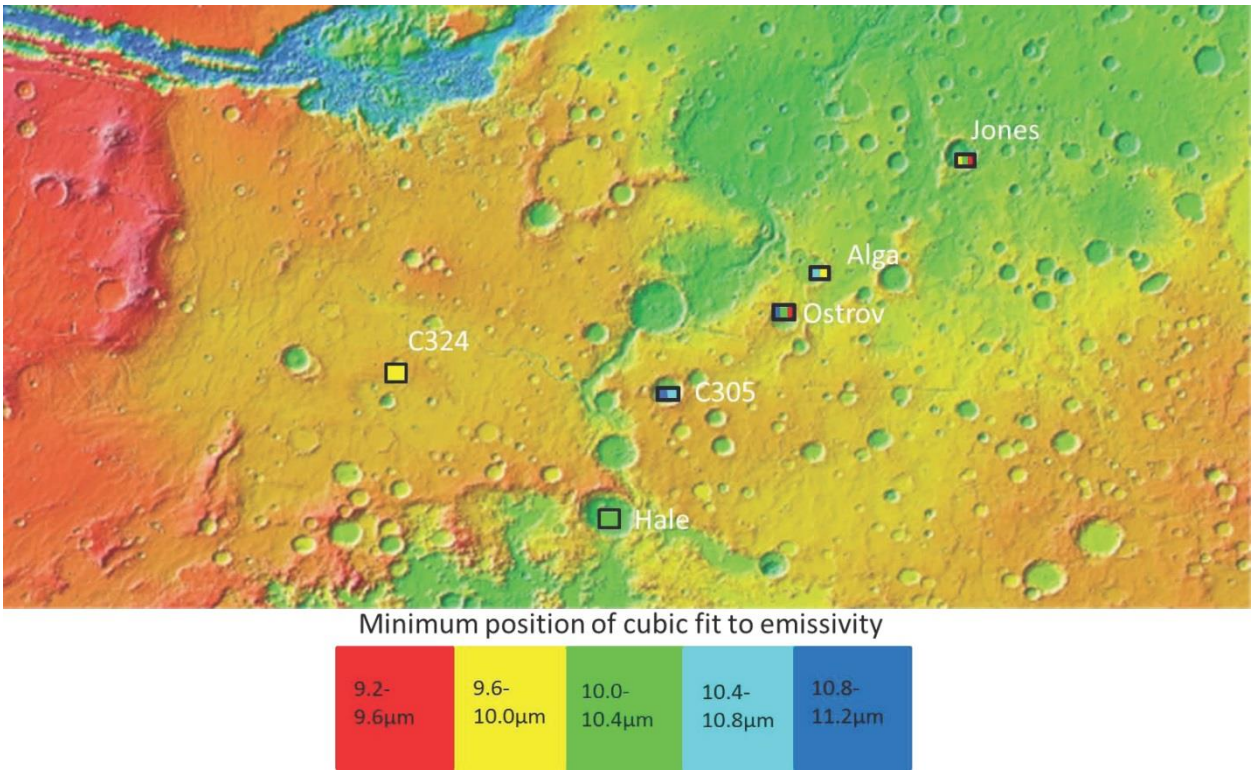

Figure 2.7 Locations of SDCPs in the western Noachis Terra region, overlain on MOLA colorized elevation and relief. For display proposes, all the spectrally distinct units are divided equally to five categories of colors based on the minimum position of cubic polynomial fits for emissivity, with interval 0.4µm (see legend). Except for Hale crater and C324, all craters expose more than one distinct spectral unit in the central peaks, in THEMIS data.

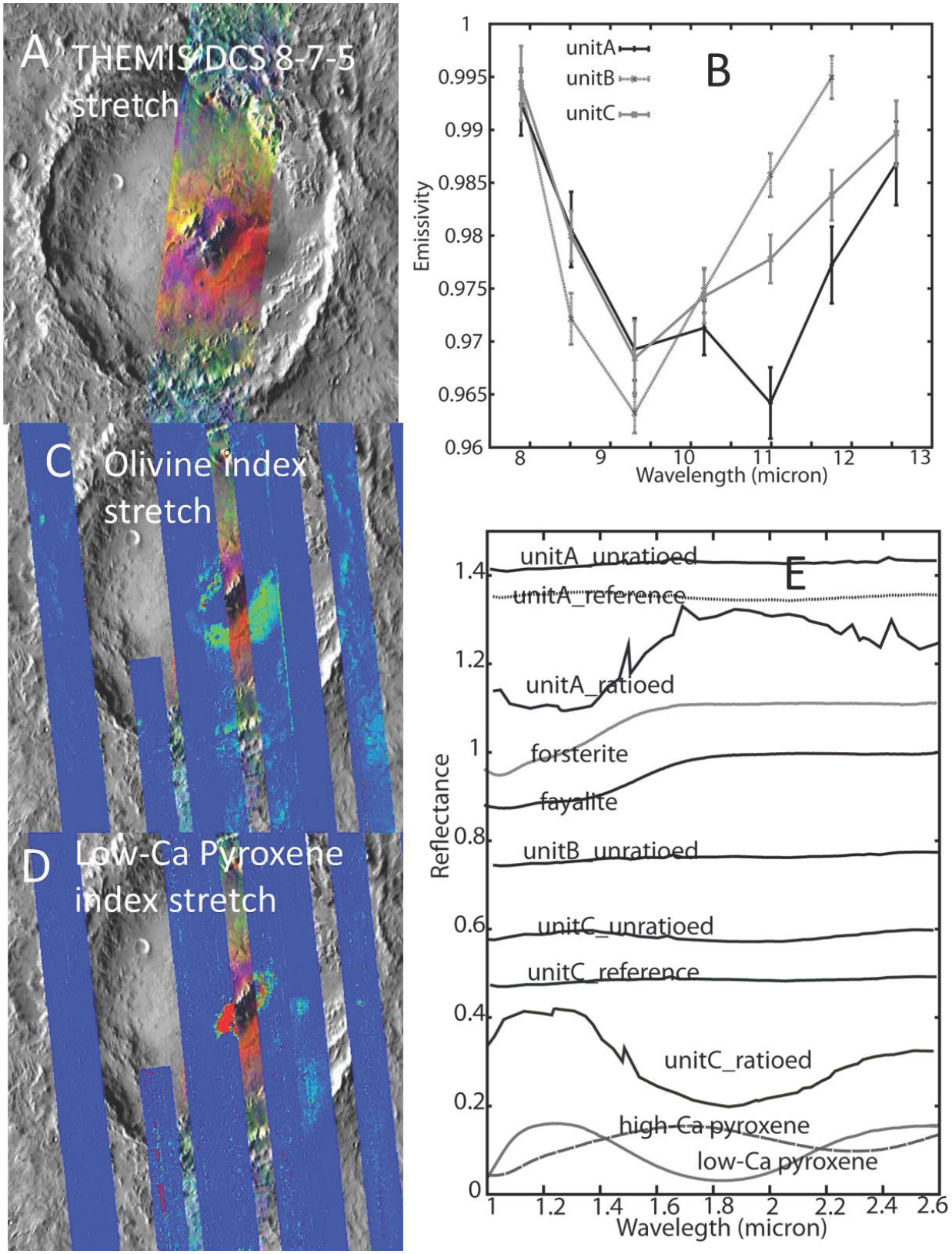

Figure 2.8 THEMIS and CRISM characteristics of spectral units in the Jones crater central peak. Unit A is olivine-enriched and feldspar-poor, unit B is olivine- and pyroxene-poor, and unit C is

pyroxene basaltic with little to no olivine. A. THEMIS bands 8(~11.8μm)-7(~11μm)-5(~9.4μm) as red-green-blue in the DCS radiance mosaic of Jones crater. The three spectral units appear as purple (Unit A), yellow/orange (Unit B), and green (Unit C) respectively (quantitative distributions shown in Figure 2.9). B. THEMIS spectra from Jones crater's three units. C. CRISM olivine index stretch map showing the olivine distribution in Unit A. The index is OLINDEX and stretch color is from 0 to 0.13. D. CRISM low-Ca pyroxene index stretch map showing the low-Ca pyroxene distribution in Unit C. The index is LCPINDEX and stretch color is from 0 to 0.1. (Note that there is no CRISM mineral detection in Unit B) E. CRISM spectra of Jones crater's three units and comparison with VNIR laboratory spectra. The spectra of units are from bright red pixels of B and C. Spectra are offset for clarity.

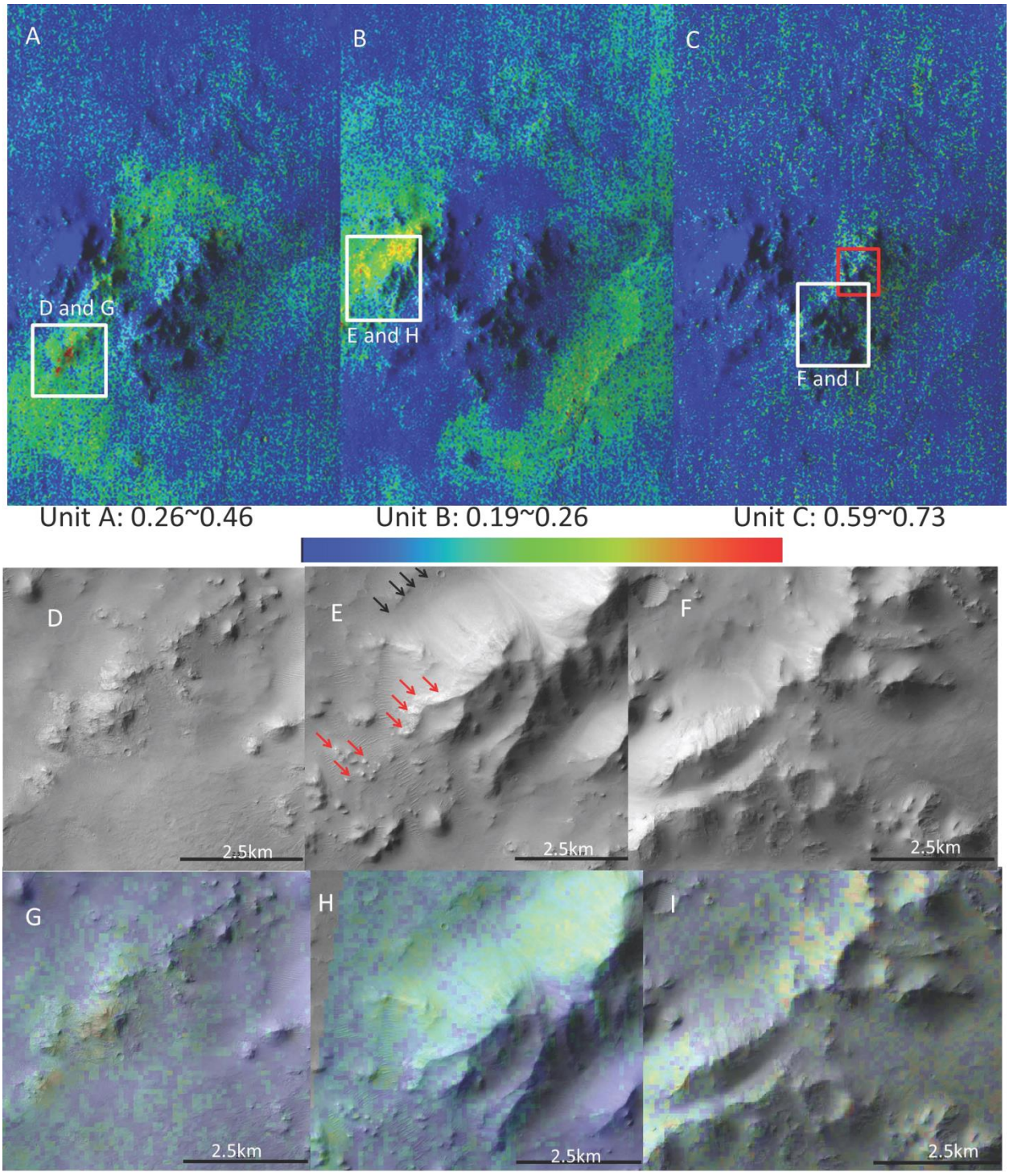

Figure 2.9 Jones THEMIS spectral unit maps (A-C), CTX images (D-F) and THEMIS spectral unit maps overlain on CTX images (G-I). The unit maps were created using spectra from Figure 2.8B. The red and yellow colors indicate high concentrations of the spectral end-member. The red box in C shows the TES pixel footprint for the spectrum in Figure 2.10. The white boxes in A-C indicates the areas shown in CTX images D and G, E and H, and F and I, respectively. The CTX overlays show that the highest concentrations of each spectral unit are associated with light-toned,

relatively unmantled ridges and buttes. In E, red arrows point to light-toned ridges and buttes, black arrows point to darker toned material at the base of the ridge, discussed in text.

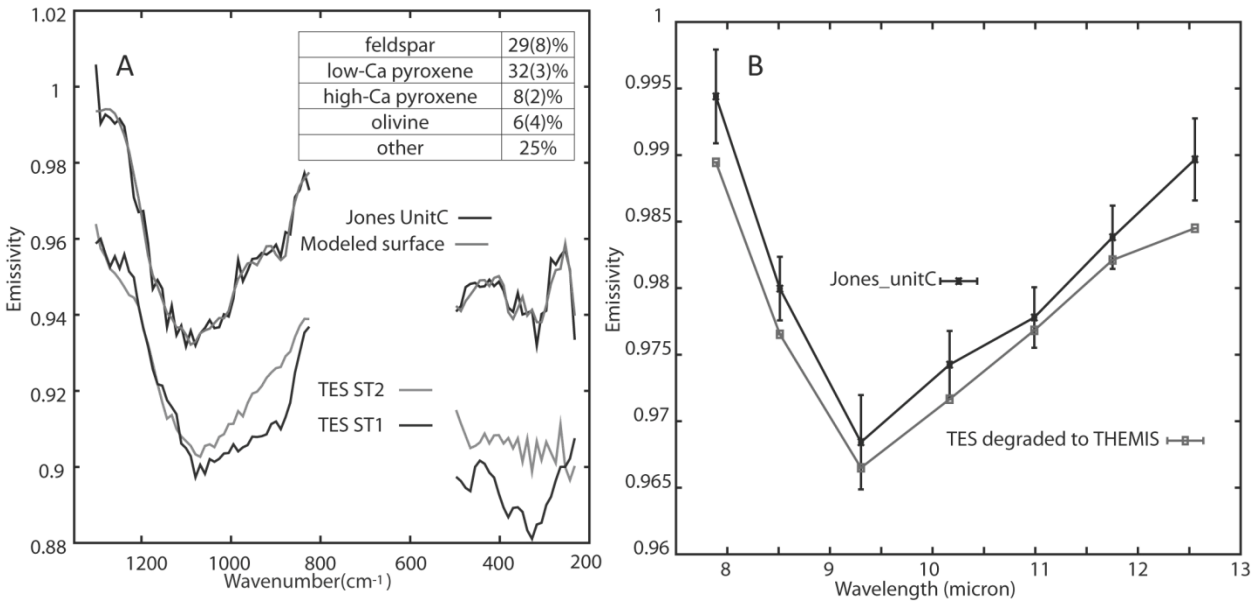

Figure 2.10 TES and THEMIS spectra show spectral consistency of Jones Unit C. A. TES spectrum of unit C from Jones crater with TES Surface Type 1 (ST1) and Surface Type 2 for comparison. The TES spectra are distinct from ST1 and ST2. The inside table shows modeled mineral abundances of Jones crater unit C from linear deconvolution of TES pixels, with statistical uncertainties on derived abundance shown in parentheses. The high abundance of feldspar and pyroxene indicate it is pyroxene-rich basaltic (intrusive vs. extrusive igneous origins cannot be distinguished from spectral data alone). B. THEMIS spectra of Jones crater's Unit C and TES spectrum of unit C degraded to THEMIS. The TES degraded spectrum is consistent with THEMIS spectrum of unit C.

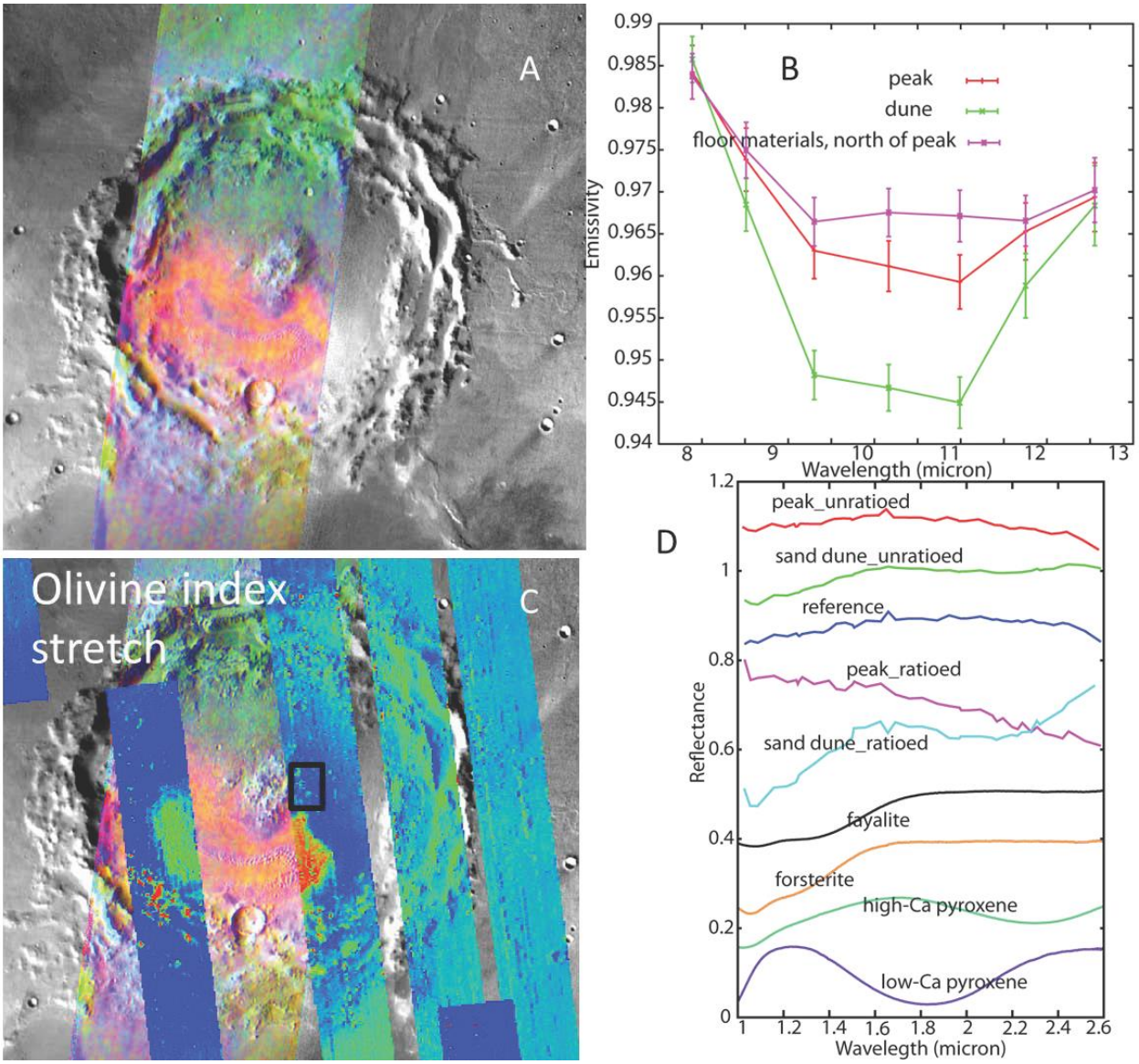

Figure 2.11 An example of a SDCP in the Cerberus plains. A. THEMIS 8-7-5 DCS mosaic. The red, green and purple boxes are areas where THEMIS spectra were selected for B. B. THEMIS spectra of crater floor, peak and the nearby sand dune. The crater peak is distinct from the floor materials to the north of the peak. The floor and peak spectra are shallow due to dust coverage. C. CRISM olivine single stretch with stretch color from 0 to 0.13. D. CRISM spectra of crater peak and sand dune. Crater peak spectrum is from the bright yellow pixels of black box of C. Sand dune spectrum is from the bright red pixels. Spectra are offset for clarity.

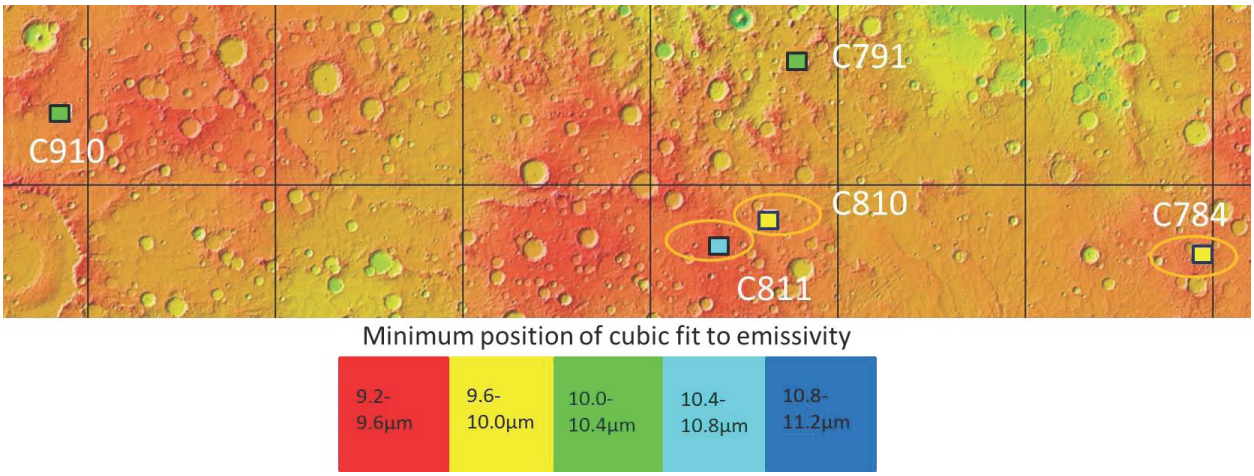

Figure 2.12 Distribution of SDCPs in Tyrrhena Terra For display proposes, all the spectrally distinct units are divided equally to five categories of colors based on the minimum position of cubic polynomial fits for emissivity, with interval 0.4μm (see legend). Craters in orange ovals have both olivine and D2300 absorptions in CRISM data.

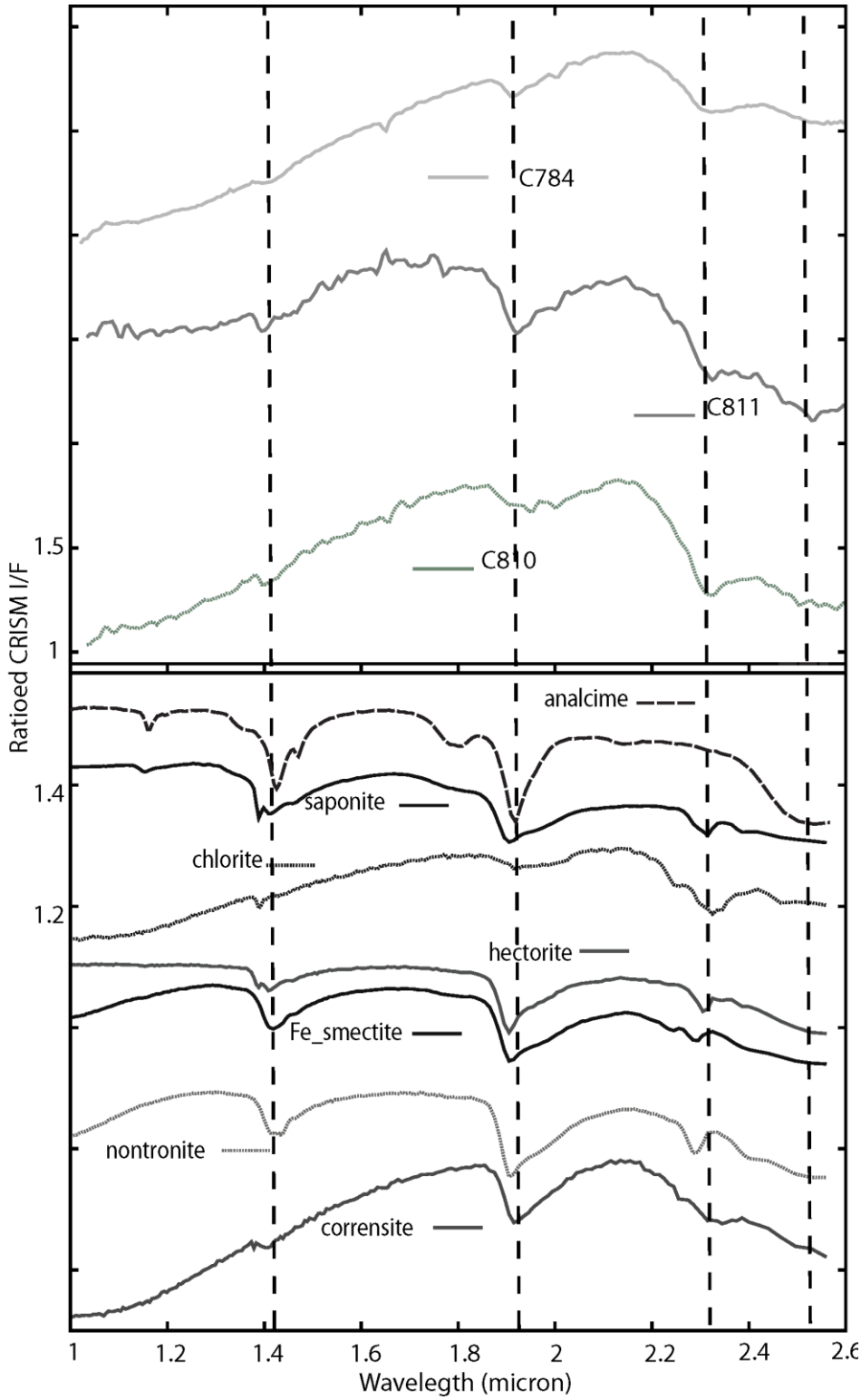

Figure 2.13 CRISM spectra from craters in the Tyrrhena Terra region with laboratory phyllosilicate spectra for comparison. The positions of dash lines are at ~1.405 μm, ~1.920 μm, ~2.308 μm, and ~2.527 μm respectively. USGS spectra: analcime GDS1, saponite SapCa-1,

chlorite SMR-13.e<30µm, corrensite corwa-1, nontronite NG-1.a, hectorite SHCa-1, Fe-smectite SWa-1. Spectra are offset for clarity.

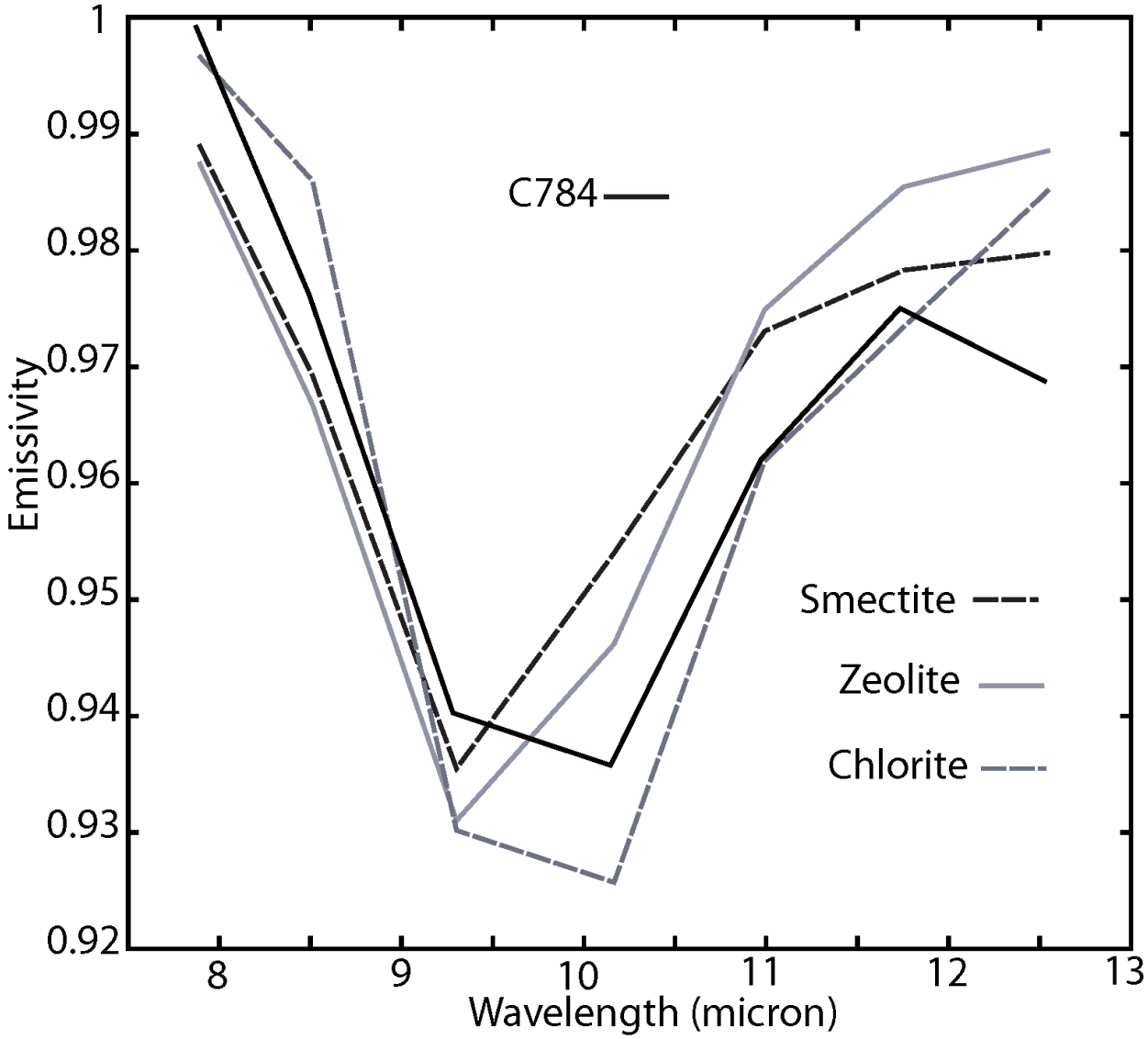

Figure 2.14 THEMIS spectrum of C784 and comparison with candidate phyllosilicate and zeolite minerals.

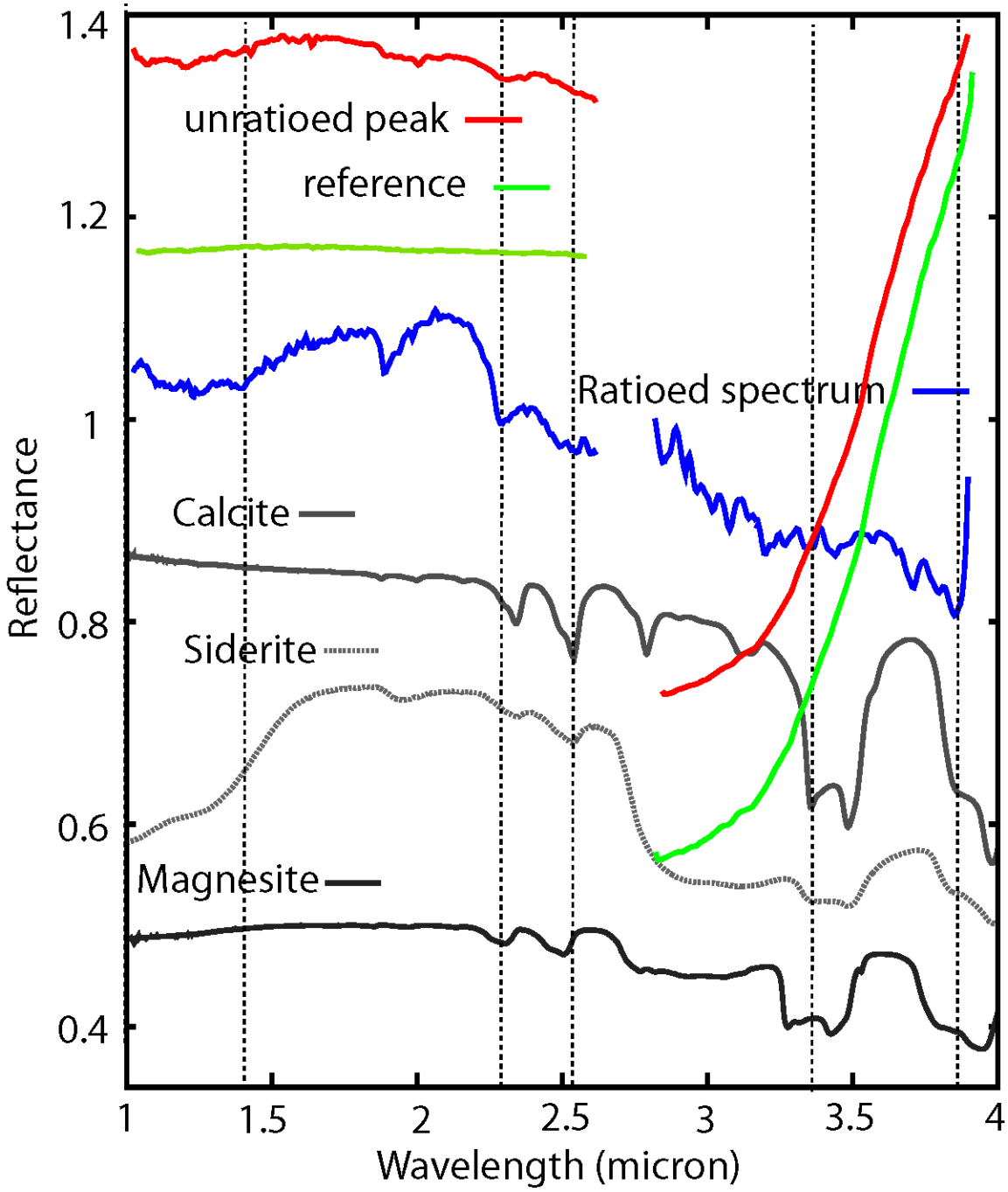

Figure 2.15 CRISM spectra from C810 in the Tyrrhena Terra region with laboratory carbonate spectra for comparison. CRISM spectral library: calcite JB-549, siderite CAGR03, magnesite CACB06. Spectra are offset for clarity. Spectra are offset for clarity. The positions of dash lines are at ~1.414 µm, ~2.302 µm, ~2.566 µm, ~3.401 µm, and ~3.876 µmrespectively.

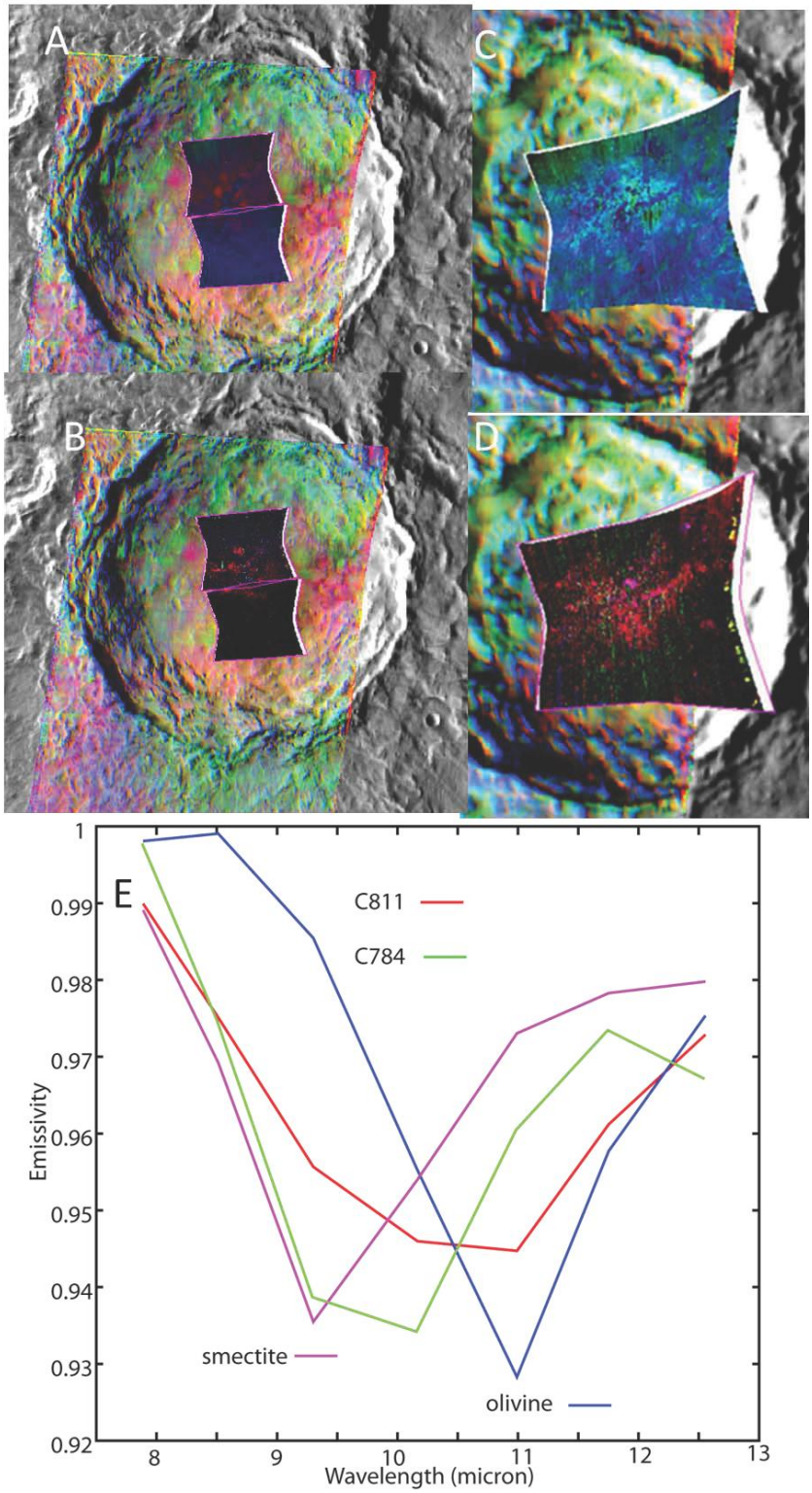

Figure 2.16 An example of phyllosilicate- and olivine-bearing SDCPs in the Tyrrhena Terra region. A. and B. CRISM mafic and hydroxylated stretch maps of C784. C. and D. CRISM mafic and hydroxylated stretch maps of C811. E. THEMIS spectra from Crater C811and C784, olivine and smectite. CRISM spectra are shown in Figure 2.13 and Figure 2.15.

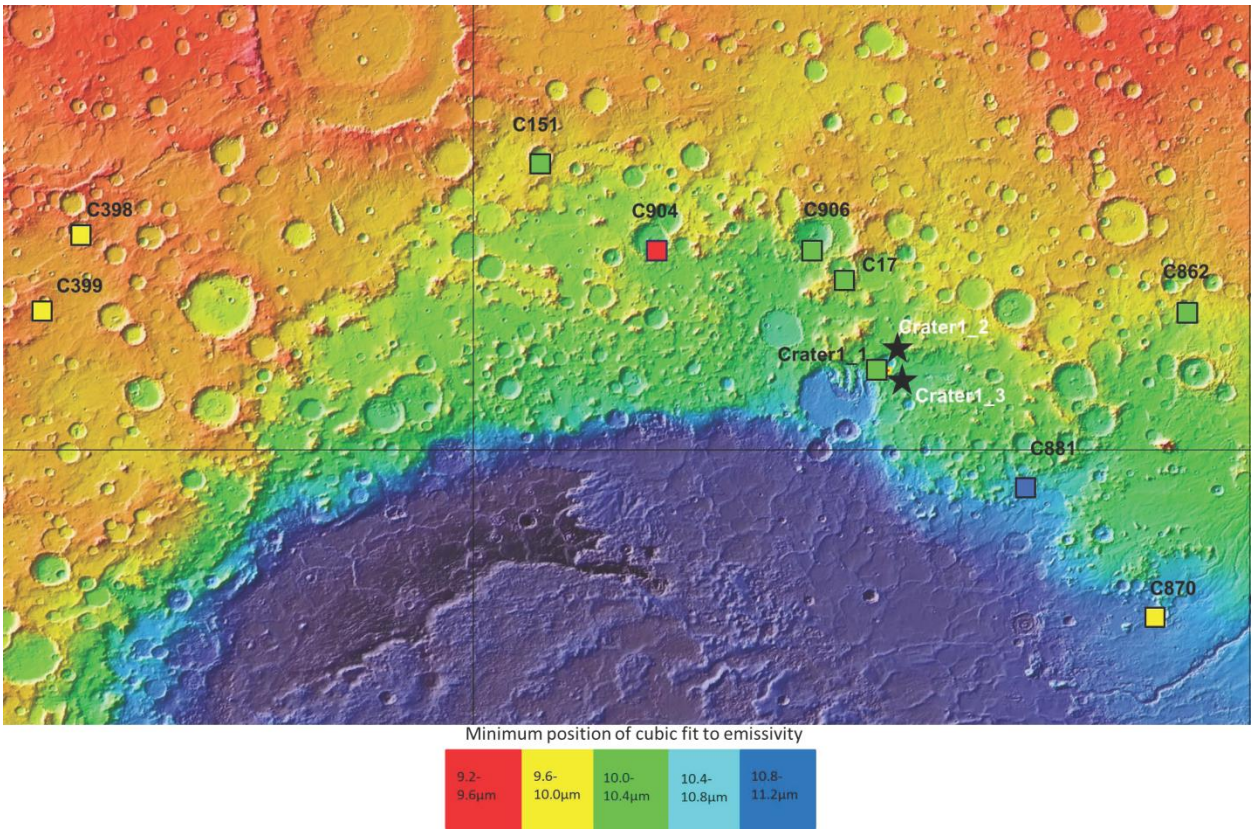

Figure 2.17 Distribution of SDCPs in the rim of Hellas Basin. For display proposes, all the spectrally distinct units are divided equally to five categories of colors based on the minimum position of cubic polynomial fits for emissivity, with interval 0.4μm (see legend). Black stars: two craters adjacent to Crater1_1 that lack central peaks, but that have spectrally distinct ejecta or central pit. Craters 1_1, 1_2 and 1_3 were studied in detail in Figure 2.18. See text for explanation.

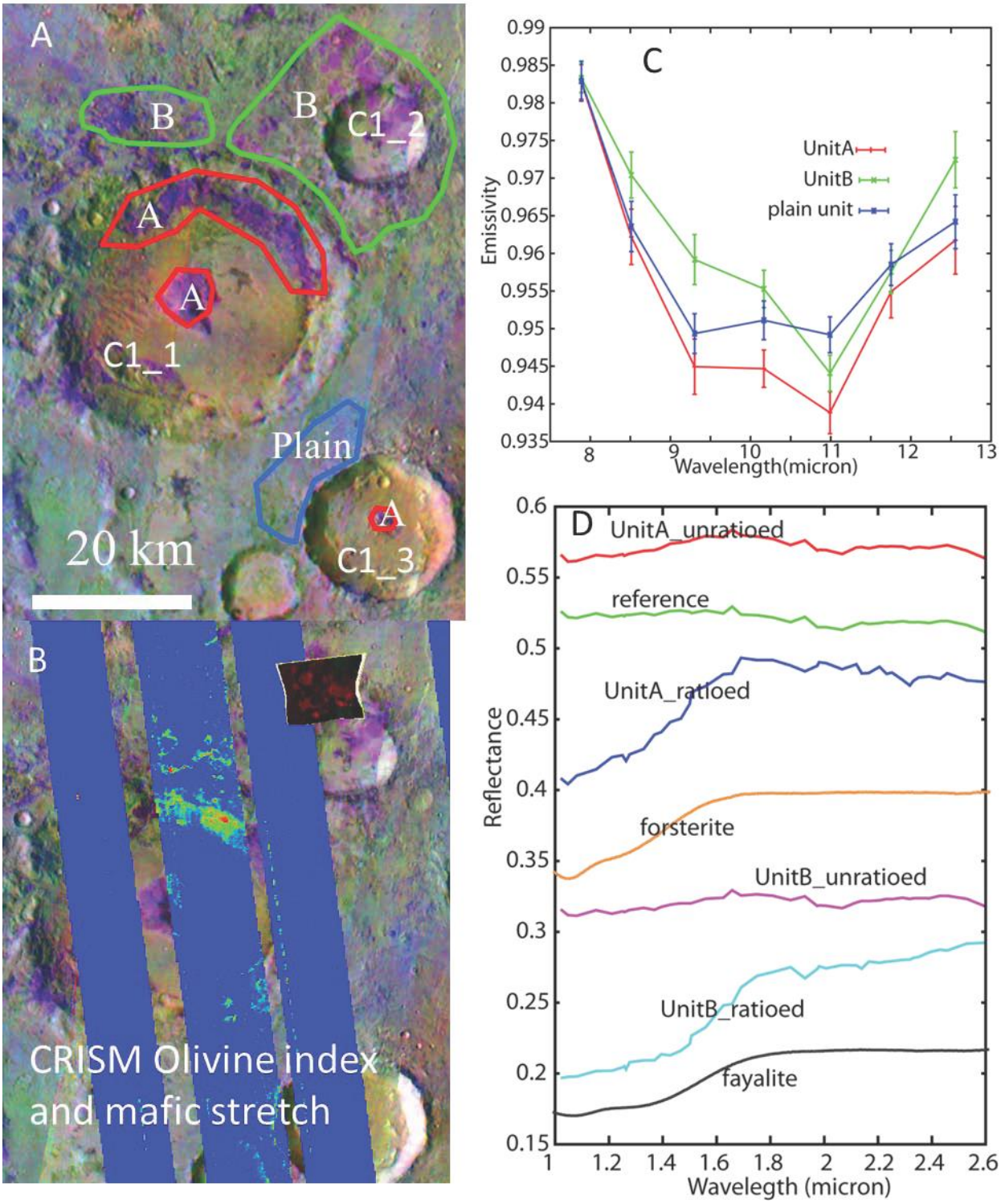

Figure 2.18 An example of craters in the northern Hellas region. A. Polygons show regions of THEMIS spectral averages shown in (D), overlain on a THEMIS 8-7-5 DCS mosaic. B. CRISM olivine single stretch with stretch color from 0 to 0.13 and mafic stretch map of CRISM targeted image with red as OLVINEX, green as LCPINDEX and blue as HCPINDEX. C. THEMIS spectra of three spectral distinct units from A. D.CRISM spectra of units from C. Unit A

spectrum is from the bright red pixels of olivine stretch and Unit B spectra is from the bright red and blue pixels of mafic stretch map. Unit A is consistent with fayalitic olivine and Unit B is consistent with fosteritic type in certain particle size, suggesting particle sizes or types of olivine difference. Unit B is also consistent with pyroxene. Spectra are offset for clarity.

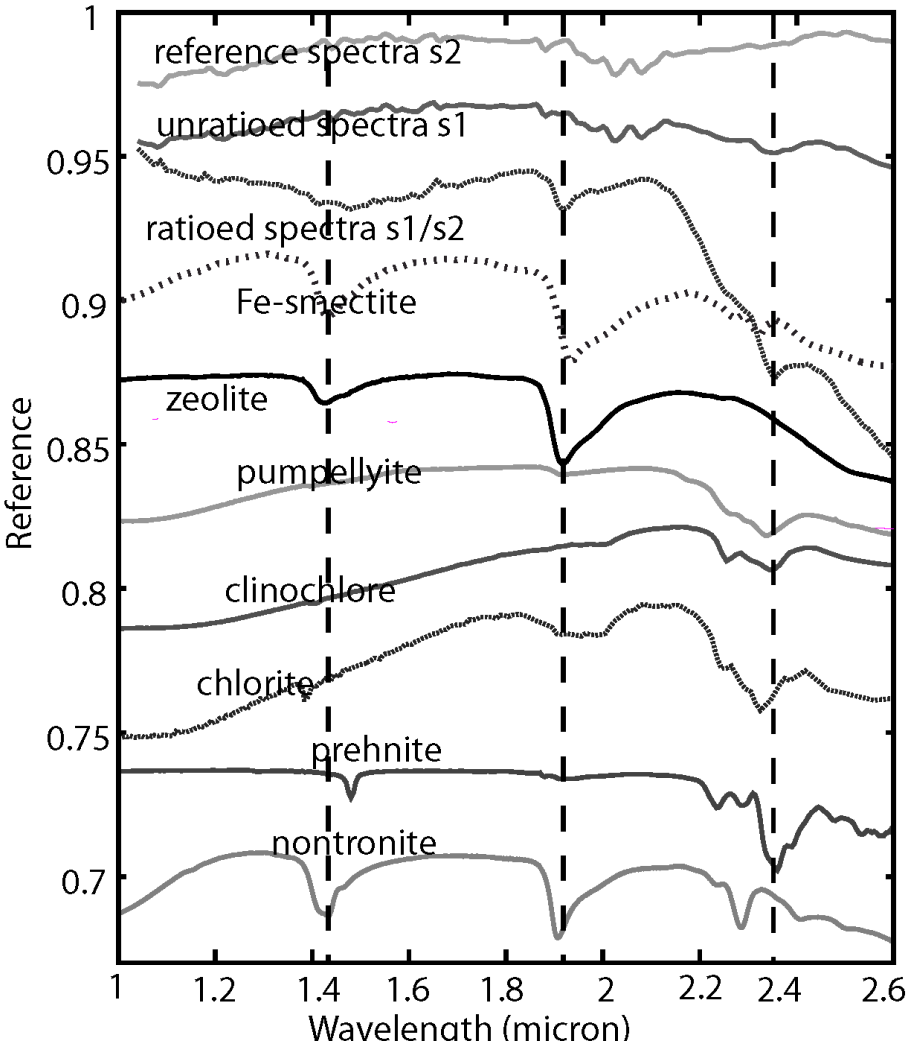

Figure 2.19 CRISM spectra of C107 with laboratory spectra for comparison. This is the only hydrated mineral observation associated with a SDCP besides those found in the Tyrrhena Terra region. However, the type of mineral is different from the Tyrrhena Terra region and it is restricted to very small exposures. CRISM spectral library: zeolite c1ze17, pumpellyite c1ze02, prehnite c1ze03. USGS library: chlorite SMR-13.e<30µm, nontronite NG-1.a, clinochlore GDS158, Fe-smectite SWa-1. The positions of dash lines are at ~1.432 µm, ~1.920 µm, and ~2.351 µm respectively. Spectra are offset for clarity.

Table 2.1 Details of each crater peak in this study, sorted by region.

Region	Crater ID	Name	Lat	Lon	Diameter	Unit	Min of Cubic Polynomial Fit[c]	CRISM Index	Avg of CRISM Index	Remarks
WNT	C165	Jones	-19.1	-19.7	90	peak_U1	10.343	MRDR OLV1	0.104	Figure8-10
WNT	C165	Jones				Peak_U2	9.2538	no mineral detection		Figure8-10
WNT	C165	Jones				peak_U3	9.6168	MRDR LCP	0.305	Figure8-10
WNT	C1001	Alga	-24.3	-26.7	20	peak_U1	10.598	OLV2	0.137	
WNT	C1001	Alga				peak_U2	9.9888	HCP	0.151	
WNT	C1002	Ostrov	-26.5	-28.1	76	Peak_U1	10.85	OLV2	0.166	
WNT	C1002	Ostrov				peak_U2	10.157	LCP	0.586	
WNT	C1002	Ostrov				peak_U3	9.5688	LCP	0.586	
WNT	C305		-30.3	-33.6	85	peak_U1	10.997	MRDR OLV1	0.143	
WNT	C305					peak_U2	10.535	MRDR LCP	0.647	
WNT	C324		-28.9	-46.2	26	peak	10.556	no mineral detection		
WNT	C153	Hale	-36	-36.2	143	peak	10.094	LCP	0.121	
NL	C945	Kunowsky	56.9	-9.71	66	peak	9.8012	OLV2	0.082	
NL	C29		9.48	150	53	peak	10.415	no data coverage		Figure11
TT	C811		-13.4	93.8	20	peak	10.505	OLV2 and D2300	0.13, 0.045	Figure13,15,16
TT	C784		-13.8	120	42	peak	9.6468	OLV2 and D2300	0.119, 0.028	Figure13,14,16
TT	C810		-11.7	96.4	21	peak	9.7148	OLV2 and D2300	0.145, 0.131	Figure13

TT	C791		-3.39	97.9	56	peak	10.017	no mineral detection		
TT	C910		-6.08	58.8	43	peak	10.075	no mineral detection		
NH	C881		-31.6	81.7	20	peak	11.157	OLV2	0.140	
NH	Crater1_2		-26.2	76.4	14	pit and ejecta	10.693	OLV2 and LCP	0.128, 0.043	Figure 18
NH	C906	Saheki	-22.1	73.2	84	peak	10.233	MRDR OLV1	0.064	
NH	Crater1_1	Runanga	-27	76	41	peak	10.231	MRDR OLV1	0.038	Figure 18
NH	C862		-24.6	87.6	29	peak	10.177	MRDR OLV1	0.146	
NH	C17		-23.4	74.4	67	peak	10.079	MRDR OLV1 and LCP	0.105, 0.323	
NH	C151		-18.9	62.8	52	peak	10.011	OLV2 and LCP	0.034,0.345	
NH	Crater1_3	Jorn	-27.2	76.4	20	ejecta	10.029	MRDR OLV1	0.098	Figure 18
NH	C398		-21.8	44.8	40	peak	9.9768	OLV2 and HCP	0.110, 0.283	
NH	C399		-24.5	43.4	23	peak	9.7328	OLV2 and LCP/HCP	0.047, 0.148/0.257	
NH	C870	Poti	-36.7	86.7	31	peak	9.8428	MRDR OLV1	0.056	
NH	C904		-22.2	66.9	83	peak	9.5788	no mineral detection		
other	C378		-6.32	19.4	22	peak	9.8048	OLV2 and HCP	0.106, 0.178	
other	C107	Horowitz	-32.3	141	67	peak	10.529	HCP and D2300	0.183, 0.017	Figure19
other	C80		-30.5	-160	84	peak	10.061	OLV2 and LCP	0.120,0.399	

a. The CRISM index values given are from averaged from the highest index values observed in the peak, rather than the average for the entire spectrally distinct unit.
b. Crater 1_2 and Crater1_3 are in the table, but do not have central peaks
c. Please refer to Figure 3-6 and Section 2.2 for more details on interpretations of THEMIS units

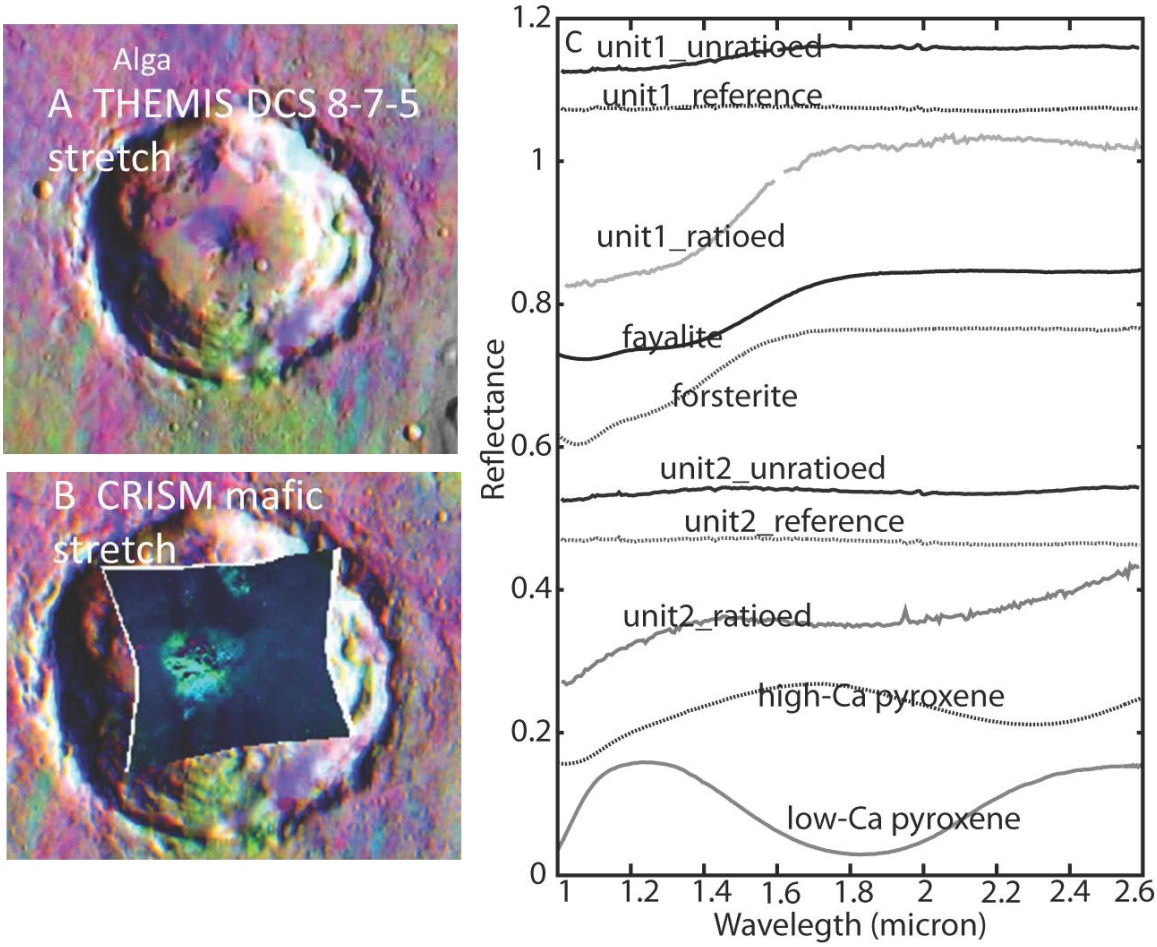

Figure 2.S1 THEMIS and CRISM characteristics of spectral units in the Alga crater central peak. A. THEMIS bands 8(~11.8µm)-7(~11µm)-5(~9.4µm) as red-green-blue in the DCS mosaic. B. CRISM mafic browse image. C. CRISM spectra and NIR laboratory spectra for comparison. Spectral unit distributions for THEMIS Units 1 and 2 are shown in Skok et al., [2012].

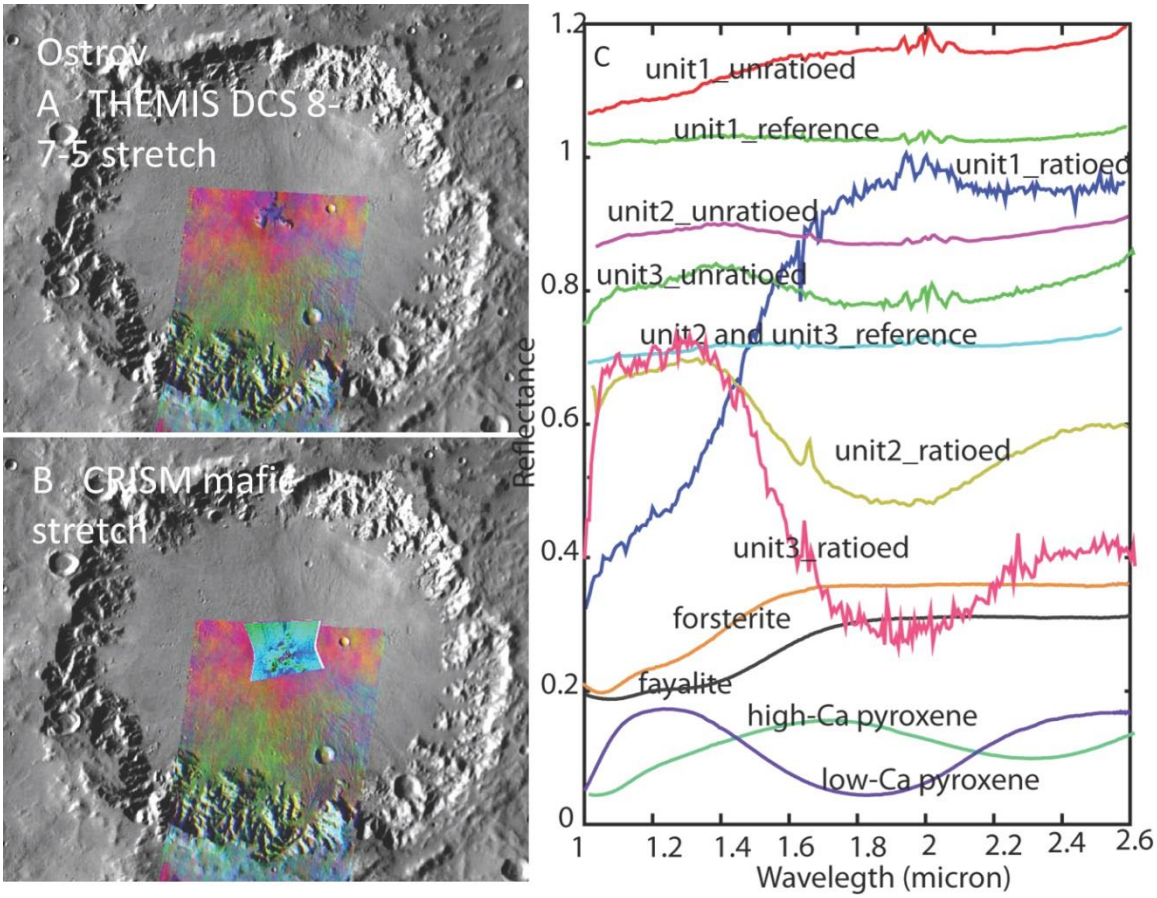

Figure 2.S2 THEMIS and CRISM characteristics of spectral units in the Ostrov crater central peak. A. THEMIS bands 8(~11.8µm)-7(~11µm)-5(~9.4µm) as red-green-blue in the DCS mosaic. B. CRISM mafic browse image. C. CRISM spectra and NIR laboratory spectra for comparison. Spectral unit distributions for THEMIS Units 1-3 are shown in Skok et al., [2012].

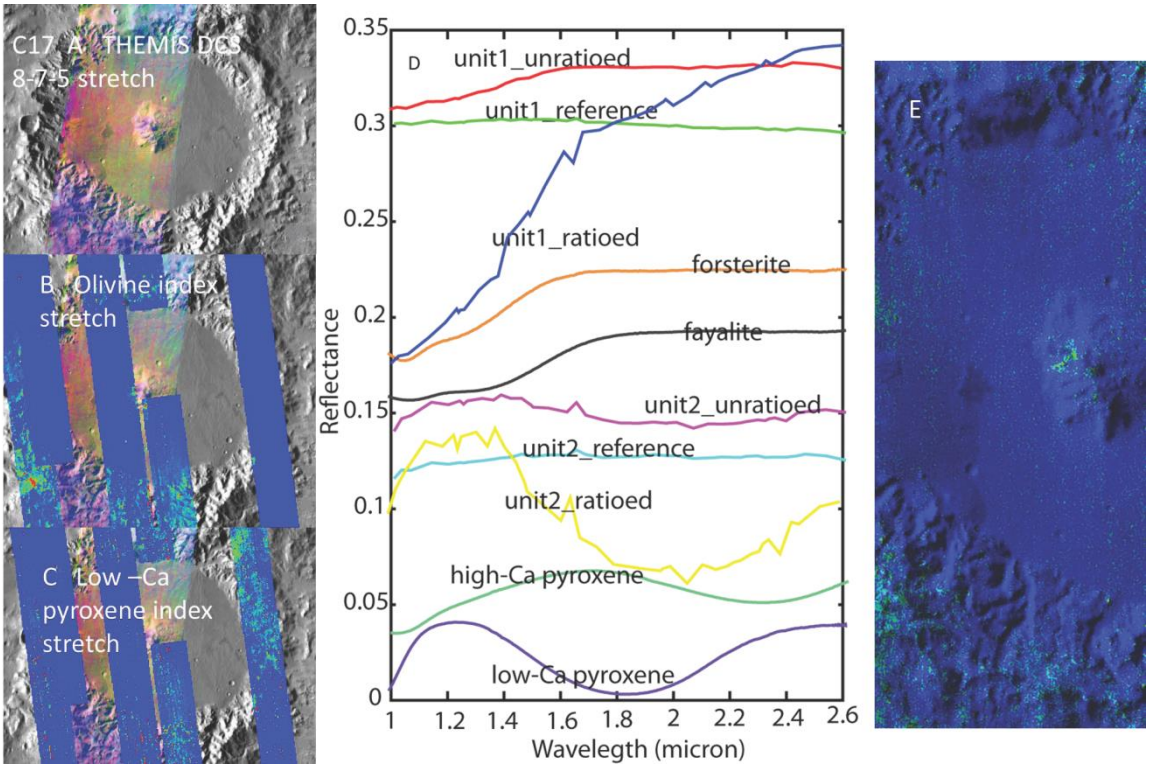

Figure 2.S3 THEMIS and CRISM characteristics of spectral units in the C17 crater central peak. A. THEMIS bands 8(~11.8μm)-7(~11μm)-5(~9.4μm) as red-green-blue in the DCS mosaic. B. CRISM olivine browse image. C. CRISM low-Ca pyroxene index browse image. D. CRISM spectra and NIR laboratory spectra for comparison. Note: CRISM "Unit 1" corresponds with the THEMIS spectrally distinct unit (shown in E). CRISM "Unit 2" was extracted from an additional area identified as distinct from Unit1 in the CRISM browse images. E. THEMIS spectra unit map shows the spectrally distinct unit in the central peak.

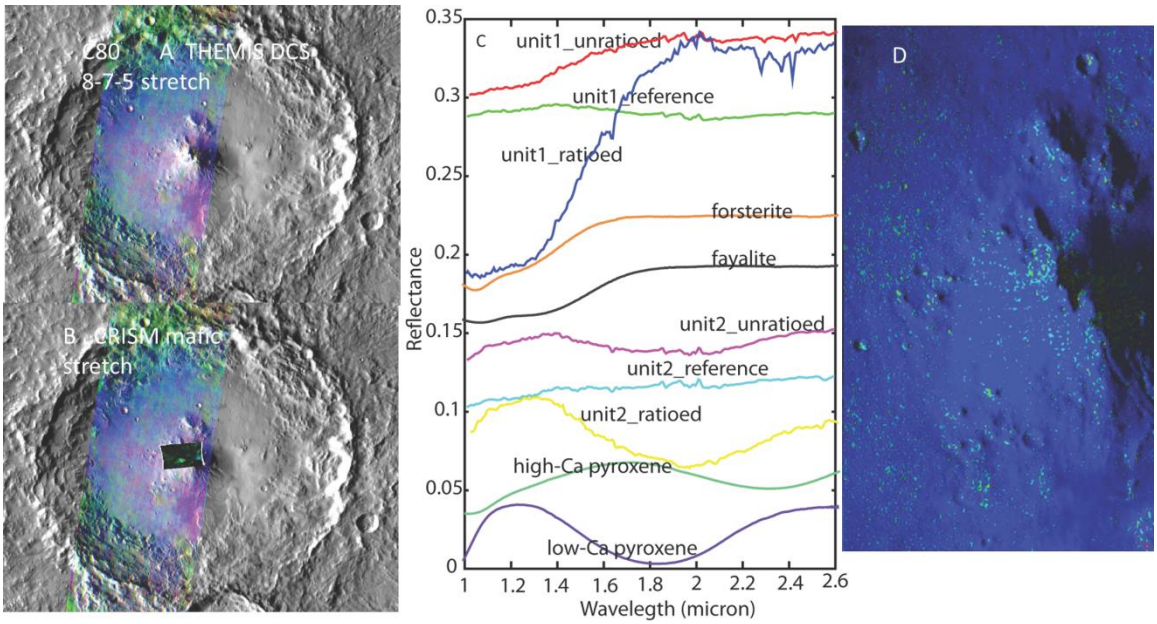

Figure 2.S4 THEMIS and CRISM characteristics of spectral units in the C80 crater central peak. A. THEMIS bands 8(~11.8µm)-7(~11µm)-5(~9.4µm) as red-green-blue in the DCS mosaic. B. CRISM mafic browse image. C. CRISM spectra and NIR laboratory spectra for comparison. Note: CRISM "Unit 1" corresponds with the THEMIS spectrally distinct unit (shown in D). CRISM "Unit 2" was extracted from an additional area identified as distinct from Unit1 in the CRISM browse images. D. THEMIS spectra unit map shows the spectrally distinct unit in the central peak.

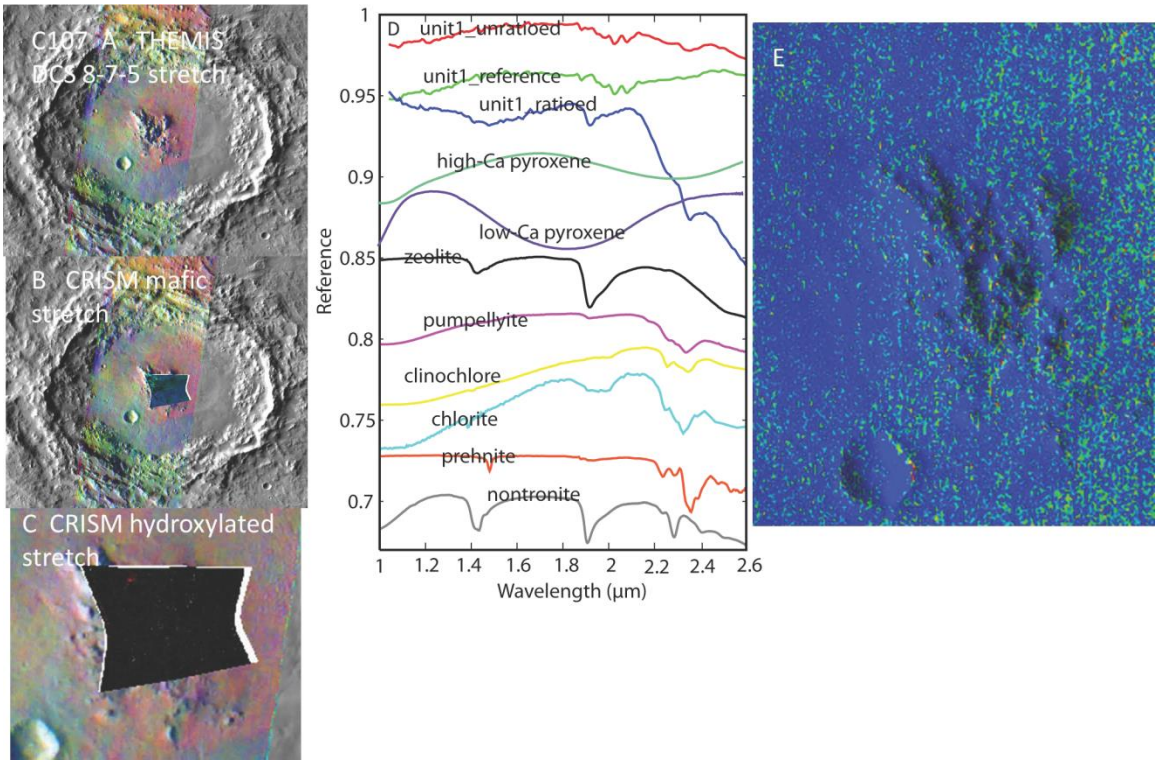

Figure 2.S5 THEMIS and CRISM characteristics of spectral units in the C107 crater central peak. A. THEMIS bands 8(~11.8μm)-7(~11μm)-5(~9.4μm) as red-green-blue in the DCS mosaic. B. CRISM mafic browse image. C. CRISM hydroxylated silicate browse image. D. CRISM spectra and NIR laboratory spectra for comparison. Note: CRISM "Unit 1" corresponds with the THEMIS spectrally distinct unit (shown in E). E. THEMIS spectra unit map shows the spectrally distinct unit in the central peak.

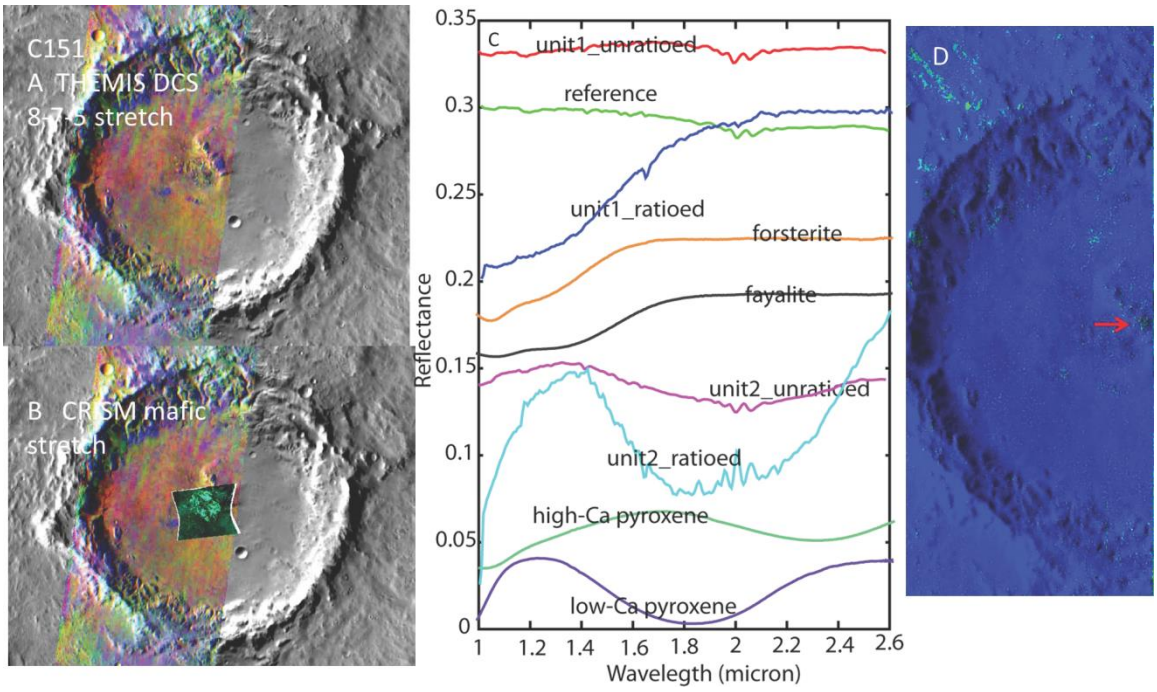

Figure 2.S6 THEMIS and CRISM characteristics of spectral units in the C151 crater central peak. A. THEMIS bands 8(~11.8µm)-7(~11µm)-5(~9.4µm) as red-green-blue in the DCS mosaic. B. CRISM mafic browse image. C. CRISM spectra and NIR laboratory spectra for comparison. Note: CRISM "Unit 2" corresponds with the THEMIS spectrally distinct unit (shown in D). CRISM "Unit 1" was extracted from an additional area identified as distinct from Unit 2 in the CRISM browse images. D. THEMIS spectra unit map shows the spectrally distinct unit in the central peak (arrow). The spectrally distinct unit is also found in a few isolated spots of the crater floor.

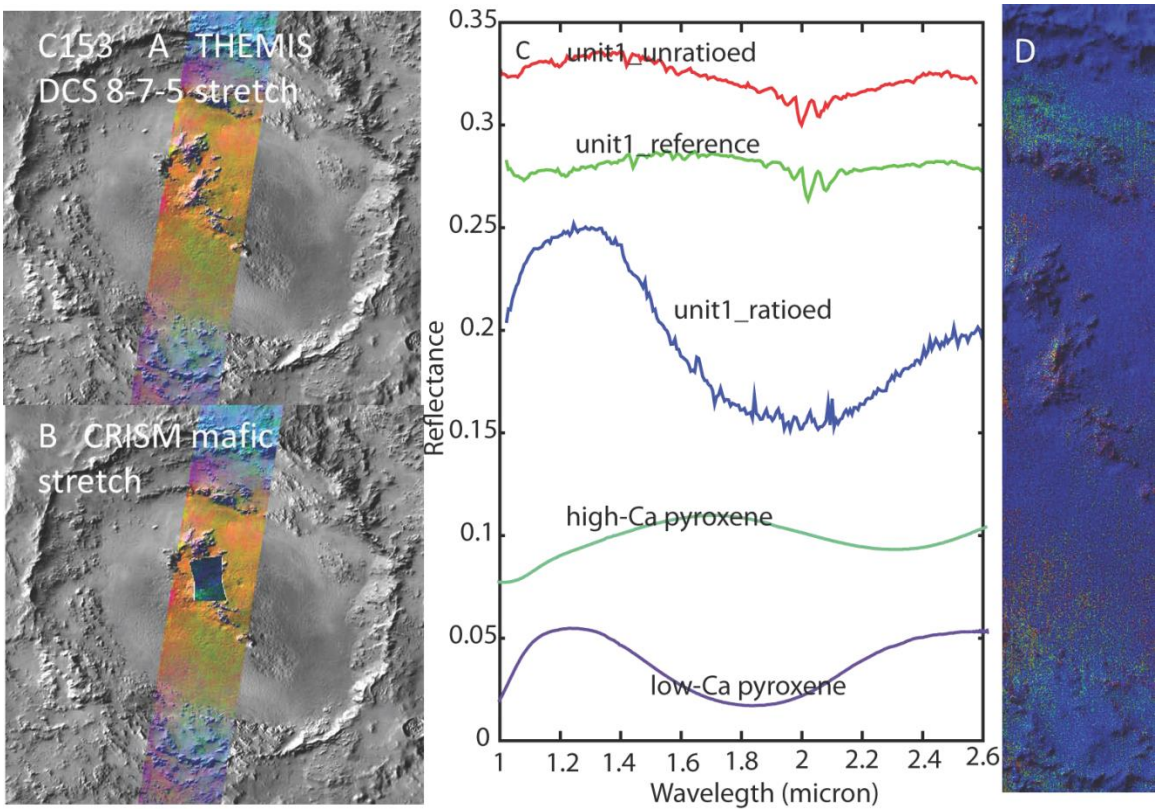

Figure 2.S7 THEMIS and CRISM characteristics of spectral units in the C153 crater central peak. A. THEMIS bands 8(~11.8µm)-7(~11µm)-5(~9.4µm) as red-green-blue in the DCS mosaic. B. CRISM mafic browse image. C. CRISM spectra and NIR laboratory spectra for comparison. Note: CRISM "Unit 1" corresponds with the THEMIS spectrally distinct unit (shown in D). D. THEMIS spectra unit map shows the spectrally distinct unit in the central peak.

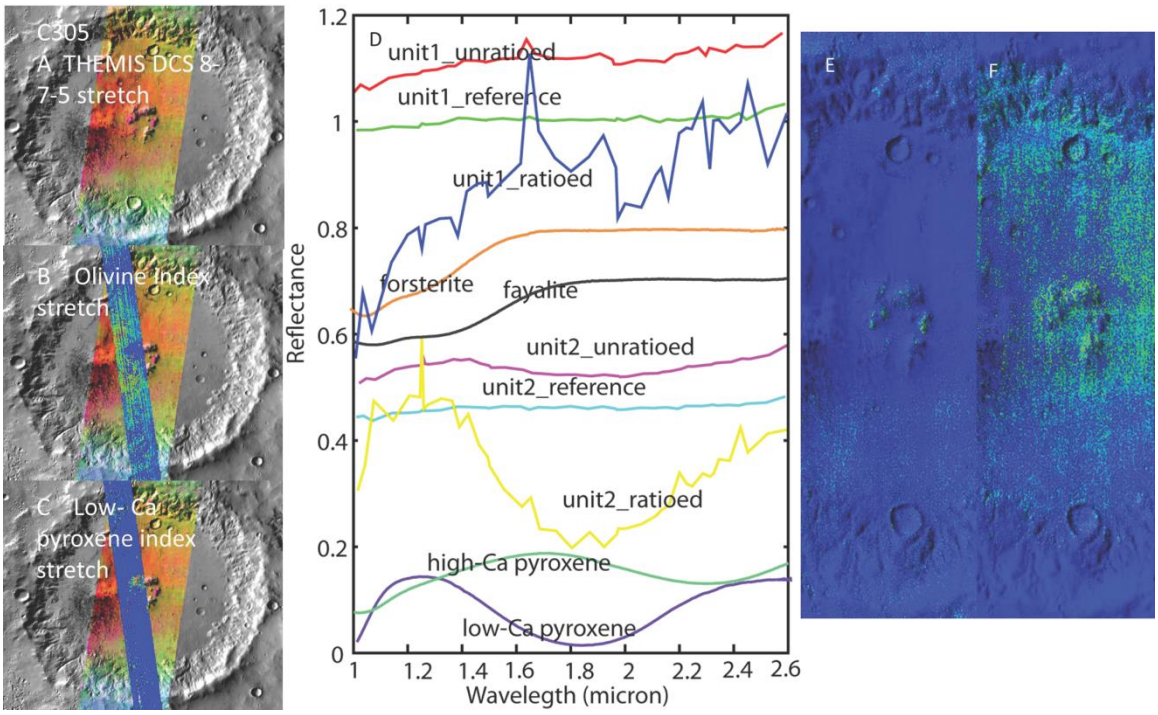

Figure 2.S8 THEMIS and CRISM characteristics of spectral units in the C305 crater central peak. A. THEMIS bands 8(~11.8µm)-7(~11µm)-5(~9.4µm) as red-green-blue in the DCS. B. CRISM olivine browse image. C. CRISM low-Ca pyroxene index browse image. D. CRISM spectra and NIR laboratory spectra for comparison. Note: CRISM "Unit 1" corresponds with the THEMIS spectrally distinct unit 1 (shown in E). CRISM "Unit 2" corresponds with the THEMIS spectrally distinct unit 2 (shown in F). E-F. THEMIS spectral unit maps show the distributions of spectrally distinct units in the central peak.

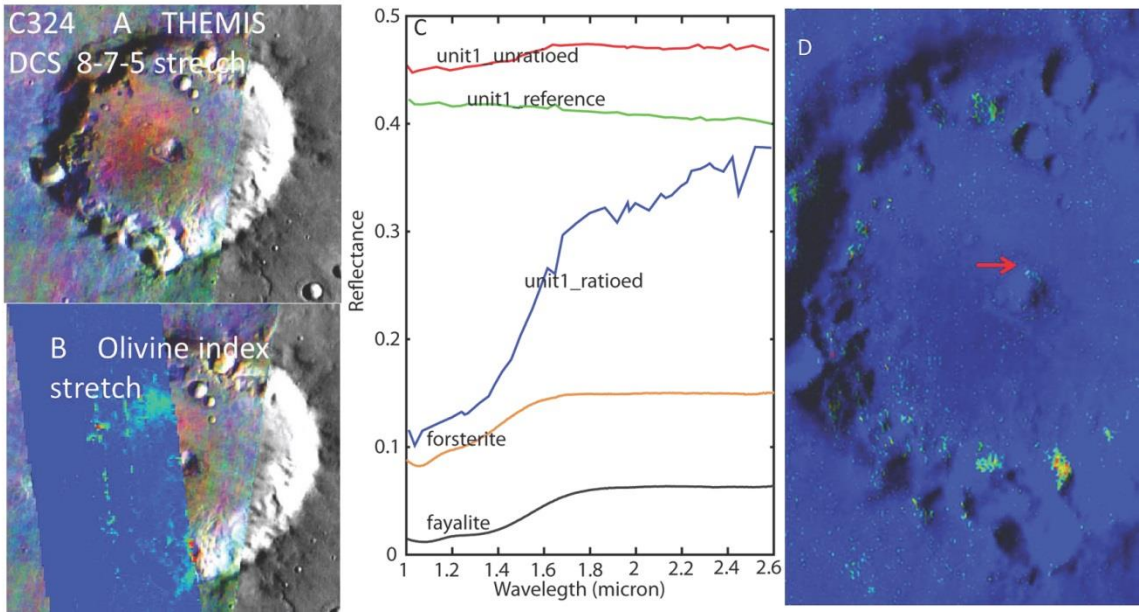

Figure 2.S9 THEMIS and CRISM characteristics of spectral units in the C324 crater central peak. A. THEMIS bands 8(~11.8µm)-7(~11µm)-5(~9.4µm) as red-green-blue in the DCS mosaic. B. CRISM olivine browse image. C. CRISM spectra and NIR laboratory spectra for comparison. Note: CRISM "Unit 1" corresponds with the THEMIS spectrally distinct unit (shown in D). D. THEMIS spectra unit map shows the spectrally distinct unit in the central peak. The spectrally distinct unit is also found on the isolated knobs around the margin of the crater floor.

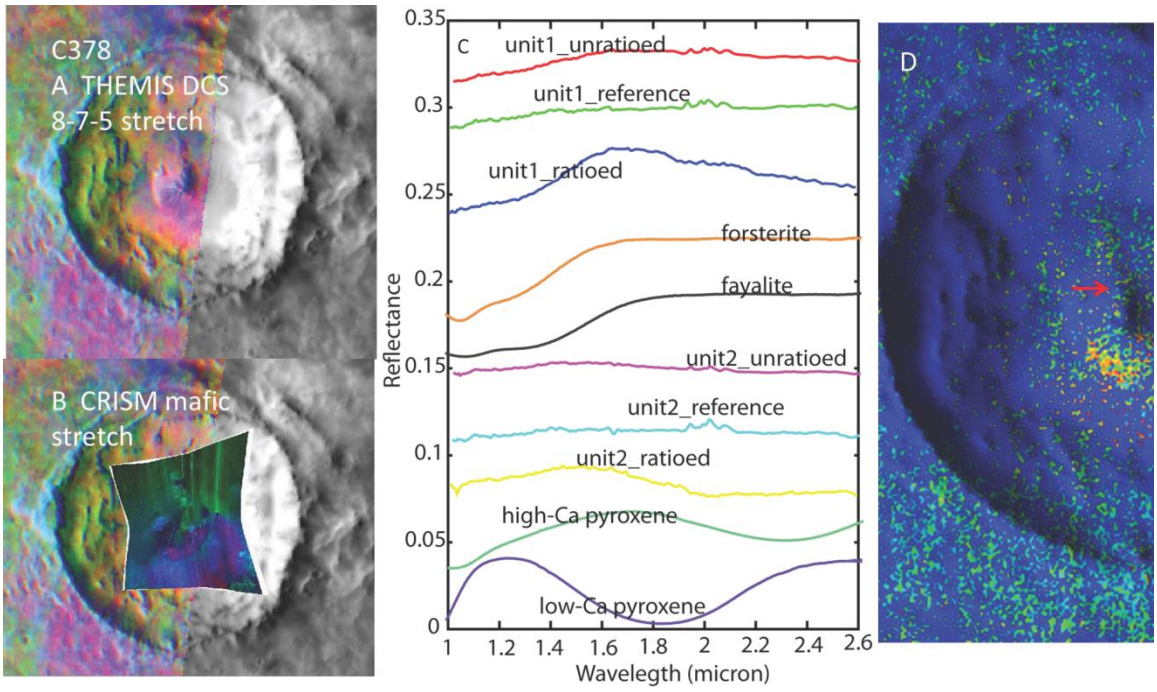

Figure 2.S10 THEMIS and CRISM characteristics of spectral units in the C378 crater central peak. A. THEMIS bands 8(~11.8µm)-7(~11µm)-5(~9.4µm) as red-green-blue in the DCS mosaic. B. CRISM mafic browse image. C. CRISM spectra and NIR laboratory spectra for comparison. Note: CRISM "Unit 1" corresponds with the THEMIS spectrally distinct unit (shown in D). CRISM "Unit 2" was extracted from an additional area identified as distinct from Unit 1 in the CRISM browse images. D. THEMIS spectral unit map shows the spectrally distinct unit in the central peak (arrow). The spectrally distinct unit is also found on the crater floor.

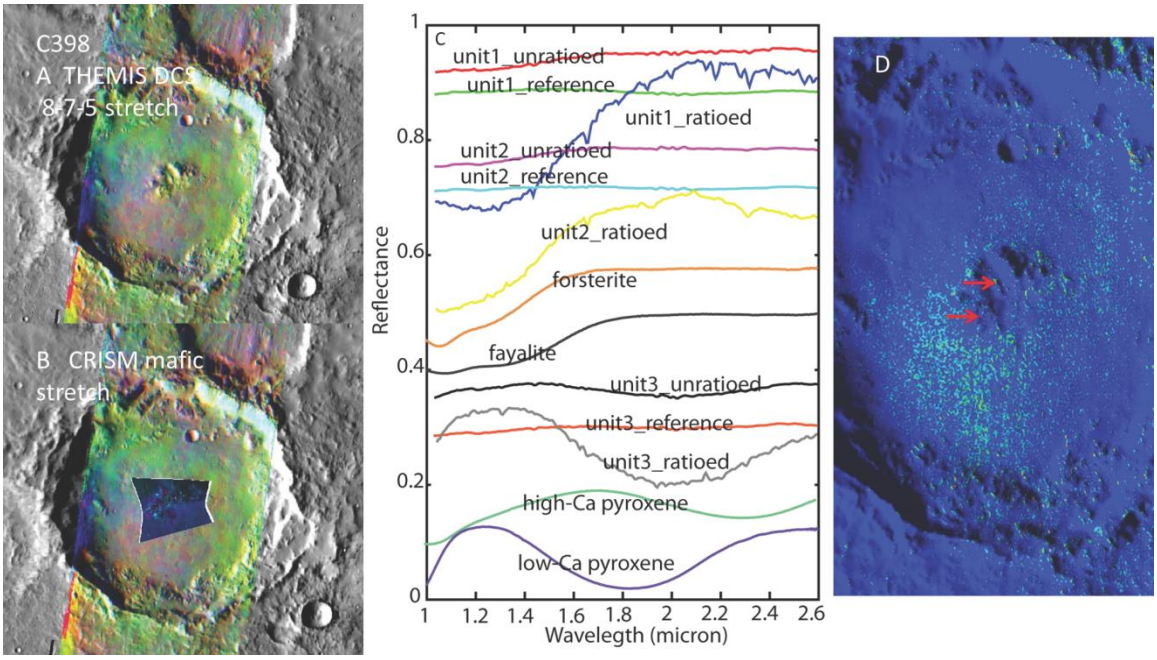

Figure 2.S11 THEMIS and CRISM characteristics of spectral units in the C398 crater central peak. A. THEMIS bands 8(~11.8µm)-7(~11µm)-5(~9.4µm) as red-green-blue in the DCS mosaic. B. CRISM mafic browse image. C. CRISM spectra and NIR laboratory spectra for comparison. Note: CRISM "Unit 1" corresponds with the THEMIS spectrally distinct unit (shown in D). CRISM "Unit 2" and "Unit 3" were extracted from additional areas identified as distinct from Unit 1 in the CRISM browse image. D. THEMIS spectral unit map shows the spectrally distinct unit in the central peak (arrows). The spectrally distinct unit is also found in a few isolated spots of the crater floor and wall.

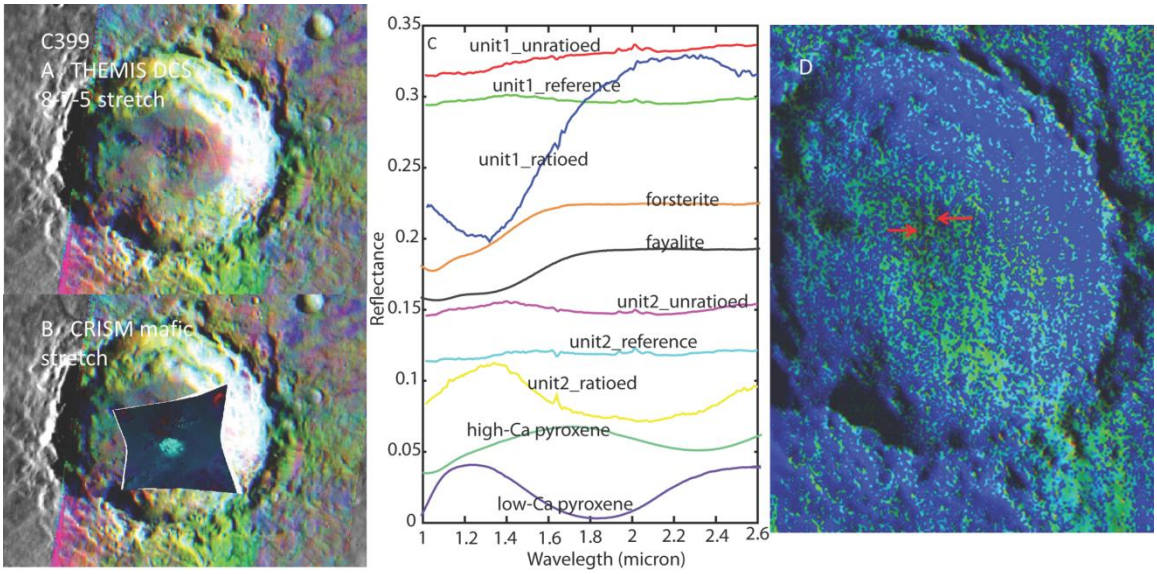

Figure 2.S12 THEMIS and CRISM characteristics of spectral units in the C399 crater central peak. A. THEMIS bands 8(~11.8µm)-7(~11µm)-5(~9.4µm) as red-green-blue in the DCS mosaic. B. CRISM mafic browse image. C. CRISM spectra and NIR laboratory spectra for comparison. Note: CRISM "Unit 1" corresponds with the THEMIS spectrally distinct unit (shown in D). CRISM "Unit 2" was extracted from an additional area identified as distinct from Unit 1 in the CRISM browse images. D. THEMIS spectra unit map shows the spectrally distinct unit in the central peak. The spectrally distinct unit is also found on the crater floor and wall.

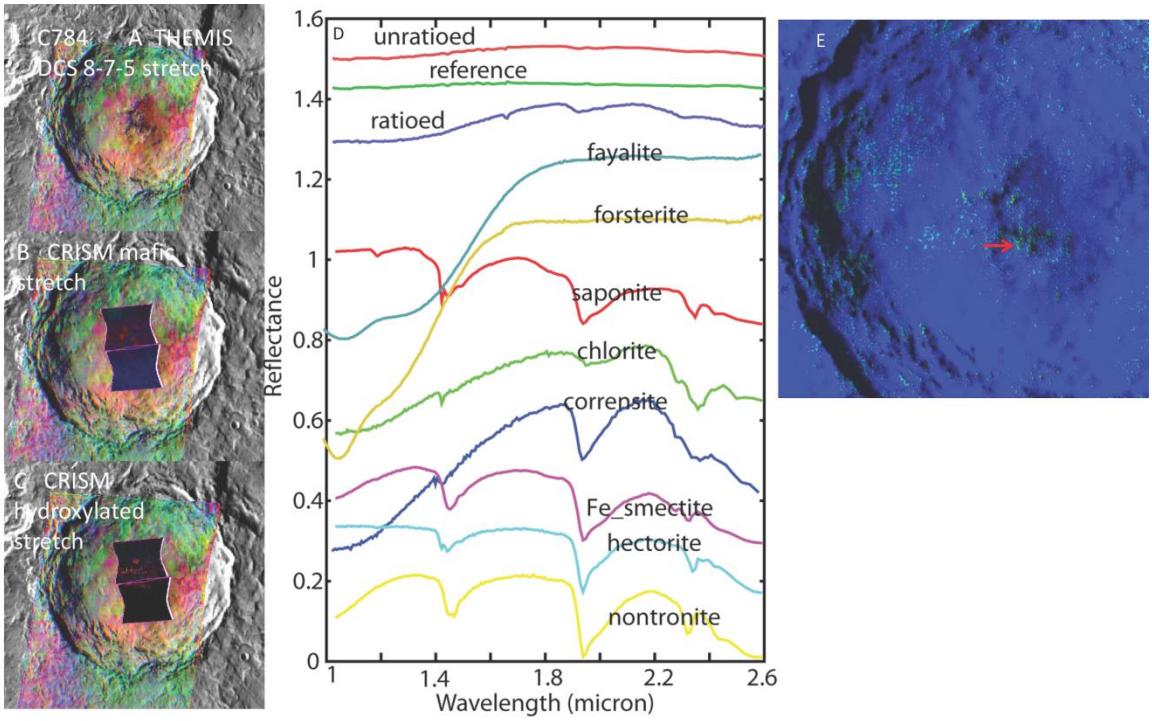

Figure 2.S13 THEMIS and CRISM characteristics of spectral units in the C784 crater central peak. A. THEMIS bands 8(~11.8µm)-7(~11µm)-5(~9.4µm) as red-green-blue in the DCS mosaic. B. CRISM mafic browse image. C. CRISM hydroxylated silicate browse image. D. CRISM spectra and NIR laboratory spectra for comparison. Note: CRISM "ratioed" corresponds with the THEMIS spectrally distinct unit (shown in E). E. THEMIS spectral unit map shows the spectrally distinct unit in the central peak. The spectrally distinct unit is also found in a few isolated spots of the crater floor.

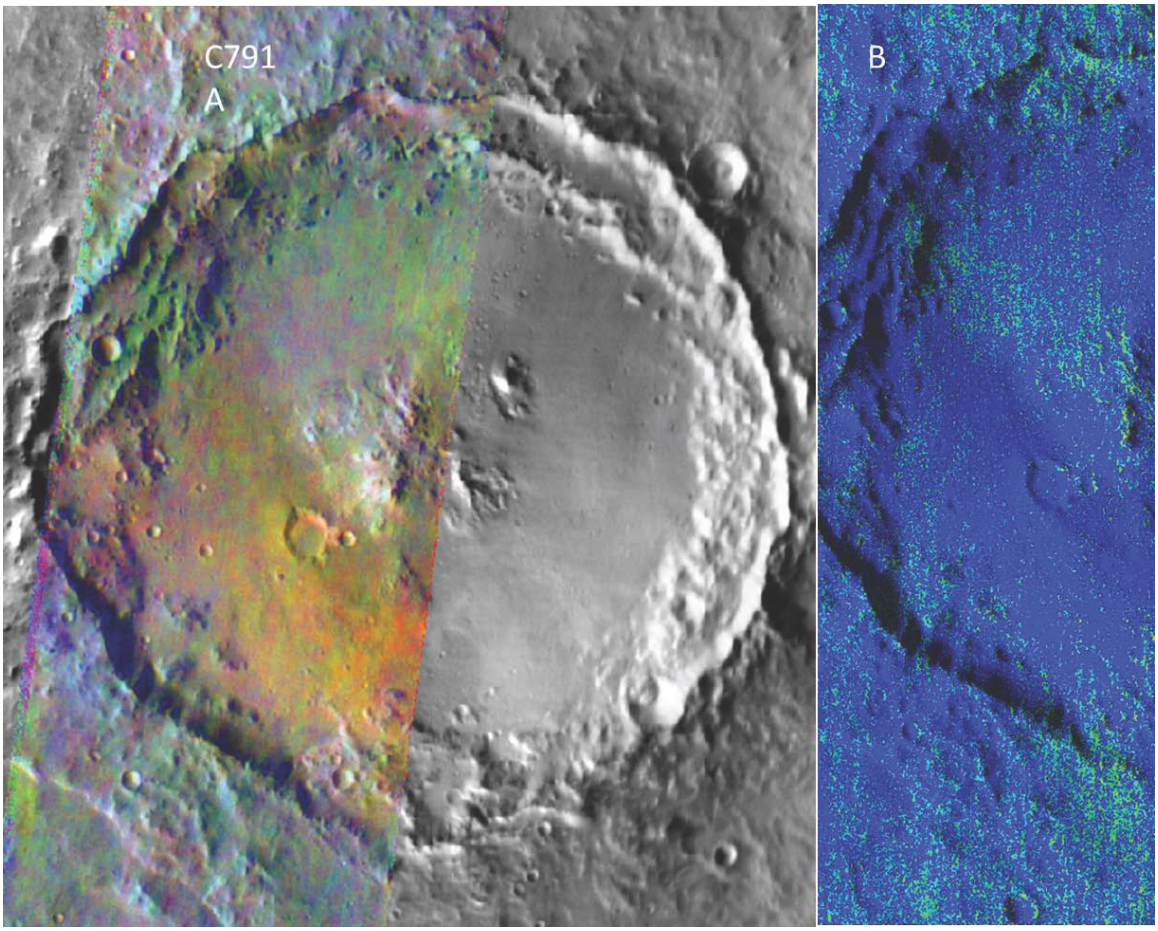

Figure 2.S14 THEMIS and CRISM characteristics of spectral units in the C791 crater central peak. A. THEMIS bands 8(~11.8μm)-7(~11μm)-5(~9.4μm) as red-green-blue in the DCS mosaic. B. THEMIS spectral unit map shows the spectrally distinct unit in the central peak.

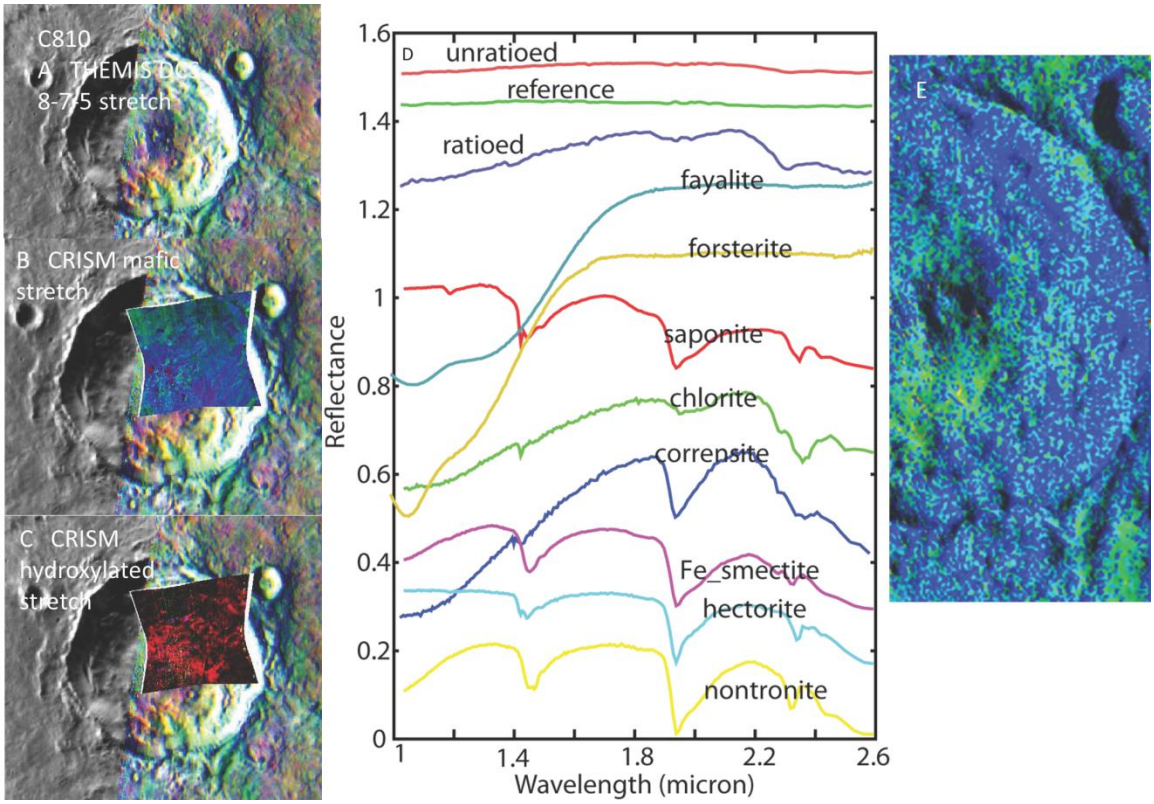

Figure 2.S15 THEMIS and CRISM characteristics of spectral units in the C810 crater central peak. A. THEMIS bands 8(~11.8µm)-7(~11µm)-5(~9.4µm) as red-green-blue in the DCS mosaic. B. CRISM olivine browse image. C. CRISM hydroxylated silicate browse image. D. CRISM spectra and NIR laboratory spectra for comparison. Note: CRISM "ratioed" corresponds with the THEMIS spectrally distinct unit (shown in E). E. THEMIS spectra unit map shows the spectrally distinct unit in the central peak. The spectrally distinct unit is also found on the crater floor.

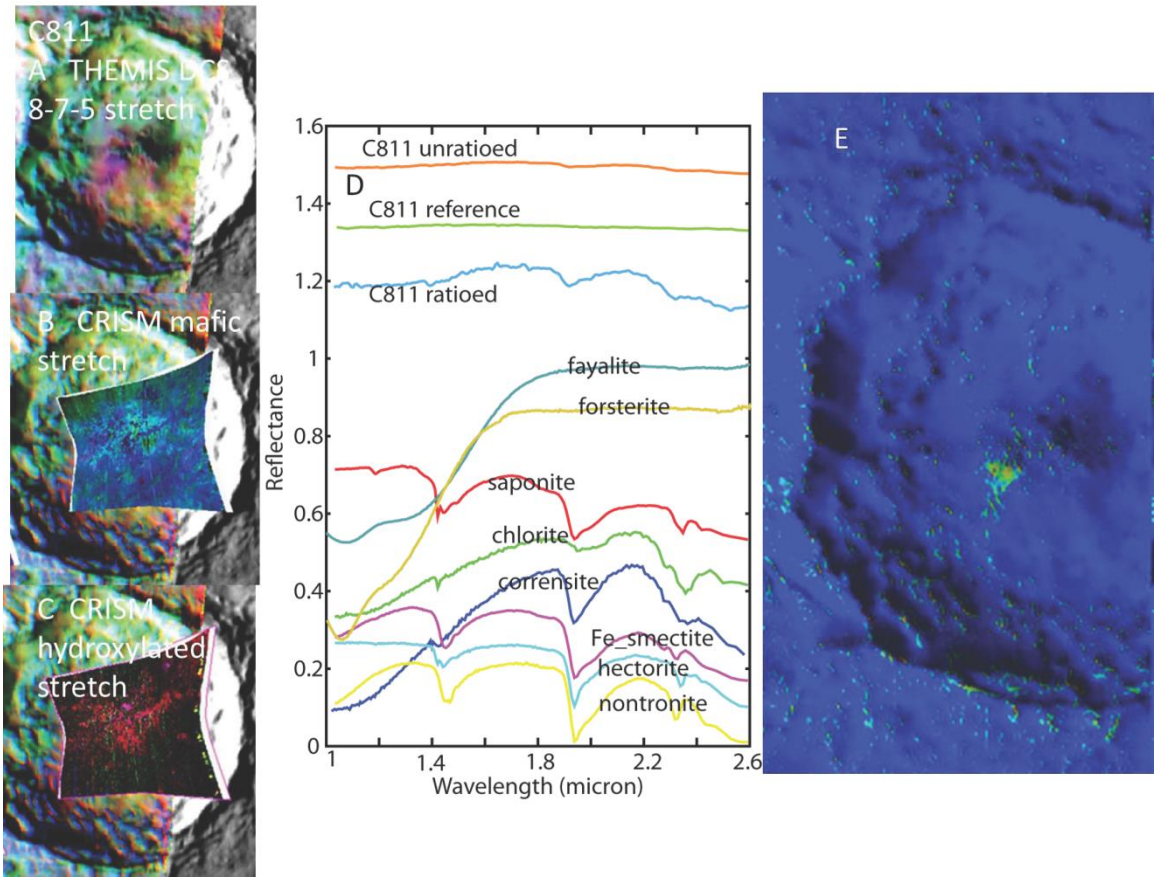

Figure 2.S16THEMIS and CRISM characteristics of spectral units in the C811 crater central peak. A. THEMIS bands 8(~11.8µm)-7(~11µm)-5(~9.4µm) as red-green-blue in the DCS mosaic. B. CRISM mafic browse image. C. CRISM hydroxylated silicate browse image. D CRISM spectra and NIR laboratory spectra for comparison. Note: CRISM "ratioed" corresponds with the THEMIS spectrally distinct unit (shown in E). E. THEMIS spectra unit map shows the spectrally distinct unit in the central peak.

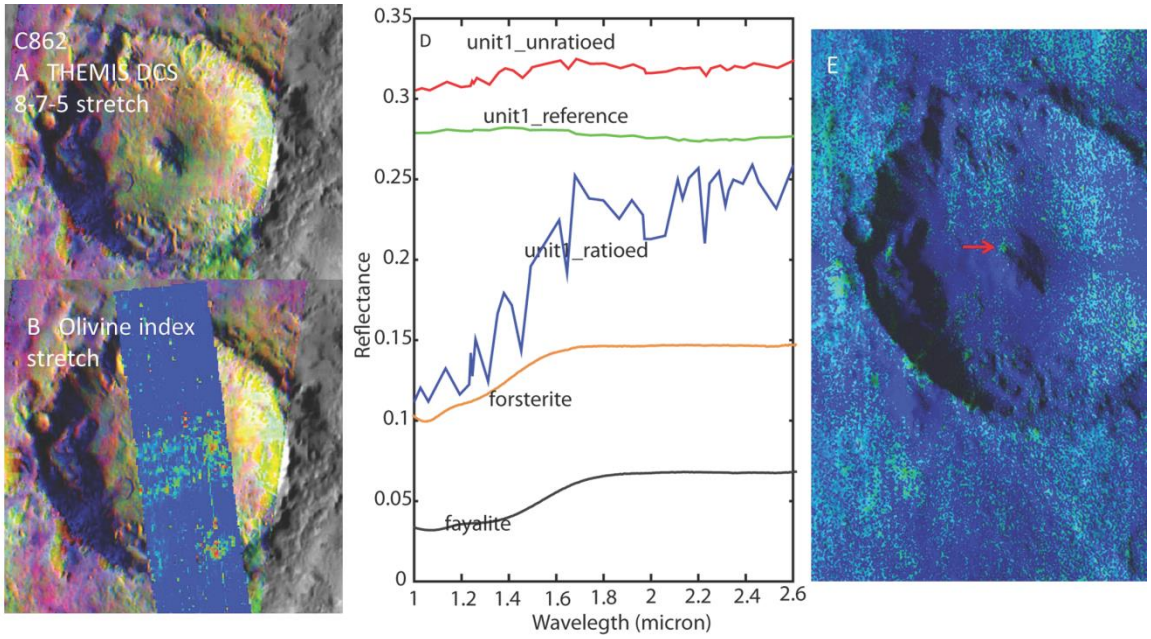

Figure 2.S17 THEMIS and CRISM characteristics of spectral units in the C862 crater central peak. A. THEMIS bands 8(~11.8µm)-7(~11µm)-5(~9.4µm) as red-green-blue in the DCS mosaic. B. CRISM olivine browse image. C. CRISM spectra and NIR laboratory spectra for comparison. Note: CRISM "Unit 1" corresponds with the THEMIS spectrally distinct unit (shown in D). D. THEMIS spectra unit map shows the spectrally distinct unit in the central peak (arrow). The spectrally distinct unit is also found in a few isolated spots of the crater floor.

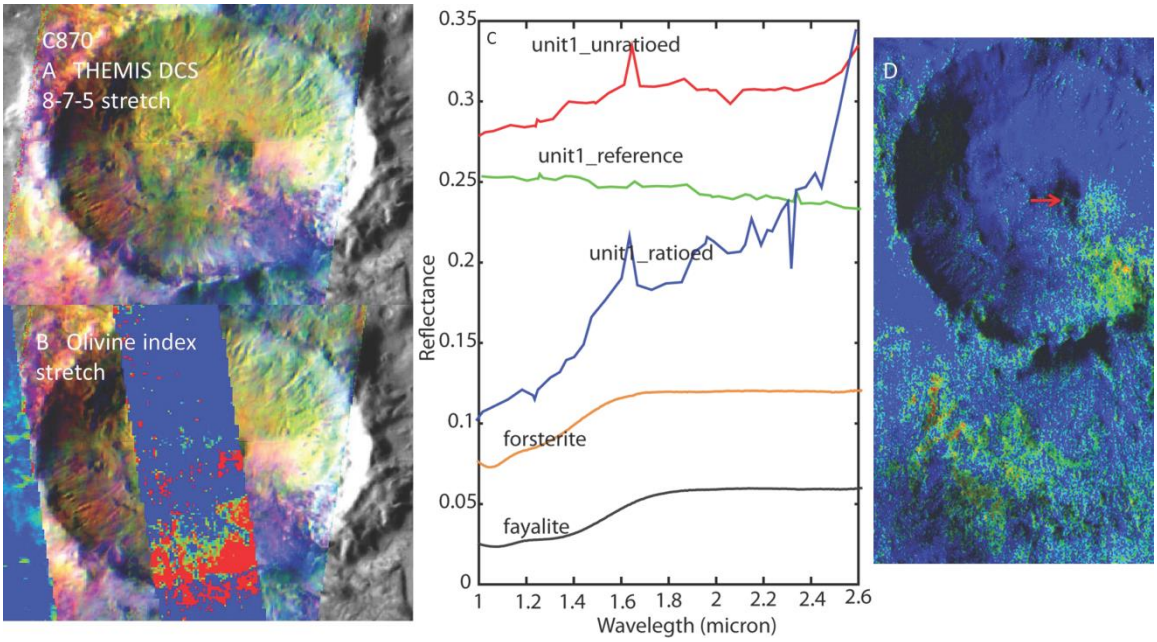

Figure 2.S18 THEMIS and CRISM characteristics of spectral units in the C870 crater central peak. A. THEMIS bands 8(~11.8µm)-7(~11µm)-5(~9.4µm) as red-green-blue in the DCS mosaic. B. CRISM olivine browse image. C. CRISM spectra and NIR laboratory spectra for comparison. Note: CRISM "Unit 1" corresponds with the THEMIS spectrally distinct unit (shown in D). D. THEMIS spectra unit map shows the spectrally distinct unit in the central peak (arrow). The spectrally distinct unit is also found in a few isolated spots of the crater floor and wall.

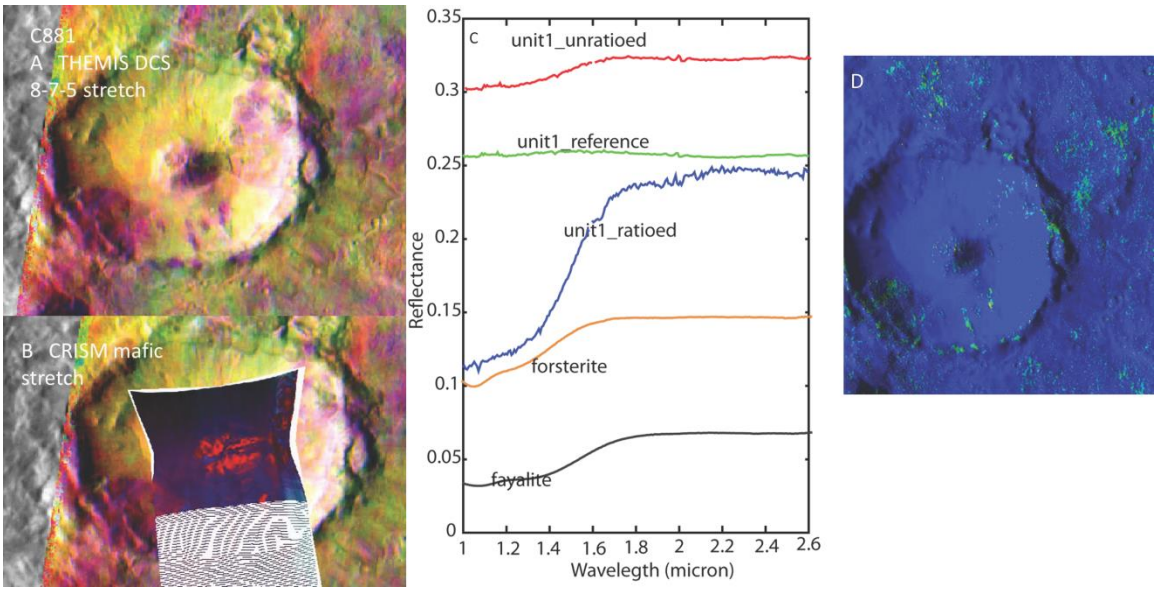

Figure 2.S19 THEMIS and CRISM characteristics of spectral units in the C881 crater central peak. A. THEMIS bands 8(~11.8µm)-7(~11µm)-5(~9.4µm) as red-green-blue in the DCS mosaic. B. CRISM mafic browse image. C. CRISM spectra and NIR laboratory spectra for comparison. Note: CRISM "Unit 1" corresponds with the THEMIS spectrally distinct unit (shown in D). D. THEMIS spectral unit map shows the spectrally distinct unit in the central peak.

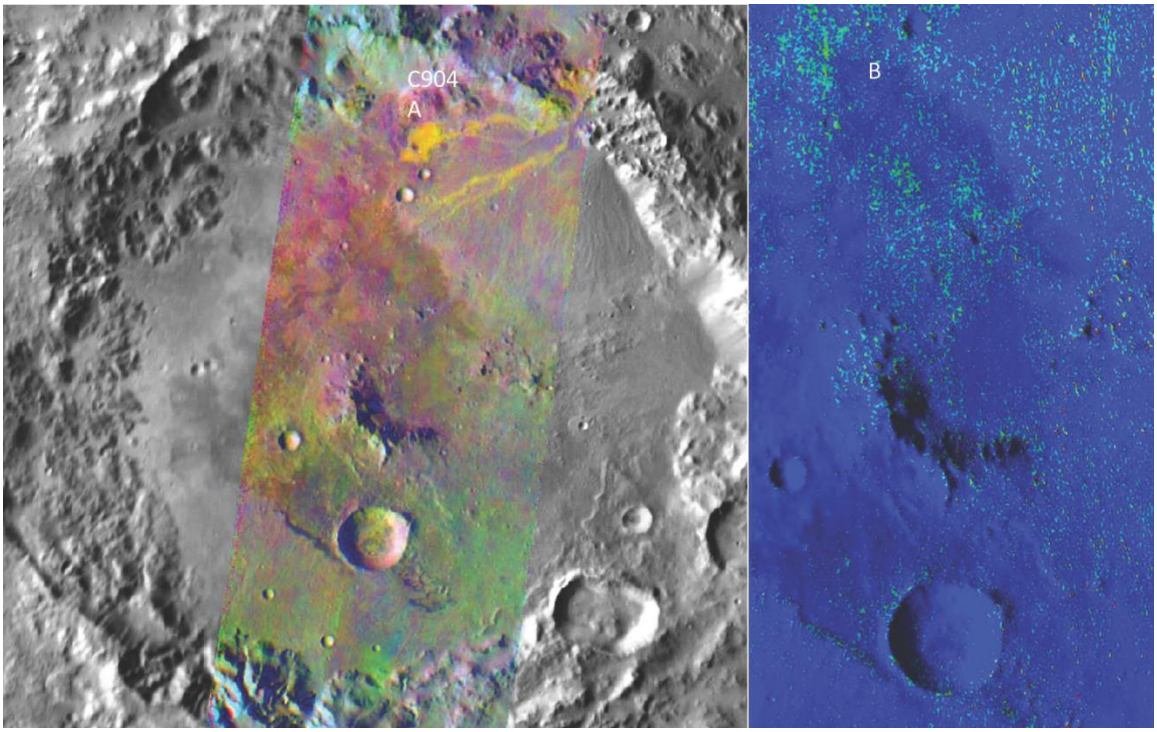

Figure 2.S20 THEMIS and CRISM characteristics of spectral units in the C904 crater central peak. A. THEMIS bands 8(~11.8μm)-7(~11μm)-5(~9.4μm) as red-green-blue in the DCS mosaic. B. THEMIS spectral unit map shows the spectrally distinct unit in the central peak.

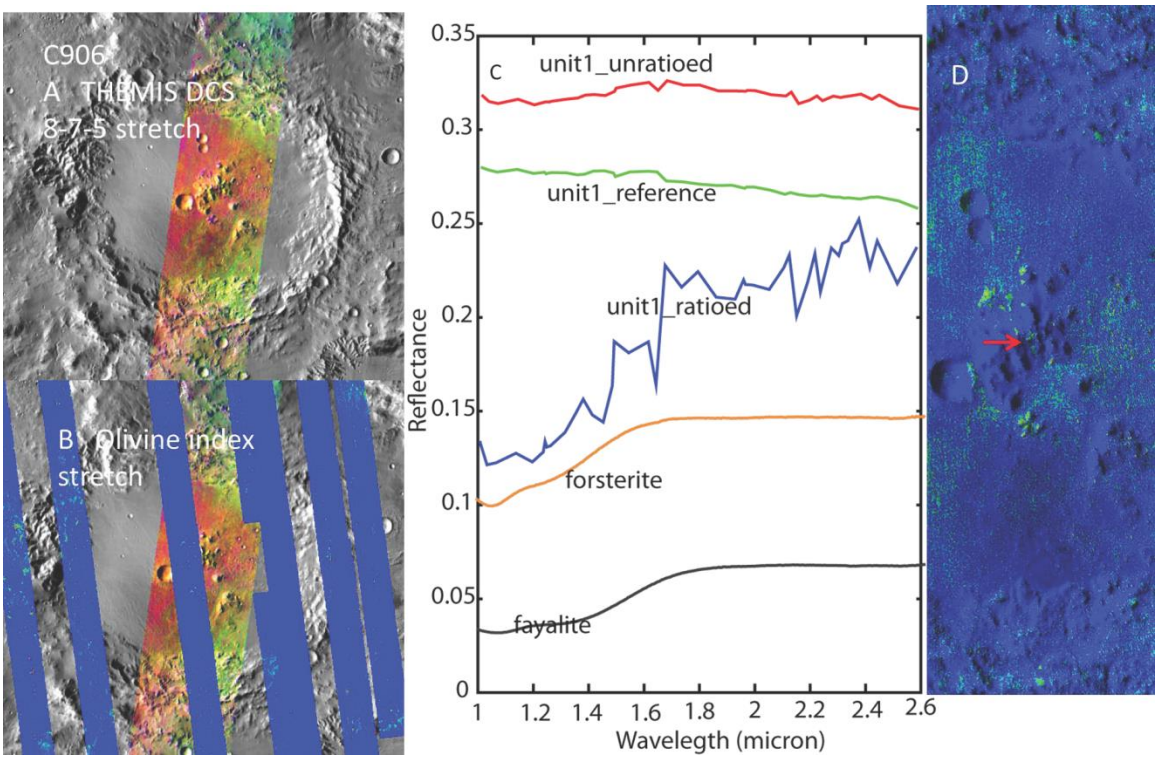

Figure 2.S21 THEMIS and CRISM characteristics of spectral units in the C906 crater central peak. A. THEMIS bands 8(~11.8µm)-7(~11µm)-5(~9.4µm) as red-green-blue in the DCS mosaic. B. CRISM olivine browse image. C. CRISM spectra and NIR laboratory spectra for comparison. Note: CRISM "Unit 1" corresponds with the THEMIS spectrally distinct unit (shown in D). D. THEMIS spectral unit map shows the spectrally distinct unit in the central peak. The spectrally distinct unit is also found in a few isolated spots of the crater floor.

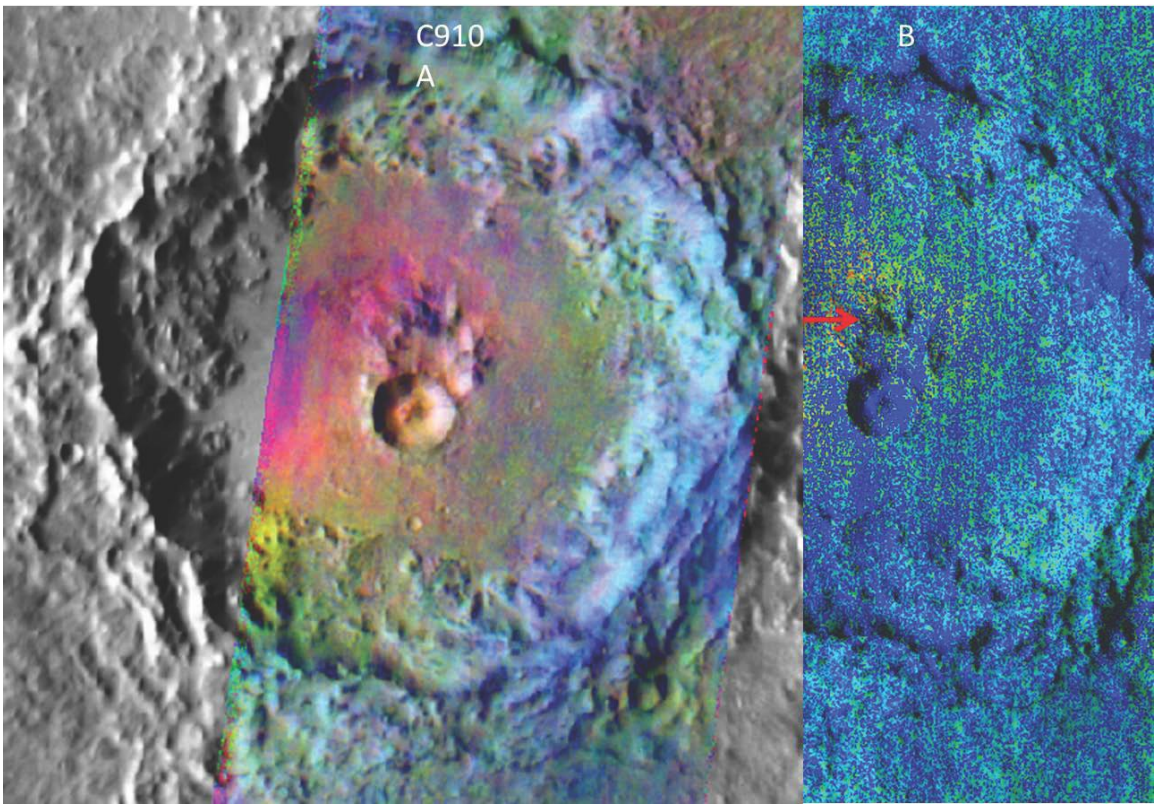

Figure 2.S22 THEMIS and CRISM characteristics of spectral units in the C910 crater central peak. A. THEMIS bands 8(~11.8μm)-7(~11μm)-5(~9.4μm) as red-green-blue in the DCS mosaic. B. THEMIS spectral unit map shows the spectrally distinct unit in the central peak. The spectrally distinct unit is also found on the crater floor.

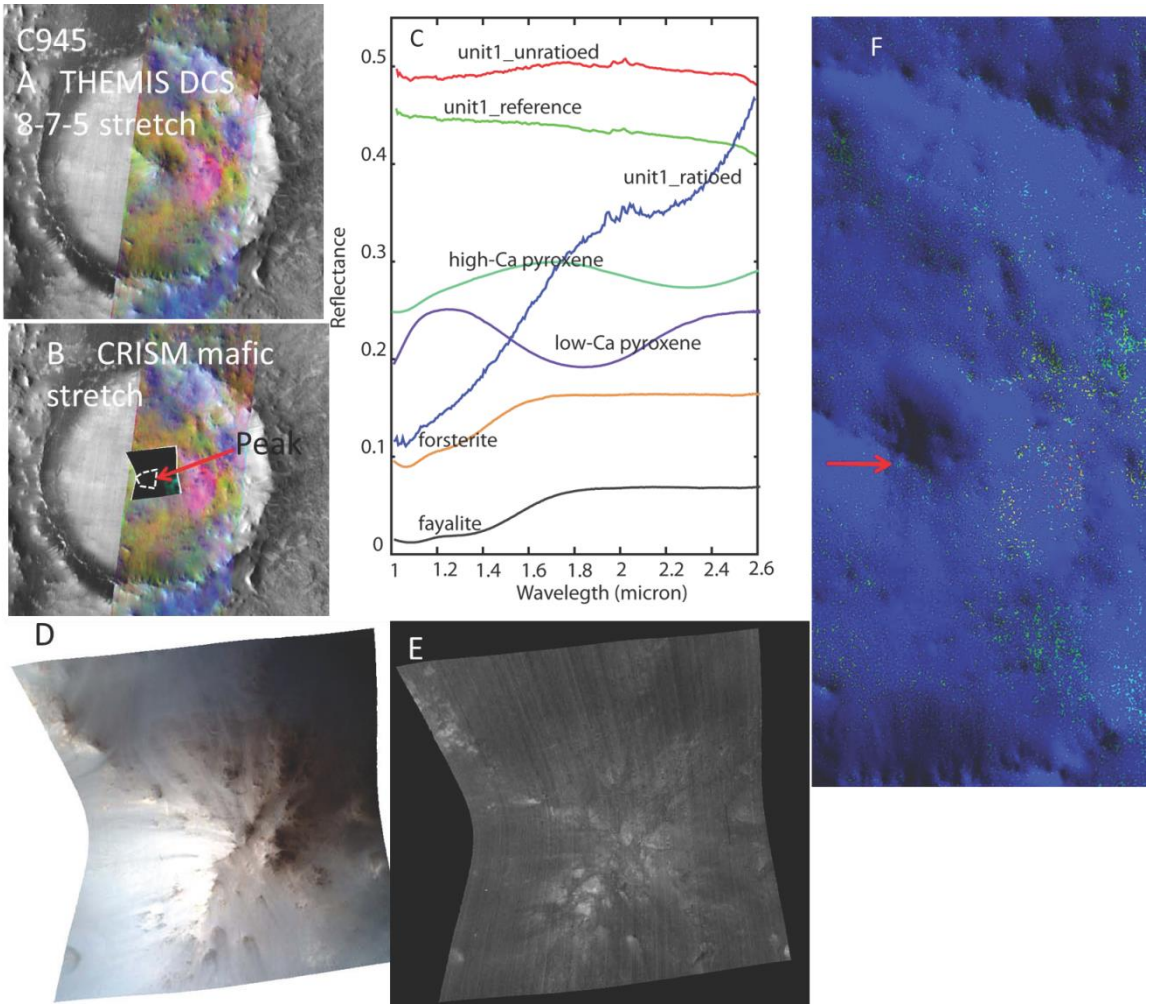

Figure 2.S23 THEMIS and CRISM characteristics of spectral units in the C945 crater central peak. A. THEMIS bands 8(~11.8µm)-7(~11µm)-5(~9.4µm) as red-green-blue in the DCS mosaic. B. CRISM mafic browse image. C. CRISM spectra and NIR laboratory spectra for comparison. Note: CRISM "Unit 1" corresponds with the THEMIS spectrally distinct unit (shown in F). D. CRISM false color image of C945 (band223(2.46 µm)-band78(1.51 µm)-band13(1.08 µm) as red-green-blue). E. CRISM OLINDEX2 stretch map (stretch parameters 0-0.13) showing the olivine-bearing pixels in bright spots. F. THEMIS spectral unit map shows the spectrally distinct unit small spots in the central peak. The spectrally distinct unit is also found in a few isolated spots of the crater floor.

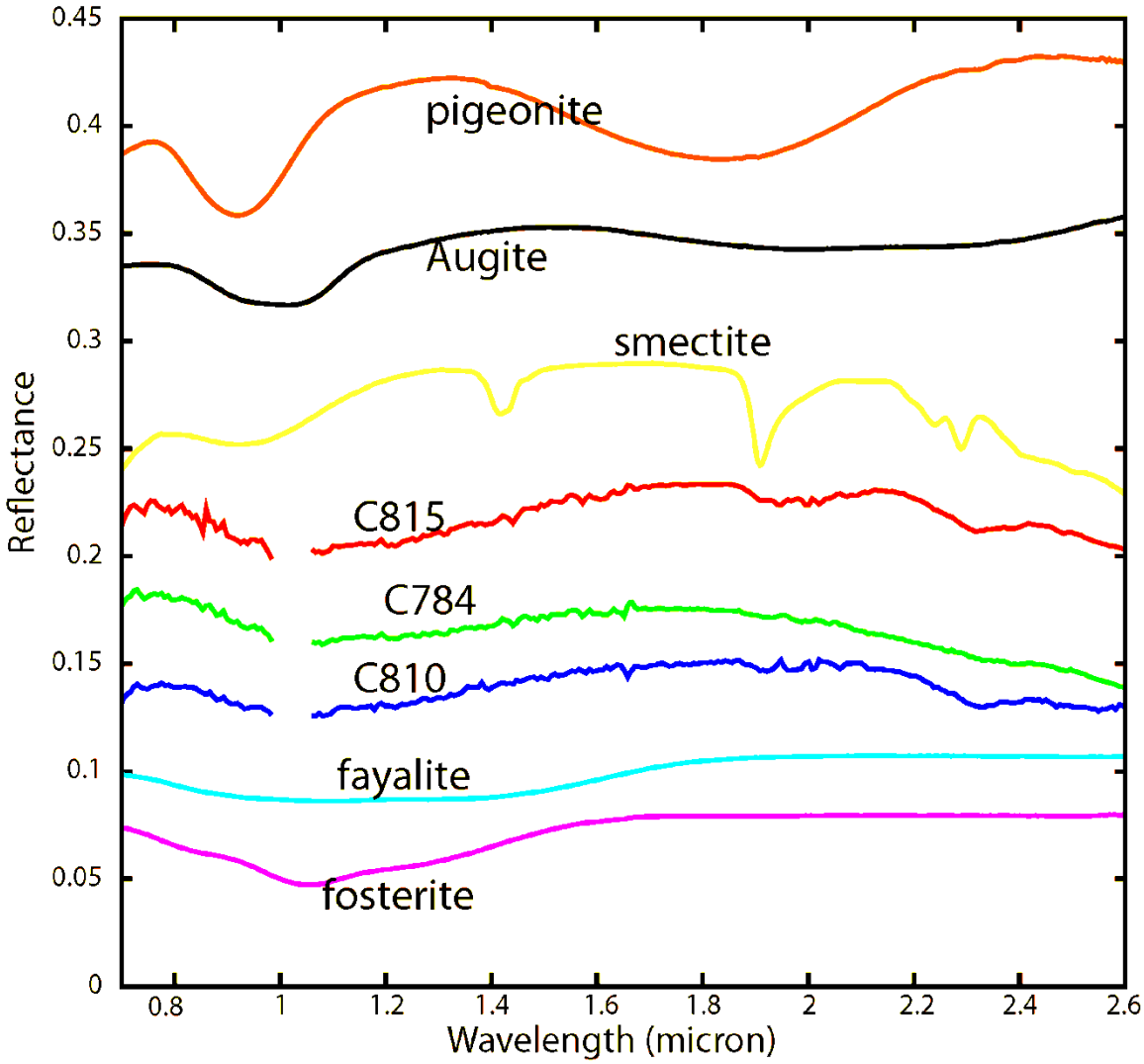

Figure 2.S24 Near infrared spectra of central peak units in the Tyrrhena Terra region and laboratory spectra of smectite, olivine and pyroxene. The spectra are consistent with the presence of both olivine and phyllosilicate minerals.

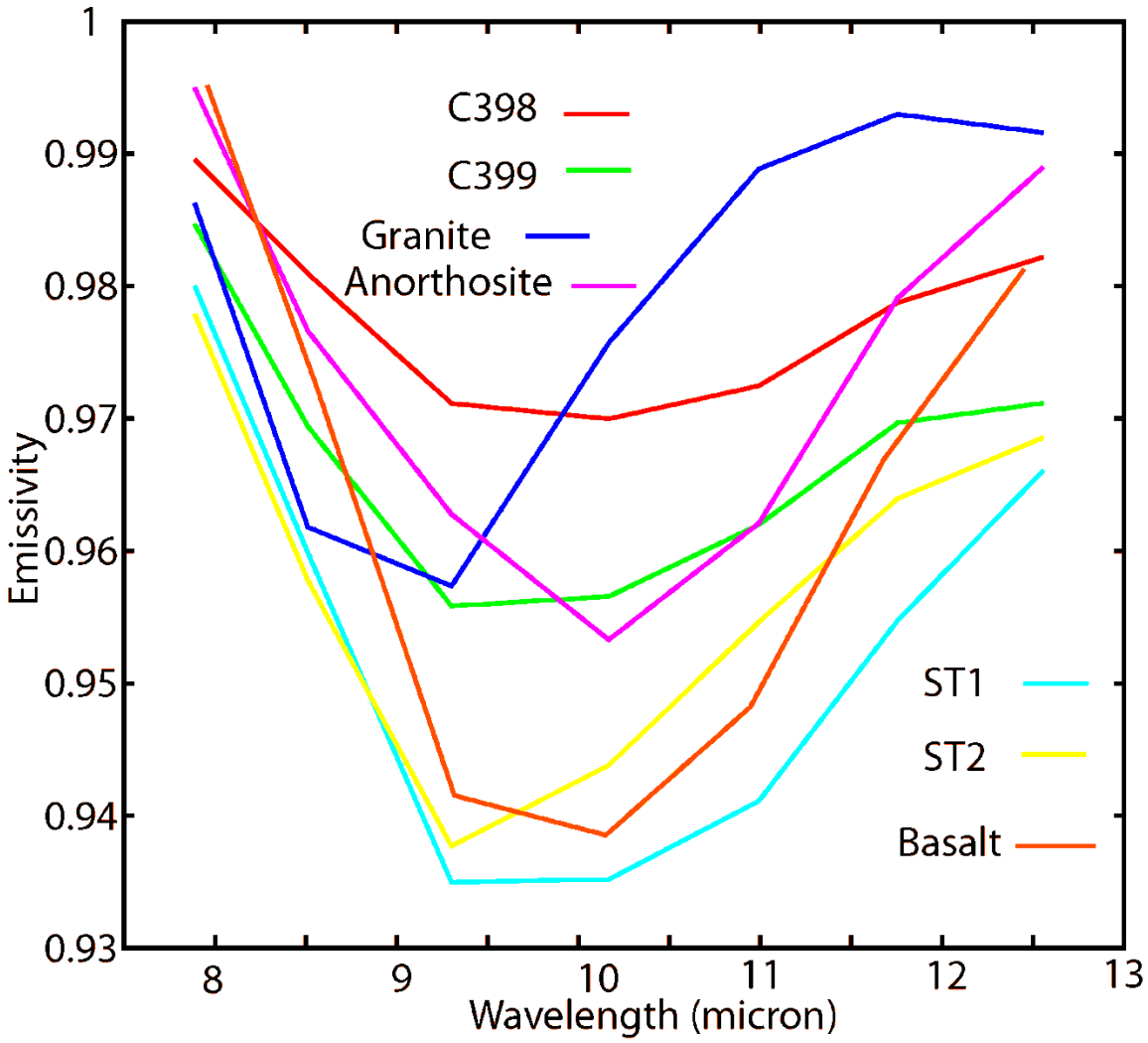

Figure 2.S25 THEMIS spectra of C398 and C399 and comparison with anorthosite, basalt, granite and TES Surface Type 1 and 2, at THEMIS resolution.

References

Baldridge, A. M., and P. R. Christensen (2009), A laboratory technique for thermal emission measurement of hydrated minerals, *Applied spectroscopy*, *63*(6), 678-688.

Bandfield, J. L. (2002), Global mineral distributions on Mars, *Journal of Geophysical Research*, *107*(E6), 5042, doi:10.1029/2001JE001510.

Bandfield, J. L., P. R. Christensen, and M. D. Smith (2000), Spectral data set factor analysis and end-member recovery: Application to analysis of Martian atmospheric particulates, *Journal of Geophysical Research-Planets*, *105*(E4), 9573-9587, doi:10.1029/1999je001094.

Bandfield, J. L., C. S. Edwards, D. R. Montgomery, and B. D. Brand (2013), The dual nature of the martian crust: Young lavas and old clastic materials, *Icarus*, *222*(1), 188-199, doi:10.1016/j.icarus.2012.10.023.

Bandfield, J. L., D. Rogers, M. D. Smith, and P. R. Christensen (2004), Atmospheric correction and surface spectral unit mapping using Thermal Emission Imaging System data, *Journal of Geophysical Research-Planets*, *109*(E10), E10008, doi:10.1029/2004je002289.

Baratoux, D., P. Pinet, A. Gendrin, L. Kanner, J. Mustard, Y. Daydou, J. Vaucher, and J. P. Bibring (2007), Mineralogical structure of the subsurface of Syrtis Major from OMEGA observations of lobate ejecta blankets, *Journal of Geophysical Research-Planets*, *112*(E8), doi:10.1029/2007je002890.

Baratoux, D., M. J. Toplis, M. Monnereau, and O. Gasnault (2011), Thermal history of Mars inferred from orbital geochemistry of volcanic provinces, *Nature*, *472*(7343), 338-U235, doi:10.1038/nature09903.

Barlow, N., J. Boyce, F. Costard, R. Craddock, J. Garvin, S. Sakimoto, R. Kuzmin, D. Roddy, and L. Soderblom (2000), Standardizing the nomenclature of Martian impact crater ejecta morphologies, *Journal of Geophysical Research*, *105*(E11), 26733, doi:10.1029/2000JE001258.

Barnhart, C. J., and F. Nimmo (2011), Role of impact excavation in distributing clays over Noachian surfaces, *Journal of Geophysical Research-Planets*, *116*, 14, doi:10.1029/2010je003629.

Bell III, J. (2008), *The Martian Surface-Composition, Mineralogy, and Physical Properties*, Cambridge University Press, Cambridge, U. K.

Boyce, J. M., and H. Garbeil (2007), Geometric relationships of pristine Martian complex impact craters, and their implications to Mars geologic history, *Geophysical Research Letters*, *34*(16), doi:10.1029/2007gl029731.

Cannon, K. M., J. F. Mustard, C. D. K. Herd, and J. Filiberto (2014), Melting Mars with impacts: proximal melt deposits and their compositions as determined by remote sensing, paper presented at Lunar and Planetary Institute Science Conference Abstracts, LPI, Houston, TX.

Carter, J., and F. Poulet (2013), Ancient plutonic processes on Mars inferred from the detection of possible anorthositic terrains, *Nature Geoscience*, *6*(12), 1008-1012, doi:10.1038/ngeo1995.

Carter, J., F. Poulet, J. P. Bibring, N. Mangold, and S. Murchie (2013), Hydrous minerals on Mars as seen by the CRISM and OMEGA imaging spectrometers: Updated global view, *Journal of Geophysical Research-Planets*, *118*(4), 831-858, doi:10.1029/2012je004145.

Carter, J., F. Poulet, J. P. Bibring, and S. Murchie (2010), Detection of hydrated silicates in crustal outcrops in the northern plains of Mars, *Science*, *328*(5986), 1682, doi:10.1126/science.1189013.

Carter, L. M., B. A. Campbell, J. W. Holt, R. J. Phillips, N. E. Putzig, S. Mattei, R. Seu, C. H. Okubo, and A. F. Egan (2009), Dielectric properties of lava flows west of Ascraeus Mons, Mars, *Geophysical Research Letters*, *36*, L23204, doi:10.1029/2009gl041234.

Caudill, C. M., L. L. Tornabene, A. S. McEwen, S. Byrne, L. Ojha, and S. Mattson (2012), Layered MegaBlocks in the central uplifts of impact craters, *Icarus*, *221*(2), 710-720, doi:10.1016/j.icarus.2012.08.033.

Christensen, P. R., et al. (1992), Thermal emission spectrometer experiment: Mars Observer Mission, *Journal of Geophysical Research-Planets*, *97*(E5), 7719-7734, doi:10.1029/2000JE001370.

Christensen, P. R., et al. (2001), Mars Global Surveyor Thermal Emission Spectrometer experiment:

Investigation description and surface science results, *Journal of Geophysical Research-Planets*, *106*(E10), 23823-23871, doi:10.1029/2000je001370.
Christensen, P. R., et al. (2004), The Thermal Emission Imaging System (THEMIS) for the Mars 2001 Odyssey Mission, *Space Sci. Rev.*, *110*(1-2), 85-130, doi:10.1023/b:spac.0000021008.16305.94.
Christensen, P. R., et al. (2005), Evidence for magmatic evolution and diversity on Mars from infrared observations, *Nature*, *436*(7052), 882-882, doi:10.1038/nature04075.
Christensen, P. R., and H. J. Moore (1992), The Martian surface layer, in *Mars*, edited by H. H. Kieffer, Jakosky, B. M. ,Snyder, C. W.,Matthews, M. S., pp. 686-729, University of Arizona Press, Tucson.
Clark, R. N. (1999), Spectroscopy of Rocks and Minerals, and Principles of Spectroscopy, in *Manual of Remote Sensing, Volume 3, Remote Sensing for the Earth Sciences*, edited by A. N. Rencz, pp. 3-58, John Wiley and Sons, New York.
Clenet, H., P. Pinet, G. Ceuleneer, Y. Daydou, F. Heuripeau, C. Rosemberg, J. P. Bibring, G. Bellucci, F. Altieri, and B. Gondet (2013), A systematic mapping procedure based on the Modified Gaussian Model to characterize magmatic units from olivine/pyroxenes mixtures: Application to the Syrtis Major volcanic shield on Mars, *Journal of Geophysical Research-Planets*, *118*(8), 1632-1655, doi:10.1002/jgre.20112.
Clenet, H., P. Pinet, Y. Daydou, F. Heuripeau, C. Rosemberg, D. Baratoux, and S. Chevrel (2011), A new systematic approach using the Modified Gaussian Model: Insight for the characterization of chemical composition of olivines, pyroxenes and olivine-pyroxene mixtures, *Icarus*, *213*(1), 404-422, doi:10.1016/j.icarus.2011.03.002.
Cloutis, E. A., P. M. Asher, and S. A. Mertzman (2002), Spectral reflectance properties of zeolites and remote sensing implications, *Journal of Geophysical Research-Planets*, *107*(E9), doi:10.1029/2000je001467.
Coblentz, W. W. (1906), *Investigations of infrared spectra*, Carnegie institution of Washington, Washington, D.C.
Croft, S. K. (1985), The scaling of complex craters, *Journal of Geophysical Research: Solid Earth 90*(S02), C828-C842.
Edwards, C. S., J. L. Bandfield, P. R. Christensen, and R. L. Fergason (2009), Global distribution of bedrock exposures on Mars using THEMIS high-resolution thermal inertia, *Journal of Geophysical Research-Planets*, *114*, E11001, doi:10.1029/2009je003363.
Ehlmann, B. L., J. F. Mustard, S. L. Murchie, J. P. Bibring, A. Meunier, A. A. Fraeman, and Y. Langevin (2011), Subsurface water and clay mineral formation during the early history of Mars, *Nature*, *479*(7371), 53-60, doi:10.1038/nature10582.
Ehlmann, B. L., et al. (2008), Orbital Identification of Carbonate-Bearing Rocks on Mars, *Science*, *322*(5909), 1828-1832, doi:10.1126/science.1164759.
Feldman, W. C., et al. (2002), Global distribution of neutrons from Mars: Results from Mars Odyssey, *Science*, *297*(5578), 75-78, doi:10.1126/science.1073541.
French, B. (1998), Traces of catastrophe: A handbook of shock-metamorphic effects in terrestrial meteorite impact structures.
Gaffey, S. J., L. A. McFadden, D. B. Nash, and C. M. Pieters (1993), Ultraviolet, Visible, and Near-Infrared Reflectance Spectroscopy: Laboratory Spectra of Geologica Materials, in *Remote Geochemical Analysis: Elemental and Mineralogical Composition*, edited by C. M. Pieters and P. A. J. Englert, Cambridge University Press, Cambridge, UK.
Gillespie, A. R. (1986), Lithologic mapping of silicate rocks using TIMS, paper presented at The TIMS Data User's Workshop., Jet Propulsion Laboratory, Jet Propulsion Laboratory, Pasadena, CA.
Gillespie, A. R., A. B. Kahle, and R. E. Walker (1986), Color enhancement of highly correlated images. 1. Decorrelaton and HSI contrast stretches, *Remote Sensing of Environment*, *20*(3), 209-235, doi:10.1016/0034-4257(86)90044-1.
Greeley, R., and J. Guest (1987), *Geologic map of the eastern equatorial region of Mars*, Geological Survey (US).

Hook, S. J., J. E. Dmochowski, K. A. Howard, L. C. Rowan, K. E. Karlstrom, and J. M. Stock (2005), Mapping variations in weight percent silica measured from multispectral thermal infrared imagery—Examples from the Hiller Mountains, Nevada, USA and Tres Virgenes-La Reforma, Baja California Sur, Mexico, *Remote sensing of environment*, *95*(3), 273-289, doi:10.1016/j.rse.2004.11.020.

Horgan, B., and J. F. Bell, III (2012), Widespread weathered glass on the surface of Mars, *Geology*, *40*(5), 391-394, doi:10.1130/g32755.1.

Horgan, B., E. A. Cloutis, P. Mann, and J. F. Bell, III (2014), Near-infrared spectra of ferrous mineral mixtures and methods for their identification in planetary surface spectra, *Icarus*, *234*, 132-154, doi:10.1016/j.icarus.2014.02.031.

Jaeger, W. L., L. P. Keszthelyi, A. S. McEwen, C. M. Dundas, and P. S. Russell (2007), Athabasca Valles, Mars: A lava-draped channel system, *Science*, *317*(5845), 1709-1711, doi:10.1126/science.1143315.

Keszthelyi, L., W. L. Jaeger, C. M. Dundas, S. Martinez-Alonso, A. S. McEwen, and M. P. Milazzo (2010), Hydrovolcanic features on Mars: Preliminary observations from the first Mars year of HiRISE imaging, *Icarus*, *205*(1), 211-229, doi:10.1016/j.icarus.2009.08.020.

Keszthelyi, L., S. Self, and T. Thordarson (2006), Flood lavas on earth, Io and Mars, *Journal of the Geological Society*, *163*, 253-264, doi:10.1144/0016-764904-503.

Korteniemi, J., V. P. Kostama, T. Törmänen, M. Aittola, T. Öhman, H. Lahtela, J. Raitala, and G. Neukum (2005), Complex geology of two large impact craters in Tyrrhena Terra, Mars: Detailed analysis using MEX HRSC camera data, *Journal of Geophysical Research: Planets 110*(E12), E12S18, doi:10.1029/2005JE002427.

Kraft, M. D., J. R. Michalski, and T. G. Sharp (2003), Effects of pure silica coatings on thermal emission spectra of basaltic rocks: Considerations for Martian surface mineralogy, *Geophysical Research Letters*, *30*(24), doi:10.1029/2003gl018848.

Kraft, M. D., M. Salvatore, C. Edwards, and P. Christensen (2014), Occurrence, Distribution and Implications of Mafic Igneous Bedrock Throughout the Uzboi-Ladon-Margaritifer Fluvial System, Mars, paper presented at Lunar and Planetary Institute Science Conference Abstracts, LPI, Houston, TX.

Leonard, G. L., and K. L. Tanaka (2001), *Geologic map of the Hellas region of Mars*, Geological Survey (US), Flagstaff, AZ.

Malin, M. C., and K. S. Edgett (2000), Sedimentary rocks of early Mars, *Science*, *290*(5498), 1927-1937, doi:10.1126/science.290.5498.1927.

Mangold, N., S. Adeli, S. Conway, V. Ansan, and B. Langlais (2012), A chronology of early Mars climatic evolution from impact crater degradation, *Journal of Geophysical Research-Planets*, *117*, 22, doi:10.1029/2011je004005.

Marzo, G. A., A. F. Davila, L. L. Tornabene, J. M. Dohm, A. G. Fairen, C. Gross, T. Kneissl, J. L. Bishop, T. L. Roush, and C. P. McKay (2010), Evidence for Hesperian impact-induced hydrothermalism on Mars, *Icarus*, *208*(2), 667-683, doi:10.1016/j.icarus.2010.03.013.

Maxwell, A. E. (1977), *Multivariate analysis in behavioural research*, Chapman and Hall London, London, U. K.

McEwen, A. S., et al. (2007), A closer look at water-related geologic activity on Mars, *Science*, *317*(5845), 1706-1709, doi:10.1126/science.1143987.

Melosh, H. J. (1989), *Impact cratering: A geologic process*, Oxford University Press, New York.

Melosh, H. J., and B. A. Ivanov (1999), Impact crater collapse, *Annual Review of Earth and Planetary Sciences*, *27*, 385-415, doi:10.1146/annurev.earth.27.1.385.

Mest, S. C., and D. A. Crown (2005), Millochau crater, Mars: Infilling and erosion of an ancient highland impact crater, *Icarus*, *175*(2), 335-359, doi:10.1016/j.icarus.2004.12.008.

Michalski, J. R., J. Cuadros, P. B. Niles, J. Parnell, A. D. Rogers, and S. P. Wright (2013), Groundwater activity on Mars and implications for a deep biosphere, *Nature Geoscience*, *6*(2), 133-138, doi:10.1038/NGEO1706.

Michalski, J. R., M. D. Kraft, T. G. Sharp, L. B. Williams, and P. R. Christensen (2006), Emission spectroscopy of clay minerals and evidence for poorly crystalline aluminosilicates on Mars from Thermal Emission Spectrometer data, *Journal of Geophysical Research-Planets*, *111*(E3), E03004, doi:10.1029/2005je002438.

Michalski, J. R., and P. B. Niles (2010), Deep crustal carbonate rocks exposed by meteor impact on Mars, *Nature Geoscience*, *3*(11), 751-755, doi:10.1038/NGEO971.

Minitti, M. E., C. M. Weitz, M. D. Lane, and J. L. Bishop (2007), Morphology, chemistry, and spectral properties of Hawaiian rock coatings and implications for Mars, *Journal of Geophysical Research-Planets*, *112*(E5), E05015, doi:10.1029/2006je002839.

Moore, J. M., and A. D. Howard (2005), Large alluvial fans on Mars, *Journal of Geophysical Research-Planets*, *110*(E4), E04005, doi:10.1029/2004je002352.

Moore, J. M., and D. E. Wilhelms (2001), Hellas as a possible site of ancient ice-covered lakes on Mars, *Icarus*, *154*(2), 258-276, doi:10.1006/icar.2001.6736.

Morris, A. R., P. J. Mouginis-Mark, and H. Garbeil (2010), Possible impact melt and debris flows at Tooting Crater, Mars, *Icarus*, *209*(2), 369-389, doi:10.1016/j.icarus.2010.05.029.

Murchie, S. L., et al. (2007), Compact reconnaissance Imaging Spectrometer for Mars (CRISM) on Mars Reconnaissance Orbiter (MRO), *Journal of Geophysical Research-Planets*, *112*(E5), E05s03, doi:10.1029/2006je002682.

Murchie, S. L., et al. (2009), A synthesis of Martian aqueous mineralogy after 1 Mars year of observations from the Mars Reconnaissance Orbiter, *Journal of Geophysical Research-Planets*, *114*, 30, doi:10.1029/2009je003342.

Murchie, S. L., J. F. Mustard, B. L. Ehlmann, R. E. Milliken, J. L. Bishop, N. K. McKeown, E. Z. Noe Dobrea, F. P. Seelos, D. L. Buczkowski, and S. M. Wiseman (2009), A synthesis of Martian aqueous mineralogy after 1 Mars year of observations from the Mars Reconnaissance Orbiter, *Journal of Geophysical Research: Planets 114*(E2), E00D06, doi:10.1029/2009JE003342.

Mustard, J. F., C. D. Cooper, and M. K. Rifkin (2001), Evidence for recent climate change on Mars from the identification of youthful near-surface ground ice, *Nature*, *412*(6845), 411-414, doi:10.1038/35086515.

Mustard, J. F., F. Poulet, A. Gendrin, J. P. Bibring, Y. Langevin, B. Gondet, N. Mangold, G. Bellucci, and F. Altieri (2005), Olivine and pyroxene, diversity in the crust of Mars, *Science*, *307*(5715), 1594-1597, doi:10.1126/science.1109098.

Ody, A., F. Poulet, J. P. Bibring, D. Loizeau, J. Carter, B. Gondet, and Y. Langevin (2013), Global investigation of olivine on Mars: Insights into crust and mantle compositions, *Journal of Geophysical Research-Planets*, *118*(2), 234-262, doi:10.1029/2012je004149.

Osinski, G. R., et al. (2013), Impact-generated hydrothermal systems on Earth and Mars, *Icarus*, *224*(2), 347-363, doi:10.1016/j.icarus.2012.08.030.

Pearson, K. (1901), On lines and planes of closest fit to systems of points in space, *Philosophical Magazine*, *2*(7-12), 559-572, doi:10.1080/14786440109462720.

Pelkey, S., J. Mustard, S. Murchie, R. Clancy, M. Wolff, M. Smith, R. Milliken, J. Bibring, A. Gendrin, and F. Poulet (2007), CRISM multispectral summary products: Parameterizing mineral diversity on Mars from reflectance, *J. Geophys. Res*, *112*(E8), E08S14, doi:10.1029/2006JE002831.

Pieters, C. M., S. Tompkins, J. W. Head, and P. C. Hess (1997), Mineralogy of the mafic anomaly in the South Pole Aitken basin: Implications for excavation of the lunar mantle, *Geophysical Research Letters*, *24*(15), 1903-1906, doi:10.1029/97gl01718.

Pinet, P., and S. Chevrel (1990), SPECTRAL IDENTIFICATION OF GEOLOGICAL UNITS ON THE SURFACE OF MARS RELATED TO THE PRESENCE OF SILICATES FROM EARTH-BASED NEAR-INFRARED TELESCOPIC CHARGE-COUPLED DEVICE IMAGING, *Journal of Geophysical Research-Solid Earth and Planets*, *95*(B9), 14435-14446, doi:10.1029/JB095iB09p14435.

Pinet, P., S. D. Chevrel, and P. Martin (1993), COPERNICUS - A REGIONAL PROBE OF THE LUNAR INTERIOR, *Science*, *260*(5109), 797-801, doi:10.1126/science.260.5109.797.

Plescia, J. B. (1990), Recent flood lavas in the Elysium region of Mars, *Icarus*, *88*(2), 465-490, doi:10.1016/0019-1035(90)90095-q.

Poulet, F., C. Gomez, J. P. Bibring, Y. Langevin, B. Gondet, P. Pinet, G. Belluci, and J. Mustard (2007), Martian surface mineralogy from Observatoire pour la Mineralogie, l'Eau, les Glaces et l'Activite on board the Mars Express spacecraft (OMEGA/MEx): Global mineral maps, *Journal of Geophysical Research-Planets*, *112*(E8), doi:10.1029/2006je002840.

Quantin, C., J. Flahaut, H. Clenet, P. Allemand, and P. Thomas (2012), Composition and structures of the subsurface in the vicinity of Valles Marineris as revealed by central uplifts of impact craters, *Icarus*, *221*(1), 436-452, doi:10.1016/j.icarus.2012.07.031.

Ramsey, M. S., and P. R. Christensen (1998), Mineral abundance determination: Quantitative deconvolution of thermal emission spectra, *Journal of Geophysical Research-Solid Earth*, *103*(B1), 577-596, doi:10.1029/97JB02784.

Realmuto, V. J. (1990), Separating the effects of temperature and emissivity: emissivity spectrum normalization, in *Proceedings of the Second TIMS Workshop*, edited, pp. 23-27, JPL Publication, Pasadena, CA.

Robbins, S. J., and B. M. Hynek (2012), A new global database of Mars impact craters≥ 1 km: 1. Database creation, properties, and parameters, *Journal of Geophysical Research*, *117*(E5), E05004, doi:10.1029/2011JE003966.

Robbins, S. J., and B. M. Hynek (2012), A new global database of Mars impact craters≥ 1 km: 2. Global crater properties and regional variations of the simple-to-complex transition diameter, *Journal of Geophysical Research: Planets (1991–2012)*, *117*(E6).

Rogers, A. D., and O. Aharonson (2008), Mineralogical composition of sands in Meridiani Planum determined from Mars Exploration Rover data and comparison to orbital measurements, *Journal of Geophysical Research-Planets*, *113*(E6), E06S14, doi:10.1029/2007je002995.

Rogers, A. D., and P. R. Christensen (2007), Surface mineralogy of Martian low-albedo regions from MGS-TES data: Implications for upper crustal evolution and surface alteration, *Journal of Geophysical Research-Planets*, *112*(E1), E01003, doi:10.1029/2006je002727.

Rogers, A. D., P. R. Christensen, and J. L. Bandfield (2005), Compositional heterogeneity of the ancient Martian crust: analysis of Ares Vallis bedrock with THEMIS and TES data, *Journal of Geophysical Research-Planets*, *110*(E5), E05010, doi:10.1029/2005je002399.

Rogers, A. D., and R. L. Fergason (2011), Regional-scale stratigraphy of surface units in Tyrrhena and Iapygia Terrae, Mars: Insights into highland crustal evolution and alteration history, *Journal of Geophysical Research-Planets*, *116*, E08005, doi:E0800510.1029/2010je003772.

Ruff, S. W., P. R. Christensen, D. L. Blaney, W. H. Farrand, J. R. Johnson, J. R. Michalski, J. E. Moersch, S. P. Wright, and S. W. Squyres (2006), The rocks of Gusev Crater as viewed by the Mini-TES instrument, *Journal of Geophysical Research-Planets*, *111*(E12), doi:10.1029/2006je002747.

Ryan, A. J., and P. R. Christensen (2012), Coils and polygonal crust in the Athabasca Valles Region, Mars, as evidence for a volcanic history, *Science*, *336*(6080), 449-452, doi:10.1126/science.1219437.

Sabine, C., V. J. Realmuto, and J. V. Taranik (1994), Quantitative estimation of granitoid composition from thermal infrared multispectral scanner (TIMS) data, Desolation Wilderness, northern Sierra Nevada, California, *Journal of Geophysical Research: Solid Earth 99*(B3), 4261-4271, doi:10.1029/93JB03127.

Salvatore, M. R., J. F. Mustard, M. B. Wyatt, and S. L. Murchie (2010), Definitive evidence of Hesperian basalt in Acidalia and Chryse planitiae, *Journal of Geophysical Research-Planets*, *115*, doi:10.1029/2009je003519.

Sautter, V., et al. (2014), Igneous mineralogy at Bradbury Rise: The first ChemCam campaign at Gale crater, *Journal of Geophysical Research-Planets*, *119*(1), 30-46, doi:10.1002/2013je004472.

Scott, D. H., and K. L. Tanaka (1986), *Geologic map of the western equatorial region of Mars*, Geological Survey (US), Flagstaff, AZ.

Sharpton, V. L. (2014), Constraints on Crater Growth Mechanisms, Ejecta Thicknesses and Excavation Depths from Target Outcrops at Fresh Lunar Craters, paper presented at Lunar and Planetary Institute Science Conference Abstracts, LPI, Houston, TX.

Skok, J., J. Mustard, L. Tornabene, C. Pan, D. Rogers, and S. Murchie (2012), A spectroscopic analysis of Martian crater central peaks: Formation of the ancient crust, *Journal of Geophysical Research: Planets 117*(E11), E00J18, doi:10.1029/2012JE004148.

Smith, M. R., J. L. Bandfield, E. A. Cloutis, and M. S. Rice (2013), Hydrated silica on Mars: Combined analysis with near-infrared and thermal-infrared spectroscopy, *Icarus, 223*(2), 633-648, doi:10.1016/j.icarus.2013.01.024.

Stockstill-Cahill, K. R., F. S. Anderson, and V. E. Hamilton (2008), A study of low-albedo deposits within Amazonis Planitia craters: Evidence for locally derived ultramafic to mafic materials, *Journal of Geophysical Research-Planets*, *113*(E7), doi:10.1029/2007je003036.

Sun, V. Z., and R. E. Milliken (2014), The geology and mineralogy of Ritchey crater, Mars: Evidence for post-Noachian clay formation, *Journal of Geophysical Research-Planets*, *119*(4), 810-836, doi:10.1002/2013je004602.

Tanaka, K. L., and G. J. Leonard (1995), Geology and landscape evolution of the Hellas region of Mars, *Journal of Geophysical Research-Planets*, *100*(E3), 5407-5432, doi:10.1029/94je02804.

Tompkins, S., and C. M. Pieters (1999), Mineralogy of the lunar crust: Results from Clementine, *Meteoritics & Planetary Science*, *34*(1), 25-41, doi: 10.1111/j.1945-5100.1999.tb01729.x.

Tornabene, L. L., A. McEwen, C. Caudill, G. Osinski, J. Wray, G. Marzo, J. Mustard, J. Skok, J. Grant, and S. Mattson (2010), A crater-exposed bedrock database for Mars with applications for determining the composition and structure of the upper crust, paper presented at Lunar and Planetary Science Conference.

Tornabene, L. L., J. E. Moersch, H. Y. McSween, V. E. Hamilton, J. L. Piatek, and P. R. Christensen (2008), Surface and crater-exposed lithologic units of the Isidis Basin as mapped by coanalysis of THEMIS and TES derived data products, *Journal of Geophysical Research-Planets*, *113*(E10), doi:10.1029/2007je002988.

Tornabene, L. L., J. E. Moersch, H. Y. McSween Jr, V. E. Hamilton, J. L. Piatek, and P. R. Christensen (2008), Surface and crater-exposed lithologic units of the Isidis Basin as mapped by coanalysis of THEMIS and TES derived data products, *Journal of Geophysical Research*, *113*(E10), E10001, doi:10.1029/2007JE002988.

Tornabene, L. L., J. E. Moersch, G. R. Osinski, P. Lee, and S. P. Wright (2005), Spaceborne visible and thermal infrared lithologic mapping of impact-exposed subsurface lithologies at the Haughton impact structure, Devon Island, Canadian High Arctic: Applications to Mars, *Meteoritics & Planetary Science*, *40*(12), 1835-1858, doi:10.1111/j.1945-5100.2005.tb00149.x.

Tornabene, L. L., G. R. Osinski, A. S. McEwen, V. Ling, C. M. Caudill, A. Nuhn, R. Hopkins, B. D. Aoust, and S. Mattson (2014), A global synthesis of the meter- to decameter-scale morphology and structure of complex crater central uplifts, *Eighth International Conference on Mars (2014)*.

Tornabene, L. L., G. R. Osinski, A. S. McEwen, J. J. Wray, M. A. Craig, H. M. Sapers, and P. R. Christensen (2013), An impact origin for hydrated silicates on Mars: A synthesis, *Journal of Geophysical Research-Planets*, *118*(5), 994-1012, doi:10.1002/jgre.20082.

Tornabene, L. L., G. R. Osinski, A. S. McEwenb, J. M. Boyce, V. J. Bray, C. M. Caudill, J. A. Grant, C. W. Hamilton, S. Mattson, and P. J. Mouginis-Mark (2012), Widespread crater-related pitted materials on Mars: Further evidence for the role of target volatiles during the impact process, *Icarus*, *220*(2), 348-368, doi:10.1016/j.icarus.2012.05.022.

Vincent, R. K., and F. Thomson (1972), Spectral compositional imaging of silicate rocks, *Journal of Geophysical Research*, *17*(14), 2465-2473.

Williams, D. A., et al. (2009), The Circum-Hellas Volcanic Province, Mars: Overview, *Planetary and Space Science*, *57*(8-9), 895-916, doi:10.1016/j.pss.2008.08.010.

Williams, D. A., R. Greeley, L. Manfredi, J. Raitala, G. Neukum, and H. C.-I. Team (2010), The Circum-Hellas Volcanic Province, Mars: Assessment of wrinkle-ridged plains, *Earth and Planetary*

Science Letters, *294*(3-4), 492-505, doi:10.1016/j.epsl.2009.10.007.
Wilson, J. H., and J. F. Mustard (2013), Exposures of olivine-rich rocks in the vicinity of Ares Vallis: Implications for Noachian and Hesperian volcanism, *Journal of Geophysical Research-Planets*, *118*(5), 916-929, doi:10.1002/jgre.20067.
Wilson, S. A., A. D. Howard, J. M. Moore, and J. A. Grant (2007), Geomorphic and stratigraphic analysis of Crater Terby and layered deposits north of Hellas basin, Mars, *Journal of Geophysical Research-Planets*, *112*(E8), E08009, doi:10.1029/2006je002830.
Wohler, C., A. Grumpe, A. Berezhnoy, M. U. Bhatt, and U. Mall (2014), Integrated topographic, photometric and spectral analysis of the lunar surface: Application to impact melt flows and ponds, *Icarus*, *235*, 86-122, doi:10.1016/j.icarus.2014.03.010.
Wray, J. J., S. T. Hansen, J. Dufek, G. A. Swayze, S. L. Murchie, F. P. Seelos, J. R. Skok, R. P. Irwin, III, and M. S. Ghiorso (2013), Prolonged magmatic activity on Mars inferred from the detection of felsic rocks, *Nature Geoscience*, *6*(12), 1013-1017, doi:10.1038/ngeo1994.
Wulf, G., M. H. Poelchau, and T. Kenkmann (2012), Structural asymmetry in martian impact craters as an indicator for an impact trajectory, *Icarus*, *220*(1), 194-204, doi:10.1016/j.icarus.2012.04.025.
Wyatt, M. B., H. Y. McSween, K. L. Tanaka, and J. W. Head (2004), Global geologic context for rock types and surface alteration on Mars, *Geology*, *32*(8), 645-648, doi:10.1130/g20527.1.

Chapter 3: Understanding the role of aeolian processes and physical sorting on Martian surface compositions through analysis of spectrally and thermophysically heterogeneous dune fields

This chapter is a preliminary manuscript that will be submitted to peer-review journal. Some of this work has been presented at the 44th Lunar and Planetary Science Conference and the 8th International Conference on Mars.

Abstract

Aeolian transport and hydrodynamic sorting have been proposed to be a significant influence on Martian sediment bulk compositions, through laboratory experiments, modeling and terrestrial analogies. But to date, few studies have directly examined compositional-grain size relationships within sediment fields on Mars; thus the prevalence of hydrodynamic sorting as well as the scales at which sorting is important remains poorly understood. To that end, we assessed the degree and occurrence of thermophysical and compositional heterogeneity for 25 dune fields within a ~42,000,000 km^2 area on Mars. Among these, only four exhibit spatial heterogeneity in spectral properties and composition. Two of these four sites show a strong positive relationship between particle size and olivine abundance. The rarity of compositional heterogeneity within dune fields may indicate phenocryst-poor source rocks; alternatively, sorting within individual bedforms may be present but is below the resolution of available instruments. In addition, we find that the bulk spectral properties of dune fields vary from one location to the next, likely indicating variations in source protolith compositions. Together, these results suggest that aeolian transport and hydrodynamic sorting have not had significant influence on Martian sediment compositions at regional (>103 km) or larger scales.

3.1 Introduction

Interpretation of sediment compositions from remote measurements requires consideration of a variety of factors, including source rock properties, chemical and mechanical alteration, transport history, and sorting processes. Presently, major questions regarding Martian sediments and aeolian processes relate to the degree to which sediments have been compositionally homogeneized by aeolian, impact and other processes, and conversely, the role that physical sorting plays in generating compositional variations with particle size. The similarity in chemical compositions of basaltic aeolian bedforms at Gale crater, Gusev crater and Meridiani Planum, measured in-situ by landed missions, has prompted the hypothesis of a "global soil", meaning that the saltatable sediment fraction has been globally homogeneized. However, from remote sensing data, variations in the average mineralogy of isolated dune fields are clearly present (e.g., [*Aben*, 2003; *Rogers and Christensen*, 2003; *Stockstill-Cahill et al.*, 2008; *Chojnacki et al.*, 2014]), and prior infrared mapping studies of Martian dune fields and nearby bedrock provide evidence that many dune field compositions are at least partially controlled by local inputs [*Fenton*, 2005; *Tirsch et al.*, 2011; *Chojnacki et al.*, 2014]. Additionally, global mapping of surface compositions from infrared and gamma ray measurements shows spatial variability, indicating that complete homogenization of the sediment fraction has not occurred [*Rogers and Hamilton*, 2015]. However, it is possible that homogenization occurs within a restricted size range of the saltatable fraction, where smaller sediments are physically separated from larger ones and homogeneized at larger scales.

Understanding the potential role of physical sorting in controlling bulk sediment composition is an important facet in interpreting surfaces from orbit. Though the processes that result in compositional fractionation from a bulk source during erosion and aeolian transport are generally well understood (**Section 3.2**), it is unclear under what scales these processes are

important, as well as how the these changes might appear on surfaces dominated by basaltic sources. Martian sediments investigated *in-situ* with landed missions show evidence of compositional and grain size sorting over the scale of individual bedforms [*Sullivan et al.*, 2008; *McGlynn et al.*, 2011; *McGlynn et al.*, 2012] and within a portion of the Gale crater dune field [*Seelos et al.*, 2014; *Lapotre et al.*, 2015]. However, studies across larger areas, such as a whole dune field, have been limited. Dune fields are natural environments in which to assess the degree to which physical sorting processes affect Martian sediments.

Aside from the in-situ observations at few landing sites (described above), and a comprehensive study of aeolian bedforms in Valles Marineris [*Chojnacki et al.*, 2014], detailed analyses of heterogeneity (or lack thereof) within Martian aeolian deposits are generally lacking. This work complements previous studies by assessing the frequency of particle size and spectral heterogeneity within dune fields in the northern hemisphere of Mars, and then characterizing compositional-particle size relationships in the heterogeneous dune fields.

3.2 Background

Variations in composition and particle size distributions within aeolian dune fields on Earth are a function of source rock composition(s), mechanical and chemical weathering, and aeolian sorting mechanisms [*Blatt et al.*, 1980; *Boggs*, 1995]. The original crystal size and composition of source rock(s) first determine the grain size and composition of sediments derived from those rocks [*Pettijjohn et al.*, 1987]. Preferential comminution and chemical alteration can change the composition of those sediments (as a function of grain size) during transport. Finally, aeolian sorting of particles leads to preferential enrichment of specific materials in certain grain-size fractions (e.g. [*Weltje and von Eynatten*, 2004; *Tolosana-Delgado and von Eynatten*, 2009]). Grain size, grain shape and density are major factors controlling the aeolian sorting (e.g. [*Anderson and*

Bunas, 1993; *Makse*, 2000]). Grain sizes are commonly segregated in individual dunes, with coarse-grained ripple crests and fine-grained troughs [*Anderson and Bunas,* 1993].

On Earth, starting composition has been shown to play a major role in affecting compositional sorting trends. Because the minerals in basaltic rocks can have a wide range of densities compared to intermediate and silicic rocks, the effects of hydraulic sorting on compositional trends with particle size can differ greatly from those of intermediate-to-silicic rocks (e.g., [*Kiminami and Fujii*, 2007]). Unfortunately, studies of aeolian sorting in basaltic terrains are rare. Spatial variations of chemical composition were observed in volcanic sands in Iceland, such that sands showed enrichments in MgO compared to the source rock and correlated with a decrease in mean grain size of sand [*Mangold et al.,* 2011]. This was explained by olivine shape, hardness and density leading to longevity as sand-sized particles compared to plagioclase. In the basaltic terrains surrounding Moses Lake, Washington, dune crests were observed to be compositionally dissimilar from the remaining dune surfaces in remotely sensed infrared data [*Bandfield et al.*, 2002]. In this example, however, the differences were due to distinct sand sources, followed by aeolian sorting, rather than preferential comminution from a single sand source. Last, particle size sorting can occur with density variations related to porosity/vesicularity, which is expected for basaltic terrains. This has been observed in granule mega-ripples in Iceland and Mono Crater, where the high density and finer obsidian grains formed the crests and the low density and coarser pumice was concentrated between the crests[*Greeley and Peterfreund,* 1981; *Peterfreund*, 1982].

Despite the shortage of terrestrial examples, combined experimental and modeling work on basaltic sediments suggests that physical processes could produce significant spatial heterogeneity in Martian sediment compositions [*Fedo et al.*, 2015]. In that study, two basalt samples differing in composition and petrographic texture were crushed and pulverized to generate synthetic

sediments [*Fedo et al.*, 2015]. The two basalt samples, trachybasalt from Cima volcanic field in Mojave Desert, CA and porphyritic vesicular basalt from Kilauea volcano in Hawaii, represent the compositions of many rocks and soils in Gusev Crater. Samples were sieved into multiple grain-size fractions; particles finer than 62 microns were not further subdivided. The mineral abundance of sieved sediments and source rocks was determined and divided to five groups: lithic fragments, olivine, plagioclase and pyroxene and opaque oxides. The compositions of the sieve fractions differed greatly with starting composition. They concluded that the crystal-size distribution of the parent material had a major influence on the compositional variability between grain size fractions. Unfortunately, the volumetric abundances of individual minerals in each bulk sediment size fraction could not be directly assessed because of the lack of measurement of groundmass mineral abundance in lithic fragments. Next, using aeolian transport models, Fedo et al [2015] showed that these compositionally distinctive size fractions could then be spatially sorted through hydrodynamic processes under Martian atmospheric conditions. They conclude that physical sorting should be likely on Mars, and that sorting is a process that should not be overlooked when assessing chemical or mineralogical variability in Martian sediments. However, the hydrodynamic effects related to density differences within basaltic sediments may have been lost or conflated during the processes of sieving, thus the likelihood of physical sorting remains unclear.

Some well-characterized dune fields on Mars do show evidence for sorting, however. The "El Dorado" dune field investigated by the Spirit Rover is characterized by olivine-enriched coarse grains and pyroxene-enriched fine grains [*Sullivan et al.*, 2008]. They speculated both types of sand were derived from a single original basalt composition, where particles dominated by one or more phenocrysts of olivine abraded more slowly due to the hardness and conchoidal fracture compared with less durable pyroxene. Thermal inertia variations have been observed in the dune

field within Proctor Crater, where both the interdunes and the dune troughs have lower thermal inertia values than the dune crests. In this case, rather than sorting, the preferred interpretation was that sand saltation may only be prevalent enough to keep the dunes crests themselves clear of dust while the interdunes and troughs are not as dust free as crests[*Fenton and Mellon*, 2006]. These terrestrial and laboratory studies provide a framework in which to evaluate our Mars observations.

3.3 Data and Methods

Twenty-five (25) dune fields within impact craters located between 0°N and -14.3°N, 43°E to 195°E were initially included as candidate areas for detailed study (**Figure 3.1**). The study region includes a variety of terrain types, ages, and elevations. Dune fields within the study region were identified by using the Mars Global Digital Dune Database [*Hayward et al.*, 2014], but additional low albedo deposits within craters were also examined. First, each dune field was closely inspected with high-resolution visible imagery from the Mars Odyssey THEMIS (Thermal Emission Imaging System) instrument (~18 m/pixel) [*Christensen et al.*, 2004] and the Mars Reconnaissance Orbiter CTX (Context Imager) instrument (~6 m/pixel) [*Malin et al.*, 2007], to assess the degree of sand cover continuity within the sand deposit or dune field. This is important because deposits with significant interdune surfaces or rocky protrusions (e.g. buttes, crater rims) could result in mis-interpreted thermal inertia or compositional variations. **Figure 3.2** shows an example dune field with incomplete sand coverage. Next, each potential dune field was independently examined for spectral or thermophysical heterogeneity using Mars Odyssey THEMIS (Thermal Emission Imaging System) thermal infrared data (100 m/pixel) [*Christensen et al.*, 2004]. Then, for the dune fields with contiguous sand cover, data from THEMIS and the Mars Reconnaissance Orbiter Compact Reconnaissance Imaging Spectrometer for Mars (CRISM) [*Murchie et al.*, 2007] were analyzed in detail to discern relationships between thermophysical and compositional properties. Finally, in order to compare bulk dune field compositions from one dune field to the next, THEMIS

spectral averages from each dune field were extracted. A polynomial fit to each average spectrum was calculated, and the minimum position of the fit was derived in order to display a rough comparison of composition between fields (example spectra shown in **Figure 3.3**). This method was previously used to compare the mineral composition from central peaks of impact craters [*Pan et al.*, 2015]. CRISM data covering the entire dune field were used to analyze the mineral composition, where available.

Thermal inertia is the measurement of a material's resistance to changes in temperature, and can be related to the average particle size of a surface [*Kieffer et al.*, 1977; *Presley and Christensen*, 1997]. Thermal inertia is defined as

$$I=(k\,\rho\,c)^{0.5} \quad (1)$$

where K is the thermal conductivity, ρ is the bulk density of the surface material and c is the specific heat. For non-indurated particulate surfaces on Mars, variations in thermal inertia are largely driven by the mean particle size of the surface [*Jakosky*, 1979; *Edgett and Christensen*, 1991]. In this work, data from the THEMIS 10-band infrared imager (~6.8 to 14.9 μm, 100 m/pixel) [*Christensen et al.*, 2004] was used to assess thermal inertia variations within each field. THEMIS-derived thermal inertia images [*Fergason et al.*, 2006; *Christensen et al.*, 2013] from nighttime, low dust opacity observing conditions over each region were selected for analysis. Effective particle sizes were determined from thermal inertia using equation (1) and the experimentally determined relationship between thermal conductivity and particle diameter for 5 torr (the average pressure of the Martian surface) [*Presley and Christensen*, 1997]. Values of 5 kgm^{-3} and 0.0015 $Jkg^{-1}K^{-1}$ where used as estimates for density and specific heat, respectively. Only areas with thermal inertia between 164 and 365 $Jm^{-2}s^{-0.5}K^{-1}$, corresponding to sand-sized

sediments, were included for further thermal inertia and composition analysis [*Presley and Christensen*, 1997].

Analysis of compositional heterogeneity was carried out using infrared images. Decorrelation stretched (DCS) [*Gillespie et al.*, 1986] THEMIS daytime thermal infrared multispectral data (with surface temperatures > 250 K) images were used to preliminarily assess whether spatial heterogeneity in composition was present within dune units (indicated by color variations within the stretch). It is important to note that DCS images, because they are stretched, can produce "false positives" when assessing spectral variability, but not "false negatives". Lack of color variation in a DCS image is a good indicator of spectral uniformity. Potential areas of compositional distinction highlighted with the DCS images were further analyzed quantitatively by extraction of surface emissivity from regions of interest identified within the scene. To extract emissivity spectra, instrument artifacts and atmospheric influences were corrected using the methods described by [*Bandfield et al.*, 2004]. As will be shown, much of the variation can be captured using varying amounts of olivine (**Section 3.4**). Thus to map compositional variations quantitatively across the scene, linear spectral unmixing [*Bandfield et al.*, 2004]) using scene-derived olivine-poor and laboratory olivine emissivity spectra as end-members was applied to each THEMIS pixel over the dune field. Olivine concentrations are normalized for blackbody and presented as areal abundance (0-100%). Last, THEMIS-derived spectral images and nighttime images were co-registered to directly compare spectral properties (including olivine abundance) and thermal inertia. Images were classified based on 20^{th} percentile thermal inertia intervals, and olivine abundance values and emissivity spectra were retrieved for each thermal inertia interval. Comparisons by thermal inertia interval, rather than pixel-to-pixel, were used due to the possibility of sub-pixel mixing and/or slight pixel mis-registration between day and nighttime images.

CRISM is a hyperspectral imaging spectrometer with 544 channels covering the visible to near-infrared spectral region from 0.4 to 4.0μm and a nominal spatial resolution of ~18 m/pixel [*Murchie et al.*, 2007]. CRISM parameters for targeted images and laboratory spectra from the CRISM spectral library were used to identify the presence and distribution of olivine, low-calcium pyroxene, high-calcium pyroxene, hydrated minerals [*Pelkey et al.*, 2007; *Viviano-Beck et al.*, 2014] and glass [*Horgan and Bell*, 2012]. OMEGA, an imaging spectrometer with comparable spectral range to CRISM, was not used in this study due to its coarser spatial resolution.

High spatial resolution visible images from CTX were used to define the boundaries of dune fields and characterize the dune morphology of spectrally or physically distinct units identified by THEMIS.

3.4 Results

Within the study region, 25 candidate dune fields were identified. All of the dune fields are within impact craters, which are major accumulation sites for sediment. The range of cubic fit minima for all the 25 dune fields is from 11.02 to 9.52 μm, indicating a wide range of compositions from olivine rich basalt to more intermediate silica contents (**Figure 3.1, 3.3**). In some areas, dune fields in close proximity to one another exhibit similar compositions, whereas in others (for example 150°E,40°N~190°E, 0°N and 60°E, 40°N~80°E, 20°N), the compositions are different from one other. All of the dune fields exhibited intra-field variability in thermal inertia, but upon closer inspection with visible imagery, only six were found to exhibit adequate continuity of sand surface coverage such that the thermal inertia variations could be attributed to variations in particle size within the sediment component (**Section 3.3)** (**Table 3.1, Figure 3.4**). The ranges of thermal inertia and effective particle size indicate that the particle size within a dune field varies considerably (**Table 3.1**). Thermal inertia values of these dunes range from 164 $Jm^{-2}s^{-0.5}K^{-1}$ to 365

$Jm^{-2}s^{-0.5}K^{-1}$, indicating very fine sand to coarse sand [*Presley and Christensen*, 1997]. With the exception of the Gale crater dune field site, TES albedo values of these dunes range from 0.1 to 0.15 and TES dust cover index values range from 0.97 to 0.98 [*Ruff and Christensen*, 2002], suggesting dust free and likely active surfaces. The low albedo and intermediate thermal inertia values suggest sand-sized material with little or no silt (e.g., [*Wentworth*, 1922; *Fergason et al.*, 2006]). In Gale, TES albedo and dust cover index values are ~0.21 and ~0.965 respectively, suggesting slightly higher dust cover.

Of the 25 sites, only four were found to exhibit clear spatial heterogeneity in spectral properties. All four of those sites are among the six contiguous-coverage dune fields described above, and also exhibit thermophysical heterogeneity. THEMIS olivine abundance maps and CRISM spectral parameter images (where available) show variable olivine signatures within the remaining four dune fields, suggesting compositional heterogeneity (**Figures 3.5-9, S1-S6**). For two sites (D20 and D1), olivine abundance derived from THEMIS is strongly related to thermal inertia and dune geomorphology across the entire field (**Figures 3.5-7, S1-S3**), where the high thermal inertia (larger particle size) portion of the dune exhibits higher olivine abundance and distinct ridge forms, and the lower thermal inertia portion is relatively olivine poor and morphologically smooth. For the remaining two sites (D21, D23), this trend is present, but only for portions of the dune field, and in general, the olivine abundance is low. Comparisons across the entire field show no strong relationship between particle size and composition. We describe one of each of these examples below.

The dune field located at 44.26°E, 42.16°N (D20) shows a strong relationship between olivine abundance and thermal inertia. From CTX imagery (**Figure 3.4**), we observe a larger size and greater areal coverage of bedforms and well defined slip faces and crescents in the northeastern

part of the site, whereas the remainder of the field is smooth and exhibits smaller bedforms and fewer slip faces. The thermal inertia of the large bedform portion is higher than the small bedform portion, indicating a decrease of effective particle size in the small bedform portion (**Figure 3.4**). Olivine abundance is higher in the high thermal inertia part compared to the low thermal inertia portion (**Figure 3.5**). Though derived thermal inertia can be affected by surface slope and aspect angle [*Jakosky*, 1979], we observe little evidence that this is a strong factor influencing the spatial variability in thermal inertia in this region, because the olivine and high thermal inertia areas are concentrated both on lee and slip faces, and in the crests as well as low-lying troughs (**Figure 3.4 and Figure 3.5**). The average THEMIS spectrum of the high thermal inertia portion exhibits low emissivity at ~11 μm relative to ~9 μm, consistent with increased olivine abundance. Conversely, the low thermal inertia portion of the dune field lacks a strong 11 μm absorption, consistent with olivine poor materials (**Figure 3.5**). The CRISM mafic parameter browse image also shows stronger olivine index values in the large bedform part, with a stronger absorption near ~1.2μm (**Figure 3.6**). The stronger ~1.2 μm absorption can indicate higher olivine abundance and/or a particle size difference [*Hapke*, 1993; *Salisbury*, 1993]. The CRISM 1.3μm albedo stretch map indicates that the dune is dark and active (**Figure 3.6.C**). In general, a positive correlation between thermal inertia and olivine abundance is observed (**Figure 3.7**). In **Figure 3.7,** average THEMIS spectra were plotted from each thermal inertia interval. With the thermal inertia increase, the absorption feature of THEMIS spectra shifts from ~9 μm to ~11 μm, indicating increase of olivine abundance. In summary, for region D20, high thermal inertia surfaces are associated with olivine rich areas, while low thermal inertia surfaces are associated with olivine poor portions. A similar pattern was observed for region D1 (**Figure 3.S2-S3**).

A contrasting example is a dune field located at 57°E, -2.1°N (D21). Transverse and barchanoid dune types with large ridge and slip faces are in the west and south, whereas the remainder of the dune is smooth and exhibits sand sheet morphology (**Figure 3.4**). These areas also exhibit lower thermal inertia values, indicating a decrease of effective particle size (**Figure 3. 4**). Olivine is lowest in some of the lowest thermal inertia areas compared to the highest thermal inertia portions based on the THEMIS spectra (**Figure 3. 8**). However, when spectra are compared with thermal inertia across the entire dune field, the relationship between spectral properties and thermal inertia becomes less clear; the change of olivine abundance and spectral properties with thermal inertia is very small. A similar pattern was observed in region D23 (**Figure 3. S4**).

The dune field (D25) within Gale Crater can be broken into two parts. To the north, there is a NE-SW trending portion that contains both barchan and longitudinal dune forms [*Seelos et al.*, 2014] and significant interdune surfaces within km scales; this portion of the dune field is currently under investigation by the Curiosity Rover. To the south, there is a "sand sea" [*Lane and Christensen*, 2013] that contains a large (300 km^2) area of contiguous sand cover. Much of the NW-SE trending portion exhibits THEMIS thermal inertia values >365 $Jm^{-2}s^{-0.5}K^{-1}$, possibly due to influence from interdune surfaces (**Figure 3.S8**). THEMIS spectra from this area are consistent with olivine- and pyroxene-bearing basaltic materials (**Figure 3.S8**), as reported by previous authors [*Rogers and Bandfield*, 2009; *Lane and Christensen*, 2013; *Seelos et al.*, 2014; *Lapotre et al.*, 2015]. The sand sea to the south exhibits color variations in the THEMIS DCS images (using bands 8-7-5 as red-green-blue), ranging from orange to pink. However, spectral averages from these different colored areas show that the spectral differences are very minor, particularly compared to other dune fields investigated (D20, D1) (**Figure 3.S8**). The subtle differences are consistent with small differences in olivine abundance. Given that compositional differences are

observed within the NE-SW trending portion of the dune (observed in higher resolution CRISM data, [*Seelos et al.*, 2014]), it is possible that the sand sea contains real variations in olivine abundance that are obscured by dust cover.

3.5 Discussion

The diversity of bulk compositions of the 25 dune fields (**Figure 3.1**) likely reflects regional variations in sand source compositions. This is consistent with global observations that show compositional heterogeneity in rock and soil compositions from region to region (e.g., [*Aben*, 2003; *Rogers and Christensen*, 2003; *Stockstill-Cahill et al.*, 2008; *Chojnacki et al.*, 2014; *Rogers and Hamilton*, 2015]), and suggests that aeolian redistribution of sands across $>10^3$ km scales is not a significant process on Mars. However, it is possible that the compositional variations are due to variable exposure of interdune surfaces, given the small number (six) of dune fields exhibiting adequate continuity of sand surface coverage.

Of the 25 sites examined, only four exhibited clear spatial heterogeneity in spectral characteristics. The rarity of spectral heterogeneity within dune fields in our study region could be attributed to one or more factors. First, drawing from the experimental results of *Fedo et al*. [2015] (**Section 3.2**), the source protoliths for many of the dune fields could have been phenocryst-poor, resulting in derived sediments that are dominated by sand-sized lithic or glass fragments rather than individual mineral grains. Based on the spectra of 12 dune fields that have CRISM data coverage, only one showed spectra that are consistent with volcanic glass (**Figure 3.S7**), which could suggest that if the sands are phenocryst poor, they are likely dominated by lithic fragments rather than glass. However, Fe-bearing glasses can be difficult to detect when mixed with other minerals such as olivine and pyroxene [*Horgan et al.*, 2014].

Alternatively, individual mineral grains may have been compositionally homogenized across size fractions through multiple impacts. We consider this to be less likely due to impact comminution experiments that show that repeated impacts lead to mineral-specific comminution [*Horz et al.*, 1984].

A third possibility is that the particle size ranges within some of these dune fields may be narrow enough such that very little sorting and separation can occur. However, spatial sorting does not necessarily require a wide particle size range. For example, the particle size range of one of the two spatially heterogeneous dune fields (D20) is 63-226μm.

Last, it is possible that the dune fields are heterogeneous at spatial scales below the resolution of the THEMIS images (<100m/pixel), but not at larger spatial scales.

Among the four spectrally heterogeneous dune fields, two (D20 and D1) show a strong positive relationship between olivine and particle size, similar to trends described for Gale crater [*Lapotre et al.*, 2015] and El Dorado [*Sullivan et al.*, 2008], but notably, opposite the trend described for basaltic sediments in Iceland [*Mangold et al.*, 2011]. The high thermal inertia (larger particle size) portions of these two dune fields exhibit higher olivine abundance and distinct bedforms, whereas the lower thermal inertia portion of the dune field is relatively olivine poor and morphologically smooth. For the remaining two dune fields (D21 and D23), spectral variation is observed, but the relationship to thermal inertia is less clear. Broad averages of spectral emissivity across high- and low-thermal inertia portions of the dune field suggest that some compositional sorting may have occurred (**Figure 3.S8 and S6**). However, there is great overlap in the spectral properties within each thermal inertia range for these two dune fields, indicating that the relationship between thermal inertia and composition is imperfect and suggesting that compositional sorting is less well-developed. The few areas of elevated olivine abundance could be due to local inputs from areally

minor olivine-rich bedrock. Other possible causes could relate to complicating factors in deriving thermal inertia (e.g. not accounting for slope/aspect angles) or to slight misregistration of daytime and nighttime THEMIS images (**Section 3.3**).

From the available data, it is difficult to determine whether the sediments in the spectrally heterogeneous dune fields are from a single source that contains large olivine pheoncrysts within a finely crystalline matrix, or from multiple sources. In any case, this study highlights the fact that relationships between aeolian sediment compositions and particle sizes cannot be easily predicted on Mars using terrestrial examples, without knowledge of the source rock petrographic textures and compositions (e.g. [*Fedo et al.*, 2015]).

3.6 Conclusion

We investigated 25 dune fields and sand deposits within impact craters located between 0°N, 43°E to -14.3°N, 195°E to assess the degree and occurrence of thermophysical and compositional heterogeneity. Mineral compositions of entire dune fields vary from dune field to dune field for the 25 sites, suggesting diverse sand source compositions at the regional scale. Of these 25 sites, only four dune fields exhibit spatial heterogeneity in spectral properties and composition. Nearly all exhibit spatial heterogeneity in thermophysical properties, but, for all but six sites, it is difficult to rule out interdune/non-sand surfaces as the dominant source of that heterogeneity.

The rarity of spectral heterogeneity within dune fields in our study region could be due to one or more factors, but is most likely related to composition and texture of the individual sediment source rocks or the spatial resolution of the thermal infrared data (100 m/pixel) used to search for heterogeneity. Phenocryst-poor source materials, such as volcaniclastic/glassy lithologies or finely crystalline basalts would not be expected to exhibit strong compositional relationships with

particle size. Alternatively, heterogeneity could be present at the individual dune scale (<100 m/pixel), as observed for El Dorado in Gusev crater [*Sullivan et al.*, 2008].

Among the four spectrally heterogeneous dune fields, two (D20 and D1) show a strong positive relationship between particle size and olivine abundance. This is similar to the observation in "El Dorado" dune field, which was investigated by the Mars Exploration Rover *Spirit* [*Sullivan et al.*, 2008]. However, this trend is opposite of what was observed by [*Mangold et al.*, 2011] for basaltic sediments on Earth. This suggests that composition and particle size relationships observed in terrestrial basaltic settings cannot be extrapolated to Mars and is dependent on source material texture and composition.

Table 3.1 Details of six dune fields exhibiting adequate continuity of sand surface coverage in this study.

Dune ID	D1	D20	D21	D23	D17	D25
Latitude	9.48°N	42.16°N	-2.1°N	-14.3°N	20.77°N	-5°N
Longitude	150°E	44.26°E	57°E	128.5°E	75.57°E	137.03°E
TES albedo	0.11	0.12	0.11	0.1	0.13	0.21
TES dust index	0.97	0.98	0.98	0.98	0.97	0.97
Thermal inertia	280-365	164-220	225-332	190-240	202-296	234-365
Effetive particle size	639-2000µm	63-226µm	249-1333µm	120-328µm	156-812	294-2000
Figure numbers	Figure S1-S3	Figure 4-7	Figure 4,8-9	Figure S4-S7	Figure 4	Figure S8

Note: thermal inertia unit is $Jm^{-2}s^{-0.5}K^{-1}$

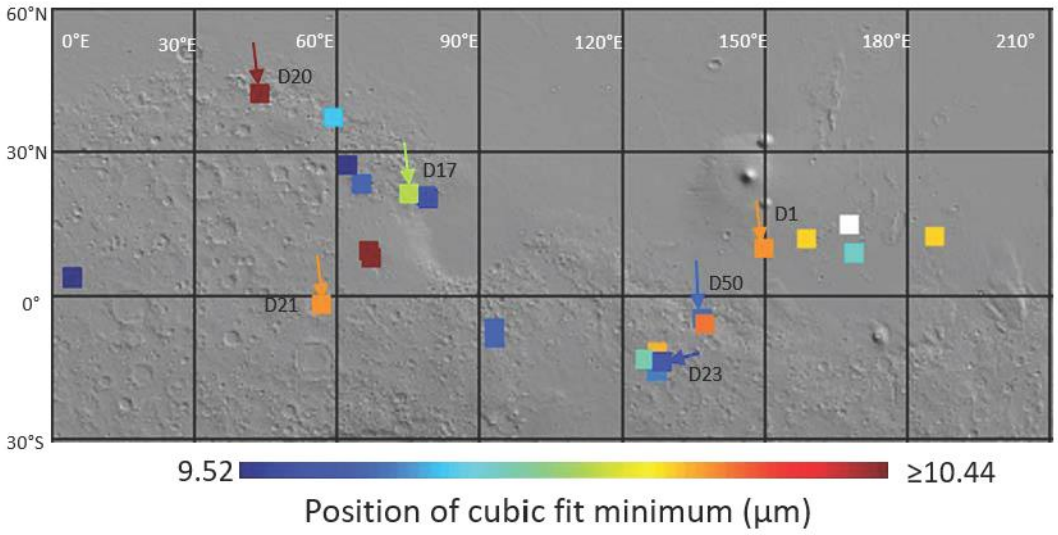

Figure 3.1 Distribution of dune fields in this study. Colors indicate the minimum positions of polynomial fits to THEMIS spectra, and are rough indicators of bulk composition (see text). The white square is a dune field without qualified THEMIS data coverage. Arrows with the same colors of squares are dune fields with contiguous sand cover and that were analyzed in detail.

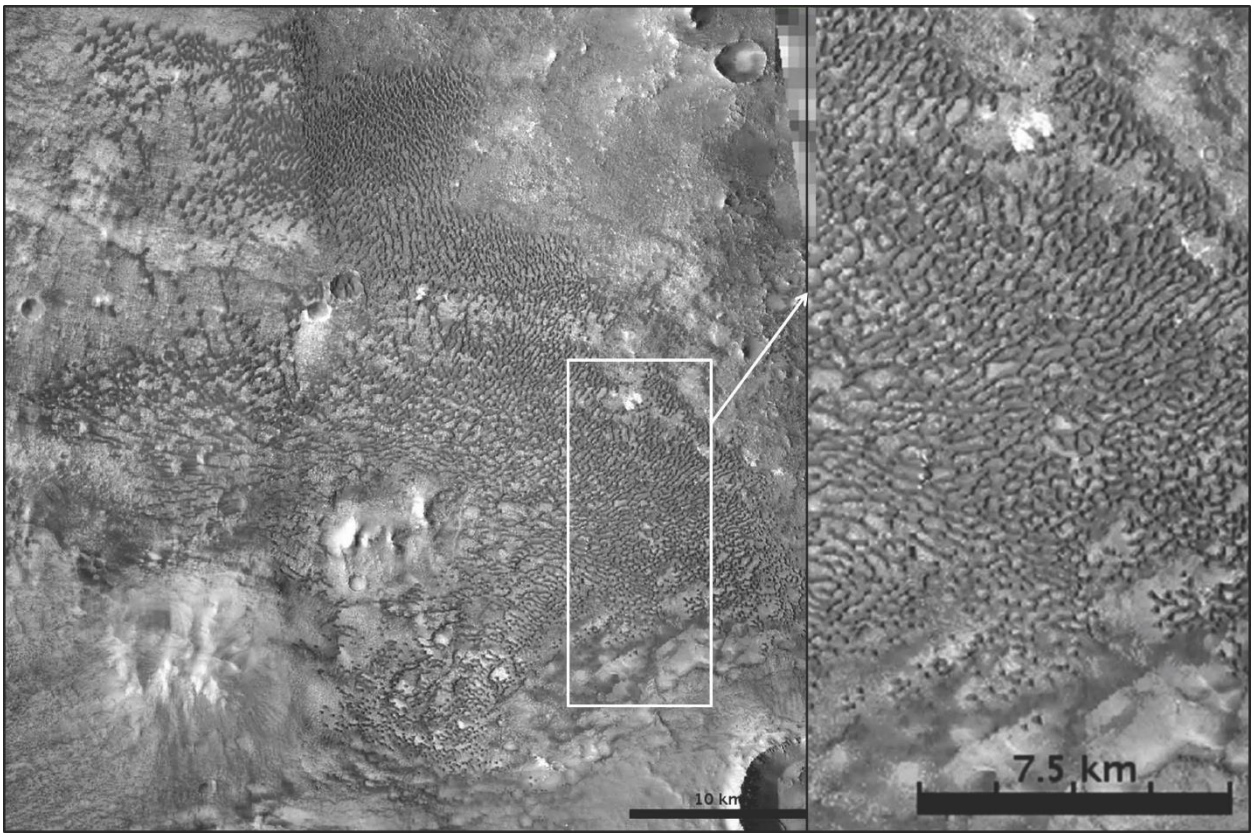

Figure 3.2 CTX images of an intracrater dune field located at 65.61°E, 23.1°N. A. CTX image shows the entire dune field. B. CTX image shows the white polygon region in A. Interdune surfaces are abundant and likely contribute to observed thermophysical heterogeneity.

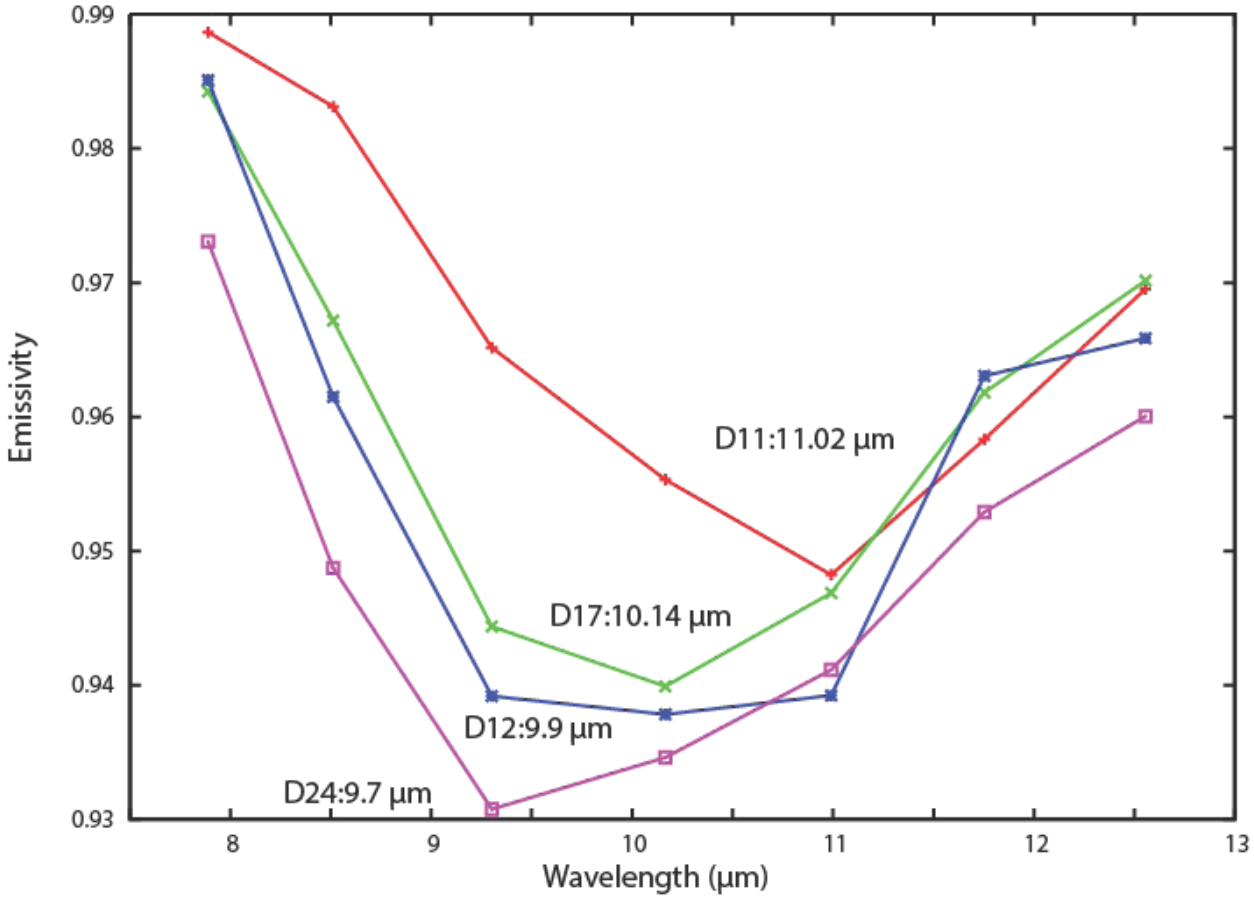

Figure 3.3 Example of THEMIS spectra with cubic fit minima from 11.02 μm to 9.7 μm.

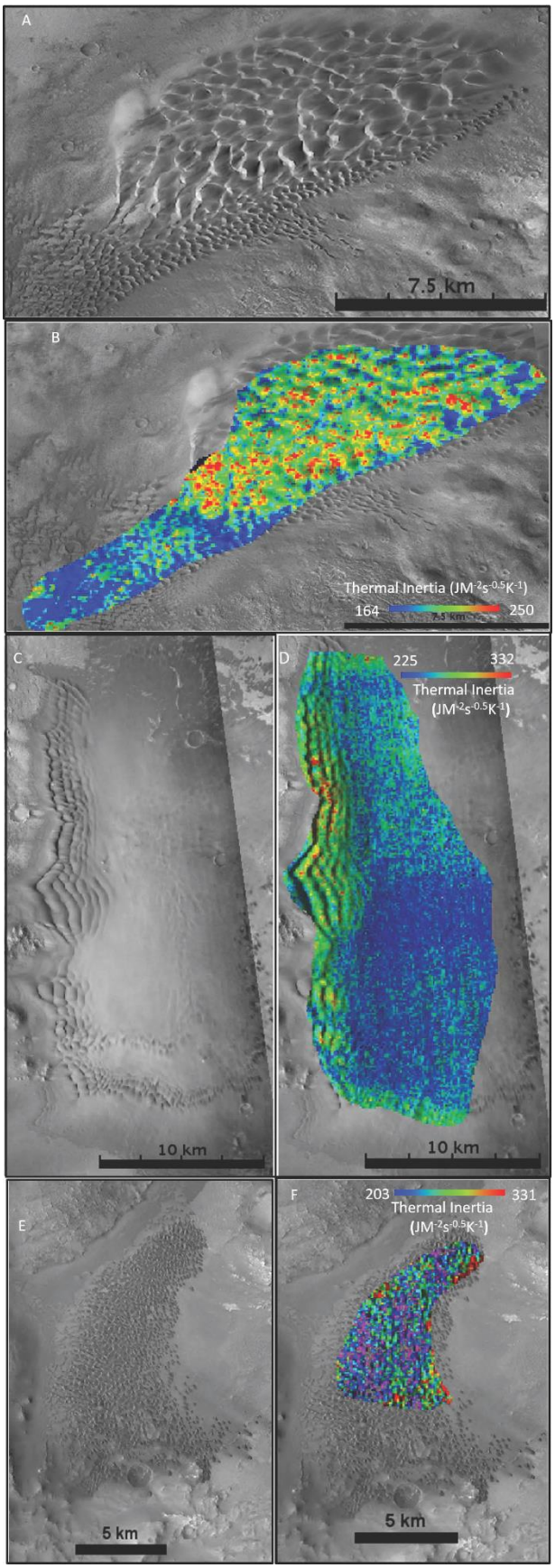

Figure 3.4 Examples of dune fields with contiguous dune coverage (D20: A-B, D21: C-D, D17: E-F). CTX images are shown in A, C, and E. THEMIS thermal inertia images are shown in B, D, and F. Spatial heterogeneity in thermal inertia is observed in all three examples. Spectral heterogeneity is observed in D20 and D21 (Figures 3.5-9) but not D17.

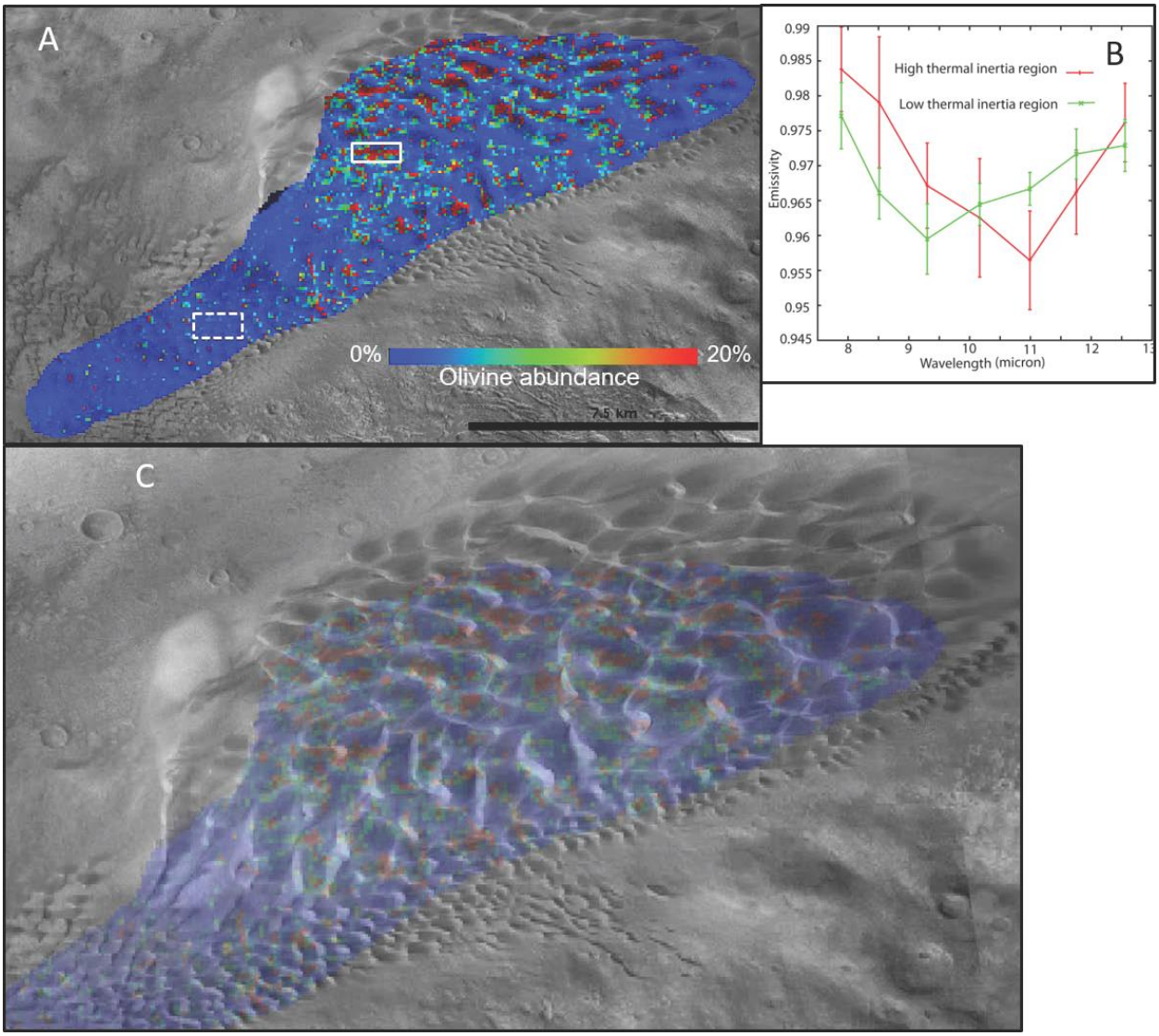

Figure 3.5 THEMIS-derived maps of dune field located at 44.26°E, 42.16°N (D20). THEMIS derived olivine abundance (A) and average spectra of high and low thermal inertia parts of the dune (B). C.THEMIS olivine abundance map overlain on CTX map showing the olivine distribution with morphology. Color scale is same as for (B).

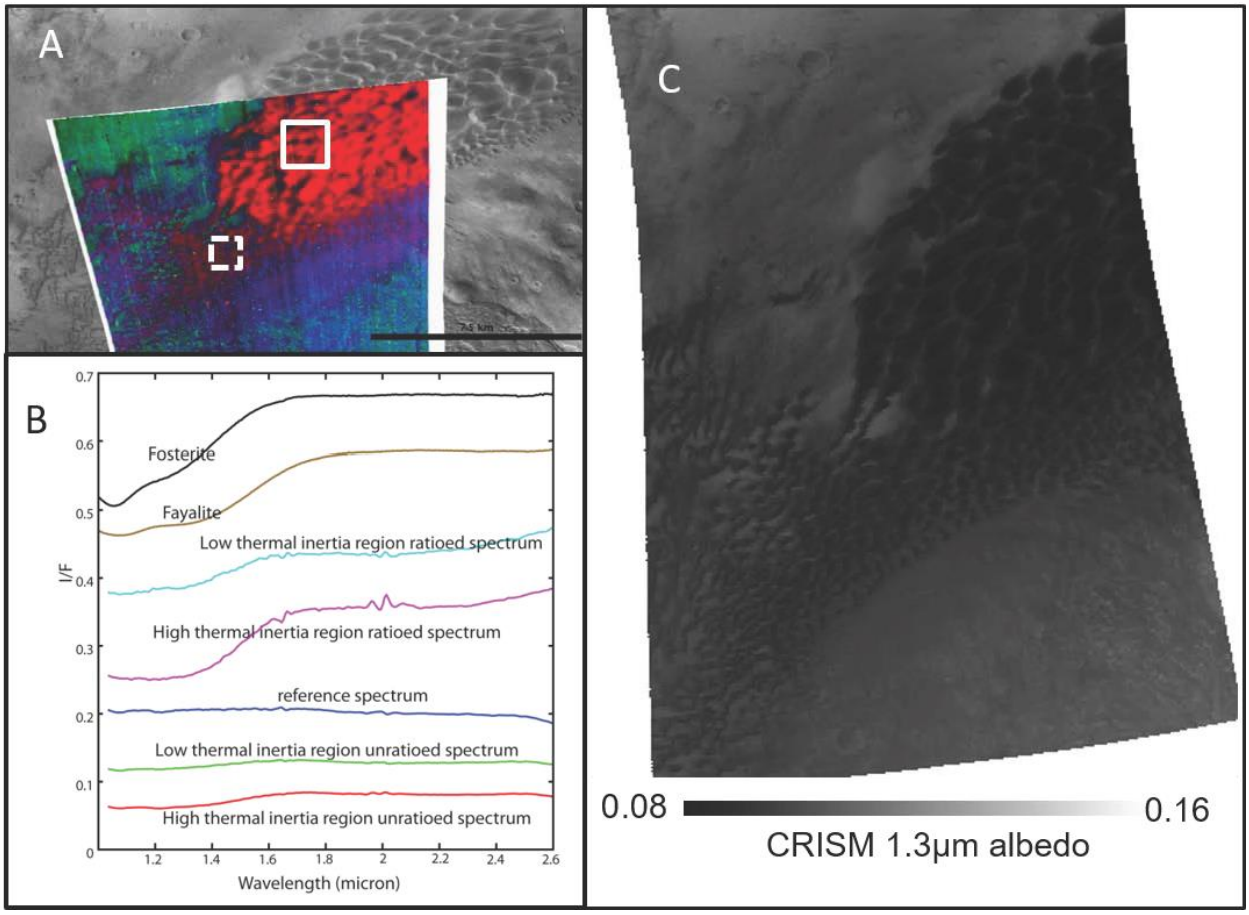

Figure 3.6 CRISM parameter maps of dune field located at 44.26°E, 42.16°N (D20). CRISM mafic index map (OLINDEX with scaling 0.00-0.13, LCPINDEX with scaling 0.00-0.1, HCPINDEX with scaling 0.00-0.2 as red green and blue) (A) and average spectra of high and low thermal inertia parts of the dune (B).

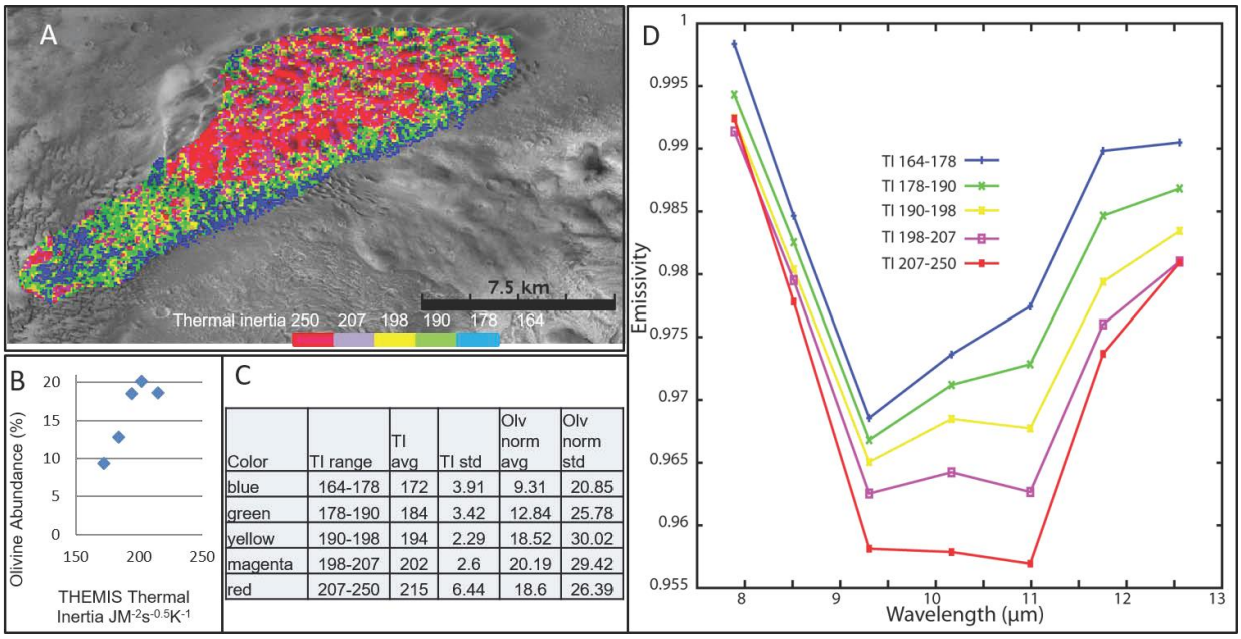

Color	TI range	TI avg	TI std	Olv norm avg	Olv norm std
blue	164-178	172	3.91	9.31	20.85
green	178-190	184	3.42	12.84	25.78
yellow	190-198	194	2.29	18.52	30.02
magenta	198-207	202	2.6	20.19	29.42
red	207-250	215	6.44	18.6	26.39

Figure 3.7 Thermal inertia classification map of dune field located at 44.26°E, 42.16°N (D20), and relationship to olivine abundance. A. Classified THEMIS thermal inertia image. Each color represents the 20th percentile of thermal inertia ranges. B. Scatter plot of thermal inertia vs. olivine abundance; average and standard deviation of thermal inertia and olivine abundance for each thermal inertia range. C. Average olivine abundance of each thermal inertia range shown in (A). D. Average THEMIS spectra from each thermal inertia range shown in (A). The colors correspond to the class colors in (A). Spectra are offset for clarity.

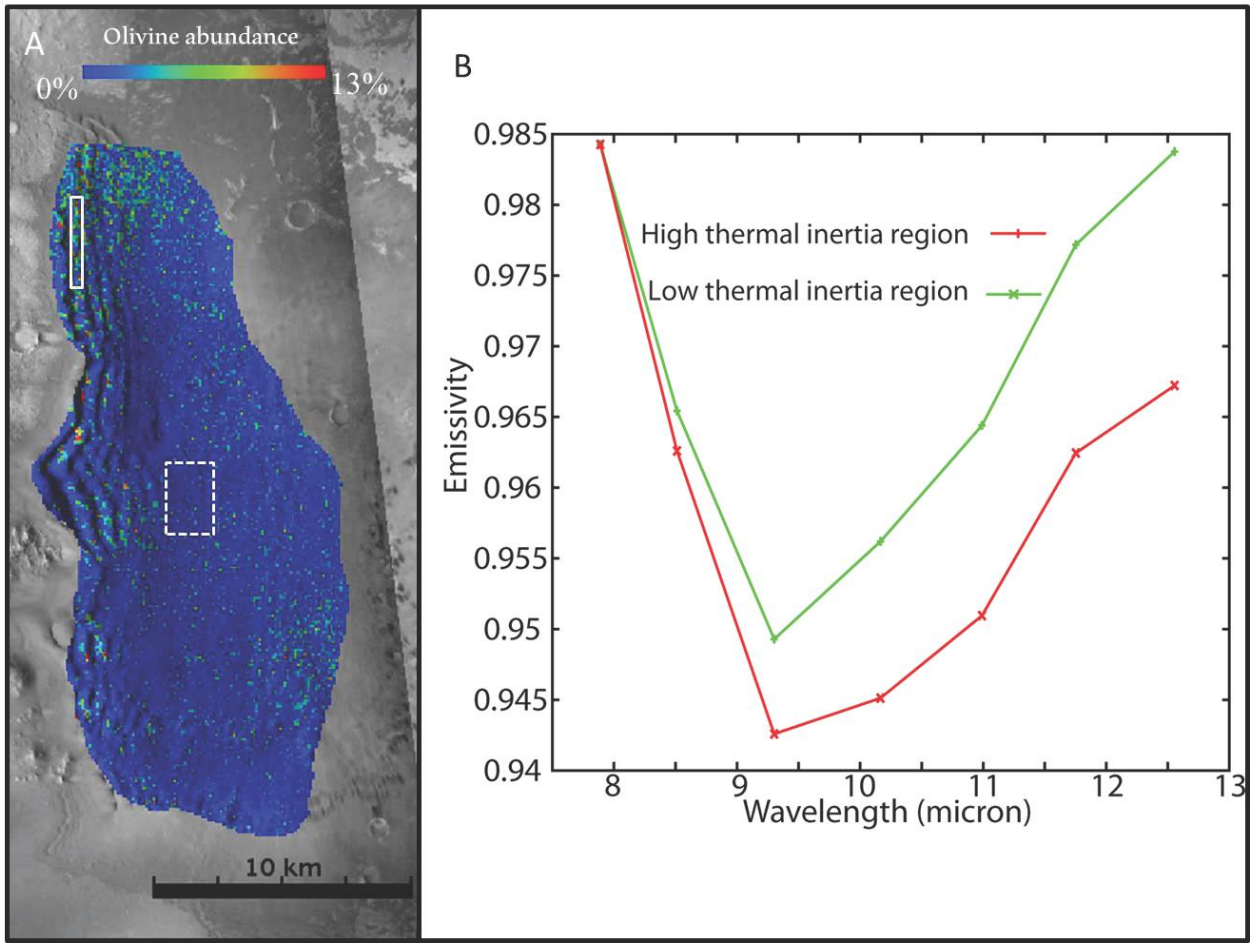

Figure 3.8 THEMIS-derived maps of dune field located at 57°E, -2.1°N (D21). THEMIS derived olivine abundance (A) and average spectra of high and low thermal inertia parts of the dune (B).

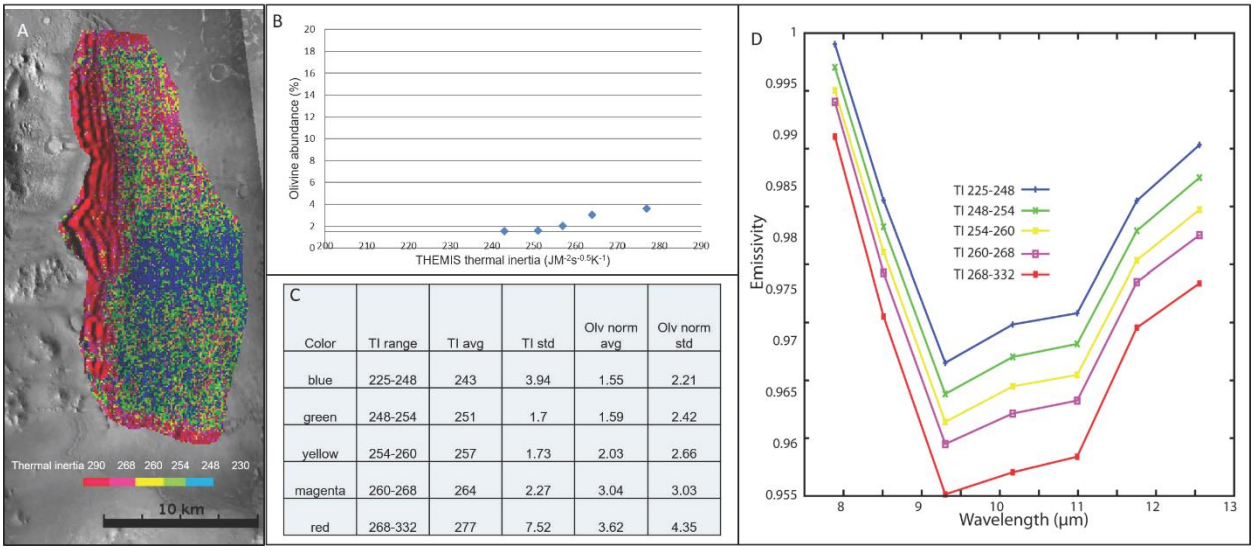

Color	TI range	TI avg	TI std	Olv norm avg	Olv norm std
blue	225-248	243	3.94	1.55	2.21
green	248-254	251	1.7	1.59	2.42
yellow	254-260	257	1.73	2.03	2.66
magenta	260-268	264	2.27	3.04	3.03
red	268-332	277	7.52	3.62	4.35

Figure 3.9 Thermal inertia classification map of dune field located at 57°E, -2.1°N (D21). A. Classified THEMIS thermal inertia image. Each color represents the 20th percentile of thermal inertia ranges. B. Scatter plot of thermal inertia vs. olivine abundance; average and standard deviation of thermal inertia and olivine abundance for each thermal inertia range. C. Average olivine abundance of each thermal inertia range. Each color represents the 20th percentile of thermal inertia ranges. D. THEMIS spectra of each thermal inertia range. The colors are correspond to the colors of thermal inertia ranges in A. Spectra are offset for clarity.

Table S3.1 Details of 25 dune fields in this study.

dune ID	longitude (°E)	latitude (°N)	THEMIS cubic fit min (μm)	CRISM index	avg of CRISM index
C1	150	9.48	10.2	no data coverage	
D2	4.57	3.11	9.52	no mineral detection	
D3	93.77	-8.9	9.7	no data coverage	
D4	79.48	19.81	9.6	no mineral detection	
D5	124.96	-13.68	9.92	OLV3	0.1357
D6	128.28	-14.22	10.16	HCP2, LCP2	0.417,0.0149
D7	62.86	26.66	9.52	no data coverage	
D8	127.9	-14.84	9.74	no data coverage	
D9	137.54	-6.03	10.2	no mineral detection	
D10	79.44	19.82	9.6	no data coverage	
D11	67.67	7.19	11.02	no data coverage	
D12	169.2	8.47	9.9	HCP2	0.0016
D13	93.85	-6.95	9.7	no data coverage	
D14	167.96	14.58	--(*)	no data coverage	
D15	185.89	11.88	10.86	HCP2	0.019
D16	159.26	11.18	10.14	no data coverage	
D17	75.57	20.77	10.14	no data coverage	
D18	59.76	36.98	9.82	no data coverage	
D19	67.12	8.83	10.44	HCP2, LCP2	0.0147,0.003
D20	44.26	42.16	10.84	OLV3	0.022
D21	57	-2.1	10.24	no data coverage	
D22	79.06	20.29	9.68	no data coverage	
D23	128.5	-14.3	9.62	Glass	0.29
D24	65.61	23.1	9.7	no mineral detection	
D25	137.03	-5	9.72	OLV3, HCP2(**)	

*No TES for atm correction.

** Seelos et al, 2014.

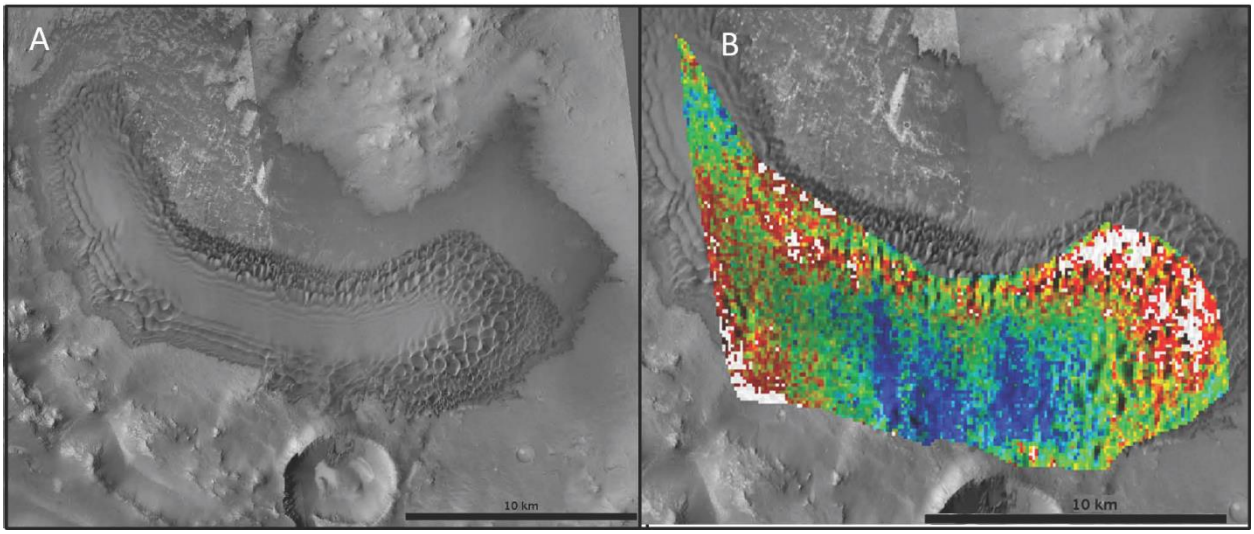

Figure S3.1 CTX and thermal inertia images for the dune field D1. A.CTX image. B. Color stretch map of THEMIS thermal inertia of the dune field.

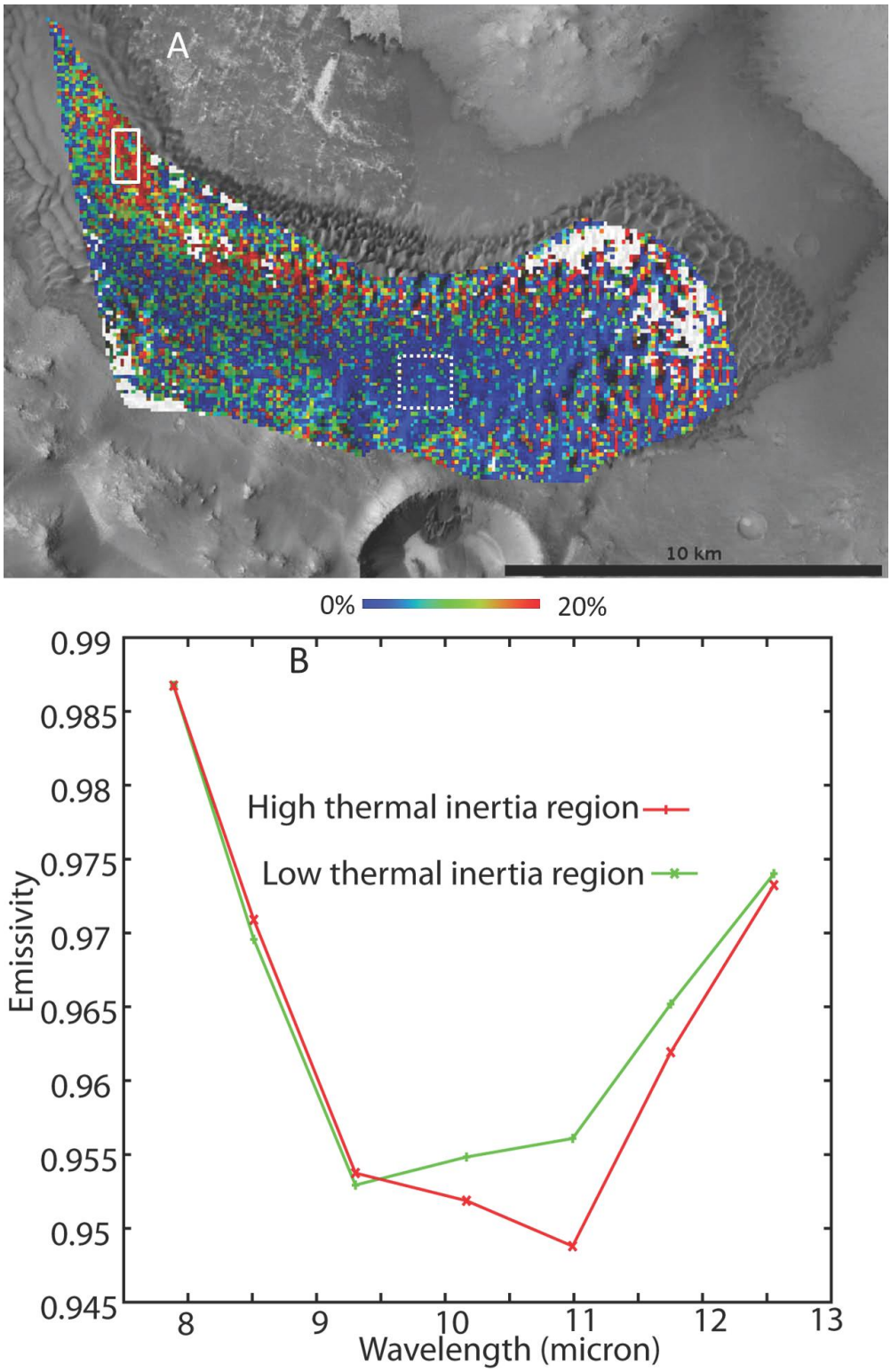

Figure S3.2 THEMIS-derived maps of dune field D1. THEMIS derived olivine abundance (A) and average spectra of high and low thermal inertia parts of the dune (B).

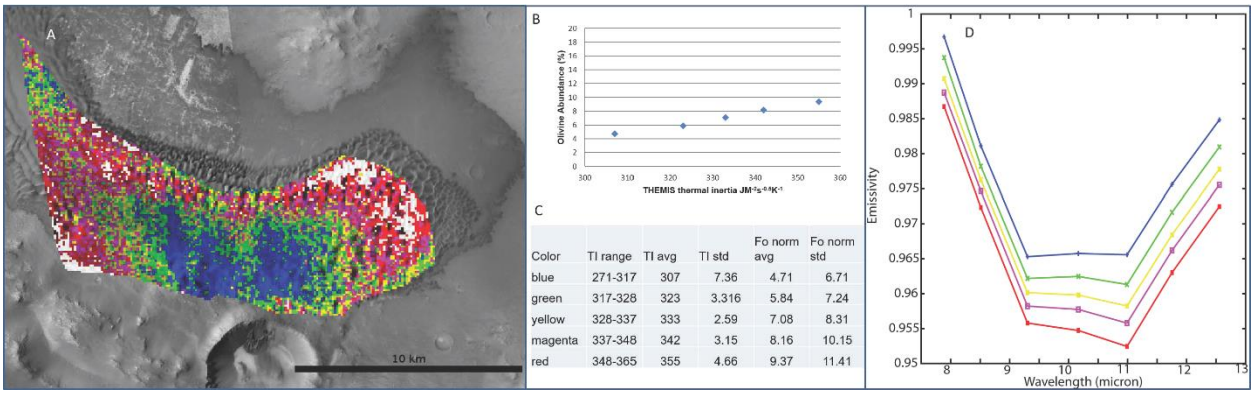

Color	TI range	TI avg	TI std	Fo norm avg	Fo norm std
blue	271-317	307	7.36	4.71	6.71
green	317-328	323	3.316	5.84	7.24
yellow	328-337	333	2.59	7.08	8.31
magenta	337-348	342	3.15	8.16	10.15
red	348-365	355	4.66	9.37	11.41

Figure S3.3 Thermal inertia classification map of dune field D1. A. Classified THEMIS thermal inertia image. Each color represents the 20th percentile of thermal inertia ranges. B. Scatter plot of thermal inertia vs. olivine abundance; average and standard deviation of thermal inertia and olivine abundance for each thermal inertia range. C. Average olivine abundance of each thermal inertia range. D. THEMIS spectra of each thermal inertia range. The colors correspond to the colors of thermal inertia ranges in A. Spectra are offset for clarity.

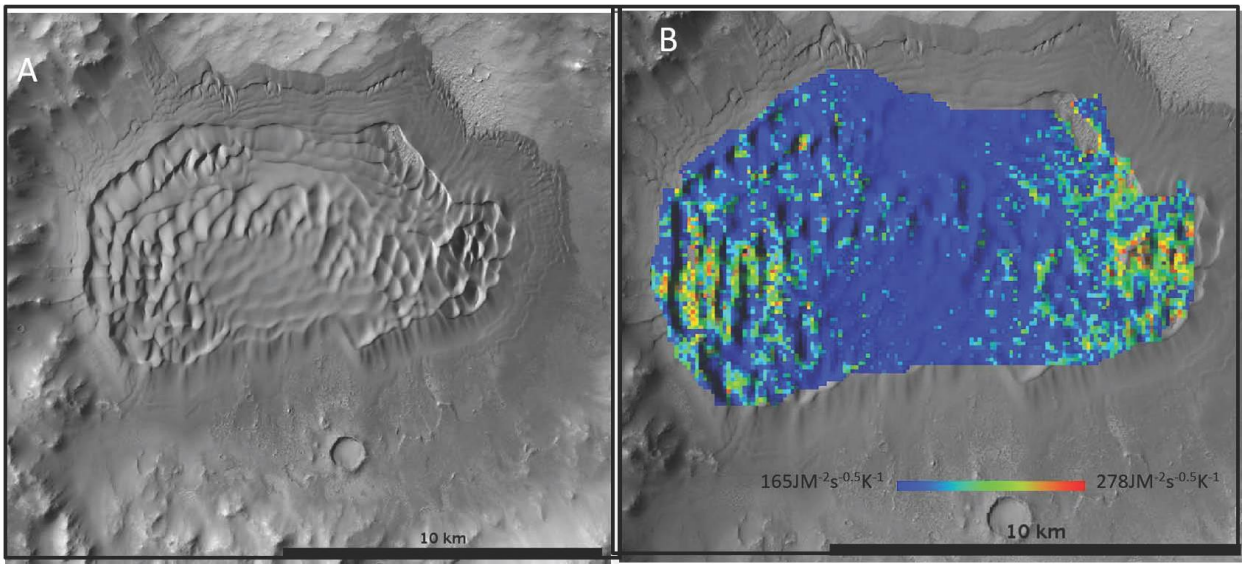

Figure S3.4 CTX and thermal inertia images for the dune field D23. A.CTX image. B. Color stretch map of THEMIS thermal inertia of the dune field.

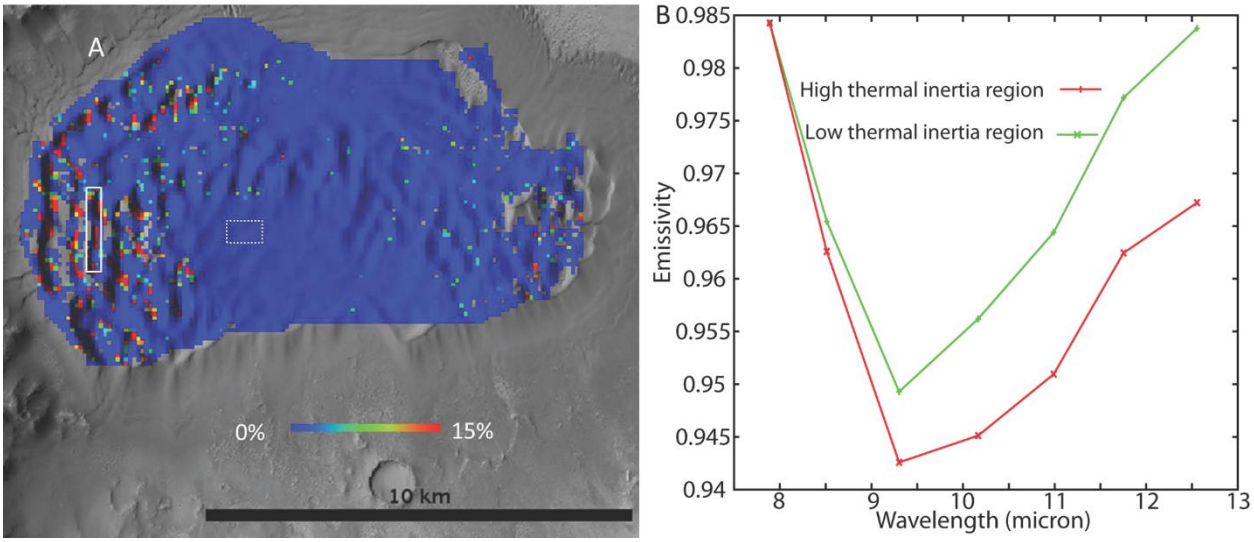

Figure S3.5 THEMIS-derived maps of dune field D23. THEMIS derived olivine abundance (A) and average spectra of high and low thermal inertia parts of the dune (B).

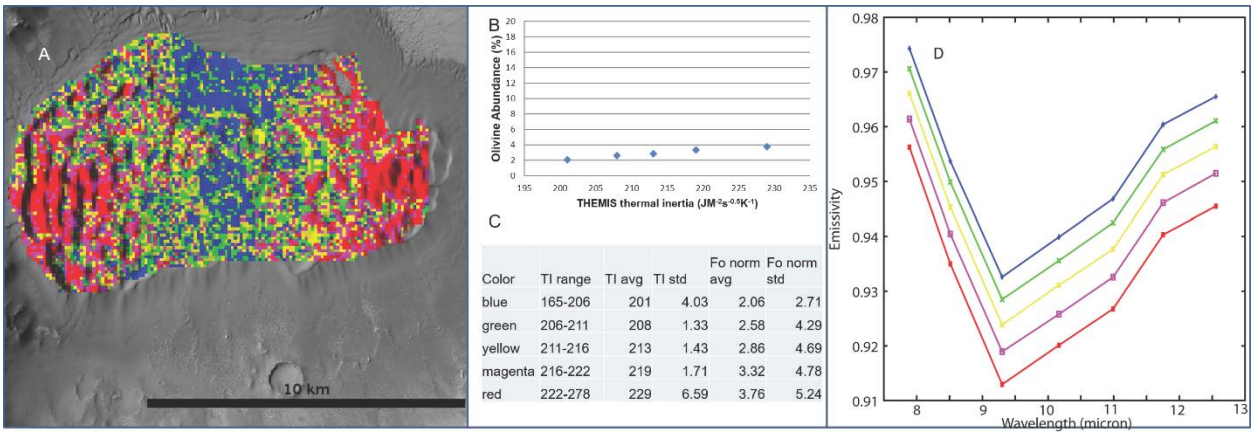

Color	TI range	TI avg	TI std	Fo norm avg	Fo norm std
blue	165-206	201	4.03	2.06	2.71
green	206-211	208	1.33	2.58	4.29
yellow	211-216	213	1.43	2.86	4.69
magenta	216-222	219	1.71	3.32	4.78
red	222-278	229	6.59	3.76	5.24

Figure S3.6 Thermal inertia classification map of dune field D23. A. Classified THEMIS thermal inertia image. Each color represents the 20th percentile of thermal inertia ranges. B. Scatter plot of thermal inertia vs. olivine abundance; average and standard deviation of thermal inertia and olivine abundance for each thermal inertia range. C. Average olivine abundance of each thermal inertia range. D. THEMIS spectra of each thermal inertia range. The colors correspond to the colors of thermal inertia ranges in A. Spectra are offset for clarity.

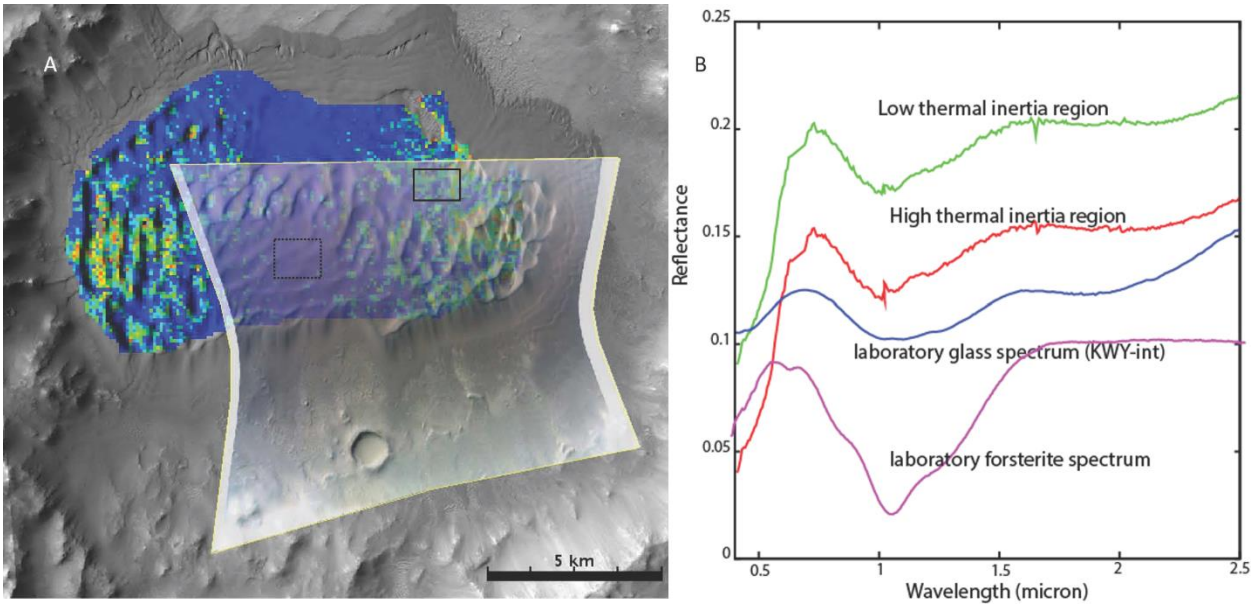

Figure S3.7 CRISM spectra of dune field D23. A. CRISM enhanced visible color image overlain on color stretch map of THEMIS thermal inertia showing the coverage of CRISM image. B. CRISM spectra of high and low thermal inertia region, comparing with laboratory spectra of glass from [Minitti et al., 2007] and forsterite. Spectra are offset for clarity.

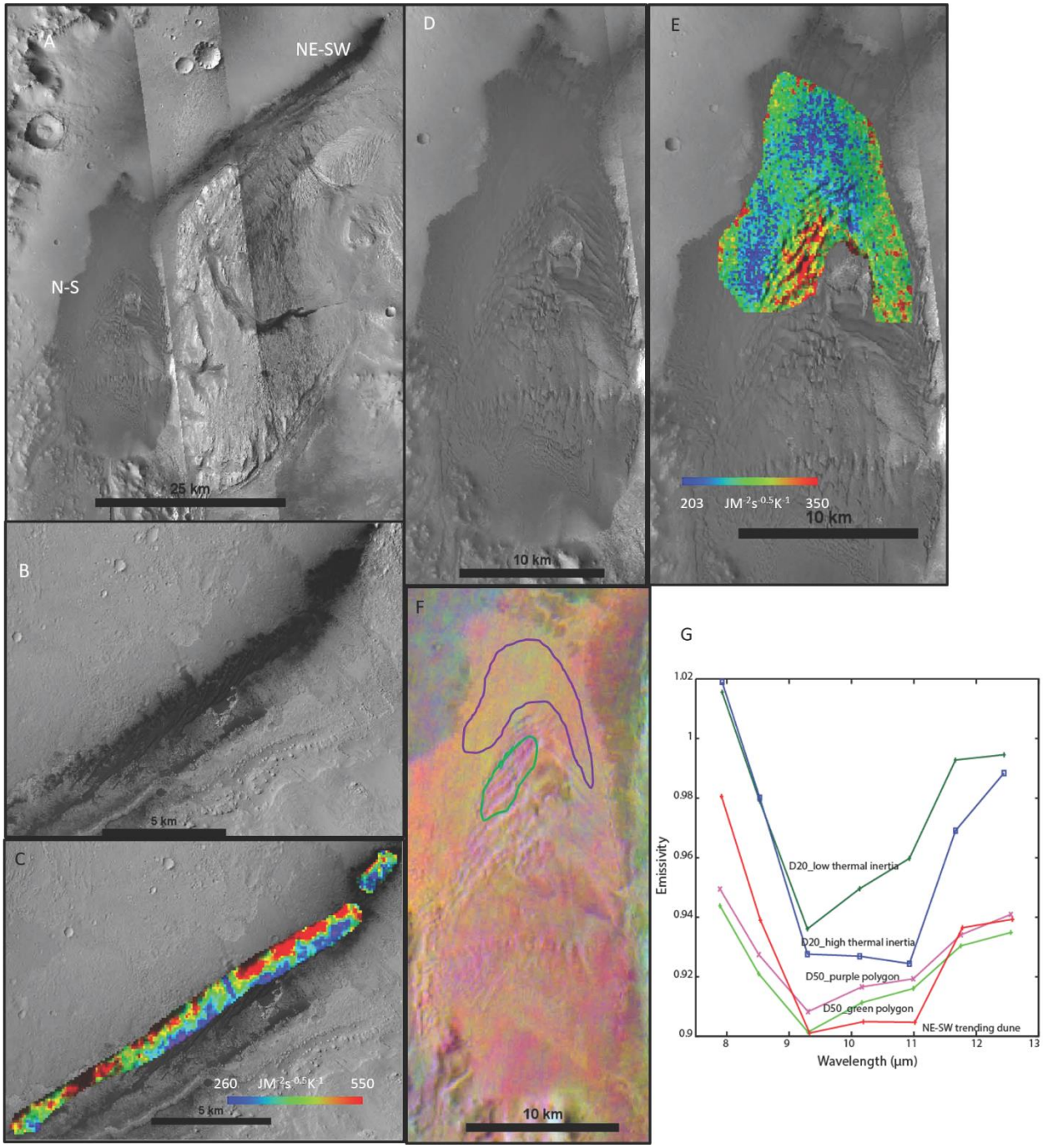

Figure S3.8 CTX, gray stretch map of THEMIS thermal inertia image, THEMIS color stretch map and THEMIS spectra of D25. A. CTX image shows the entire dune filed within Gale crater. B. CTX image shows the NE-SW trending dune. C. Color stretch map of THEMIS thermal inertia image of NE-SW trending dune. D. CTX image shows the N-S trending dune. E. Color stretch map of THEMIS thermal inertia image of N-S trending dune showing the portion of the dune field with contiguous sand cover in CTX. F. THEMIS bands 8 (~11.8μm)-7 (~11μm)-5 (~9.4μm) as red-green-blue in the DCS radiance mosaic of N-S trending dune. Purple and green polygons are two areas with color variation in DCS image which may indicate composition variation. G. THEMIS spectra of the NE-SW trending portion of the dune field, as well as from two areas within

the sand sea (areas indicated with purple and green polygons in Figure S8F. For comparison, THEMIS spectra of low and high thermal inertia areas within dune field D20 are also shown. Spectra are offset for clarity.

Reference

Aben, L. K. (2003), Extraterrestrial dunes: An introduction to the special issue on planetary dune systems, Arizona State University Tempe, Arizona.

Anderson, R. S., and K. L. Bunas (1993), GRAIN-SIZE SEGREGATION AND STRATIGRAPHY IN AEOLIAN RIPPLES MODELED WITH A CELLULAR-AUTOMATON, *Nature*, *365*(6448), 740-743, doi:10.1038/365740a0.

Bandfield, J. L., K. S. Edgett, and P. R. Christensen (2002), Spectroscopic study of the Moses Lake dune field, Washington: Determination of compositional distributions and source lithologies, *Journal of Geophysical Research-Planets*, *107*(E11), doi:10.1029/2000je001469.

Bandfield, J. L., D. Rogers, M. D. Smith, and P. R. Christensen (2004), Atmospheric correction and surface spectral unit mapping using Thermal Emission Imaging System data, *Journal of Geophysical Research-Planets*, *109*(E10), doi:E1000810.1029/2004je002289.

Blatt, H., G. Middleton, and R. Murray (1980), *Origiin of Sedimentary Rocks*, Prentice-Hall, Englewood Cliffs, New Jersey.

Boggs, S. (1995), *Principles of Seimentology and Stratigraphy*, Prentice Hall, Englewood Cliffs, New Jersey.

Chojnacki, M., D. M. Burr, and J. E. Moersch (2014), Valles Marineris dune fields as compared with other martian populations: Diversity of dune compositions, morphologies, and thermophysical properties, *Icarus*, *230*, 96-142, doi:10.1016/j.icarus.2013.08.018.

Christensen, P. R., R. L. Fergason, C. S. Edwards, and J. Hill (2013), THEMIS-derived thermal inertia mosaic of Mars: Product description and science results, paper presented at Lunar and Planetary Science Conference.

Christensen, P. R., et al. (2004), The Thermal Emission Imaging System (THEMIS) for the Mars 2001 Odyssey Mission, *Space Sci. Rev.*, *110*(1-2), 85-130, doi:10.1023/b:spac.0000021008.16305.94.

Edgett, K. S., and P. R. Christensen (1991), THE PARTICLE-SIZE OF MARTIAN AEOLIAN DUNES, *Journal of Geophysical Research-Planets*, *96*(E5), 22765-22776, doi:10.1029/91je02412.

Fedo, C. M., I. O. McGlynn, and H. Y. McSween (2015), Grain size and hydrodynamic sorting controls on the composition of basaltic sediments: Implications for interpreting martian soils, *Earth and Planetary Science Letters*, *423*, 67-77, doi:10.1016/j.epsl.2015.03.052.

Fenton, L. K. (2005), Potential sand sources for the dune fields in Noachis Terra, Mars, *Journal of Geophysical Research-Planets*, *110*(E11), doi:10.1029/2005je002436.

Fenton, L. K., and M. T. Mellon (2006), Thermal properties of sand from Thermal Emission Spectrometer (TES) and Thermal Emission Imaging System (THEMIS): Spatial variations within the Proctor Crater dune field on Mars, *Journal of Geophysical Research-Planets*, *111*(E6), doi:10.1029/2004je002363.

Fergason, R. L., P. R. Christensen, J. F. Bell, M. P. Golombek, K. E. Herkenhoff, and H. H. Kieffer (2006), Physical properties of the Mars Exploration Rover landing sites as inferred from Mini-TES-derived thermal inertia, *Journal of Geophysical Research-Planets*, *111*(E2), doi:10.1029/2005je002583.

Gillespie, A. R., A. B. Kahle, and R. E. Walker (1986), Color enhancement of highly correlated images. 1. Decorrelaton and HSI contrast stretches, *Remote Sensing of Environment*, *20*(3), 209-235, doi:10.1016/0034-4257(86)90044-1.

Greeley, R., and A. R. Peterfreund (1981), Aeolian" megaripples" examples from Mono Craters, California and northern Iceland [abs], paper presented at Geological Society of America, Abstracts with Programs.

Hapke, B. W. (1993), *Theory of Reflectance and Emittance Spectroscopy*, Cambridge University Press, Cambridge, U.K.

Hayward, R. K., L. K. Fenton, and T. N. Titus (2014), Mars Global Digital Dune Database (MGD(3)): Global dune distribution and wind pattern observations, *Icarus*, *230*, 38-46, doi:10.1016/j.icarus.2013.04.011.

Horgan, B., and J. F. Bell, III (2012), Widespread weathered glass on the surface of Mars, *Geology*, *40*(5), 391-394, doi:10.1130/g32755.1.

Horgan, B., E. A. Cloutis, P. Mann, and J. F. Bell (2014), Near-infrared spectra of ferrous mineral mixtures and methods for their identification in planetary surface spectra, *Icarus*, *234*, 132-154, doi:10.1016/j.icarus.2014.02.031.

Horz, F., M. J. Cintala, T. H. See, F. Cardenas, and T. D. Thompson (1984), GRAIN-SIZE EVOLUTION AND FRACTIONATION TRENDS IN AN EXPERIMENTAL REGOLITH, *Journal of Geophysical Research*, *89*, C183-C196, doi:10.1029/JB089iS01p0C183.

Jakosky, B. M. (1979), EFFECTS OF NONIDEAL SURFACES ON THE DERIVED THERMAL-PROPERTIES OF MARS, *Journal of Geophysical Research*, *84*, 8252-8262, doi:10.1029/JB084iB14p08252.

Kieffer, H. H., T. Martin, A. R. Peterfreund, B. M. Jakosky, E. D. Miner, and F. D. Palluconi (1977), Thermal and albedo mapping of Mars during the Viking primary mission, *Journal of Geophysical Research*, *82*(28), 4249-4291, doi:doi:10.1029/JS082i028p0424.

Kiminami, K., and K. Fujii (2007), The relationship between major element concentration and grain size within sandstones from four turbidite sequences in Japan, *Sedimentary Geology*, *195*(3-4), 203-215, doi:10.1016/j.sedgeo.2006.08.002.

Lane, M. D., and P. R. Christensen (2013), Determining olivine composition of basaltic dunes in Gale Crater, Mars, from orbit: Awaiting ground truth from Curiosity, *Geophys. Res. Lett.*, *40*(14), 3517-3521, doi:10.1002/grl.50621.

Lapotre, M., B. Ehlmann, F. Ayoub, S. Minson, N. Bridges, A. Fraeman, R. Arvidson, J. Eigenbrode, R. Ewing, and J. Johnson (2015), The Bagnold Dunes at Gale Crater---A Key to Reading the Geologic Record of Mount Sharp, paper presented at Lunar and Planetary Science Conference.

Makse, H. A. (2000), Grain segregation mechanism in aeolian sand ripples, *European Physical Journal E*, *1*(2-3), 127-135, doi:10.1007/pl00014592.

Malin, M. C., et al. (2007), Context Camera Investigation on board the Mars Reconnaissance Orbiter, *Journal of Geophysical Research-Planets*, *112*(E5), 25, doi:10.1029/2006je002808.

Mangold, N., D. Baratoux, O. Arnalds, J. M. Bardintzeff, B. Platevoet, M. Gregoire, and P. Pinet (2011), Segregation of olivine grains in volcanic sands in Iceland and implications for Mars, *Earth and Planetary Science Letters*, *310*(3-4), 233-243, doi:10.1016/j.epsl.2011.07.025.

McGlynn, I. O., C. M. Fedo, and H. Y. McSween (2011), Origin of basaltic soils at Gusev crater, Mars, by aeolian modification of impact-generated sediment, *Journal of Geophysical Research-Planets*, *116*, 15, doi:10.1029/2010je003712.

McGlynn, I. O., C. M. Fedo, and H. Y. McSween, Jr. (2012), Soil mineralogy at the Mars Exploration Rover landing sites: An assessment of the competing roles of physical sorting and chemical weathering, *Journal of Geophysical Research-Planets*, *117*, doi:10.1029/2011je003861.

Minitti, M. E., C. M. Weitz, M. D. Lane, and J. L. Bishop (2007), Morphology, chemistry, and spectral properties of Hawaiian rock coatings and implications for Mars, Journal of Geophysical Research-Planets, 112(E5), 24, doi:10.1029/2006je002839.

Murchie, S. L., et al. (2007), Compact reconnaissance Imaging Spectrometer for Mars (CRISM) on Mars Reconnaissance Orbiter (MRO), *Journal of Geophysical Research-Planets*, *112*(E5), E05s03, doi:10.1029/2006je002682.

Pan, C., A. D. Rogers, and J. R. Michalski (2015), Thermal and near-infrared analyses of central peaks of Martian impact craters: Evidence for a heterogeneous Martian crust, *Journal of Geophysical Research-Planets*, *120*(4), 662-688, doi:10.1002/2014je004676.

Pelkey, S., J. Mustard, S. Murchie, R. Clancy, M. Wolff, M. Smith, R. Milliken, J. Bibring, A. Gendrin, and F. Poulet (2007), CRISM multispectral summary products: Parameterizing mineral diversity on Mars from reflectance, *J. Geophys. Res*, *112*(E8), E08S14, doi:10.1029/2006JE002831.

Peterfreund, A. R. (1982), Formation of aeolian megaripples, Mono Craters, California [abs]: International Congress on Sedimentology, paper presented at Abstracts.

Pettijjohn, F. J., P. E. Potter, and R. Siever (1987), *Sand and Sandstone*, Springer Science & Business Media, New York,US.

Presley, M. A., and P. R. Christensen (1997), Thermal conductivity measurements of particulate materials .2. Results, *Journal of Geophysical Research-Planets*, *102*(E3), 6551-6566, doi:10.1029/96je03303.

Rogers, A. D., and J. L. Bandfield (2009), Mineralogical characterization of Mars Science Laboratory candidate landing sites from THEMIS and TES data, *Icarus*, *203*(2), 437-453, doi:10.1016/j.icarus.2009.04.020.

Rogers, A. D., and P. R. Christensen (2003), Age relationship of basaltic and andesitic surface compositions on Mars: Analysis of high-resolution TES observations of the northern hemisphere, *Journal of Geophysical Research-Planets*, *108*(E4), doi:10.1029/2002je001913.

Rogers, A. D., and V. E. Hamilton (2015), Compositional provinces of Mars from statistical analyses of TES, GRS, OMEGA and CRISM data, *Journal of Geophysical Research-Planets*, *120*(1), 62-91, doi:10.1002/2014je004690.

Ruff, S. W., and P. R. Christensen (2002), Bright and dark regions on Mars: Particle size and mineralogical characteristics based on Thermal Emission Spectrometer data, *Journal of Geophysical Research-Planets*, *107*(E12), 22, doi:10.1029/2001je001580.

Salisbury, J. W. (1993), Mid-infrared spectroscopy laboratory data, in *Remote Geochemical Analysis: Elemental and Mineralogical Composition*, edited by C. M. Pieters and P. A. Englert, pp. 79-98, Cambridge University Press, Cambridge, U.K.

Seelos, K. D., F. P. Seelos, C. E. Viviano-Beck, S. L. Murchie, R. E. Arvidson, B. L. Ehlmann, and A. A. Fraeman (2014), Mineralogy of the MSL Curiosity landing site in Gale crater as observed by MRO/CRISM, *Geophys. Res. Lett.*, *41*(14), 4880-4887, doi:10.1002/2014gl060310.

Stockstill-Cahill, K. R., F. S. Anderson, and V. E. Hamilton (2008), A study of low-albedo deposits within Amazonis Planitia craters: Evidence for locally derived ultramafic to mafic materials, *Journal of Geophysical Research-Planets*, *113*(E7), doi:10.1029/2007je003036.

Sullivan, R., et al. (2008), Wind-driven particle mobility on mars: Insights from Mars Exploration Rover observations at "El Dorado" and surroundings at Gusev Crater, *Journal of Geophysical Research-Planets*, *113*(E6), doi:10.1029/2008je003101.

Tirsch, D., R. Jaumann, A. Pacifici, and F. Poulet (2011), Dark aeolian sediments in Martian craters: Composition and sources, *Journal of Geophysical Research-Planets*, *116*, doi:10.1029/2009je003562.

Tolosana-Delgado, R., and H. von Eynatten (2009), Grain-Size Control on Petrographic Composition of Sediments: Compositional Regression and Rounded Zeros, *Mathematical Geosciences*, *41*(8), 869-886, doi:10.1007/s11004-009-9216-6.

Viviano-Beck, C. E., et al. (2014), Revised CRISM spectral parameters and summary products based on the currently detected mineral diversity on Mars, *Journal of Geophysical Research-Planets*, *119*(6), 1403-1431, doi:10.1002/2014je004627.

Weltje, G. J., and H. von Eynatten (2004), Quantitative provenance analysis of sediments: review and outlook, *Sedimentary Geology*, *171*(1-4), 1-11, doi:10.1016/j.sedgeo.2004.05.007.

Wentworth, C. K. (1922), A scale of grade and class terms for clastic sediments, *Journal of Geology*, *30*(5), 377-392.

Chapter 4: Quantitative Compositional Analysis of Sedimentary Materials Using Thermal Emission Spectroscopy: Application to Compacted Fine-grained Mineral Mixtures and Assessment of Applicability of Partial Least Squares (PLS) Methods

This chapter is a manuscript that is under revision at Journal of Geophysical Research-Planets with the same name.

Pan, C., A. D. Rogers, and M.T. Thorpe (2015), Quantitative Compositional Analysis of Sedimentary Materials Using Thermal Emission Spectroscopy: 2. Application to Compacted Fine-grained Mineral Mixtures and Assessment of Applicability of Partial Least Squares (PLS) Methods

Abstract

Fine-grained sedimentary deposits on planetary surfaces require quantitative assessment of mineral abundances in order to better understand the environments in which they formed. One way that planetary surface mineralogy is commonly assessed is through thermal emission (~6-50 μm) spectroscopy. To that end, we characterized the TIR spectral properties of compacted, very fine-grained mineral mixtures of oligoclase, augite, calcite, montmorillonite and gypsum. Non-negative linear least squares minimization (NNLS) is used to assess the linearity of spectral combination. A partial least squares (PLS) method is also applied to emission spectra of fine-grained synthetic mixtures and natural mudstones to assess its applicability to fine-grained rocks. The NNLS modeled abundances for all five minerals investigated are within ±10% of the known abundances for 39% of the mixtures, showing the relationships between known and modeled abundance follow non-linear curves. The poor performance of NNLS is due to photon transmission through small grains over portions of the wavelength range and multiple reflections in the volume. The PLS method was able to accurately recover the known abundances (to within +/-10%) for 78-90% of synthetic mixtures and for 85% of the mudstone samples chosen for this study. The excellent agreement between known and modeled abundances is likely due to high absorption coefficients

over portions of the thermal infrared (TIR) spectral range, and thus combinations are linear over portions of the range. PLS can be used to recover abundances from very fine-grained rocks from TIR measurements, and could potentially be applied to landed or orbital TIR observations.

4.1 Introduction

Sedimentary deposits, including fine-grained siliciclastic materials, clay, sulfate and hematite have been found on the Martian surface, and their formation may indicate liquid water activity for a period of time in early Martian history (e.g. [*Christensen et al.*, 2000a; *Malin and Edgett*, 2000; *Squyres et al.*, 2004; *Ehlmann et al.*, 2008b; *Grotzinger et al.*, 2014; *McLennan et al.*, 2014]). For example, sandstones in the Burns formation, Meridiani Planum, contain significant abundances of sulfate and hematite, indicating possible evaporitic and diagenetic processes [e.g. *Christensen et al.*, 2004b; *McLennan et al.*, 2005; *Glotch et al.*, 2006]. Carbonate minerals are identified in the soils at the Mars Phoenix Landing site [*Boynton et al*, 2009], in rare outcrops [Ehlmann et al., 2008], as well as in low quantities in the global Martian dust [Bandfield et al., 2003]. Last, clay minerals have been identified in numerous geologic settings [e.g. Poulet et al., 2005; Ehlmann et al., 2011; Carter et al., 2013], including in fans and deltas within sedimentary basins, which may indicate alteration by substantial amounts of water.

Interpreting the origin of sedimentary materials requires detailed analysis of geologic context, stratigraphy, mineral assemblages, and mineral abundances (e.g. [*McLennan et al.*, 2005; *Tornabene et al.*, 2008; *Wray et al.*, 2008; *Mustard et al.*, 2009; *Dobrea et al.*, 2010; *Michalski and Niles*, 2010; *Roach et al.*, 2010; *Ehlmann et al.*, 2011; *Grotzinger and Milliken*, 2012]). One of the ways to characterize mineral assemblage and abundances remotely is through thermal emission spectral measurements (e.g. [*Lyon*, 1965; *Kahle et al.*, 1984; *Christensen et al.*, 2000b; *Lucey*, 2004; *Hook et al.*, 2005]), which have been acquired of Martian surfaces both from orbit

and from the Mars Exploration Rover (MER) missions. Data from the Mars Global Surveyor Thermal Emission Spectrometer [*Christensen et al.*, 2001] (200-1650 cm^{-1}, 3 x 8 km spatial resolution) have been used to determine the distribution and abundance of minerals at global and regional scales.. Miniature Thermal Emission Spectrometers [*Christensen et al.*, 2004a; *Christensen et al.*, 2004b], onboard the Spirit and Opportunity rovers, measured thermally emitted radiance from soils, outcrops and float rocks over the 400-1650 cm^{-1} range. And the Mars Odyssey Thermal Emission Imaging System [*Christensen et al.*, 2003] measures emitted energy over 9 broad spectral channels between ~650-1550 cm^{-1}, with a spatial resolution of 100 m/pixel, allowing for discrimination of compositional units at the outcrop scale.

Spectral absorptions measured in the thermal infrared (TIR) range arise from molecular vibrations in the material of interest. The vibrations occur at specific frequencies based on the chemical composition and structure of the mineral of interest (e.g. [*Farmer*, 1974]). For mineral mixtures (e.g. rocks), the spectra of the individual components of the rock combine to produce the mixed spectrum. Previous studies of igneous and metamorphic rocks, as well as coarse-grained sand mixtures, have shown that the component spectra combine in proportion to their volume abundance in the mixed spectrum when grains are larger than ~>60 μm [*Ramsey and Christensen*, 1998; *Feely and Christensen*, 1999]. On this basis, linear spectral models of thermal emission spectra measured remotely have been used to estimate mineral abundances of Martian surface materials in low-dust regions [e.g., *Bandfield*, 2002; *Rogers and Christensen*, 2007; *Huang and Xiao*, 2014]. However, the spectral mixing behavior of compacted, fine-grained mineral mixtures that would be characteristic of sedimentary depositional environments (e.g. paleosols, mudstones, mixed-phase cements) has received little attention.

A difference in spectral mixing behavior for fine-grained rocks might be expected, given previous work demonstrating spectral dependence on grain size and porosity in the thermal infrared (TIR) (e.g. [*Hunt and Vincent*, 1968; *Clark and Roush*, 1984; *Salisbury and Wald*, 1992; *Hapke*, 1993; *Mustard and Hays*, 1997]. In a non-compacted volume consisting of particles whose diameters are on the order of the measured wavelength, there are proportionally more surface and internal reflections compared to larger grains. In spectral regions where the absorption index (*k*) is large (strongly absorbing), a reduction in spectral contrast with decreasing particle size is observed due to increased opportunities for absorption. In spectral regions where *k* is small (weakly absorbing), spectral contrast increases, due to increased opportunity for photons to exit the surface through refraction at each grain interface [*Hunt and Vincent*, 1968; *Moersch and Christensen*, 1995]. For mixtures of non-compacted particles whose diameters are on the order of the measured wavelength, the increased number of reflections described above leads to photon interaction with multiple phases before exiting the mixture, and thus the observed absorptions are not predictive of volume abundances (non-linear mixing) (e.g., [*Mustard and Hays*, 1997; *Ramsey and Christensen*, 1998]).

In a volume where small particles are closely packed, multiple surface reflections are reduced, and spectra more closely resemble those from coarse-grained materials [*Salisbury and Wald*, 1992]. Despite this, a volume scattering component remains due to the grain size being equal to or smaller than the mean optical path length (e.g. [*Hunt and Logan*, 1972; *Clark and Roush*, 1984]). These effects of compaction on fine grained *mixtures* have not been examined in a systematic manner, however. Because *k* is wavelength-dependent for each mineral, and transmission through small grains occurs where *k* is small (e.g. [*Hunt and Logan*, 1972; *Salisbury et al.*, 1987; *Cooper and Mustard*, 2002]), we would expect a mixture of linear and non-linear mixing behavior that

varies with wavelength. Characterizing the TIR spectral mixing behavior of compacted fine-grained mineral assemblages is necessary for facilitating quantitative mineralogy of sedimentary surfaces and understanding their origins from spectral measurements.

In a companion paper (*Thorpe et al., 2015*, hereafter referred to as "Paper 1"), we characterize the spectral mixing behavior of a suite of terrestrial sandstones and mudstones to assess the accuracy of quantitative mineral abundance estimates derived from thermal emission spectra of sedimentary rocks. In this paper, we characterize the spectral properties of compacted, very fine-grained (<10-25 μm) mineral mixtures to assess spectral mixing behavior of very fine-grained materials. For the first time, we also apply a partial least squares (PLS) method to model mineral abundance from thermal emission spectra and provide an assessment of the applicability of PLS to fine-grained rocks.

4.2 Data and Methods

4.2.1 Sample preparation

Five minerals including oligoclase, augite, calcite, gypsum and montmorillonite were used for this study. These five minerals were chosen to encompass a suite of basaltic minerals as well as alteration products that have been identified on Mars. Montmorillonite was purchased from the Clay Minerals Society and the other four were from Ward's Science. The oligoclase sample from Ward's was labeled "albite", but is actually oligoclase, confirmed by electron microprobe (**Table 4.1**). The gypsum sample was already in powdered form. The oligoclase, augite and calcite samples were crushed with an agate mortar and pestle. Except for gypsum, all samples were then centrifuged to obtain particle sizes less than 10 μm [*Jackson*, 1967] and to reduce impurities for montmorillonite [*Moore and Reynolds*, 1997] (**Table 4.1**). Particle size was measured using a

Malvern Instruments Mastersizer 2000 laser diffractometer with Hydro 2000MU pump accessory at Stony Brook University. The median particle sizes used in this study were: 3 μm for oligoclase, 3 μm for montmorillonite, 4 μm for augite, 2.5 μm for calcite and 23 μm for gypsum (**Table 4.1**). Mixtures of two, three and four components were made in varying proportions by volume (**Table 4.2**). Single phase and mixture samples were pressed into ~3 mm thick pellets with ~1 cm in diameter at 15000 PSI (pound-force per square inch) to generate compacted samples. The pellets were not made from binding agents. Pellets were visually shiny and reflective, suggesting an absence of clinging fines. Though pressing can result in a preferred grain orientation, this should not negatively influence our results because we are using pressed pellets for both the mixed spectra and the end-member spectra, and thus orientations should be similar. Coarse-grained samples with particle size larger than 500 μm of oligoclase, augite and calcite, and loose powder of all five minerals were also prepared for spectroscopic measurements and comparison.

4.2.2 Raman microspectroscopy

To validate whether the targeted volume percentages in **Table 4.2** are close to areal abundance in the pellets, Raman spectral images of some mixture pellets were measured. The Raman spectra were measured using a WITec alpha300R confocal Raman imaging system at the Stony Brook University Vibrational Spectroscopy Lab. For each pellet, hyperspectral Raman images of three 75x75 μm areas were measured for three different pellets with 1 cm^{-1} spectral resolution. The spectral angle mapping (SAM) [*Kruse et al.*, 1993] supervised classification method was used to determine the areal abundance of minerals in each area. SAM analysis of Raman spectral images results showed that areal abundance is within +/- 5% of targeted volume percentage in these pellets. An example is shown in the supplementary materials (**Figure 4.S16)**.

4.2.3 Thermal infrared spectroscopic measurements

Thermal infrared spectra of pellets were measured at the Stony Brook University Vibrational Spectroscopy Lab from ~225 to 2000 cm^{-1} at 2 cm^{-1} spectral sampling using a Nicolet 6700 FTIR spectrometer. Except for gypsum-bearing samples, samples were heated and maintained at 80°C to provide adequate signal to noise ratio. In order to avoid dehydration of gypsum during measurement, gypsum-bearing mixtures were cooled with dry ice for several hours and then measured [*Baldridge and Christensen*, 2009]. Sample temperatures during measurement were ~-10°C, approximately ~35°C below detector temperature. This results in slightly lower signal-to-noise ratios than the conventional emissivity measurement method (where samples are heated, e.g. *Ruff et al*. [1997]), but because the samples for measurement exhibit high spectral contrast, the quality of the measured spectra are more than sufficient for resolving all features [*Baldridge and Christensen*, 2009]. A blackbody heated to 70°C and 100°C was used to generate the instrument response function, which is then use to convert measured sample signal to radiance units. Environmental radiance contributions are controlled using a temperature-regulated sample chamber; these contributions are mathematically removed from the measured radiance using the methods of [*Ruff et al.*, 1997].

4.2.4 Non-negative linear least squares (NNLS) minimization

To assess linearity of spectral combination in compacted fine-grained mixtures, non-negative linear least squares minimization (NNLS) [*Lawson and Hanson*, 1974] using spectra of pellets and powders of the end-member minerals (**Table 4.1**) was used to model mineral abundance of mixtures over the 350-1650 cm^{-1} spectral range. Most of the major and minor minerals found on the Martian surface have thermal infrared absorption features in these spectral ranges, and the range is comparable to that of the Mars Global Surveyor TES and Mars Exploration Rover Mini-TES instruments. Linear least squares minimization has been widely used to derive surface

emissivity and mineral abundance from TES and Mini-TES data (e.g., [*Smith et al.*, 2000; *Bandfield*, 2002; *Glotch et al.*, 2006; *Ruff et al.*, 2006; *Rogers and Christensen*, 2007; *Koeppen and Hamilton*, 2008; *Rogers and Aharonson*, 2008; *Ruff et al.*, 2011; *Hamilton and Ruff*, 2012; *Pan et al.*, 2015]. The use of this method assumes linear spectral mixing across the entire spectral range (**Section 4.4.1**).

4.2.5 Partial least squares (PLS)

Partial least squares (PLS) is an extension of a multiple linear regression statistical method that assumes a system of observations can be described with a small number of unobservable (or "latent") variables, similar to principal component or factor analysis techniques. PLS generalizes predictive models from these latent variables [*H Wold*, 1982; *S Wold et al.*, 2001], and is widely used in chemometrics, bioinformatics and related fields. For example, it is one of the primary data reduction techniques employed by the Mars Science Laboratory Rover Curiosity ChemCam team [*Clegg et al.*, 2009; *Dyar et al.*, 2012]. It has been successfully applied to thermal reflectance spectra of granites [*Hecker et al*., 2012], and was also investigated as a possible technique to retrieve mineral abundance from near-infrared spectra of mineral mixtures [*Li et al*., 2012] (discussed further in **Section 4.3**). PLS analysis [*H Wold*, 1982] was employed to generate a calibration model from which unknown mineral abundance of mixture spectra (testing data set) can be predicted using spectra with known mineral abundance (training data set). Both NNLS and PLS involve generating regression models to solve the linear multivariate problem:

$$Y = \beta_0 + \beta_1 X_1 + \beta_2 X_2 + \cdots + \beta_n X_n$$

where Y is one or several dependent variables, X is the independent variable or predictor variable, β_0 is the regression coefficient for the intercept, and β_i $(i = 1 \cdots n)$ is the matrix of regression coefficients. For NNLS, Y is the mixture spectrum, X_i is the spectral library (usually consisting of

well-characterized, "pure" mineral sample spectra) [*Lawson and Hanson*, 1974; *Ramsey and Christensen*, 1998], and β_i is a function of the number of library spectra. For PLS, X_i is a matrix containing the emissivity spectra of mixtures with known abundances, where *i* is the number of spectral channels, Y is the corresponding matrix of known mineral abundances (vol %), and β_i is the regression coefficient for each spectral channel *i*. PLS analysis determines the statistical linear correlation between the known mineral abundance and observed spectra (both of these constitute the training set).

Single-phase pellets and powders and all of the mixtures from **Table 4.2** were used as the training data set for PLS, and based on this training set, regression coefficients were derived for each mineral. The derived regression coefficients vary as a function of wavelength, and are related to the thermal infrared spectral features that most strongly drive the correlations between mineral abundance and spectral properties in the mixed set of spectra. This is described in more detail in **Section 4.3.1.2**. The "PLS-2" method commonly applied to ChemCam data [*Clegg et al.*, 2009; *Dyar et al*., 2012], where multiple Y variables are simultaneously analyzed, was used. PLS-2 allows for better prediction of regression coefficients over PLS-1, because of correlations between mineral components within the mixtures (e.g., as one component is increased, there must be a decrease in another component) [e.g. *Dyar et al.*, 2012]. In this work, the number of latent variables within the training set was estimated by examining the percentage of variance explained in the response variable Y as a function of the number of components **(Figure 4.S17 and S18)**. Higher-number components correspond with smaller contribution to total variance. The number of components chosen for our predictive models for the compacted fine-grained mixtures was 15, based on an iterative process of examining the percent of variance contribution and checking the modeled abundance results for changes with increasing number of components. Using higher

numbers of components beyond 15 was found to have little effect on the predictive performance of the model (<3% change in modeled abundance, on average); these first 15 components account for >90% of the variance within the training set. Next, a "leave-one-out" approach was used to generate regression coefficients from the original training data set, excluding one spectrum from the set. Those coefficients were then applied to the excluded spectrum to retrieve mineral abundance for that spectrum. This process was repeated for all of the mixtures from **Table 4.2**, and then compared with the known abundances for each mixture to evaluate the PLS model accuracy.

Lastly, we applied the same method to the mudstone samples from paper 1 with the same wavenumber range as paper 1 (230-1650 cm^{-1}), in order to examine the performance of PLS applied to natural rock samples. There are 14 mudstone samples, whose mineral abundances were determined by X-Ray diffraction (XRD) [*Thorpe et al., 2015*] (given also in **Table 4.3**). The mudstone samples are from the Huronian Supergroup (2.5-2.2 Ga) outcrop belt on the northern shore of Lake Huron, Canada. As described in paper 1, they vary in their abundances of sericite, chlorite, and framework minerals. Only the minerals with abundances more than 3 vol%, as determined by XRD, and minerals that were clearly present in almost all of the mudstone samples were included as inputs to our PLS model. These minerals groups are: feldspar, quartz, clays and mica. Thus the training set for the mudstone samples consists of the XRD-determined abundances for each of these four groups, as well as the mudstone spectra. The number of components chosen for mudstone models was five (**Figure 4.S18**), which represents more than 95% of the variance. Using higher numbers of components had negligible effects on the final modeled abundances.

4.3 Results

4.3.1 Sand samples and pressed pellets

Figure 4.1 shows a comparison of TIR spectra of sand (500-841 μm) and pellet samples of oligoclase, augite and calcite. Notable differences between the sand and pellet versions of each mineral are present, both in terms of spectral contrast and spectral shape. These differences likely arise from an increased contribution of volume scattering in the compacted fine-grained material relative to that in the larger, optically thick sand grains.

4.3.1.1 NNLS

In this section, we present the spectra from each set of mineral mixtures (**Table 4.2**), along with the best-fit spectral model from NNLS (**Figures 4.2-4.4**). Due to space limitations, only one representative set of spectra from the binary, ternary, and quarternary mixtures is shown. The remaining sets of spectra are shown in the supplementary information (**Figures 4.S1-4.S15**). In **Figure 4.5**, we show the modeled abundances for all mixtures, compared with the known abundance.

Figures 4.2-4.4 show representative model fits from three of the 18 mixtures examined. Some of the mixtures are well-modeled by their end-member pellet components, whereas others are not. Additionally, some spectra are well-modeled over portions of the spectral range, with other portions showing large misfits. Because each spectrum was modeled with its known components, the possibility of missing end-members may be ruled out, and the misfits may be attributed directly to non-linear spectral mixing.

For oligoclase-bearing mixtures, approximately 60% of modeled oligoclase abundances fall within ±10% of the true abundance, with remaining mixtures generally overestimated. Model accuracy was generally better for two component mixtures than for more complex mixtures with

three or more components (**Figure 4.5a**). Modeled abundance accuracy is generally better for higher true abundances of oligoclase.

For augite-bearing mixtures, approximately half of the results fall within ±10% of the true abundance, with the remaining half generally over-estimated (**Figure 4.5b**). There is no clear trend of the model accuracy with mixture complexity or true abundance.

Approximately 60% of the modeled calcite abundances are within ±10% of true abundance, whereas the remainder are generally over-estimated (**Figure 4.5c**). For the three- and four-component mixtures, smaller abundances (<20%) are more accurately modeled.

For montmorillonite-bearing mixtures, ~30% of the results fall within 10% from the known, with most modeled abundances under-estimated (**Figure 4.5d**). The modeled abundance accuracy improves when the true abundance of montmorillonite is less than 10%.

For gypsum-bearing mixtures, less than 40% of the results are within 10% of the known abundance (**Figure 4.5e**). The model accuracy improves slightly for lower abundances.

In summary, modeled abundances for all five minerals investigated are within ±10% of the known abundances for 39% of the mixtures. Model accuracy varies for each mineral group, and also depends on what other mixture components are present. For example montmorillonite abundances in binary mixtures with gypsum are accurately determined, whereas montmorillonite abundances in binary mixtures with augite are generally underestimated. For each mixture in a given series (e.g. 10:90, 20:80, 50:50, etc), differences from the known abundance generally do not follow a constant offset from the known, Rather, the relationships between known and modeled abundance follow non-linear curves (**Figure 4.5**).

4.3.1.2 PLS

In this section, we present the regression coefficients derived from PLS using a training set containing all mixture series shown in **Table 4.2**, along with the endmembers in both powder and pellet form (**Figure 4.6**). The inclusion of both powder and pellet end-member spectra in our training set allows us to better account for possible volume scattering features that are not fully diminished in spectra from the pelletized mixtures (**Section 4.1**). The training set included 88 spectra in total. Then, using a "leave-one-out" approach, we repeatedly generate new sets of regression coefficients, and then apply those to the missing sample (**Section 4.2.5**), in order to determine the accuracy to which PLS can predict the mixture abundances (**Figure 4.7**).

For oligoclase, the strongest regression coefficients from PLS are located at ~1170, 870, 850, and between 750-790 cm^{-1} (**Figure 4.6a**). Of these, only the features near ~850 and 870 cm^{-1} correspond directly with the center of a major absorption (in this case, the powdered version of oligoclase). The regression coefficient peak near ~1170 cm^{-1} corresponds with the shoulder of the broad fundamental absorption in oligoclase, rather than the center of the absorption, and the strong coefficients between 750-790 cm^{-1} do not appear to correspond with any particular absorption in the pellet or powder versions of these samples. Pelletized oligoclase exhibits a deep absorption near ~1010 cm^{-1}, which corresponds with a moderately strong negative regression coefficient "dip", but this feature is not as strongly predictive as some of the other frequencies described above. Despite the lack of clear correspondence between regression coefficient values and emissivity features, the coefficients accurately predict the abundance of oligoclase, with more than 84% of the modeled oligoclase abundances falling within ±10% of the known abundance (**Figure**

4.7a). False positives were observed for some non-oligoclase-bearing mixtures; these most commonly occurred in montmorillonite-bearing mixtures, and modeled abundances were generally <20% (**Table 4.S**2)

For augite**,** the strongest regression coefficients are at ~1170, 850, 670, 500, 460 and 400 cm^{-1} (**Figure 4.6b**). As with oligoclase, most of these do not correspond with the strongest emissivity absorptions or peaks. The ~1170 cm^{-1} coefficient corresponds to the Christiansen feature of augite. The ~460 cm^{-1} coefficient corresponds to the near-center of a low-frequency major absorption of the augite pellet, and the ~400 cm^{-1} value to a minor absorption feature of both augite powder and pellet. The ~850 cm^{-1} coefficient is co-located with the shoulder of the broad fundamental absorption, and the ~670 cm^{-1} value is not correlated with any absorption. Augite abundances for approximately 22% of the mixtures are incorrectly modeled by more than ±10% (**Figure 4.7b**). The accuracy of modeled abundance increases as the number of mixture components increase (**Figure 4.7b**). In some mixtures where augite is not truly present, low abundances of augite (<20%) were modeled with PLS, with one mixture (oligoclase-montmorillonite-gypsum) exhibiting 45% modeled abundance of augite (**Table 4.S2**). These false positives are discussed further in **Section 4.4**.

For calcite, in general, the regression coefficients overall are lower than those of the other four minerals. As discussed in **Section 4.4**, this is likely due to the very low degree of overlap between absorptions in the pellet and powder versions of calcite, as well as the presence of features for calcite powder occurring across much of the spectral range. Though they are generally low, the strongest regression coefficients are located near ~1590, 1550, 1280, 1010 and 1050 cm^{-1}. The ~1550, 1280, 1010 and 1050 cm^{-1} coefficients correspond to absorption features of calcite powder while the coefficient at ~1590 cm^{-1} is near the Christiansen frequency (**Figure 4.6c**). The strongest

absorption feature of calcite pellet at ~1500 cm^{-1} corresponds to only a moderately strong regression coefficient compared to the other features. Modeled calcite abundances for more than 90% of the mixtures fall within the ±10% of known abundance. Modeled abundances for the remaining mixtures are generally underestimated, except for one false detection (**Figure 4.7c**). Calcite abundances from the three component mixtures are modeled less accurately than those from two- and four-component mixtures (**Figure 4.7c**).

Montmorillonite exhibits a fewer number of strong regression coefficients, but those values are amongst the highest observed for all five minerals of this study. As described in **Section 4.4**, this is likely due to similarities between the powdered and pellet versions of montmorillonite. Two of the strongest regression coefficients, at ~500 and 470 cm^{-1} correspond directly with the peak and valley of one-half of the spectral doublet that is characteristic of dioctahedral smectite clays [*Michalski et al.*, 2006; *Ruff and Christensen*, 2007] (**Figure 4.6d**). A strong coefficient at ~550 cm^{-1} corresponds to the shoulder of the higher-frequency portion of the doublet. Last, a strong coefficient at ~670 cm^{-1} is not related to any particular absorption or peak. The strong absorption feature of montmorillonite pellet and powder at ~1040 cm^{-1} corresponds to only a weak regression coefficient. Modeled montmorillonite abundances for ~13% of the mixtures fall outside ±10% of known abundance (**Figure 4.7d**). As with the calcite results, modeled montmorillonite abundances for the remaining mixtures are all generally underestimated, with a few exceptions (**Figure 4.7d**).

For gypsum, the strongest regression coefficients are at ~1600- 1630, 1550, 1160 and 1130 cm^{-1}. The values in the ~1600-1630 cm^{-1} range correspond to a small bound-water peak [*Salisbury et al.*, 1991] in the gypsum powder, which is manifested as a minor absorption in the gypsum pellet. The other strongest coefficients correspond to the shoulders of the broad fundamental absorption centered at ~1150 cm^{-1}. Modeled gypsum abundances for more than 90% of the

mixtures fall within ±10% of known abundance, with no false detections (**Figure 4.7e**). Four of the mixtures, however exhibit modeled gypsum abundances greater than 20% from the known value.

Note that PLS has no constraint to sum to 100%; in addition, negative abundance values are permitted by the algorithm (**Figure 4.7, Table 4.S2**). In our results, negative values are usually between 0 and -5%. Small negative values likely arise from subtle, non-systematic differences in slope between samples. The slight differences in spectral slope can arise from variable temperatures in the field of view during the measurement. This would result in over- or under-estimates of one component, resulting in compensation using negative abundances of other components.

4.3.2 Mudstone samples

Figure 4.8 compares NNLS-derived mineral abundances with PLS-derived abundances to that of XRD abundances for the mudstone samples from paper 1 [*Thorpe et al., 2015*]. The PLS method retrieved known abundances to within ±10% for the majority of the mudstones, with no more than three samples falling outside this range. Modeled mica abundances are significantly improved using the PLS method. For the remaining three mineral groups, model accuracy from PLS and NNLS are comparable, with perhaps slightly better accuracy for PLS on quartz and clay abundances (**Figure 4.8**).

4.4 Discussion

4.4.1 Spectral characteristics of compacted fine-grained particulates

Figure 4.1 demonstrates that the spectral characteristics of compacted fine grains exhibit non-negligible differences from coarse-grained sands of identical composition. Compared to sand samples, compressed powders show reduced spectral contrast and shifts in the position of some

absorption features. As described in **Section 4.4.1**, this is to be expected given that both surface and volume scattering occur within a particulate medium [*Hunt and Vincent*, 1968; *Salisbury and Eastes*, 1985; *Salisbury and Wald*, 1992]. Compaction of the fine particles minimizes (or eliminates) the multiple surface reflections, but some amount of the volume scattered component remains [*Salisbury and Wald*, 1992]. Because the magnitude of k is wavelength-dependent, spectral changes due to transmission through small grains and multiple reflections in the volume are only observed across portions of the spectrum.

4.4.2 Applicability of NNLS to compacted fine-grained mixtures

Compared to coarse-grained (>~60 μm) particulate mixtures and rocks [*Ramsey and Christensen*, 1998; *Feely and Christensen*, 1999; *paper 1*], the accuracy of the NNLS model is poor for compacted fine-grained mixtures (**Figure 4.5**). Though many of the modeled abundances are within +/- 10% of the known abundance, approximately 40~70% were not, depending on which minerals were present in each combination. For oligoclase, augite and calcite, the modeled abundances are overestimated in most of the cases, whereas for montmorillonite and gypsum, the modeled abundances are generally underestimated.

Clues to the cause(s) of the poor performance of NNLS come from **Figure 4.1**, which shows noticeable spectral changes between pressed fine grains and coarse-grained sands of the same composition. This suggests that transmission through small grains is occurring over portions of the wavelength range, due to small absorption coefficients in those ranges. In addition, the larger number of grains per volume results in multiple reflections in the volume (**Section 4.4.1**). With mixtures, these volume scattering effects would result in a disproportionate number of photon interactions with the more strongly absorbing phases (which varies as a function of wavelength), and thus reduces the ability to model abundances accurately with NNLS.

Over portions of the spectral range, however, the features scale predictably with abundance. For example, in the oligoclase-augite binary mixture (**Figure 4.2**), an augite fundamental feature near ~1070 cm^{-1} decreases in strength with decreasing abundance, and is replaced by an oligoclase peak at that location. In another example, using the gypsum-oligoclase binary mixture (**Figure 4.S2**), the gypsum Restrahlen band decreases with gypsum abundance, and the oligoclase fundamental feature near 1010 cm^{-1} begins to appear. These examples indicate that volume scattering is not significant for the entire wavelength range for many of the mixtures. However, because NNLS treats each channel equally, it is unable to produce a linear combination across the entire wavelength range used for modeling.

4.4.3 Applicability of PLS to compacted fine-grained mixtures

The PLS method was able to accurately recover the known abundances (to within +/-10%) for 78-90% our synthetic mixtures and for 85 % of the mudstone samples. This is in contrast to model accuracies found by a similar study investigating a lunar sample [*Li et al.*, 2012], in which PLS was applied to visible/near-infrared (VNIR) spectra of mineral mixtures. We suggest that the difference in applicability findings are due to the higher *k* values that are typically found in the TIR range; because *k* is usually very high (>1) over some portion of the TIR, combinations are linear (or close to linear) over portions of the range. However, in the VNIR, the low *k* values (usually $<\sim10^{-2}$) across the full wavelength range results in non-linear combinations across that range. In that situation, PLS cannot be used to retrieve accurate abundances.

Despite the excellent agreement between known and modeled abundances for most of our mixtures, there are a few issues worthy of discussion. First, false positive detections were observed for some minerals (for example **Section 4.3.1.2**). We suggest that this is likely due to overlap in the wavelength locations of strong regression coefficients for some of our minerals. For example,

PLS identified a moderately strong regression coefficient at ~550 cm^{-1} and ~660 cm^{-1} for both oligoclase and montmorillonite. Correspondingly, oligoclase was identified at low levels in montmorillonite-bearing mixtures, even where oligoclase was absent. Second, the regression coefficients derived from some of our mixtures are relatively low compared to others. For example, regression coefficients derived for calcite are much lower than those derived from montmorillonite. This is likely due to the grouping of both powders and pellet samples in the training set; the drastically different absorption features in different wavelength ranges between powders and pellets may result in less of a correlation and lower regression coefficients for a single calcite "group". The regression coefficients are indicators of the importance of each wavelength for predicting the abundance within the system from which they were derived. The importance of a particular wavelength for a given mineral may be obscured or diluted if the absorption features for powders and pellets are in different locations. In future work, a potential way to overcome this would be to treat these as subgroups for a given mineral, and combine abundances for each subgroup. Third, the strongest regression coefficients are sometimes correlated with a strong emissivity absorption, but in other cases, are not; this varies from mineral to mineral. For example, the regression coefficients for montmorillonite at ~470 and 500 cm^{-1} are correlated to strong absorption features of montmorillonite, but most of the coefficients for augite are not correlated to strong emissivity features of augite. A similar phenomenon was described for LIBS data [*Dyar et al.*, 2012], where the strongest regression coefficients were sometimes associated with the weaker atomic emission lines. As described above, one possible explanation is that the spectral shapes of powder and pellet for montmorillonite are similar, whereas for augite, they are different. However, this is also strongly controlled by the spectral characteristics of all other components in the training set. For example, for a given mineral whose major absorptions overlap fully or partially

with another mineral, the shoulder of a feature or the absence of a feature may prove to be the strongest drivers of the coefficients for that mineral.

In summary, all of these issues can be generally attributed to the appropriateness of the training set; thus, the training set is the key to model accuracy of PLS. This can include either adding mixtures of additional varying proportions, but also deleting non-relevant mixtures from the training set.

PLS offers many advantages over NNLS, but like any technique, also has its limitations. The major advantage of PLS is improved accuracy for fine-grained compacted mixtures (compare **Figures 4.5** and **4.7**). In addition, PLS allows an unlimited number of samples in the training dataset. In contrast, NNLS requires that the number of library spectra be less than or equal to the number of channels in the mixed spectrum. A third advantage is the ability to retrieve mineral abundances without a complete library of isolated, pure end-members. This could prove useful in cases where rocks contain phases that are difficult to isolate for spectral measurement; example phases include pigeonite [*Hamilton and Christensen*, 2000] and sericite [*paper 1*], which are underrepresented or absent from spectral libraries. As long as these phases can be quantified in the training set through other techniques (e.g., XRD, petrographic imaging), it should be possible to retrieve their abundance from the mixed spectrum of interest despite absence of spectral library data. The biggest practical limitation of PLS is the need to first develop a well-characterized training set of relevant mixtures. This requires either preparation of numerous synthetic mixtures and/or characterization of natural samples through independent quantitative techniques (e.g. XRD, petrographic imaging). A second limitation of PLS applied to TIR spectra is that, like NNLS, abundances cannot be retrieved for minerals that are spectrally transparent across much of the wavelength range, such as chlorides (e.g., [*Lane and Christensen*, 1998; *Baldridge et al.*, 2004]).

Last, as with NNLS, differences in spectral contrast within the training set, such as those that might arise if spectra of both coarse particulate mixtures and rocks are included, can affect the derived abundances from PLS (Supplementary Text S1). Ideal training sets for PLS would include spectra from samples of similar particle size or similar compaction. An exception to this would be the inclusion of samples which have unique features due to their particle size (for example, fine powders, which have transparency features that are not observable in coarse grained samples).

Though not investigated in this study, PLS might be applicable to *non-compacted* fine-grained (<60 μm) mixtures or to coated rocks, provided some portions of the wavelength range were dominated by surface reflections. For some non-compacted mixtures of only a few components, it is possible that this condition could be met. This is an area deserving more attention in future studies.

4.4.4 Implications for mineral abundance estimation on Martian surfaces

Results from our study indicate that the NNLS-modeled abundances of clays, in compacted fine-grained (<10-25 μm) mixtures are commonly underestimated. This differs somewhat from previous results using natural mudstones [*Michalski et al., 2006; Thorpe et al., 2015*], where clay abundances were commonly predicted to within 10% of the known, or in some cases, slightly overestimated [*Michalski et al., 2006*]. The differences may be related to differences in the host matrix (e.g., what other minerals are present in the mixtures, such as augite), or perhaps differences in bulk grain size. In any case, the possibility of underestimating clay abundances in fine-grained compacted mixtures is relevant to interpreting mineral abundances from known phyllosilicate-bearing regions from the higher spatial-resolution NIR imaging spectrometers CRISM and OMEGA. For example, from radiative transfer modeling of OMEGA NIR spectra, select regions of Mawrth Vallis exhibit modeled abundances as high as 65%; modeled abundances are as high as

35% in other locations in the southern highlands [*Poulet et al.*, 2008]. However, conventional linear least squares models of TES spectra show less than 15% of phyllosilicate at Mawrth Vallis and ~30% or less in the southern highlands [*McDowell and Hamilton*, 2009; *Michalski and Fergason*, 2009; *Michalski et al.*, 2010]. Though differences in spatial resolution are likely major contributors to these discrepancies, spatial resolution cannot fully account for the differences [*Viviano and Moersch*, 2013]. Our results demonstrate that clay abundances in some fine-grained compacted mixtures could be underestimated by ~10-40% in linear least squares models of TIR spectra.

More broadly, our study indicates that TIR spectra from very fine-grained sedimentary rocks (e.g. <~10 μm) cannot be modeled reliably with the conventional least squares methods [*Ramsey and Christensen*, 1998; *Rogers and Aharonson*, 2008]. But, PLS can be used to recover abundances from very fine-grained rocks to within +/- 10% (absolute) from TIR datasets, provided a suitable training set is available. Mini-TES observations of fine-grained rocks at Gusev crater and Meridiani Planum [*Christensen et al.*, 2004a; *Christensen et al.*, 2004b; *Grotzinger et al.*, 2005; *McLennan et al.*, 2005] could be ideal data sets in which to apply PLS. PLS could also potentially be applied to orbital observations, provided atmospheric components were first removed (e.g. [*Bandfield and Smith*, 2003]). Low-dust sedimentary deposits hosting phyllosilicates such as Mawrth Vallis, Jezero crater, and Eberswalde crater [*Ehlmann et al.*, 2008a; *Murchie et al.*, 2009; *Dehouck et al.*, 2010; *Milliken and Bish*, 2010; *Milliken et al.*, 2010; *Ansan et al.*, 2011; *Wray et al.*, 2011] would be ideal for analyzing mineral abundance with PLS, due to the likely mixture of both coarse and fine grains.

4.5 Conclusions

We characterized the thermal infrared spectral properties of compacted, very fine-grained (<10 μm) mineral mixtures of oligoclase, augite, calcite, montmorillonite and gypsum. Non-negative linear least squares minimization (NNLS) using spectra of pellets and powders of the end-member minerals was used to assess the linearity of spectral combination of fine-grained mixtures, by modeling mineral abundance of mixtures over the 350-1650 cm^{-1} spectral range. For the first time, we also applied a partial least squares (PLS) model to thermal emission spectra of synthetic mixtures and natural mudstones to assess its applicability for retrieving mineral abundances from to fine-grained rocks. We have made the following major observations and conclusions:

1. Notable differences between thermal infrared spectra of the sand and compacted powder (pellet) versions of minerals are present, both in terms of spectral contrast and spectral shape. These differences are likely due to an increased contribution of volume scattering in the compacted fine-grained material relative to that in the larger, optically thick sand grains (**Section 4.4.1**).

2. The NNLS-modeled abundances for all five minerals investigated are within ±10% of the known abundances for 39% of the mixtures. Model accuracy varies depending on the mineral and also on other mixture components (**Figure 4.5**). For oligoclase, augite and calcite, the modeled abundances are overestimated in most of the cases whereas for montmorillonite and gypsum, the modeled abundances are generally underestimated. However, these trends depend greatly on other components present in the mixture, and cannot be universally applied (**Section 4.4.4**). Results show that the relationships between known and modeled abundance follow non-linear curves. Drawing from the literature, we suggest the poor performance of NNLS is due to a combination

of transmission through small grains over portions of the wavelength range and multiple photon reflections in the volume.

3. The PLS method was able to accurately recover the known abundances (to within +/-10%) for 78-90% our synthetic mixtures. We suggest that the excellent agreement between known and modeled abundances is due to the higher *k* values that are typically found in the TIR range; because *k* is usually very high (>1) over some portion of the TIR range, combinations are linear over portions of the range.

4. The PLS method retrieved known abundances to within ±10% for 85% of the mudstone samples, with no more than three out of 14 samples falling outside this range. Modeled mica abundances are significantly improved using the PLS method, compared to NNLS.

5. Our study indicates that thermal infrared spectra from very fine-grained (<10 μm) rocks cannot be modeled reliably with NNLS. But, PLS can be used to recover abundances from very fine-grained rocks to within +/- 10% (absolute) from TIR datasets, provided a suitable training set is available. PLS could also potentially be applied to orbital observations, provided atmospheric components were first removed.

Acknowledgements

We thank Jacob Gardner and Kaitlin McIntosh for assistance with the sample preparation. We are grateful to Jun Huang and Christina Viviano-Beck for thorough and constructive reviews, which greatly improved this manuscript. We acknowledge funding from the NASA Mars Fundamental Research Program grant #NNX09AL22G to A. D. Rogers. All spectral data presented in this work are available in table form in the Supplementary information, and are also available upon request from the authors.

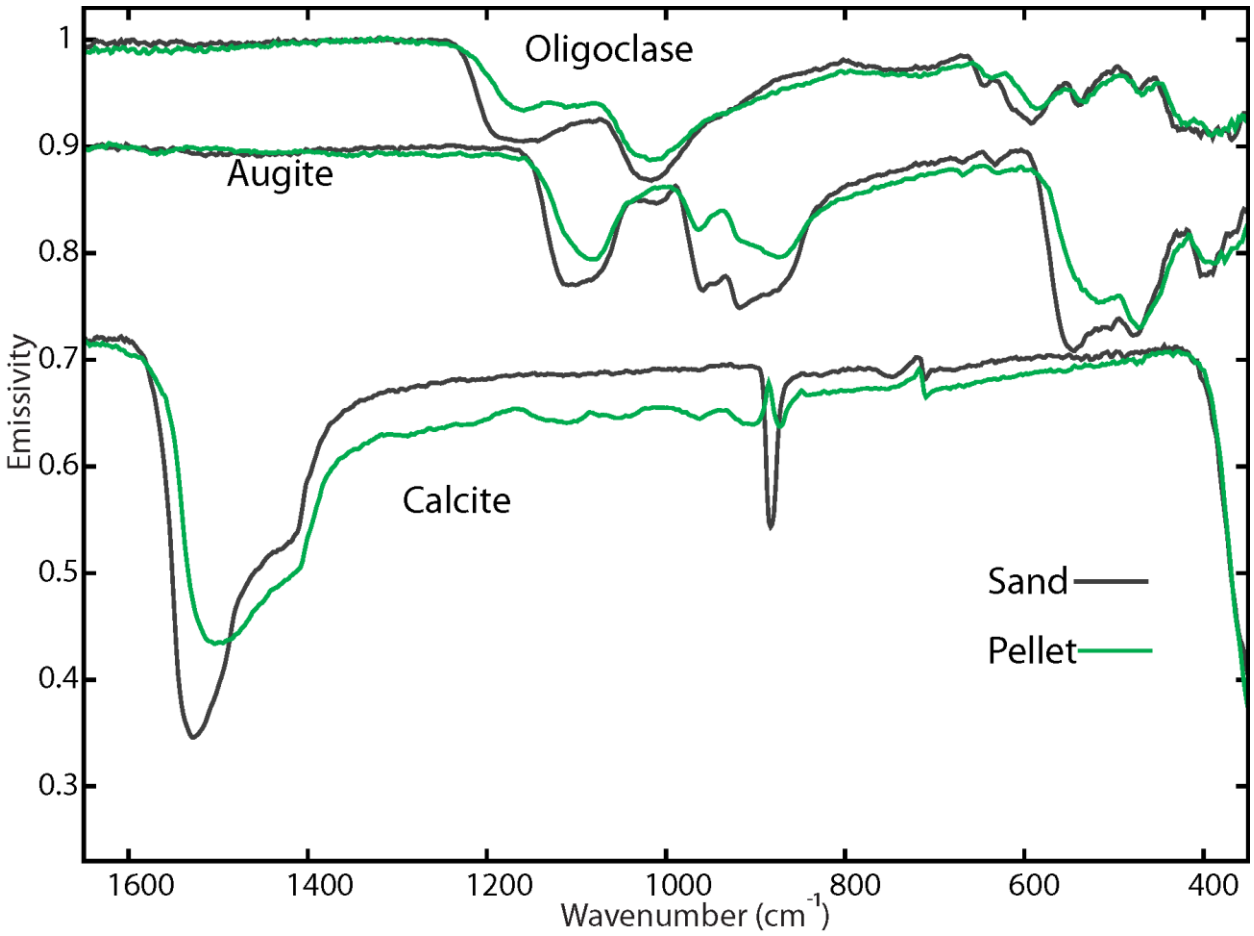

Figure 4.1 Spectral comparison of sand (500-841 µm) and pellet samples of oligoclase, augite and calcite. Spectral pairs are offset for clarity. No scaling factors were applied.

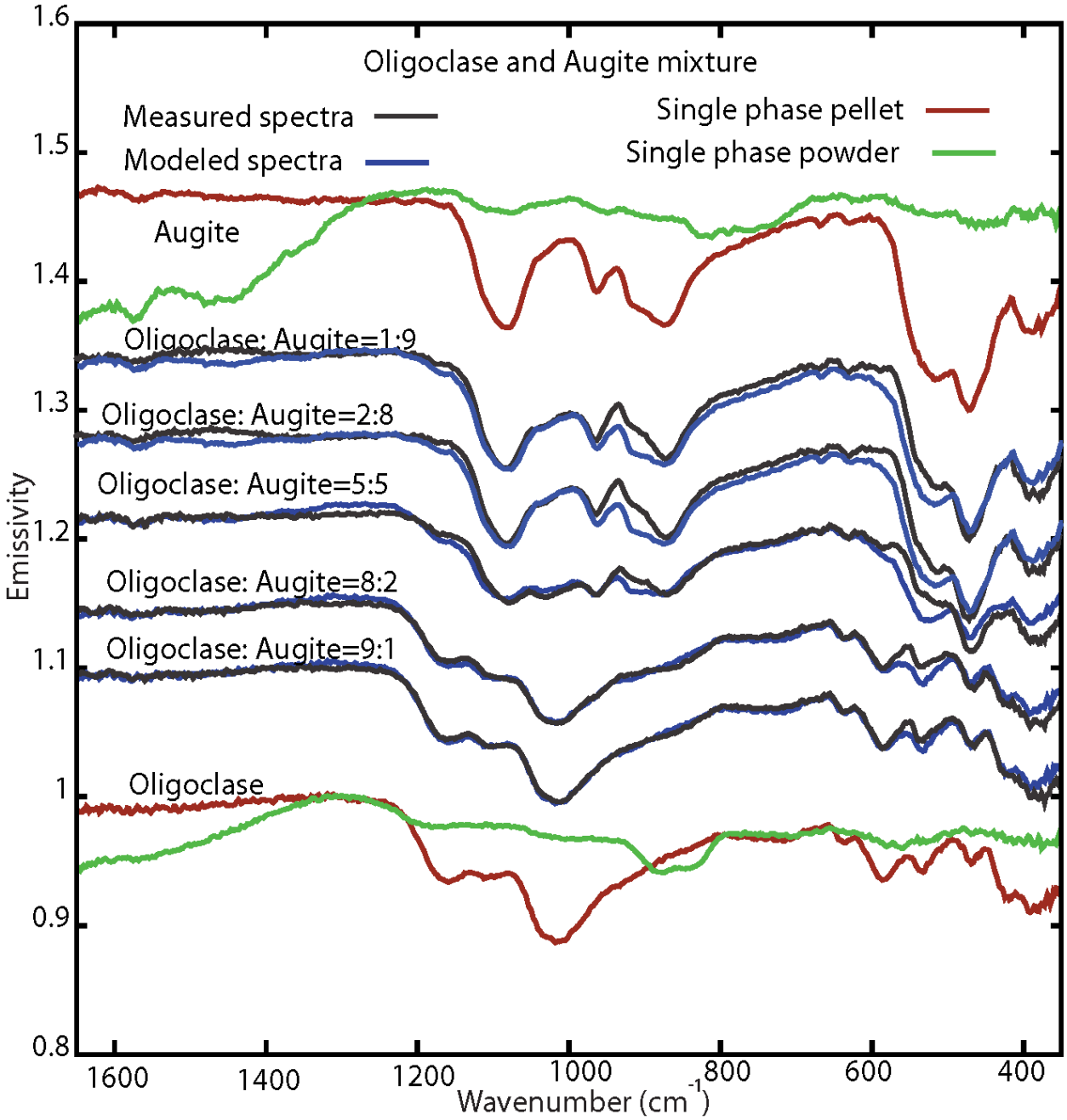

Figure 4.2 Measured and modeled spectra of oligoclase and augite compacted mixtures derived from NNLS. The mixtures were modeled with compacted oligoclase and compacted augite only. Both pellet and powder spectra of single phase end-members were plotted for comparison. Spectral pairs are offset for clarity. No scaling factors were applied.

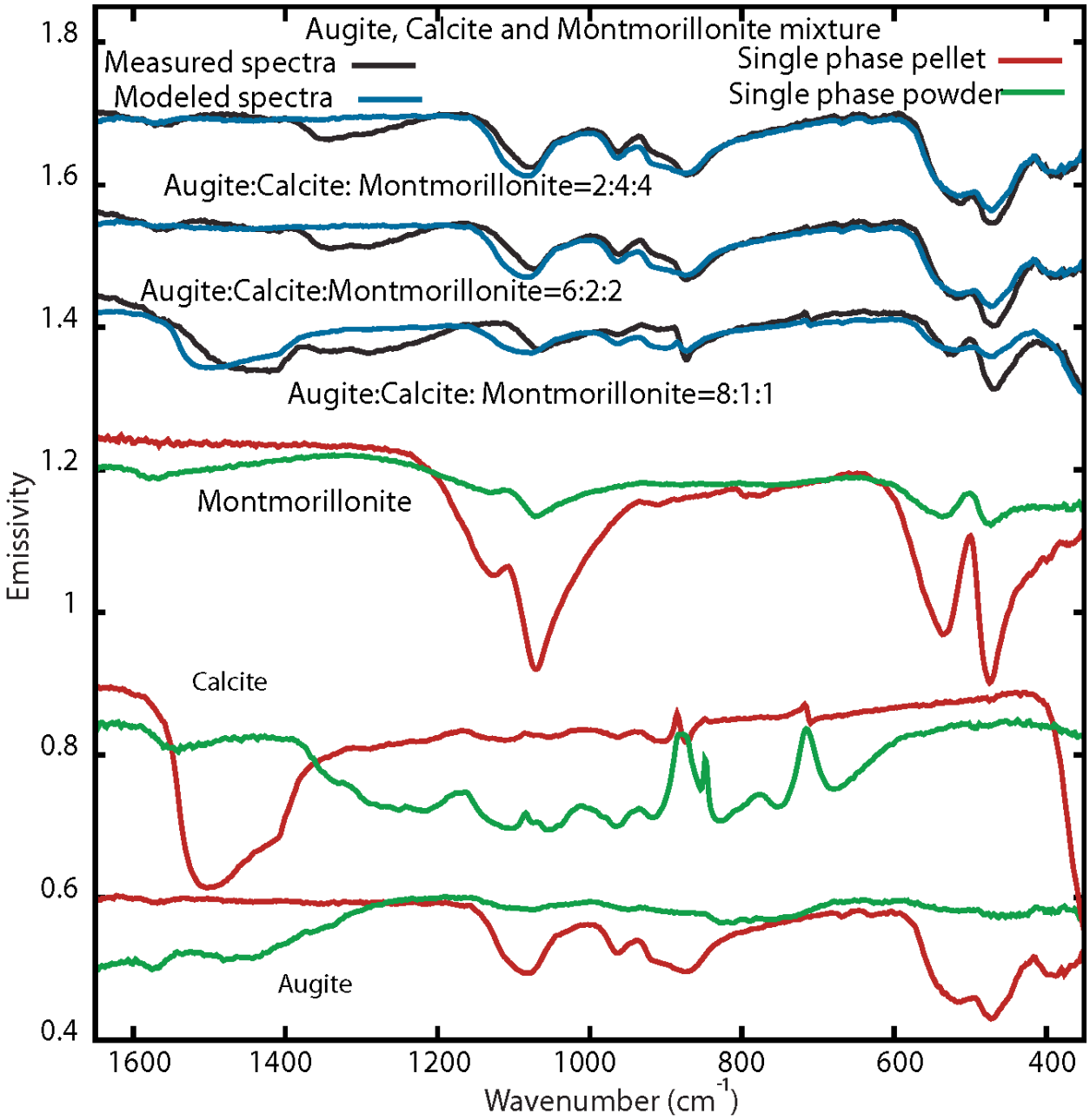

Figure 4.3 Measured and modeled spectra of augite, calcite and montmorillonite compacted mixtures from NNLS. The mixtures were modeled with compacted augite, calcite and montmorillonite only. Both pellet and powder spectra of single phase end-members were plotted for comparison. Spectra are offset for clarity. No scaling factors were applied.

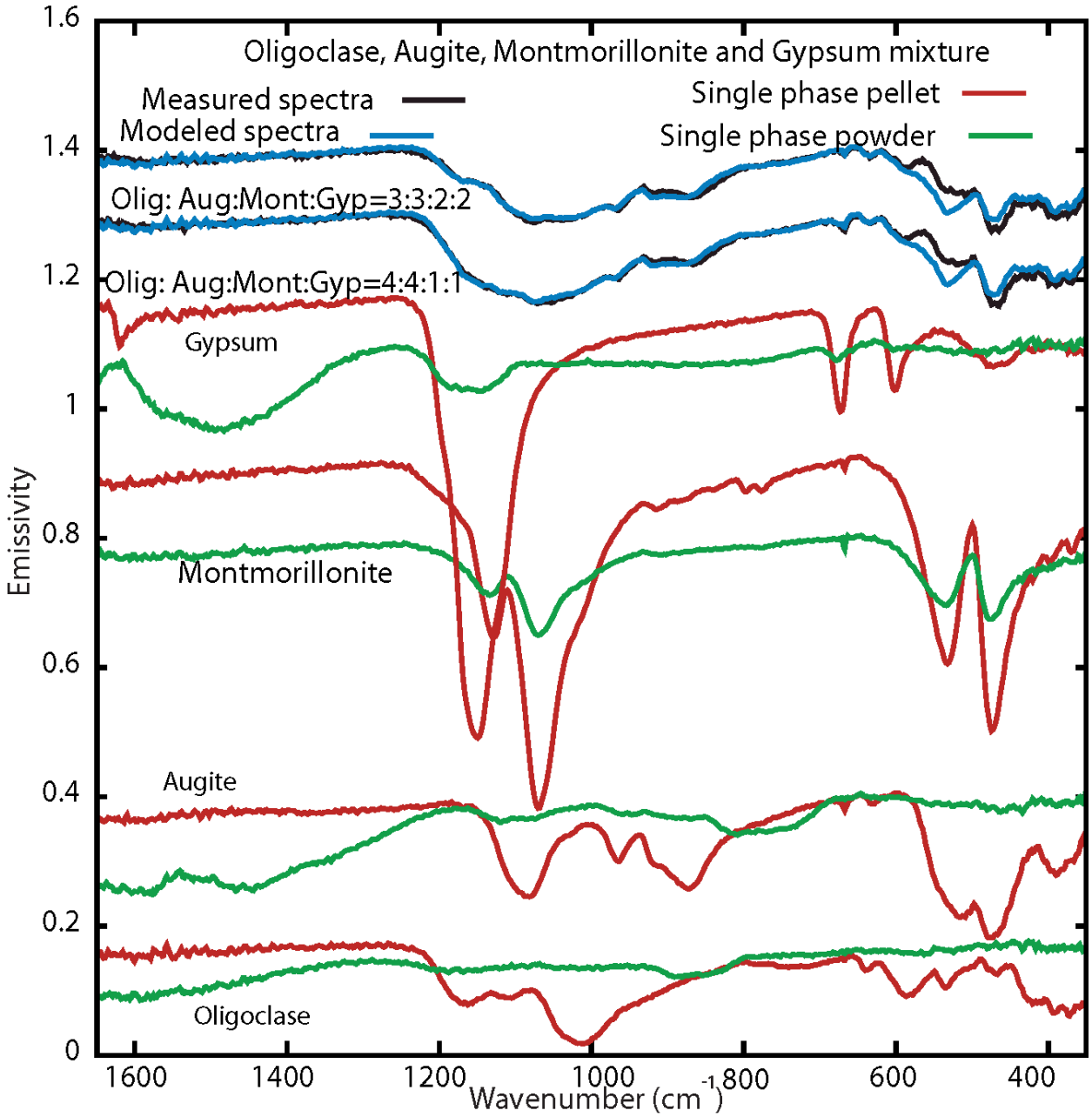

Figure 4.4 Measured and modeled spectra of oligoclase, augite, montmorillonite and gypsum compacted. mixtures from NNLS. Spectra of single phases were plotted for comparison. Spectral pairs are offset for clarity. No scaling factors were applied.

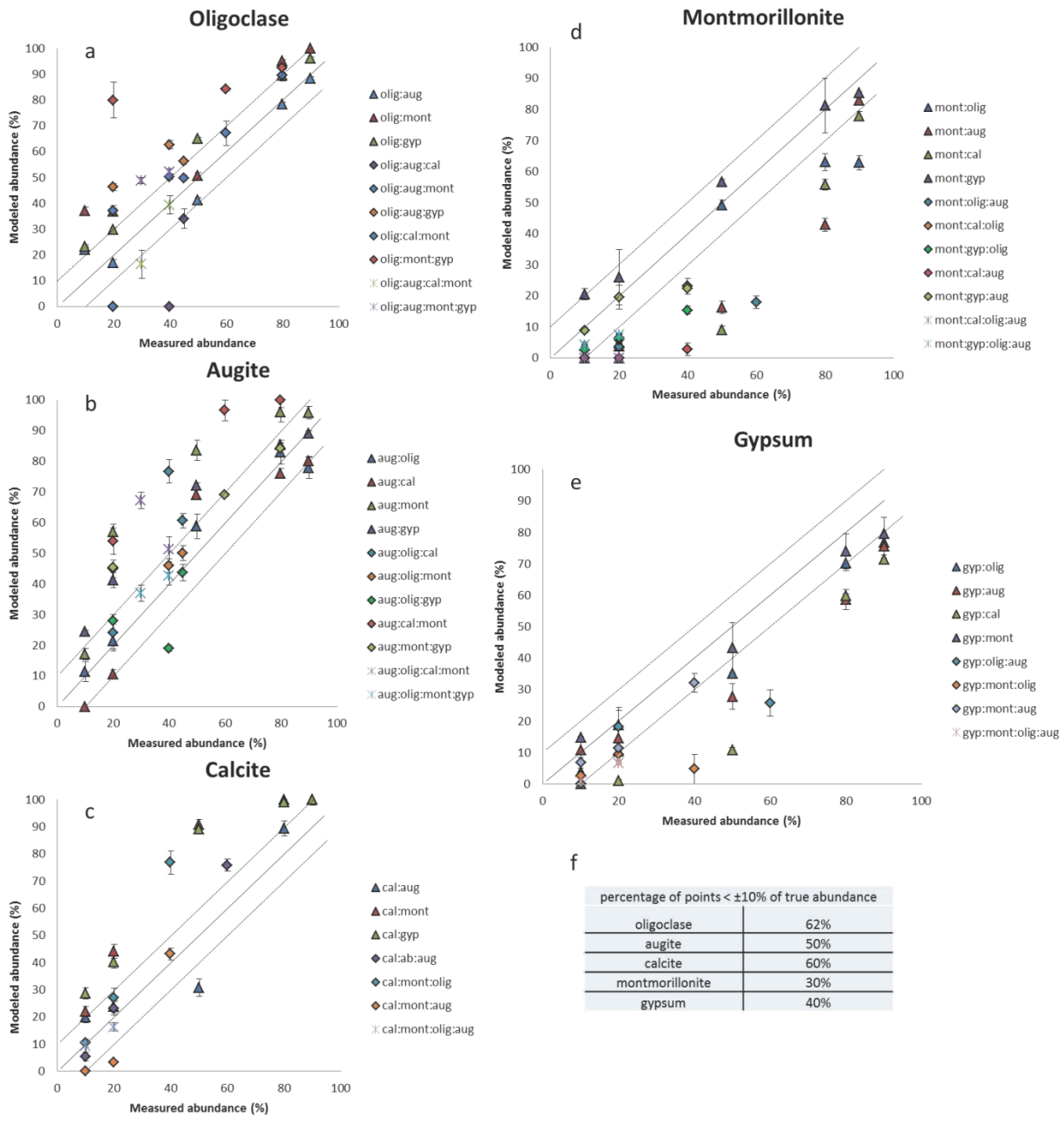

percentage of points < ±10% of true abundance	
oligoclase	62%
augite	50%
calcite	60%
montmorillonite	30%
gypsum	40%

Figure 4.5 Measured abundance and modeled abundance derived from NNLS for oligoclase (a), augite (b), calcite (c), montmorillonite (d) and gypsum (e), and percentage of points < ±10% of true abundance (f). The solid line represents a perfect correspondence between known abundance and NNLS modeled abundance, and the dashed lines are ±10% from the 1:1 correspondence line. The error bars are statistical errors from NNLS [*Rogers and Aharonson*, 2008].

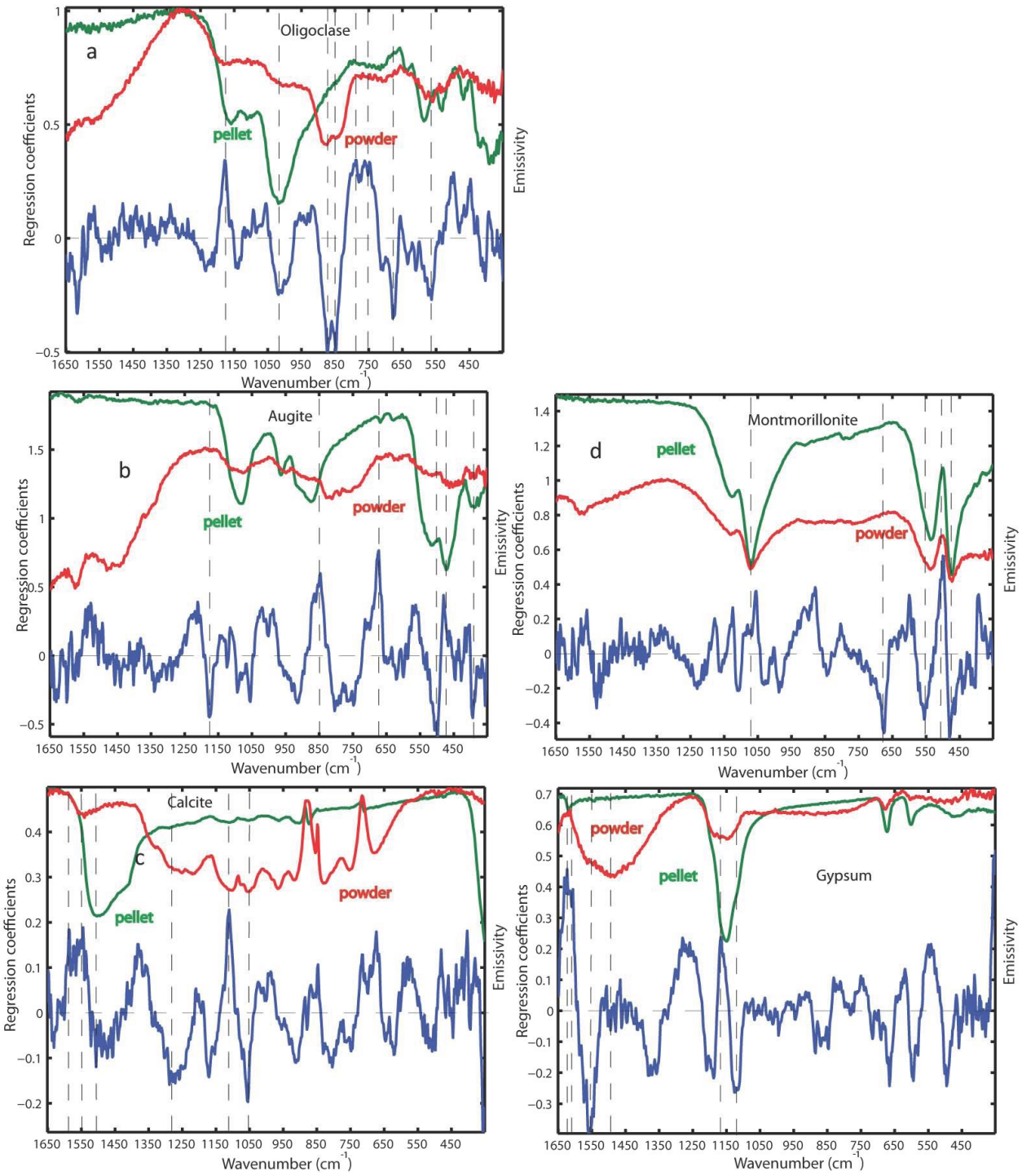

Figure 4.6 Regression coefficients derived from PLS for oligoclase (a), augite (b), calcite (c), montmorillonite (d) and gypsum (e). The blue lines are regression coefficients for each mineral. Spectra of single phases were plotted for comparison and offset for clarity. No scaling or offset factors were applied for regression coefficients. Vertical dashed lines indicate the strongest regression coefficients and/or other features discussed in the text. Vertical dash lines are strongest regression coefficients and emissivity absorption features. Horizontal lines are zero reference for regression coefficients.

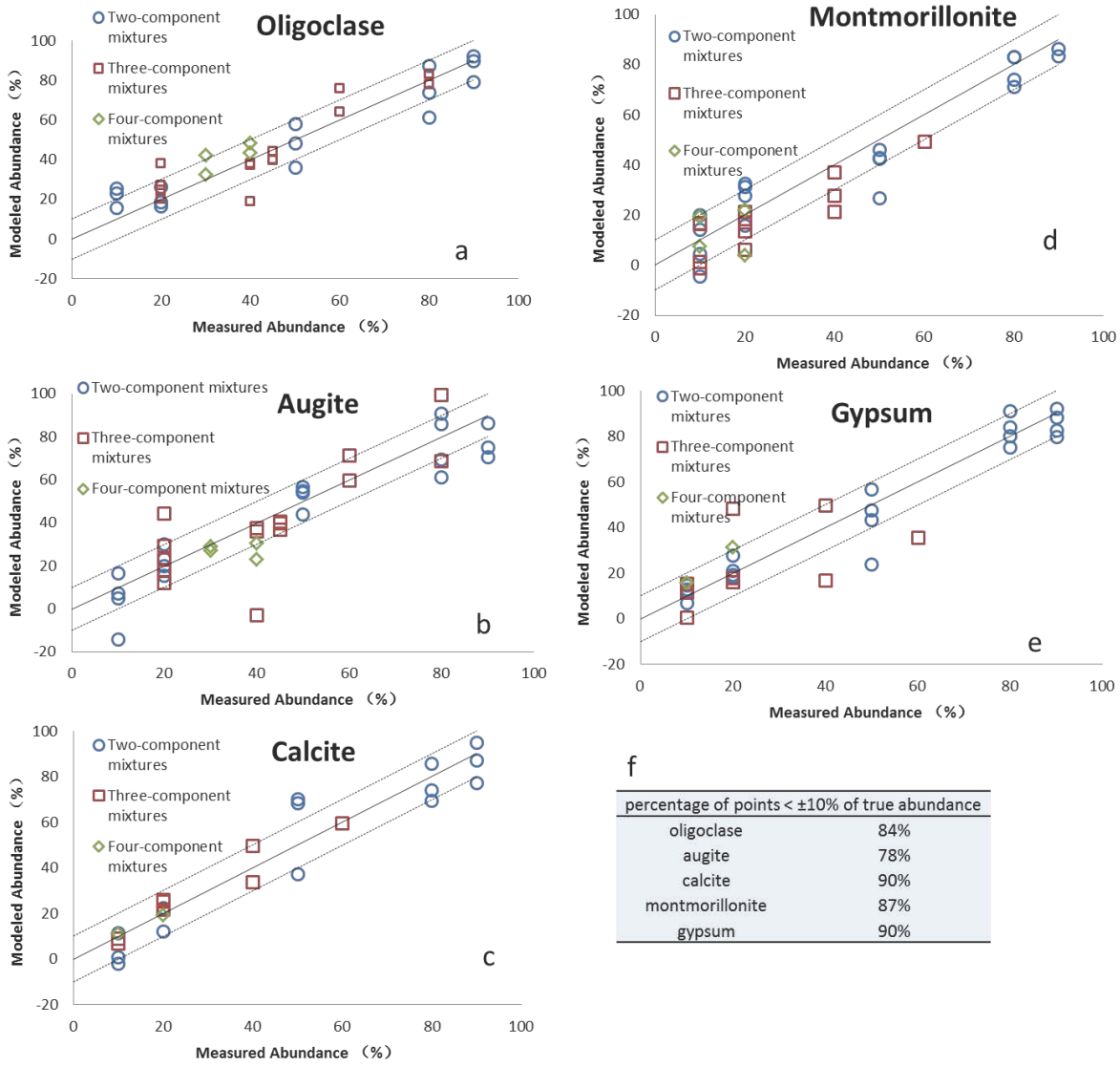

f

percentage of points < ±10% of true abundance	
oligoclase	84%
augite	78%
calcite	90%
montmorillonite	87%
gypsum	90%

Figure 4.7 Measured abundance and modeled abundance derived from PLS for oligoclase (a), augite (b), calcite (c), montmorillonite (d) and gypsum (e), and percentage of points < ±10% of true abundance (f). The solid line represents a perfect correspondence between known abundance and PLS modeled abundance, and the dashed lines are ±10% from the 1:1 correspondence line.

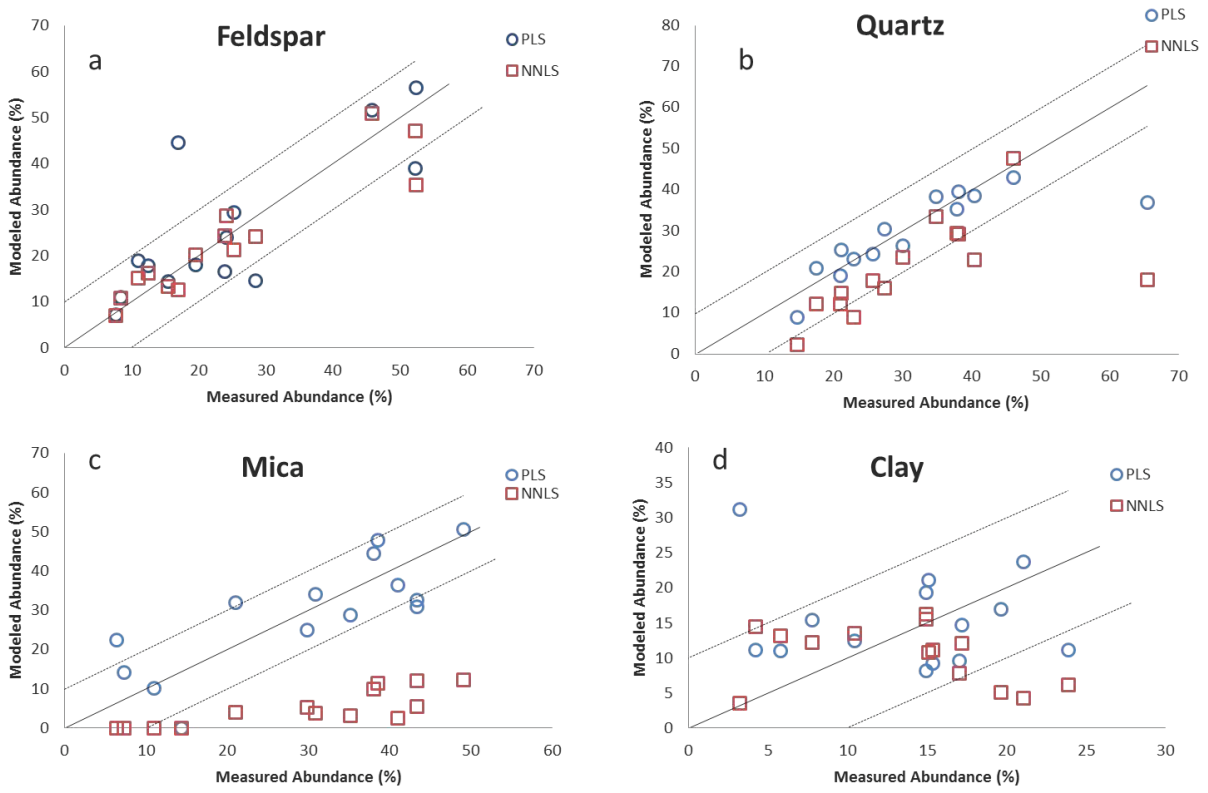

Figure 4.8 Measured XRD abundances and Modeled abundance derived from PLS for feldspar (a), quartz (b), mica (c) and clays (d) for mudstone samples. Modeled abundance derived from NNLS were plotted for comparison. The solid line represents a perfect correspondence between known abundance and modeled abundance, and the dashed lines are ±10% from the 1:1 correspondence line.

Table 4.1 Samples and particle size distributions.

	10th percentile	20th percentile	50th percentile	80th percentile	90th percentile
oligoclase	0.9μm	1.4μm	2.9μm	5.5μm	7.8μm
augite	0.8μm	1.7μm	4.1μm	7.3μm	9.4μm
calcite	0.9μm	1.3μm	2.5μm	4.9μm	7.5μm
gypsum	4.8μm	10.0μm	23.7μm	45.1μm	62.2μm
montmorillonite	0.9μm	1.4μm	2.8μm	6.6μm	17.9μm

Note: 1. Oligoclase (WAR-0234), Augite (WAR-6474), Calcite (WAR-1604),Montmorillonite (SWy-1),Gypsum (CAS-10101414)

2. The median grain size of montmorillonite, derived from laser diffraction, is larger than expected for pure clay.This may be due to either particle flocculation during measurement [Sperazza et al., 2004], or possibly larger-grained impurities [Chipera and Bish, 2001].

3. Oligoclase and augite compositions were confirmed with electron microprobe. Calcite and gypsum samples are spectrally indistinguishable from well characterized samples in Lane and Christensen [1997] and Lane [2007], confirming the quality of these samples. The montmorillonite sample was characterized using X-ray diffraction, and contains ~6% quartz. No other impurities were detected.

Table 4.2 Synthetic mineral mixture proportions.

Mixtures	Proportion (vol%)
oligoclase:augite	10:90, 20:80, 50:50, 80:20, 90:10
oligoclase:montmorillonite	10:90, 20:80, 50:50, 80:20, 90:10
oligoclase:gypsum	10:90, 20:80, 50:50, 80:20, 90:10
augite:montmorillonite	10:90, 20:80, 50:50, 80:20, 90:10
augite:calcite	10:90, 20:80, 50:50, 80:20, 90:10
augite:gypsum	10:90, 20:80, 50:50, 80:20, 90:10
montmorillonite:calcite	10:90, 20:80, 50:50, 80:20, 90:10
montmorillonite:gypsum	10:90, 20:80, 50:50, 80:20, 90:10
calcite:gypsum	10:90, 20:80, 50:50, 80:20, 90:10
oligoclase:augite:calcite	20:20:60, 40:40:20, 45:45:10
oligoclase:augite:montmorillonite	20:20:60, 40:40:20, 45:45:10
oligoclase:augite:gypsum	20:20:60, 40:40:20, 45:45:10
oligoclase:montmorillonite:gypsum	80:10:10, 60:20:20, 20:40:40
augite:montmorillonite:gypsum	80:10:10, 60:20:20, 20:40:40
oligoclasemontmorillonite:calcite	80:10:10, 60:20:20, 20:40:40
augite:montmorillonite:calcite	80:10:10, 60:20:20, 20:40:40
oligoclase:augite:montmorillonite:calcite	40:40:10:10, 30:30:20:20
oligoclase:augite:montmorillonite:gypsum	40:40:10:10, 30:30:20:20

Table 4.3 Modeled abundance derived from PLS for mudstones.

Sample Label	Mineral abundance from XRD				PLS modeled Abundance				NNLS modeled Abundance			
	Felds par	Quartz	Clay	Mica	Felds par	Quartz	Clay	Mica	Felds par	Quartz	Clay	Mica
sm-75-165	47.13	12.17	4.34	0.00	39.02	20.95	23.79	14.22	47.13	12.17	4.34	0.00
sm-75-103	21.26	14.84	12.08	3.25	29.55	25.32	14.73	28.81	21.26	14.84	12.08	3.25
sm-75-104	20.21	9.02	15.62	2.57	18.11	23.18	19.35	36.53	20.21	9.02	15.62	2.57
sm-75-105	51.01	12.30	5.13	0.00	51.72	19.11	16.98	10.19	51.01	12.30	5.13	0.00
sm-75-107	35.35	2.27	6.23	0.00	56.62	9.04	11.16	22.42	35.35	2.27	6.23	0.00
sm-75-134	28.67	33.45	13.50	5.27	24.03	38.31	12.47	24.92	28.67	33.45	13.50	5.27
sm-75-140	24.40	22.89	14.45	3.91	16.56	38.51	11.17	34.04	24.40	22.89	14.45	3.91
sm-75-158	12.64	18.17	3.52	0.00	44.59	37.03	31.21	0.00	12.64	18.17	3.52	0.00
sm-75-113	16.25	29.25	13.19	5.62	17.98	39.47	11.02	30.84	16.25	29.25	13.19	5.62
sm-75-120	7.10	29.41	11.18	11.47	7.33	35.35	9.27	47.89	7.10	29.41	11.18	11.47
sm-75-142	10.83	15.98	16.26	12.33	10.99	30.37	8.25	50.61	10.83	15.98	16.26	12.33
sm-75-115	15.15	23.53	10.86	12.07	18.99	26.43	21.12	32.68	15.15	23.53	10.86	12.07
sm-75-117	13.44	47.69	7.84	4.04	14.41	42.92	9.61	31.99	13.44	47.69	7.84	4.04
sm-75-123	24.29	17.90	12.22	10.06	14.61	24.38	15.42	44.58	24.29	17.90	12.22	10.06

Text 4.S1. Effect of spectral contrast on derived abundances

The depth of fundamental absorptions (restrahlen bands) in thermal emission spectra is affected by particle size; for example, coarse grained sands exhibit lower spectral contrast than rocks [e.g., *Christensen et al.*, 2000]. Thus in this section, we address the effect of variable spectral contrast on the derived abundances. Specifically, we ask, 1) how does variable spectral contrast between the training set and test spectrum affect the modeled abundances, and 2) how does variable spectral contrast within the training set affect the modeled abundances? To address the first question, we adjusted the spectral contrast of all of the training spectra in Table 2 by 150%, and then recalculated the regression coefficients and modeled abundances. We found that the differences between modeled abundances from the original and adjusted training set were negligible, with a mean difference of 2 ± 3% (**Table 4.S3**). To investigate the effect of varying spectral contrast within the training set, we adjusted the contrast of ~20% of the training set by 150%, and recalculated the regression coefficients and modeled abundances. In this case, we found that the modeled abundances differed from the original by 4 ± 4% (**Table 4.S3**). The number of possible combinations of mixture composition and spectral contrast prohibits a complete assessment of the effect of variable spectral contrast; however, this preliminary analysis demonstrates that variable spectral contrast within the training set can have an effect on modeled abundance. This suggests that, while the training set need not have the same spectral contrast as the unknown spectrum, the ideal training set would have minimal variability in particle size or compaction. For example, pressed pellets and rocks have similar compaction and thus should have similar contrast. But coarse particulate sands have reduced spectral contrast compared to rocks, and thus mixtures of rocks and coarse particulate sands in training sets should be avoided. An exception to this notion of uniform particle size would be the inclusion of fine-grained powders, which have unique spectral features due to grain transparency (e.g. see **Section 4.1** of the main article) that are not accounted for by coarse-grained particulates or hand samples.

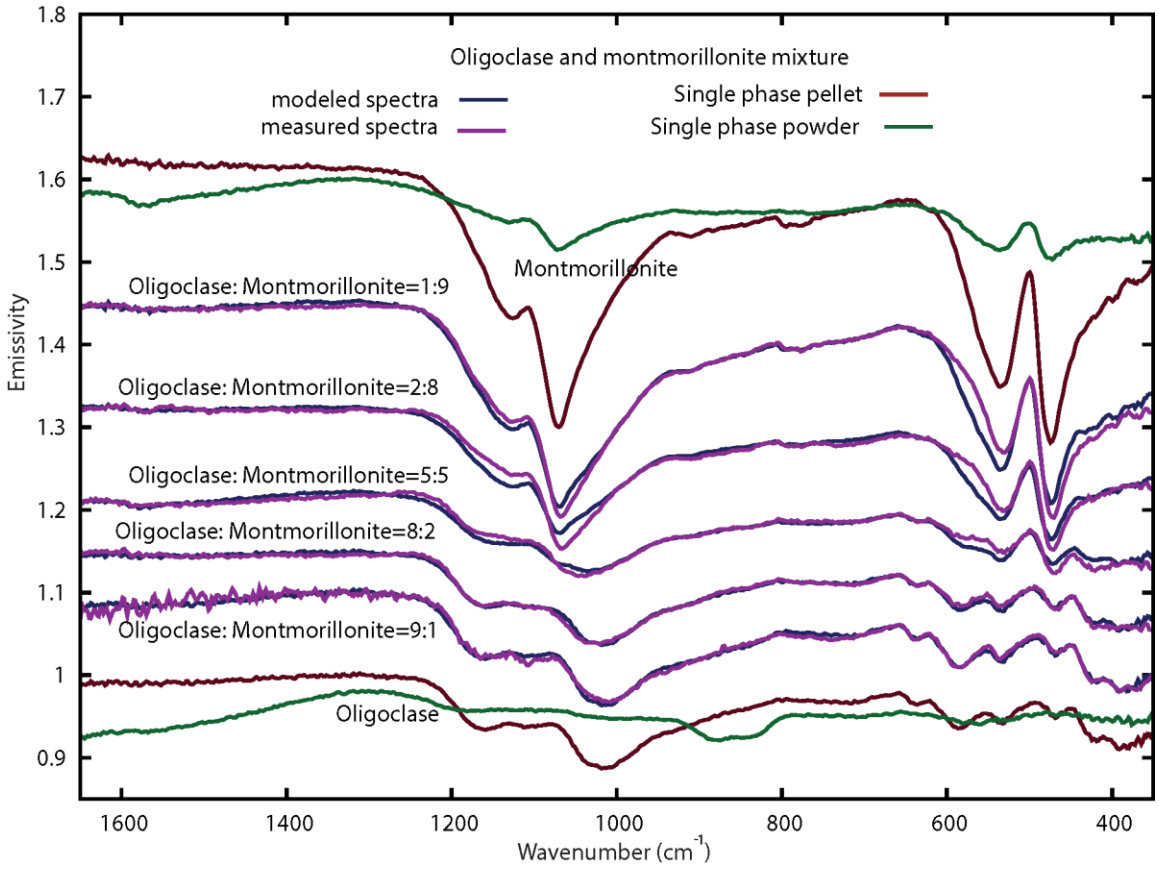

Figure 4.S1 Measured and modeled spectra of oligoclase and montmorillonite mixtures derived from NNLS. Spectra of single phase were plotted for comparison. Spectra are offset for clarity. No scaling factors were applied.

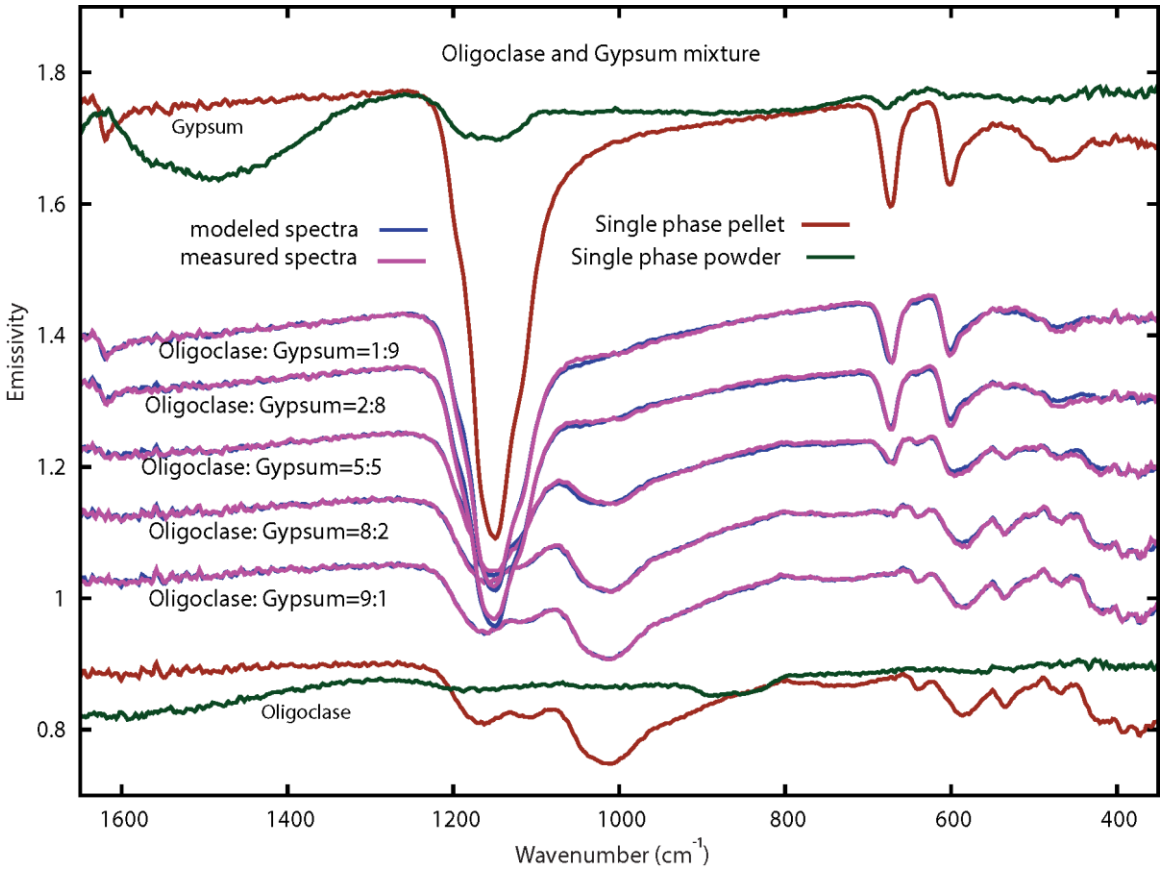

Figure 4.S2 Measured and modeled spectra of oligoclase and gypsum mixtures derived from NNLS. Spectra of single phase were plotted for comparison. Spectra are offset for clarity. No scaling factors were applied.

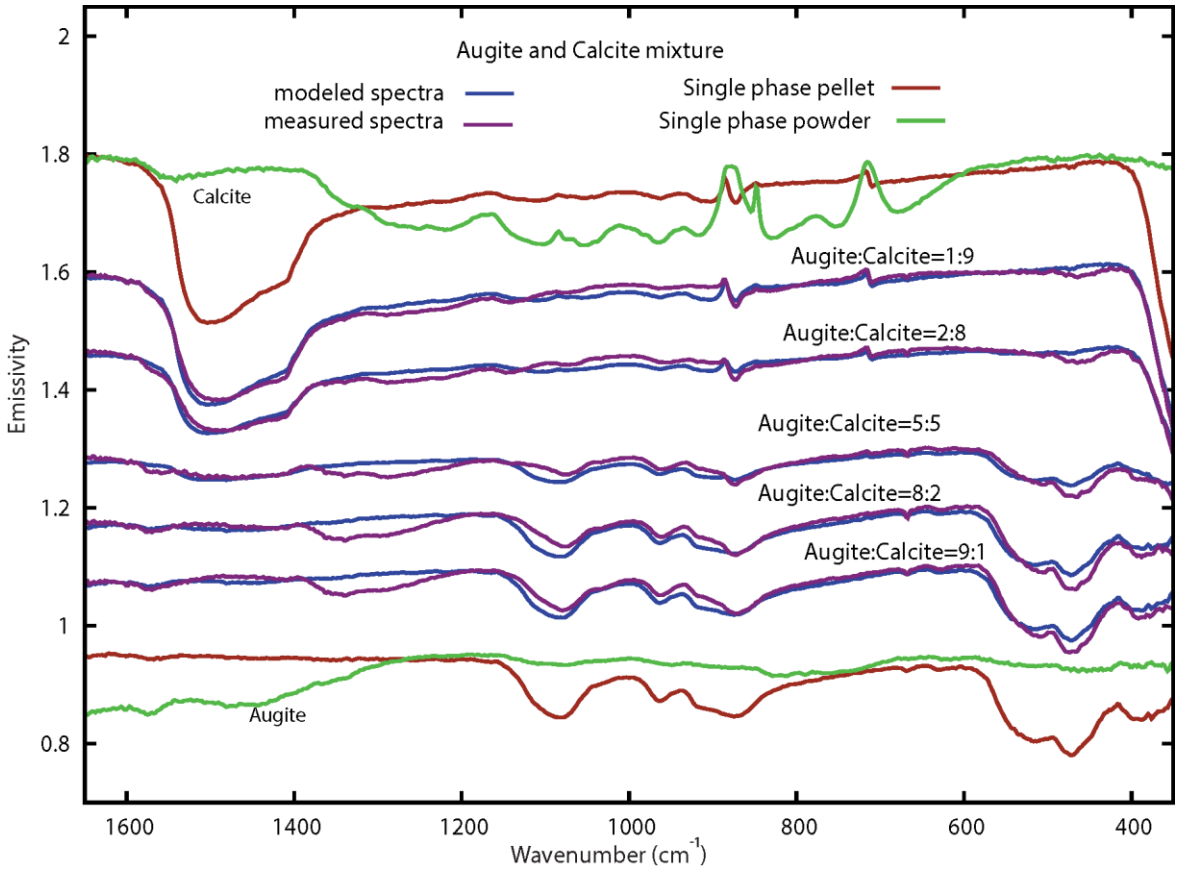

Figure 4.S 3 Measured and modeled spectra of augite and calcite mixtures derived from NNLS. Spectra of single phase were plotted for comparison. Spectra are offset for clarity. No scaling factors were applied.

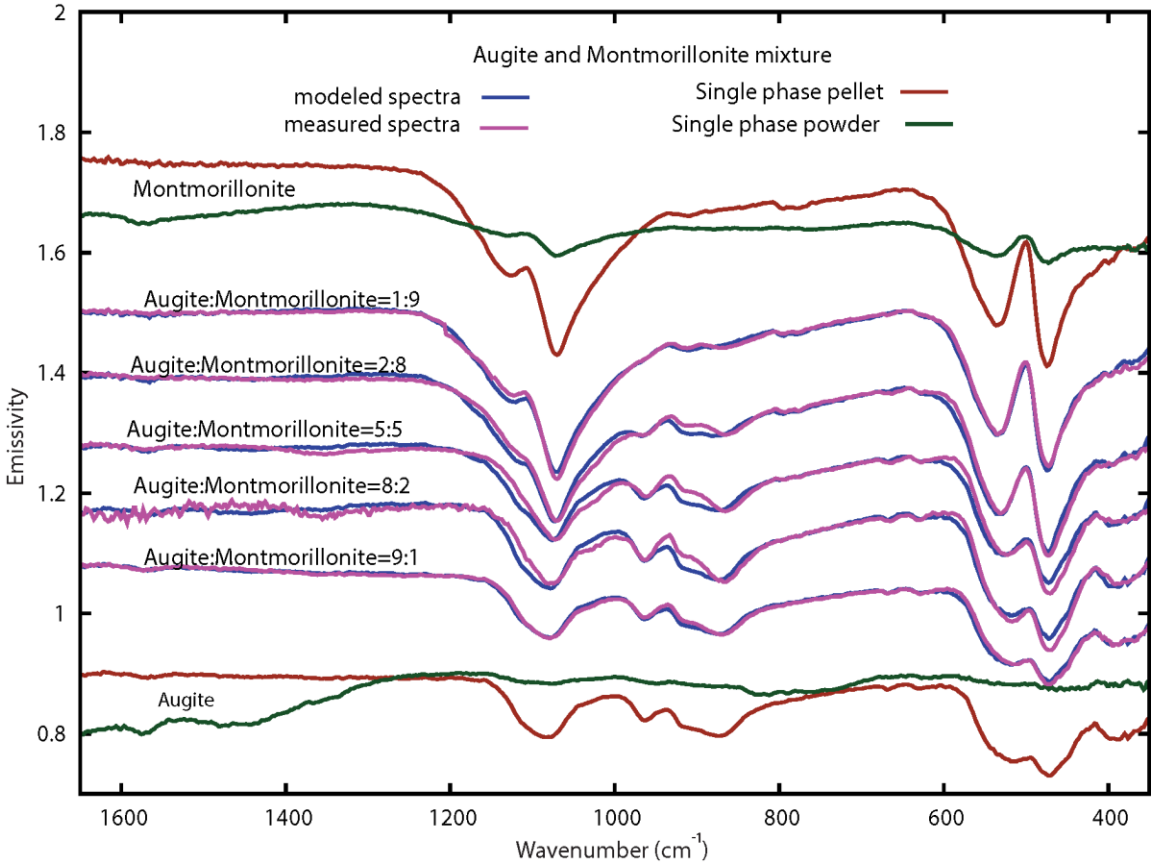

Figure 4.S4 Measured and modeled spectra of augite and montmorillonite mixtures derived from NNLS. Spectra of single phase were plotted for comparison. Spectra are offset for clarity. No scaling factors were applied.

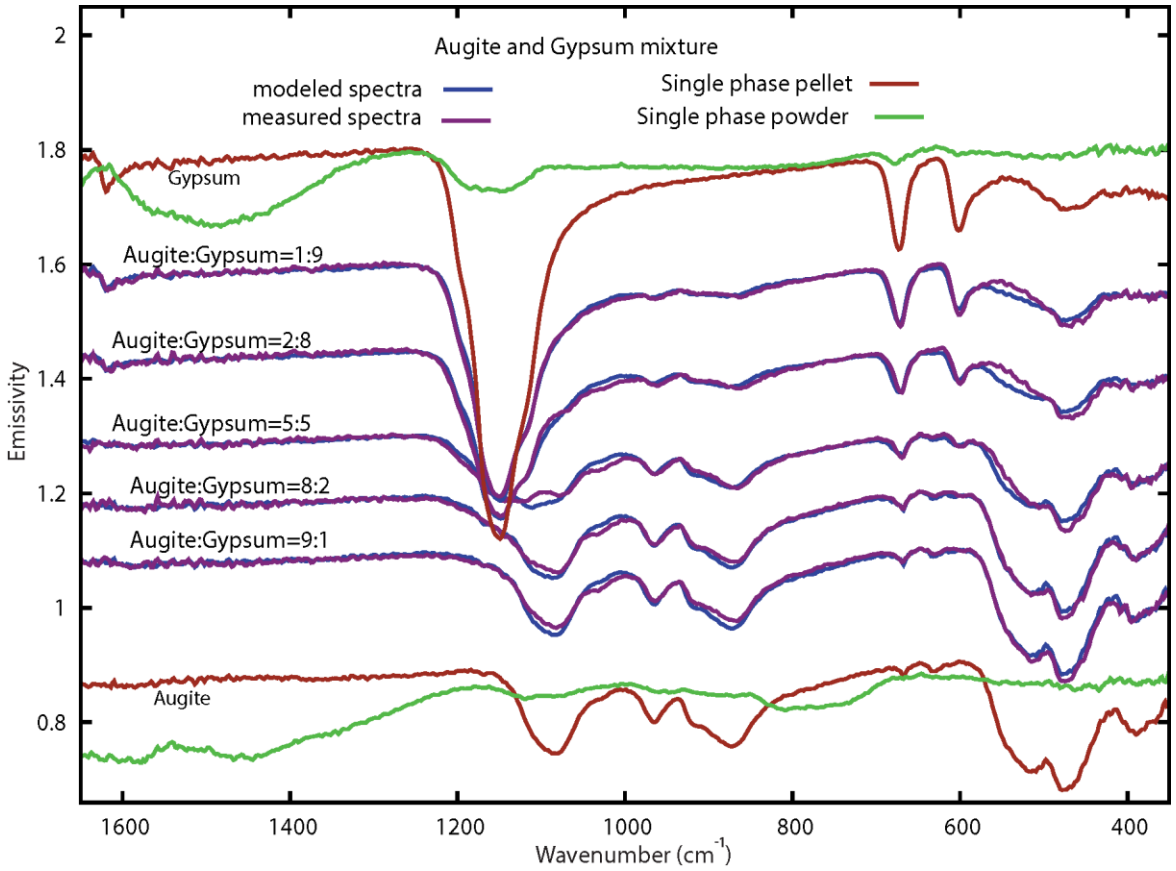

Figure 4.S5 Measured and modeled spectra of augite and gypsum mixtures derived from NNLS. Spectra of single phase were plotted for comparison. Spectra are offset for clarity. No scaling factors were applied.

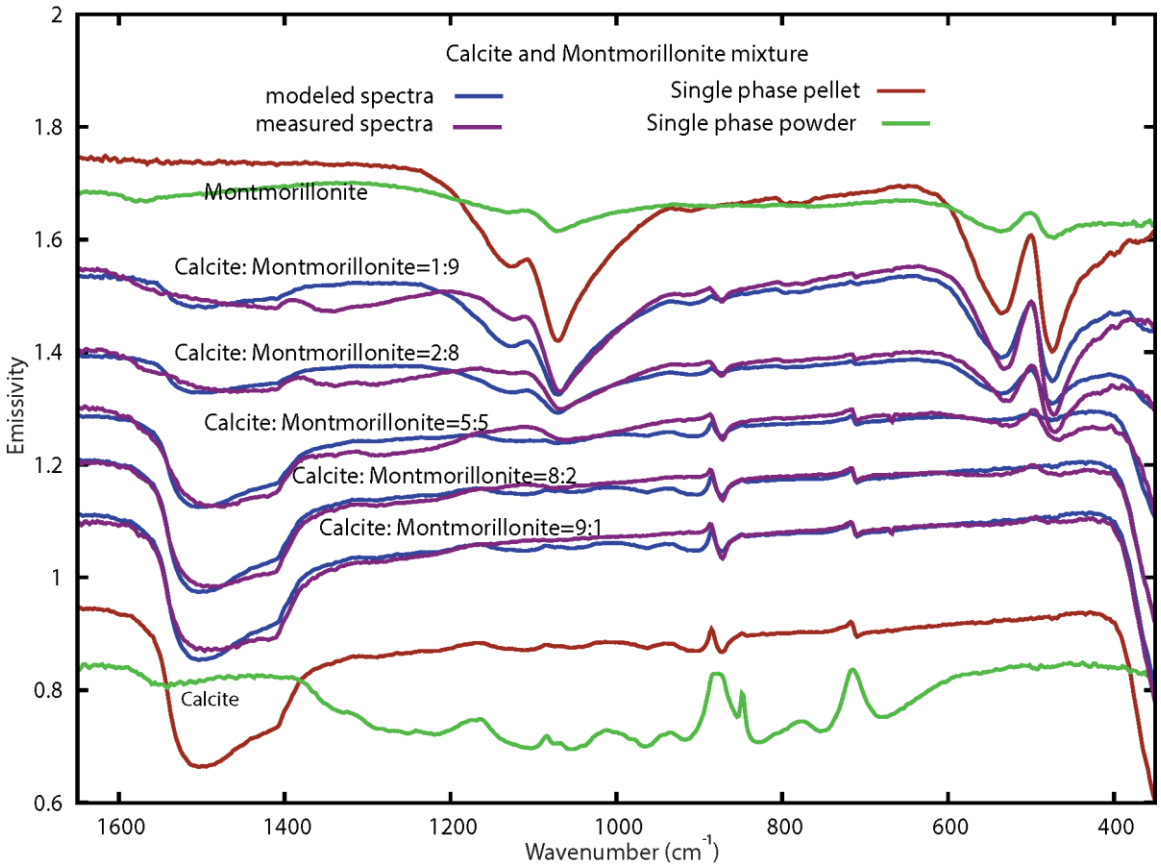

Figure 4.S6 Measured and modeled spectra of calcite and montmorillonite mixtures derived from NNLS. Spectra of single phase were plotted for comparison. Spectra are offset for clarity. No scaling factors were applied.

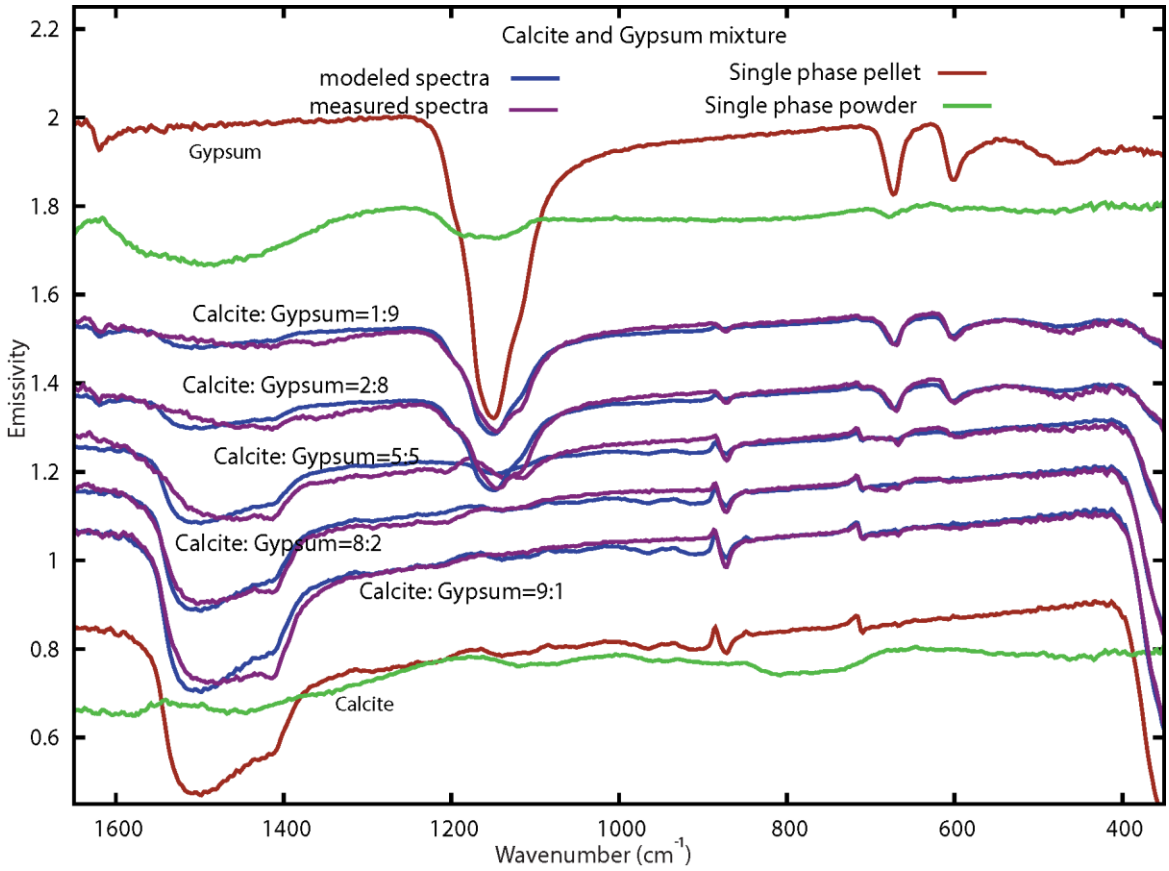

Figure 4.S7 Measured and modeled spectra of calcite and gypsum mixtures derived from NNLS. Spectra of single phase were plotted for comparison. Spectra are offset for clarity. No scaling factors were applied.

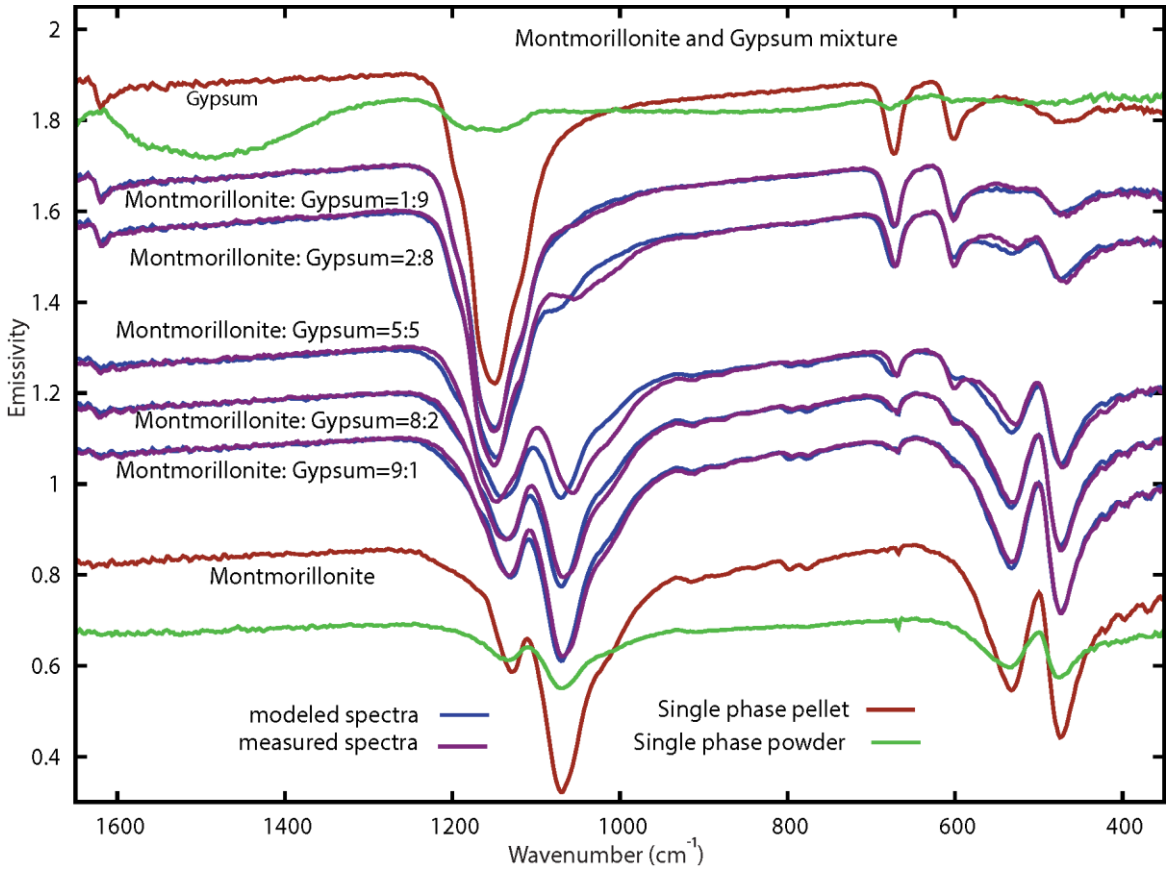

Figure 4.S8 Measured and modeled spectra of montmorillonite and gypsum mixtures derived from NNLS. Spectra of single phase were plotted for comparison. Spectra are offset for clarity. No scaling factors were applied.

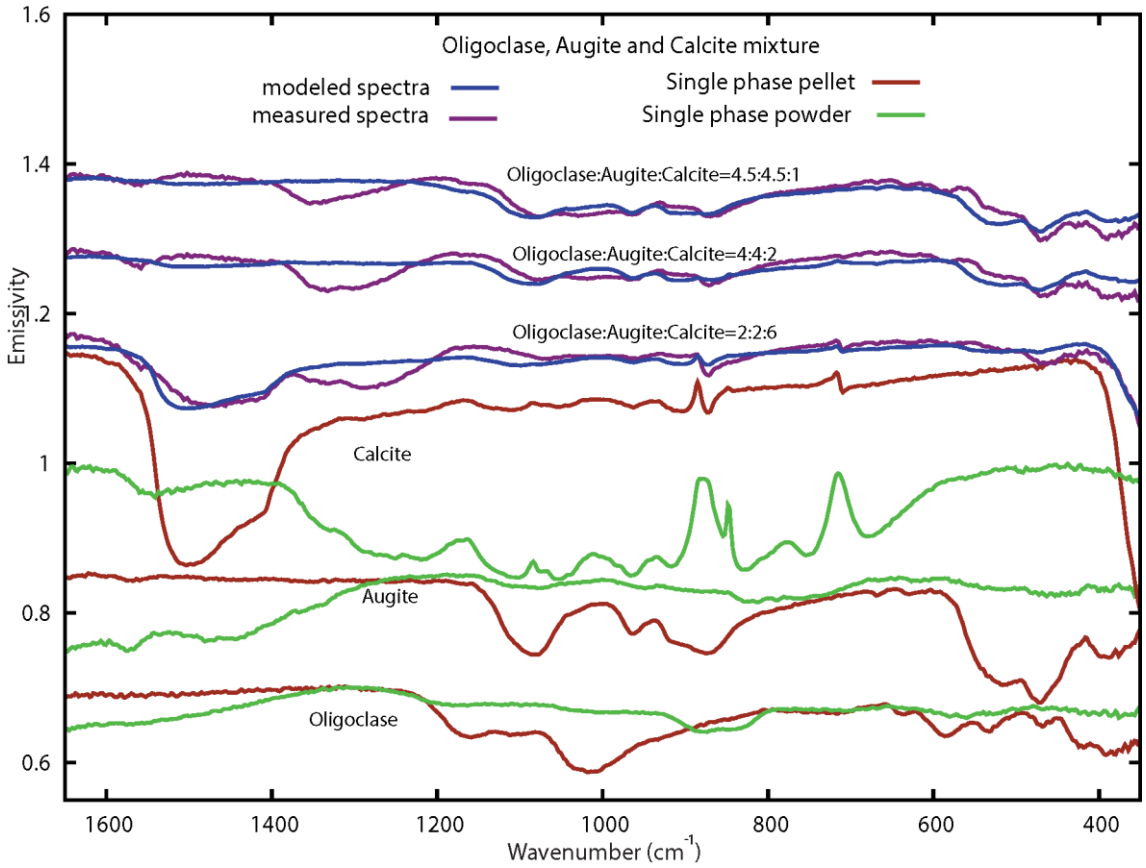

Figure 4.S9 Measured and modeled spectra of oligoclase, augite and calcite mixtures derived from NNLS. Spectra of single phase were plotted for comparison. Spectra are offset for clarity. No scaling factors were applied.

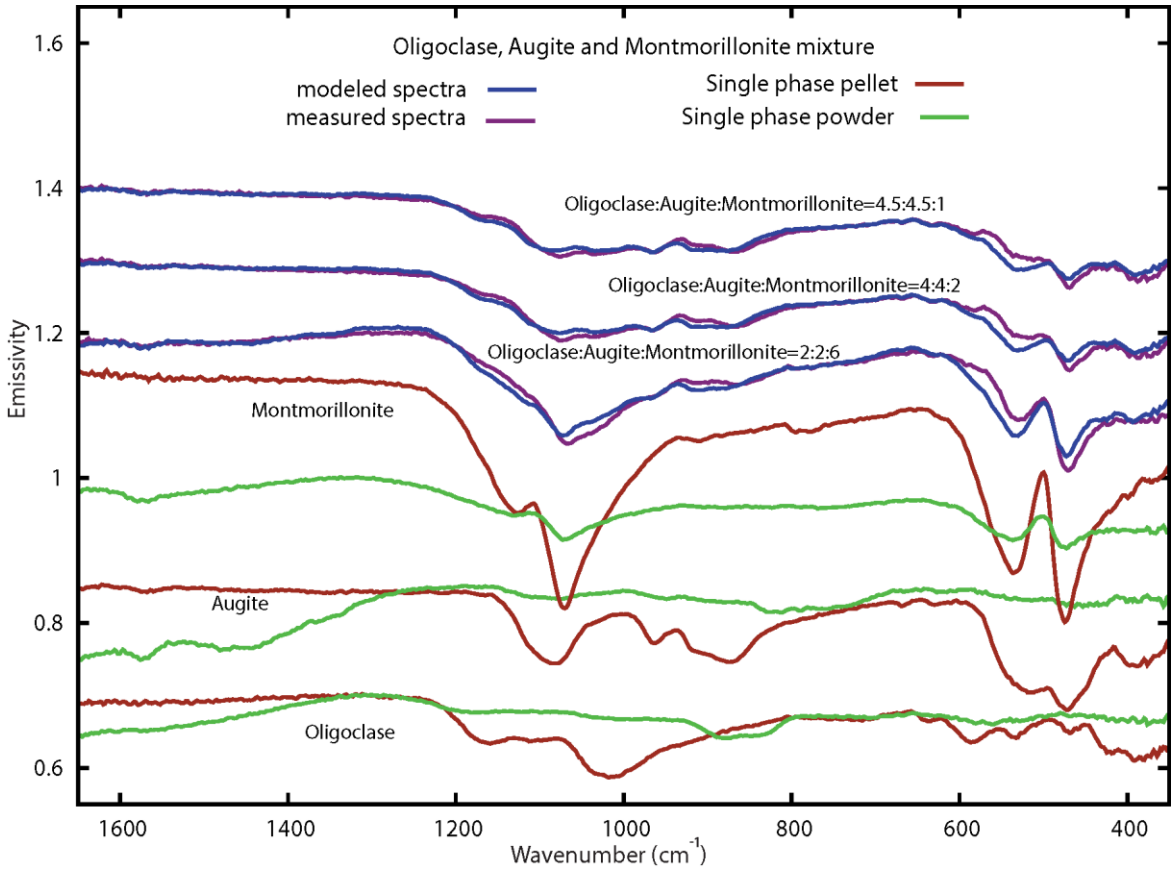

Figure 4.S10 Measured and modeled spectra of oligoclase, augite and montmorillonite mixtures derived from NNLS. Spectra of single phase were plotted for comparison. Spectra are offset for clarity. No scaling factors were applied.

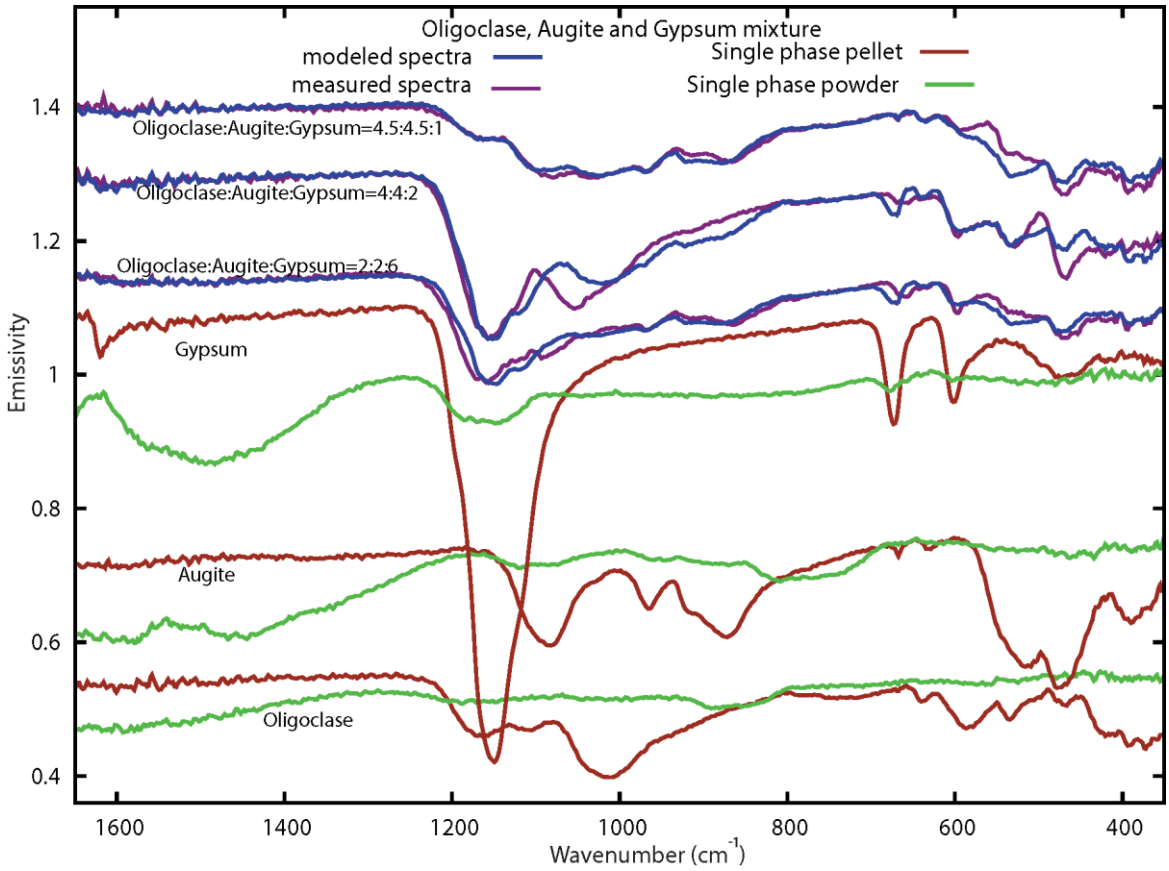

Figure 4.S11 Measured and modeled spectra of oligoclase, augite and gypsum mixtures derived from NNLS. Spectra of single phase were plotted for comparison. Spectra are offset for clarity. No scaling factors were applied.

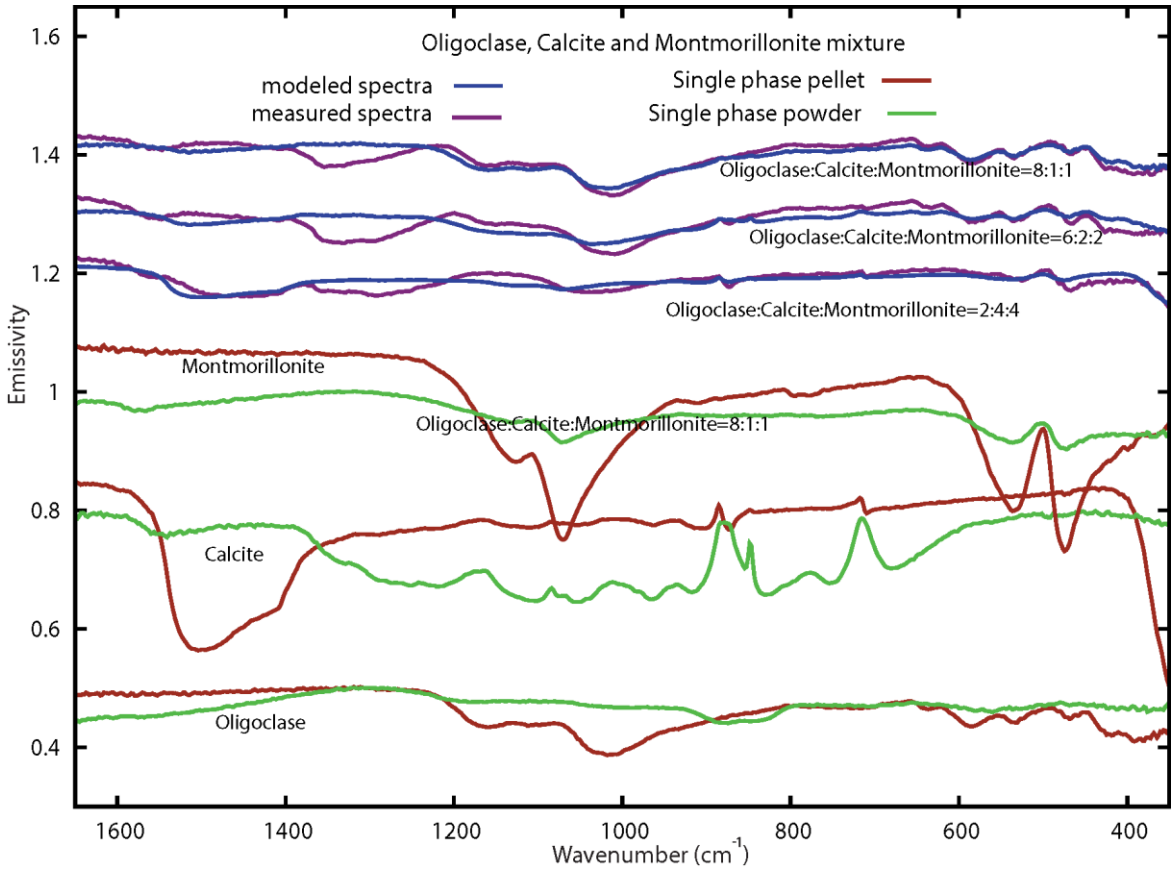

Figure 4.S12 Measured and modeled spectra of oligoclase, calcite and montmorillonite mixtures derived from NNLS. Spectra of single phase were plotted for comparison. Spectra are offset for clarity. No scaling factors were applied.

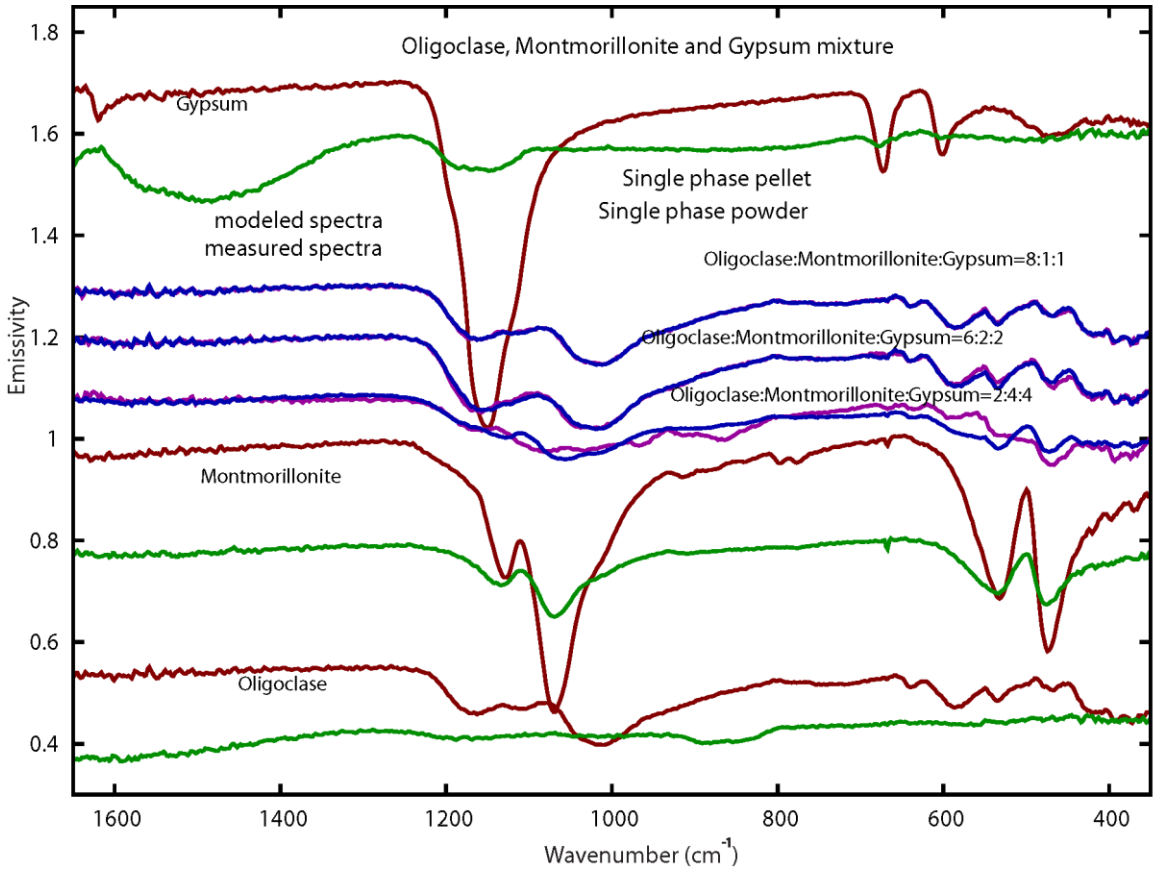

Figure 4.S13 Measured and modeled spectra of oligoclase, montmorillonite and gypsum mixtures derived from NNLS. Spectra of single phase were plotted for comparison. Spectra are offset for clarity. No scaling factors were applied.

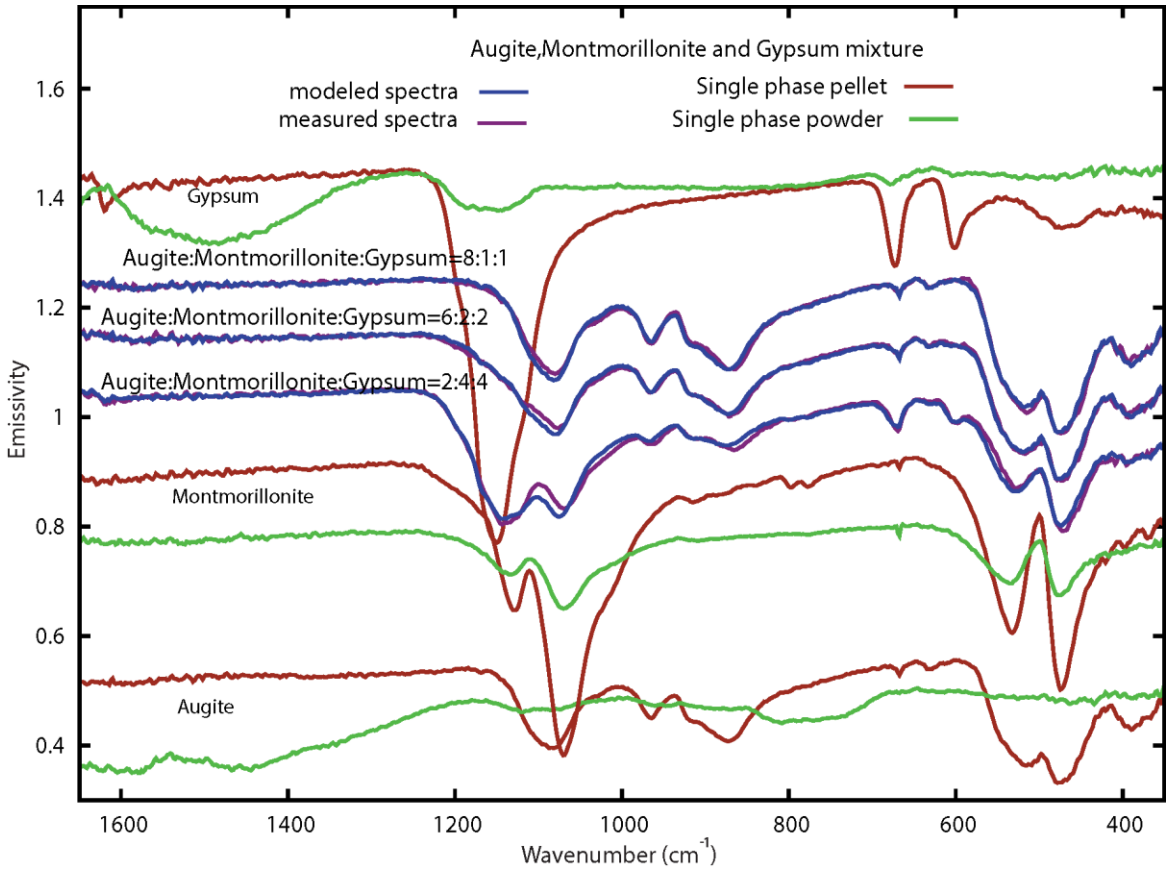

Figure 4.S14 Measured and modeled spectra of augite, montmorillonite and gypspum mixtures derived from NNLS. Spectra of single phase were plotted for comparison. Spectra are offset for clarity. No scaling factors were applied.

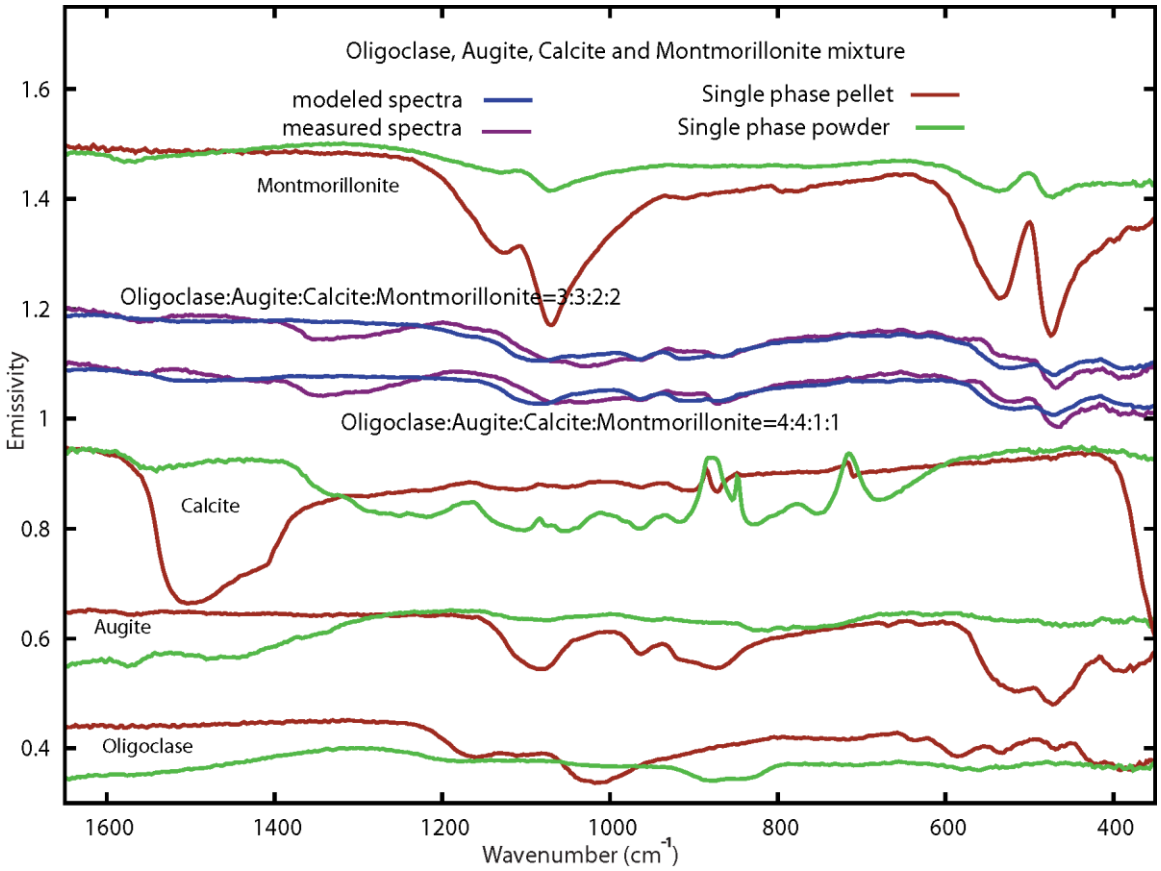

Figure 4.S15 Measured and modeled spectra of oligoclase, augite, calcite and montmorillonite mixtures derived from NNLS. Spectra of single phase were plotted for comparison. Spectra are offset for clarity. No scaling factors were applied.

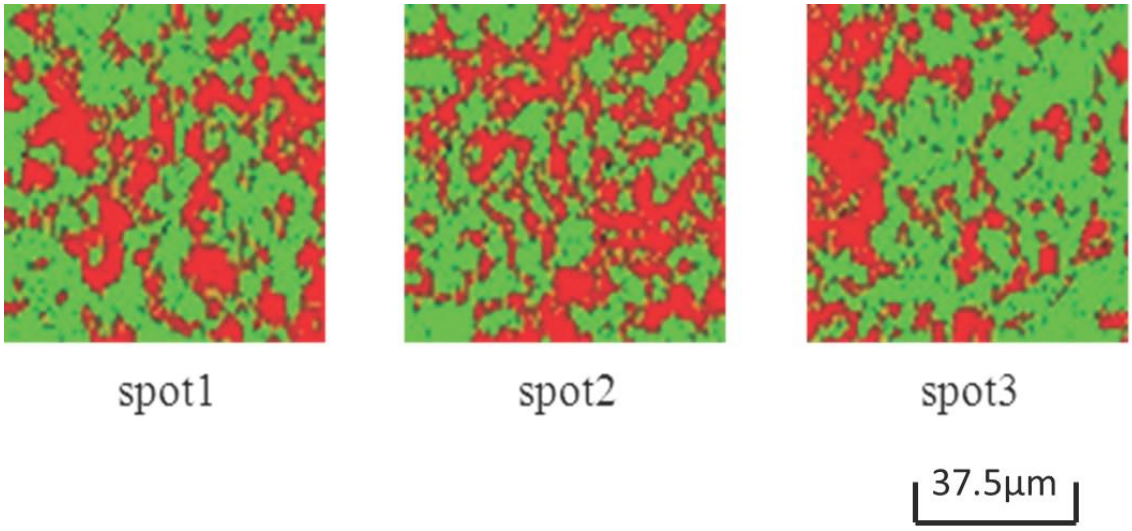

Figure 4.S16 SAM results of three images of Raman spectra for a pellet mixture of calcite and gypsum in 1:1 proportions. Green is calcite and red is gypsum. Measured mineral proportions in Spot1 are: gypsum: 48.3%, calcite: 52.7%. Spot2: gypsum: 42.8%, calcite:56.2%. Spot3: gypsum: 46.6%, calcite:46.5%. The average abundance in the mixture pellet is: gypsum:46.2%, calcite: 53.8%.

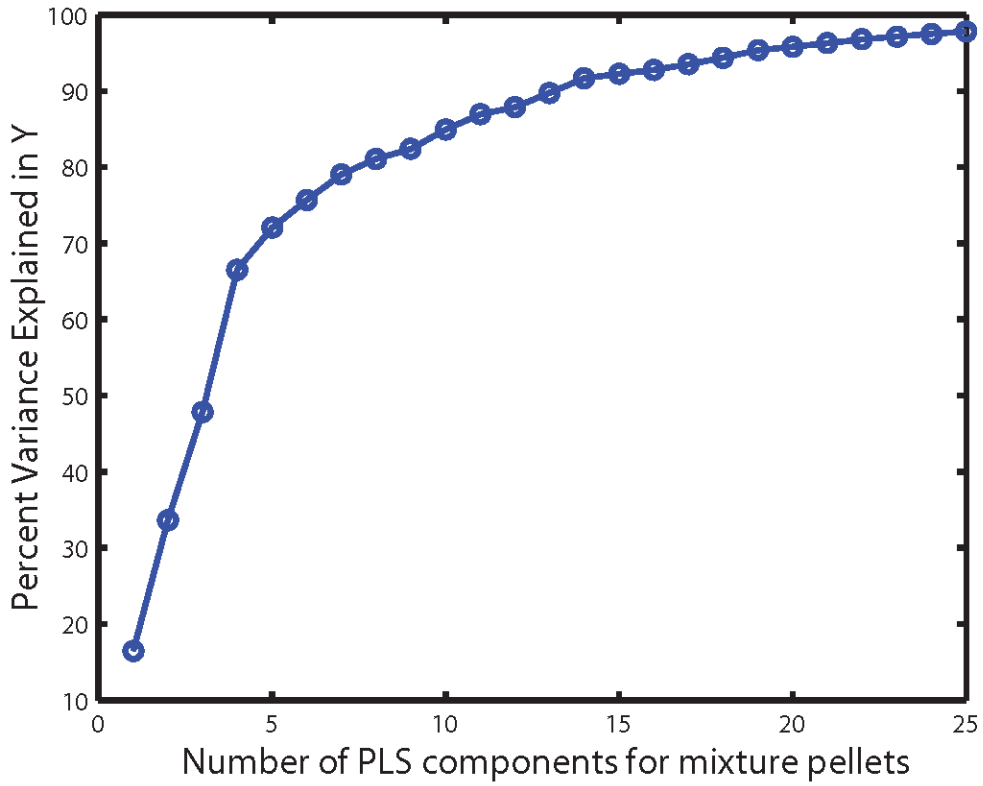

Figure 4.S17 Percentage of variance explained in the response variable (Y) as a function of the number of components for mixture pellets in PLS.. For the mixture pellet training set, the number of components was set to 15. This number accounts for more than 90% of the variance, with little difference in predictive performance beyond this number.

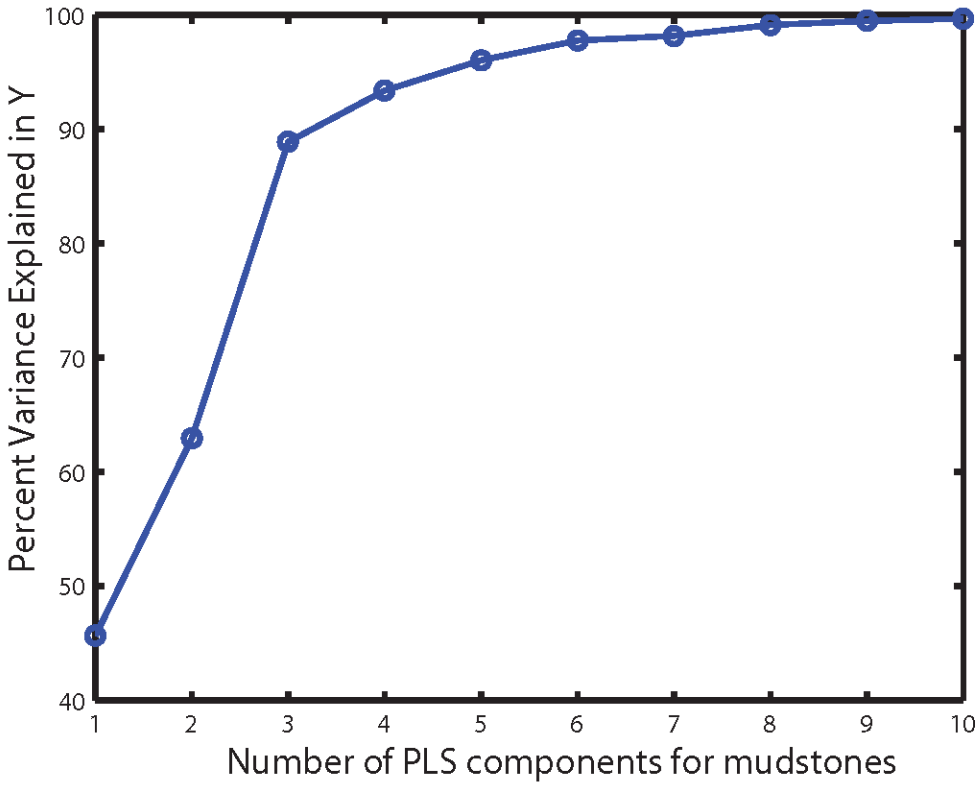

Figure 4.S18 Percentage of variance explained in the response variable (Y) as a function of the number of components for mudstones in PLS. The number of components chosen for the predictive model was based on searching for an infection in this curve. For the mudstone training set, the number of components was set to five. This number accounts for more than 95% of the variance , with little change in predictive performance beyond this number.

Table 4.S1 Measured abundance and modeled abundance derived from NNLS

Mixture labels	Measured abundance						NNLS Modeled abundance				
	oligoclase	augite	calcite	montmorillonite	gypsum		oligoclase	augite	calcite	montmorillonite	gypsum
olig-augite	10.00	90.00	0.00	0.00	0.00		22.05	77.95	0.00	0.00	0.00
	20.00	80.00	0.00	0.00	0.00		16.87	83.14	0.00	0.00	0.00
	50.00	50.00	0.00	0.00	0.00		41.13	58.87	0.00	0.00	0.00
	80.00	20.00	0.00	0.00	0.00		78.50	21.49	0.00	0.00	0.00
	90.00	10.00	0.00	0.00	0.00		88.48	11.51	0.00	0.00	0.00
olig-mont	10.00	0.00	0.00	90.00	0.00		37.18	0.00	0.00	62.81	0.00
	20.00	0.00	0.00	80.00	0.00		36.96	0.00	0.00	63.04	0.00
	50.00	0.00	0.00	50.00	0.00		50.84	0.00	0.00	49.17	0.00
	80.00	0.00	0.00	20.00	0.00		95.13	0.00	0.00	4.87	0.00
	90.00	0.00	0.00	10.00	0.00		99.99	0.00	0.00	0.00	0.00
olig-gyp	10.00	0.00	0.00	0.00	90.00		23.36	0.00	0.00	0.00	76.64
	20.00	0.00	0.00	0.00	80.00		29.87	0.00	0.00	0.00	70.13
	50.00	0.00	0.00	0.00	50.00		64.97	0.00	0.00	0.00	35.03
	80.00	0.00	0.00	0.00	20.00		89.69	0.00	0.00	0.00	10.30
	90.00	0.00	0.00	0.00	10.00		96.14	0.00	0.00	0.00	3.86
augite-calcite	0.00	10.00	90.00	0.00	0.00		0.00	0.00	100.00	0.00	0.00
	0.00	20.00	80.00	0.00	0.00		0.00	10.59	89.42	0.00	0.00
	0.00	50.00	50.00	0.00	0.00		0.00	69.22	30.77	0.00	0.00
	0.00	80.00	20.00	0.00	0.00		0.00	76.13	23.87	0.00	0.00
	0.00	90.00	10.00	0.00	0.00		0.00	80.16	19.84	0.00	0.00
aug-mont	0.00	10.00	0.00	90.00	0.00		0.00	17.17	0.00	82.83	0.00
	0.00	20.00	0.00	80.00	0.00		0.00	57.12	0.00	42.88	0.00
	0.00	50.00	0.00	50.00	0.00		0.00	83.70	0.00	16.30	0.00
	0.00	80.00	0.00	20.00	0.00		0.00	96.13	0.00	3.87	0.00
	0.00	90.00	0.00	10.00	0.00		0.00	95.94	0.00	4.06	0.00
aug-gyp	0.00	10.00	0.00	0.00	90.00		0.00	24.50	0.00	0.00	75.50
	0.00	20.00	0.00	0.00	80.00		0.00	41.42	0.00	0.00	58.58
	0.00	50.00	0.00	0.00	50.00		0.00	72.22	0.00	0.00	27.78
	0.00	80.00	0.00	0.00	20.00		0.00	85.47	0.00	0.00	14.53

	0.00	90.00	0.00	0.00	10.00		0.00	89.18	0.00	0.00	10.82
cal-mont	0.00	0.00	10.00	90.00	0.00		0.00	0.00	22.06	77.94	0.00
	0.00	0.00	20.00	80.00	0.00		0.00	0.00	44.17	55.83	0.00
	0.00	0.00	50.00	50.00	0.00		0.00	0.00	90.90	9.10	0.00
	0.00	0.00	80.00	20.00	0.00		0.00	0.00	100.00	0.00	0.00
	0.00	0.00	90.00	10.00	0.00		0.00	0.00	100.00	0.00	0.00
cal-gyp	0.00	0.00	10.00	0.00	90.00		0.00	0.00	28.70	0.00	71.30
	0.00	0.00	20.00	0.00	80.00		0.00	0.00	40.29	0.00	59.71
	0.00	0.00	50.00	0.00	50.00		0.00	0.00	89.18	0.00	10.82
	0.00	0.00	80.00	0.00	20.00		0.00	0.00	99.06	0.00	0.94
	0.00	0.00	90.00	0.00	10.00		0.00	0.00	100.00	0.00	0.00
mont-gyp	0.00	0.00	0.00	10.00	90.00		0.00	0.00	0.00	20.58	79.42
	0.00	0.00	0.00	20.00	80.00		0.00	0.00	0.00	26.05	73.95
	0.00	0.00	0.00	50.00	50.00		0.00	0.00	0.00	56.71	43.29
	0.00	0.00	0.00	80.00	20.00		0.00	0.00	0.00	81.20	18.81
	0.00	0.00	0.00	90.00	10.00		0.00	0.00	0.00	85.30	14.71
olig-aug-calc	20.00	20.00	60.00	0.00	0.00		0.00	24.11	75.89	0.00	0.00
	40.00	40.00	20.00	0.00	0.00		0.00	76.80	23.20	0.00	0.00
	45.00	45.00	10.00	0.00	0.00		34.02	60.67	5.33	0.00	0.00
olig-aug-mont	20.00	20.00	0.00	60.00	0.00		37.00	45.06	0.00	17.93	0.00
	40.00	40.00	0.00	20.00	0.00		50.35	46.02	0.00	3.63	0.00
	45.00	45.00	0.00	10.00	0.00		49.83	50.18	0.00	0.00	0.00
olig-aug-gyp	20.00	20.00	0.00	0.00	60.00		46.24	28.02	0.00	0.00	25.75
	40.00	40.00	0.00	0.00	20.00		62.70	19.09	0.00	0.00	18.21
	45.00	45.00	0.00	0.00	10.00		56.23	43.74	0.00	0.00	0.03
olig-cal-mont	20.00	0.00	40.00	40.00	0.00		0.00	0.00	76.94	23.07	0.00
	60.00	0.00	20.00	20.00	0.00		67.14	0.00	27.06	5.80	0.00
	80.00	0.00	10.00	10.00	0.00		89.62	0.00	10.38	0.00	0.00
olig-mont-gyp	20.00	0.00	40.00	0.00	40.00		79.91	0.00	0.00	0.00	20.09
	60.00	0.00	20.00	0.00	20.00		84.14	0.00	0.00	0.00	15.86
	80.00	0.00	10.00	0.00	10.00		92.39	0.00	0.00	0.00	7.61

aug-cal-mont	0.00	20.00	40.00	40.00	0.00		0.00	53.98	43.19	2.83	0.00
	0.00	60.00	20.00	20.00	0.00		0.00	96.70	3.30	0.00	0.00
	0.00	80.00	10.00	10.00	0.00		0.00	100.00	0.00	0.00	0.00
aug-mont-gyp	0.00	20.00	0.00	40.00	40.00		0.00	45.50	0.00	22.39	32.11
	0.00	60.00	0.00	20.00	20.00		0.00	69.20	0.00	19.50	11.31
	0.00	80.00	0.00	10.00	10.00		0.00	84.38	0.00	8.92	6.70
olig-aug-cal-mont	30.00	30.00	20.00	20.00	0.00		16.36	67.30	16.34	0.00	0.00
	40.00	40.00	10.00	10.00	0.00		39.40	51.36	9.32	0.00	0.00
olig-aug-mont-gyp											
	30.00	30.00	0.00	20.00	20.00		48.79	37.10	0.00	7.45	6.67
	40.00	40.00	0.00	10.00	10.00		52.30	42.70	0.00	4.22	0.79

Table 4.S2 Measured abundance and modeled abundance derived from PLS

Mixture label	Measured abundance						PLS Modeled abundance				
	oligoclase	augite	calcite	montmorillonite	gypsum		oligoclase	augite	calcite	montmorillonite	gypsum
olig-augite	10.00	90.00	0.00	0.00	0.00		22.97	70.60	-0.56	9.88	-1.03
	20.00	80.00	0.00	0.00	0.00		16.58	69.54	-0.65	15.76	0.30
	50.00	50.00	0.00	0.00	0.00		36.14	55.11	2.50	6.80	-0.13
	80.00	20.00	0.00	0.00	0.00		74.03	23.61	3.29	-1.42	-2.05
	90.00	10.00	0.00	0.00	0.00		79.45	16.69	1.83	2.12	-3.10
olig-mont	10.00	0.00	0.00	90.00	0.00		15.70	12.34	-2.61	83.60	-3.32
	20.00	0.00	0.00	80.00	0.00		26.21	7.51	3.47	71.12	-7.20
	50.00	0.00	0.00	50.00	0.00		48.53	11.10	0.33	42.99	-1.68
	80.00	0.00	0.00	20.00	0.00		61.57	3.11	7.87	27.65	-2.18
	90.00	0.00	0.00	10.00	0.00		89.97	18.02	3.17	-4.49	-10.90
olig-gyp	10.00	0.00	0.00	0.00	90.00		25.66	-0.40	2.84	-7.89	82.80
	20.00	0.00	0.00	0.00	80.00		18.61	-5.15	-2.62	6.76	84.16
	50.00	0.00	0.00	0.00	50.00		58.12	-5.25	-0.46	0.00	47.83
	80.00	0.00	0.00	0.00	20.00		87.59	-6.82	-1.86	3.48	18.17
	90.00	0.00	0.00	0.00	10.00		92.41	-5.85	2.79	-2.63	11.91
augite-calcite	0.00	10.00	90.00	0.00	0.00		-3.12	5.06	95.01	-6.03	4.68
	0.00	20.00	80.00	0.00	0.00		-3.55	15.74	74.20	4.17	4.42
	0.00	50.00	50.00	0.00	0.00		-1.87	54.18	37.57	3.89	0.75
	0.00	80.00	20.00	0.00	0.00		-4.81	86.09	22.07	-7.47	-0.50
	0.00	90.00	10.00	0.00	0.00		-0.56	86.34	11.48	0.26	0.44
aug-mont	0.00	10.00	0.00	90.00	0.00		20.06	-13.80	8.92	86.37	2.01
	0.00	20.00	0.00	80.00	0.00		-0.64	30.22	-5.68	83.19	-0.23
	0.00	50.00	0.00	50.00	0.00		-6.42	56.97	1.97	46.00	5.07
	0.00	80.00	0.00	20.00	0.00		16.84	61.47	-7.08	32.76	-2.48
	0.00	90.00	0.00	10.00	0.00		1.54	75.34	2.33	19.96	-0.05
aug-gyp	0.00	10.00	0.00	0.00	90.00		-7.50	7.37	2.29	6.35	92.27

	0.00	20.00	0.00	0.00	80.00		-1.01	20.25	6.87	-1.77	75.18
	0.00	50.00	0.00	0.00	50.00		1.67	44.32	7.79	-2.46	43.29
	0.00	80.00	0.00	0.00	20.00		-16.57	91.10	1.09	-6.59	27.79
	0.00	90.00	0.00	0.00	10.00		-13.97	103.33	1.47	-8.74	14.86
cal-mont	0.00	0.00	10.00	90.00	0.00		-16.33	-5.77	0.91	125.23	5.21
	0.00	0.00	20.00	80.00	0.00		-5.81	13.80	22.53	74.11	-1.88
	0.00	0.00	50.00	50.00	0.00		7.57	-7.99	68.64	26.96	4.01
	0.00	0.00	80.00	20.00	0.00		6.19	-8.40	69.64	31.18	0.31
	0.00	0.00	90.00	10.00	0.00		10.58	-2.51	77.35	14.19	-1.92
cal-gyp	0.00	0.00	10.00	0.00	90.00		-4.78	16.30	-1.72	12.45	80.01
	0.00	0.00	20.00	0.00	80.00		-1.88	8.59	12.20	-3.86	80.14
	0.00	0.00	50.00	0.00	50.00		-13.97	-16.64	70.40	-1.29	56.73
	0.00	0.00	80.00	0.00	20.00		3.11	-9.47	85.84	7.65	19.29
	0.00	0.00	90.00	0.00	10.00		24.03	25.85	87.21	-34.82	6.89
mont-gyp	0.00	0.00	0.00	10.00	90.00		-6.64	17.29	-3.31	4.63	88.45
	0.00	0.00	0.00	20.00	80.00		-3.01	-9.74	-0.44	15.95	91.07
	0.00	0.00	0.00	50.00	50.00		12.24	13.36	0.20	42.48	23.93
	0.00	0.00	0.00	80.00	20.00		0.32	-1.44	-9.04	83.20	21.26
	0.00	0.00	0.00	90.00	10.00		-8.54	-15.56	5.95	100.12	12.90
olig-aug-calc	20.00	20.00	60.00	0.00	0.00		20.41	18.13	59.71	5.41	-7.48
	40.00	40.00	20.00	0.00	0.00		38.35	36.20	26.22	3.97	-7.37
	45.00	45.00	10.00	0.00	0.00		44.26	40.18	6.86	5.23	4.75
olig-aug-mont	20.00	20.00	0.00	60.00	0.00		24.66	29.44	-0.03	49.26	2.61
	40.00	40.00	0.00	20.00	0.00		37.38	37.94	4.68	21.49	2.04
	45.00	45.00	0.00	10.00	0.00		39.64	40.92	3.36	16.40	1.36
olig-aug-gyp	20.00	20.00	0.00	0.00	60.00		20.36	44.58	28.93	-28.87	35.79
	40.00	40.00	0.00	0.00	20.00		19.26	-2.57	4.30	39.29	48.29
	45.00	45.00	0.00	0.00	10.00		40.28	37.16	8.08	5.79	15.38
olig-cal-mont	20.00	0.00	40.00	40.00	0.00		27.25	6.84	33.88	37.15	-5.96
	60.00	0.00	20.00	20.00	0.00		64.25	4.66	25.30	6.30	-1.97

	80.00	0.00	10.00	10.00	0.00		78.08	2.64	9.03	1.50	7.72
olig-mont-gyp	20.00	0.00	40.00	0.00	40.00		38.05	42.56	1.65	4.36	16.73
	60.00	0.00	20.00	0.00	20.00		75.90	2.04	2.72	1.26	17.89
	80.00	0.00	10.00	0.00	10.00		83.31	-0.88	7.04	-3.17	11.56
aug-cal-mont	0.00	20.00	40.00	40.00	0.00		2.80	23.27	49.94	27.85	-3.24
	0.00	60.00	20.00	20.00	0.00		-3.43	59.73	21.71	17.02	3.20
	0.00	80.00	10.00	10.00	0.00		-1.65	68.70	9.24	16.80	5.72
aug-mont-gyp	0.00	20.00	0.00	40.00	40.00		11.13	12.30	-0.73	21.45	49.66
	0.00	60.00	0.00	20.00	20.00		-2.81	71.61	0.47	13.59	16.09
	0.00	80.00	0.00	10.00	10.00		-2.87	99.50	4.68	-1.17	0.43
olig-aug-cal-mont	30.00	30.00	20.00	20.00	0.00		32.66	27.15	19.19	22.12	-0.73
	40.00	40.00	10.00	10.00	0.00		43.49	23.29	11.05	19.57	6.56
olig-aug-mont-gyp											
	30.00	30.00	0.00	20.00	20.00		42.25	29.19	-2.06	3.99	31.36
	40.00	40.00	0.00	10.00	10.00		48.29	30.54	4.86	7.67	15.96

Table 4.S3 Comparison of PLS results with: no contrast adjustment, 150% adjustment of all training set spectra, and 150% adjustment for 20% of training set

Mixture label	no adjustment						150% adjustment				
	oligo clase	augite	calcite	mont morill onite	gypsum		oligo clase	augite	calcite	mont morill onite	gypsum
olig-augite	22.97	70.60	-0.56	9.88	-1.03		18.92	82.32	-1.79	4.93	-0.44
	16.58	69.54	-0.65	15.76	0.30		8.17	82.50	-2.99	13.53	1.67
	36.14	55.11	2.50	6.80	-0.13		35.35	61.99	2.15	0.08	1.54
	74.03	23.61	3.29	-1.42	-2.05		92.39	16.35	2.22	-13.75	-0.93
	79.45	16.69	1.83	2.12	-3.10		98.95	6.30	-0.08	-6.84	-2.45
olig-mont	15.70	12.34	-2.61	83.60	-3.32		17.44	11.01	-2.88	82.38	-3.34
	26.21	7.51	3.47	71.12	-7.20		31.80	10.01	1.66	66.16	-7.86
	48.53	11.10	0.33	42.99	-1.68		49.70	12.93	0.09	41.28	-2.75
	61.57	3.11	7.87	27.65	-2.18		61.15	7.44	7.93	27.37	-2.90
	89.97	18.02	3.17	-4.49	-10.90		80.95	18.36	3.54	2.83	-10.16
olig-gyp	25.66	-0.40	2.84	-7.89	82.80		24.67	-2.22	3.76	-7.78	83.76
	18.61	-5.15	-2.62	6.76	84.16		20.21	-5.32	-2.27	4.38	83.95
	58.12	-5.25	-0.46	0.00	47.83		57.18	-3.75	-0.21	-1.09	47.72
	87.59	-6.82	-1.86	3.48	18.17		85.35	-4.88	-2.24	3.65	18.00
	92.41	-5.85	2.79	-2.63	11.91		92.28	-4.71	2.08	-3.01	11.19
augite-calcite	-3.12	5.06	95.01	-6.03	4.68		0.76	9.44	92.28	-9.36	3.65
	-3.55	15.74	74.20	4.17	4.42		2.48	20.11	71.50	-0.80	2.93
	-1.87	54.18	37.57	3.89	0.75		1.70	52.48	37.43	4.03	-0.42
	-4.81	86.09	22.07	-7.47	-0.50		-5.79	83.41	23.49	-6.04	-0.91
	-0.56	86.34	11.48	0.26	0.44		1.08	80.23	13.21	0.81	-0.49
aug-mont	20.06	-13.80	8.92	86.37	2.01		25.77	-7.04	2.69	79.22	0.85
	-0.64	30.22	-5.68	83.19	-0.23		-5.68	27.55	-4.21	85.34	0.53
	-6.42	56.97	1.97	46.00	5.07		-5.31	54.66	2.69	45.92	4.55
	16.84	61.47	-7.08	32.76	-2.48		16.80	60.99	-7.03	32.23	-2.79
	1.54	75.34	2.33	19.96	-0.05		-0.05	72.18	3.73	23.01	0.30

aug-gyp	-7.50	7.37	2.29	6.35	92.27		-5.15	7.56	2.28	4.67	92.50
	-1.01	20.25	6.87	-1.77	75.18		0.52	21.20	6.78	-2.95	75.21
	1.67	44.32	7.79	-2.46	43.29		4.65	45.17	7.99	-3.76	42.63
	-16.57	91.10	1.09	-6.59	27.79		-15.45	88.40	1.85	-4.80	28.02
	-13.97	103.33	1.47	-8.74	14.86		-14.69	98.24	3.51	-5.33	14.89
cal-mont	-16.33	-5.77	0.91	125.23	5.21		-17.13	-6.63	0.50	121.91	6.11
	-5.81	13.80	22.53	74.11	-1.88		-0.19	9.64	22.25	71.88	-3.21
	7.57	-7.99	68.64	26.96	4.01		1.69	-12.97	73.72	34.80	3.84
	6.19	-8.40	69.64	31.18	0.31		8.66	-7.21	70.11	30.35	-0.72
	10.58	-2.51	77.35	14.19	-1.92		13.64	2.08	75.93	11.73	-3.48
cal-gyp	-4.78	16.30	-1.72	12.45	80.01		2.28	17.93	-0.95	6.66	78.67
	-1.88	8.59	12.20	-3.86	80.14		4.50	19.20	11.08	-10.05	79.27
	-13.97	-16.64	70.40	-1.29	56.73		-10.04	-6.36	68.63	-5.58	57.11
	3.11	-9.47	85.84	7.65	19.29		-2.08	-18.99	89.02	13.27	18.79
	24.03	25.85	87.21	-34.82	6.89		7.08	12.77	90.43	-18.97	11.24
mont-gyp	-6.64	17.29	-3.31	4.63	88.45		-10.30	12.13	-1.91	10.65	88.46
	-3.01	-9.74	-0.44	15.95	91.07		-5.27	-9.38	-1.37	17.82	91.79
	12.24	13.36	0.20	42.48	23.93		11.71	14.39	-2.28	42.87	24.93
	0.32	-1.44	-9.04	83.20	21.26		-1.64	-3.55	-7.74	86.34	20.97
	-8.54	-15.56	5.95	100.12	12.90		-3.40	-11.81	5.27	96.39	12.16
olig-aug-calc	20.41	18.13	59.71	5.41	-7.48		14.42	17.79	60.21	10.58	-5.57
	38.35	36.20	26.22	3.97	-7.37		39.21	35.46	26.33	4.49	-7.99
	44.26	40.18	6.86	5.23	4.75		40.77	39.00	9.08	8.66	4.75
olig-aug-mont	24.66	29.44	-0.03	49.26	2.61		26.13	26.26	0.46	49.52	1.84
	37.38	37.94	4.68	21.49	2.04		33.43	32.55	6.64	25.28	2.42
	39.64	40.92	3.36	16.40	1.36		36.05	36.21	5.06	22.03	1.50
olig-aug-gyp	20.36	44.58	28.93	-28.87	35.79		23.87	42.58	29.94	-28.99	36.29
	19.26	-2.57	4.30	39.29	48.29		17.16	-0.56	4.18	36.45	49.51
	40.28	37.16	8.08	5.79	15.38		43.05	30.41	10.06	9.78	14.74

olig-cal-mont	27.25	6.84	33.88	37.15	-5.96		26.32	7.27	34.15	37.11	-4.82
	64.25	4.66	25.30	6.30	-1.97		59.50	7.49	25.58	7.05	-0.86
	78.08	2.64	9.03	1.50	7.72		73.86	6.66	9.84	2.00	7.69
olig-mont-gyp	38.05	42.56	1.65	4.36	16.73		41.32	40.73	2.32	6.20	15.81
	75.90	2.04	2.72	1.26	17.89		70.54	5.37	2.63	2.52	18.71
	83.31	-0.88	7.04	-3.17	11.56		80.35	0.36	6.73	-1.21	11.42
aug-cal-mont	2.80	23.27	49.94	27.85	-3.24		-5.49	25.33	49.07	33.43	-1.11
	-3.43	59.73	21.71	17.02	3.20		-0.34	59.91	19.88	15.00	2.65
	-1.65	68.70	9.24	16.80	5.72		3.79	69.53	7.95	12.43	4.10
aug-mont-gyp	11.13	12.30	-0.73	21.45	49.66		5.96	21.31	-0.88	20.58	50.21
	-2.81	71.61	0.47	13.59	16.09		-3.66	77.34	-1.22	11.35	16.63
	-2.87	99.50	4.68	-1.17	0.43		-2.15	99.81	3.14	-0.55	0.53
olig-aug-cal-mont	32.66	27.15	19.19	22.12	-0.73		34.11	32.83	16.59	19.40	-1.02
	43.49	23.29	11.05	19.57	6.56		39.24	23.53	12.01	20.62	7.04
olig-aug-mont-gyp	42.25	29.19	-2.06	3.99	31.36		45.61	28.78	-1.86	3.73	30.61
	48.29	30.54	4.86	7.67	15.96		51.62	27.72	5.52	8.37	14.81
Mixture label	no adjustment						150% adjustment for 20% of the spectra				
	oligo clase	augite	calcite	mont morillonite	gypsum		oligo clase	augite	calcite	mont morillonite	gypsum
olig-augite	22.97	70.60	-0.56	9.88	-1.03		18.33	83.48	-2.41	4.07	-1.32
	16.58	69.54	-0.65	15.76	0.30		6.37	81.97	-4.05	11.90	4.64
	36.14	55.11	2.50	6.80	-0.13		35.54	61.77	1.20	0.04	0.01
	74.03	23.61	3.29	-1.42	-2.05		85.29	17.00	1.16	-7.99	-1.49
	79.45	16.69	1.83	2.12	-3.10		88.75	9.58	-0.47	-1.30	-1.80
olig-mont	15.70	12.34	-2.61	83.60	-3.32		2.98	6.60	-6.56	106.39	-4.06
	26.21	7.51	3.47	71.12	-7.20		25.24	4.57	1.37	80.92	-9.05
	48.53	11.10	0.33	42.99	-1.68		53.73	11.15	-2.27	42.54	-3.92
	61.57	3.11	7.87	27.65	-2.18		69.54	3.75	10.31	19.21	-2.32
	89.97	18.02	3.17	-4.49	-10.90		98.72	21.82	3.43	-13.75	-19.19
olig-gyp	25.66	-0.40	2.84	-7.89	82.80		14.93	-5.46	5.00	-12.73	103.52

	18.61	-5.15	-2.62	6.76	84.16		3.43	-8.02	-2.45	9.75	101.55
	58.12	-5.25	-0.46	0.00	47.83		58.36	-6.74	-0.95	-0.45	50.95
	87.59	-6.82	-1.86	3.48	18.17		98.17	-11.30	-7.04	3.79	17.26
	92.41	-5.85	2.79	-2.63	11.91		109.58	-12.54	-0.07	-10.81	10.07
augite-calcite	-3.12	5.06	95.01	-6.03	4.68		-0.05	8.11	90.95	-6.27	2.91
	-3.55	15.74	74.20	4.17	4.42		2.40	18.37	70.78	0.37	3.66
	-1.87	54.18	37.57	3.89	0.75		2.19	51.59	37.21	5.92	-1.25
	-4.81	86.09	22.07	-7.47	-0.50		-5.75	82.96	23.37	-4.47	-2.14
	-0.56	86.34	11.48	0.26	0.44		0.16	79.42	12.52	2.17	0.54
aug-mont	20.06	-13.80	8.92	86.37	2.01		28.53	-6.19	1.77	79.25	-1.70
	-0.64	30.22	-5.68	83.19	-0.23		-4.05	27.30	-4.20	81.02	2.21
	-6.42	56.97	1.97	46.00	5.07		-3.04	54.18	2.77	40.52	8.52
	16.84	61.47	-7.08	32.76	-2.48		8.10	62.13	-5.55	38.51	1.17
	1.54	75.34	2.33	19.96	-0.05		1.70	71.04	3.98	17.29	4.71
aug-gyp	-7.50	7.37	2.29	6.35	92.27		-0.19	11.65	4.10	8.29	78.71
	-1.01	20.25	6.87	-1.77	75.18		2.64	22.74	7.48	-0.50	68.19
	1.67	44.32	7.79	-2.46	43.29		2.68	47.75	8.61	-0.08	38.36
	-16.57	91.10	1.09	-6.59	27.79		-17.70	89.43	2.13	-4.13	25.20
	-13.97	103.33	1.47	-8.74	14.86		-16.21	98.85	3.22	-3.68	11.62
cal-mont	-16.33	-5.77	0.91	125.23	5.21		-9.58	-3.76	3.41	114.31	-0.96
	-5.81	13.80	22.53	74.11	-1.88		4.64	10.83	24.21	66.45	-5.77
	7.57	-7.99	68.64	26.96	4.01		3.39	-13.24	71.63	35.60	2.76
	6.19	-8.40	69.64	31.18	0.31		7.53	-6.86	69.40	31.72	0.14
	10.58	-2.51	77.35	14.19	-1.92		13.74	2.87	75.89	11.69	-3.22
cal-gyp	-4.78	16.30	-1.72	12.45	80.01		6.33	18.89	-0.61	7.79	71.66
	-1.88	8.59	12.20	-3.86	80.14		8.28	18.74	11.01	-9.57	75.24
	-13.97	-16.64	70.40	-1.29	56.73		-15.69	-9.66	66.76	-4.07	64.30
	3.11	-9.47	85.84	7.65	19.29		-0.04	-18.02	88.76	13.47	18.47
	24.03	25.85	87.21	-34.82	6.89		9.44	13.86	89.21	-22.69	14.97
mont-gyp	-6.64	17.29	-3.31	4.63	88.45		-6.66	12.53	-3.70	8.54	85.90
	-3.01	-9.74	-0.44	15.95	91.07		-2.21	-10.89	-4.16	14.65	92.85

	12.24	13.36	0.20	42.48	23.93		10.14	9.88	-3.01	34.76	32.55
	0.32	-1.44	-9.04	83.20	21.26		-1.86	-2.37	-7.14	85.21	19.75
	-8.54	-15.56	5.95	100.12	12.90		-4.94	-10.69	6.21	94.64	14.40
olig-aug-calc	20.41	18.13	59.71	5.41	-7.48		13.60	17.66	60.46	13.76	-6.94
	38.35	36.20	26.22	3.97	-7.37		39.13	35.21	26.16	6.63	-7.96
	44.26	40.18	6.86	5.23	4.75		42.62	38.84	8.81	7.24	5.91
olig-aug-mont	24.66	29.44	-0.03	49.26	2.61		30.95	27.70	3.39	38.99	3.07
	37.38	37.94	4.68	21.49	2.04		36.22	31.69	6.66	23.86	4.86
	39.64	40.92	3.36	16.40	1.36		38.33	35.26	4.63	18.82	4.87
olig-aug-gyp	20.36	44.58	28.93	-28.87	35.79		23.61	39.61	27.63	-24.53	36.64
	19.26	-2.57	4.30	39.29	48.29		19.20	2.93	7.04	28.28	47.38
	40.28	37.16	8.08	5.79	15.38		43.97	30.72	8.51	7.56	17.33
olig-cal-mont	27.25	6.84	33.88	37.15	-5.96		25.25	9.14	36.44	33.34	-4.21
	64.25	4.66	25.30	6.30	-1.97		54.44	9.72	25.90	12.36	-1.34
	78.08	2.64	9.03	1.50	7.72		70.31	10.13	10.36	4.95	6.28
olig-mont-gyp	38.05	42.56	1.65	4.36	16.73		42.31	38.62	2.45	7.42	16.38
	75.90	2.04	2.72	1.26	17.89		67.41	10.13	4.76	2.56	16.32
	83.31	-0.88	7.04	-3.17	11.56		74.28	5.61	8.19	2.35	8.67
aug-cal-mont	2.80	23.27	49.94	27.85	-3.24		-3.72	25.39	49.49	28.23	0.01
	-3.43	59.73	21.71	17.02	3.20		-1.25	58.51	19.41	16.15	5.23
	-1.65	68.70	9.24	16.80	5.72		2.58	68.74	7.49	14.72	5.62
aug-mont-gyp	11.13	12.30	-0.73	21.45	49.66		3.82	22.04	0.15	24.38	48.72
	-2.81	71.61	0.47	13.59	16.09		-6.13	76.67	-1.22	11.46	19.04
	-2.87	99.50	4.68	-1.17	0.43		-1.88	100.13	2.44	0.16	-0.59
olig-aug-cal-mont	32.66	27.15	19.19	22.12	-0.73		34.52	32.61	17.38	16.82	1.00
	43.49	23.29	11.05	19.57	6.56		40.44	21.90	11.65	20.74	9.42
olig-aug-mont-gyp	42.25	29.19	-2.06	3.99	31.36		48.15	28.97	-0.55	3.03	27.42
	48.29	30.54	4.86	7.67	15.96		53.22	28.58	5.80	7.84	13.19

Reference

Ansan, V., et al. (2011), Stratigraphy, mineralogy, and origin of layered deposits inside Terby crater, Mars, *Icarus*, *211*(1), 273-304, doi:10.1016/j.icarus.2010.09.011.

Baldridge, A. M., and P. R. Christensen (2009), A laboratory technique for thermal emission measurement of hydrated minerals, *Applied spectroscopy*, *63*(6), 678-688.

Baldridge, A. M., J. D. Farmer, and J. E. Moersch (2004), Mars remote-sensing analog studies in the Badwater Basin, Death Valley, California, *Journal of Geophysical Research-Planets*, *109*(E12), 18, doi:10.1029/2004je002315.

Bandfield, J. L. (2002), Global mineral distributions on Mars, *Journal of Geophysical Research*, *107*(E6), 5042, doi:10.1029/2001JE001510.

Bandfield, J. L., and M. D. Smith (2003), Multiple emission angle surface-atmosphere separations of Thermal Emission Spectrometer data, *Icarus*, *161*(1), 47-65, doi:10.1016/s0019-1035(02)00025-8.

Boynton, W. V., et al. (2009), Evidence for Calcium Carbonate at the Mars Phoenix Landing Site, *Science*, *325*(5936), 61-64, doi:10.1126/science.1172768.

Braak, C. J. F., and S. De Jong (1998), The objective function of partial least squares regression, *J. Chemometr.*, *12*(1), 41-54, doi:10.1002/(sici)1099-128x(199801/02)12:1<41::aid-cem500>3.0.co;2-f.

Chipera, S. J., and D. L. Bish (2001), Baseline studies of The Clay Minerals Society Source Clays: Powder X-ray diffraction analyses, Clay Clay Min., 49(5), 398-409, doi:10.1346/ccmn.2001.0490507.

Christensen, P. R., et al. (1992), Thermal emission spectrometer experiment: Mars Observer Mission, *Journal of Geophysical Research-Planets*, *97*(E5), 7719-7734, doi:10.1029/2000JE001370.

Christensen, P. R., et al. (2003), Morphology and composition of the surface of Mars: Mars Odyssey THEMIS results, *Science*, *300*(5628), 2056-2061, doi:10.1126/science.1080885.

Christensen, P. R., et al. (2000a), Detection of crystalline hematite mineralization on Mars by the Thermal Emission Spectrometer: Evidence for near-surface water, *Journal of Geophysical Research-Planets*, *105*(E4), 9623-9642, doi:10.1029/1999je001093.

Christensen, P. R., et al. (2001), Mars Global Surveyor Thermal Emission Spectrometer experiment: Investigation description and surface science results, *Journal of Geophysical Research-Planets*, *106*(E10), 23823-23871, doi:10.1029/2000JE001370.

Christensen, P. R., J. L. Bandfield, M. D. Smith, V. E. Hamilton, and R. N. Clark (2000b), Identification of a basaltic component on the Martian surface from Thermal Emission Spectrometer data, *Journal of Geophysical Research-Planets*, *105*(E4), 9609-9621, doi:10.1029/1999je001127.

Christensen, P. R., et al. (2004a), Initial results from the Mini-TES experiment in Gusev crater from the Spirit rover, *Science*, *305*(5685), 837-842, doi:10.1126/science.1100564.

Christensen, P. R., et al. (2004b), Mineralogy at Meridiani Planum from the Mini-TES experiment on the Opportunity Rover, *Science*, *306*(5702), 1733-1739, doi:10.1126/science.1104909.

Clark, R. N., and T. L. Roush (1984), REFLECTANCE SPECTROSCOPY - QUANTITATIVE-ANALYSIS TECHNIQUES FOR REMOTE-SENSING APPLICATIONS, *Journal of Geophysical Research*, *89*(NB7), 6329-6340, doi:10.1029/JB089iB07p06329.

Clegg, S. M., E. Sklute, M. D. Dyar, J. E. Barefield, and R. C. Wiens (2009), Multivariate analysis of remote laser-induced breakdown spectroscopy spectra using partial least squares, principal component analysis, and related techniques, *Spectrochimica Acta Part B-Atomic Spectroscopy*, *64*(1), 79-88, doi:10.1016/j.sab.2008.10.045.

Cooper, C. D., and J. F. Mustard (2002), Spectroscopy of loose and cemented sulfate-bearing soils: Implications for duricrust on Mars, *Icarus*, *158*(1), 42-55, doi:10.1006/icar.2002.6874.

Dehouck, E., N. Mangold, S. Le Mouelic, V. Ansan, and F. Poulet (2010), Ismenius Cavus, Mars: A deep paleolake with phyllosilicate deposits, *Planet Space Sci.*, *58*(6), 941-946, doi:10.1016/j.pss.2010.02.005.

Dobrea, E. Z. N., et al. (2010), Mineralogy and stratigraphy of phyllosilicate-bearing and dark mantling units in the greater Mawrth Vallis/west Arabia Terra area: Constraints on geological origin, *Journal of Geophysical Research-Planets*, *115*, doi:10.1029/2009je003351.

Dyar, M. D., M. L. Carmosino, E. A. Breves, M. V. Ozanne, S. M. Clegg, and R. C. Wiens (2012), Comparison of partial least squares and lasso regression techniques as applied to laser-induced breakdown spectroscopy of geological samples, *Spectrochimica Acta Part B-Atomic Spectroscopy*, *70*, 51-67, doi:10.1016/j.sab.2012.04.011.

Ehlmann, B. L., J. F. Mustard, C. I. Fassett, S. C. Schon, J. W. Head, D. J. D. Marais, J. A. Grant, and S. L. Murchie (2008a), Clay minerals in delta deposits and organic preservation potential on Mars, *Nat. Geosci.*, *1*(6), 355-358, doi:10.1038/ngeo207.

Ehlmann, B. L., J. F. Mustard, S. L. Murchie, J. P. Bibring, A. Meunier, A. A. Fraeman, and Y. Langevin (2011), Subsurface water and clay mineral formation during the early history of Mars, *Nature*, *479*(7371), 53-60, doi:10.1038/nature10582.

Ehlmann, B. L., et al. (2008b), Orbital Identification of Carbonate-Bearing Rocks on Mars, *Science*, *322*(5909), 1828-1832, doi:10.1126/science.1164759.

Ehlmann, B. L., and C. S. Edwards (2014), Mineralogy of the Martian Surface, *Annu. Rev. Earth Planet. Sci.*, *42*, 291-315, doi:10.1146/annurev-earth-060313-055024.

Farmer, V. C. (1974), The layer silicates, in *Infrared spectra of minerals*, 331-363, Mineralogical society, London.

Feely, K. C., and P. R. Christensen (1999), Quantitative compositional analysis using thermal emission spectroscopy: Application to igneous and metamorphic rocks, *Journal of Geophysical Research-Planets*, *104*(E10), 24195-24210, doi:10.1029/1999JE001034.

Glotch, T. D., J. L. Bandfield, P. R. Christensen, W. M. Calvin, S. M. McLennan, B. C. Clark, A. D. Rogers, and S. W. Squyres (2006), Mineralogy of the light-toned outcrop at Meridiani Planum as seen by the Miniature Thermal Emission Spectrometer and implications for its formation, *Journal of Geophysical Research-Planets*, *111*(E12), 14, doi:10.1029/2005je002672.

Grotzinger, J. P., et al. (2005), Stratigraphy and sedimentology of a dry to wet eolian depositional system, Burns formation, Meridiani Planum, Mars, *Earth Planet. Sci. Lett.*, *240*(1), 11-72, doi:10.1016/j.epsl.2005.09.039.

Grotzinger, J. P., and R. E. Milliken (2012), THE SEDIMENTARY ROCK RECORD OF MARS: DISTRIBUTION, ORIGINS, AND GLOBAL STRATIGRAPHY, in *Sedimentary Geology of Mars*, edited by J. P. Grotzinger and R. E. Milliken, pp. 1-48.

Grotzinger, J. P., et al. (2014), A Habitable Fluvio-Lacustrine Environment at Yellowknife Bay, Gale Crater, Mars, *Science*, *343*(6169), 14, doi:10.1126/science.1242777.

Hamilton, V. E., and P. R. Christensen (2000), Determining the modal mineralogy of mafic and ultramafic igneous rocks using thermal emission spectroscopy, *Journal of Geophysical Research-Planets*, *105*(E4), 9717-9733, doi:10.1029/1999je001113.

Hamilton, V. E., and S. W. Ruff (2012), Distribution and characteristics of Adirondack-class basalt as observed by Mini-TES in Gusev crater, Mars and its possible volcanic source, *Icarus*, *218*(2), 917-949, doi:10.1016/j.icarus.2012.01.011.

Hapke, B. (1993), *Introduction to the Theory of reflectance and Emittance Spectroscopy*, Cambridge University Press, New York.

Hecker, C., J. H. Dilles, M. van der Meijde, and F. D. van der Meer (2012), Thermal infrared spectroscopy and partial least squares regression to determine mineral modes of granitoid rocks, Geochemistry Geophysics Geosystems, 13, doi:10.1029/2011gc004004.

Hook, S. J., J. E. Dmochowski, K. A. Howard, L. C. Rowan, K. E. Karlstrom, and J. M. Stock (2005), Mapping variations in weight percent silica measured from multispectral thermal infrared imagery - Examples from the Hiller Mountains, Nevada, USA and Tres Virgenes-La Reforma, Baja

California Sur, Mexico, *Remote Sensing of Environment*, *95*(3), 273-289, doi:10.1016/j.rse.2004.11.020.
Horgan, B. H., J. F. Bell, III, E. Z. N. Dobrea, E. A. Cloutis, D. T. Bailey, M. A. Craig, L. H. Roach, and J. F. Mustard (2009), Distribution of hydrated minerals in the north polar region of Mars, *Journal of Geophysical Research-Planets*, *114*, doi:10.1029/2008je003187.
Huang, J., and L. Xiao (2014), Compositional evolution of lava plains in the Syria-Thaumasia Block, Mars, *Science China-Physics Mechanics & Astronomy*, *57*(5), 994-1000, doi:10.1007/s11433-014-5407-3.
Hunt, G. R., and L. M. Logan (1972), VARIATION OF SINGLE-PARTICLE MID-INFRARED EMISSION-SPECTRUM WITH PARTICLE-SIZE, *Appl. Optics*, *11*(1), 142-&, doi:10.1364/ao.11.000142.
Hunt, G. R., and R. K. Vincent (1968), The behavior of spectral features in the infrared emission from particulate surfaces of various grain sizes, *Journal of Geophysical Research*, *73*(18), 6039-6046, doi:10.1029/JB073i018p06039.
Jackson, M. L. (1967), Soil Chemical Analysis, edited, pp. 146-157, Prentice Hall of India, New Delhi, India.
Kahle, A. B., M. S. Shumate, and D. B. Nash (1984), ACTIVE AIRBORNE INFRARED-LASER SYSTEM FOR IDENTIFICATION OF SURFACE ROCK AND MINERALS, *Geophysical Research Letters*, *11*(11), 1149-1152, doi:10.1029/GL011i011p01149.
Koeppen, W. C., and V. E. Hamilton (2008), Global distribution, composition, and abundance of olivine on the surface of Mars from thermal infrared data, *Journal of Geophysical Research-Planets*, *113*(E5), E05001, doi:10.1029/2007je002984.
Kruse, F., A. Lefkoff, J. Boardman, K. Heidebrecht, A. Shapiro, P. Barloon, and A. Goetz (1993), The spectral image processing system (SIPS)--interactive visualization and analysis of imaging spectrometer data, *Remote sensing of environment*, *44*(2-3), 145-163.
Lane, M. D., and P. R. Christensen (1998), Thermal infrared emission spectroscopy of salt minerals predicted for Mars, Icarus, 135(2), 528-536, doi:10.1006/icar.1998.5998.
Lane, M. D., and P. R. Christensen (1998), Thermal infrared emission spectroscopy of salt minerals predicted for Mars, *Icarus*, *135*(2), 528-536, doi:10.1006/icar.1998.5998.
Lane, M. D. (2007), Mid-infrared emission spectroscopy of sulfate and sulfate-bearing minerals, American Mineralogist, 92(1), 1-18, doi:10.2138/am.2007.2170.
Lawson, C. L., and R. J. Hanson (1974), *Solving least squares problems*, Society for Industrial and Applied Mathematics (SIAM), doi:10.1137/1.9781611971217.
Li, S., L. Li, R. Milliken, and K. Song (2012), Hybridization of partial least squares and neural network models for quantifying lunar surface minerals, *Icarus*, *221*(1), 208-225, doi:10.1016/j.icarus.2012.07.023.
Lucey, P. G. (2004), Mineral maps of the Moon, *Geophysical Research Letters*, *31*(8), doi:10.1029/2003gl019406.
Lyon, R. (1965), Analysis of rocks by spectral infrared emission (8 to 25 microns), *Economic Geology*, *60*(4), 715-736.
Malin, M. C., and K. S. Edgett (2000), Sedimentary rocks of early Mars, *Science*, *290*(5498), 1927-1937, doi:10.1126/science.290.5498.1927.
Masse, M., O. Bourgeois, S. Le Mouelic, C. Verpoorter, L. Le Deit, and J. P. Bibring (2010), Martian polar and circum-polar sulfate-bearing deposits: Sublimation tills derived from the North Polar Cap, *Icarus*, *209*(2), 434-451, doi:10.1016/j.icarus.2010.04.017.
McDowell, M. L., and V. E. Hamilton (2009), Seeking phyllosilicates in thermal infrared data: A laboratory and Martian data case study, *Journal of Geophysical Research-Planets*, *114*, 21, doi:10.1029/2008je003317.
McLennan, S. M., et al. (2014), Elemental Geochemistry of Sedimentary Rocks at Yellowknife Bay, Gale Crater, Mars, *Science*, *343*(6169), 10, doi:10.1126/science.1244734.

McLennan, S. M., et al. (2005), Provenance and diagenesis of the evaporite-bearing Burns formation, Meridiani Planum, Mars, *Earth Planet. Sci. Lett.*, *240*(1), 95-121, doi:10.1016/j.epsl.2005.09.041.

McLennan, S. M., B. J. Fryer, and G. M. Young (1979), Rare-Earth elements in Huronian (lower proterozoic) sedimentary-rocks-composition and evolution of the post-Kenoran upper crust, *Geochimica Et Cosmochimica Acta*, *43*(3), 375-388, doi:10.1016/0016-7037(79)90202-3.

Michalski, J. R., and R. L. Fergason (2009), Composition and thermal inertia of the Mawrth Vallis region of Mars from TES and THEMIS data, *Icarus*, *199*(1), 25-48, doi:10.1016/j.icarus.2008.08.016.

Michalski, J. R., M. D. Kraft, T. G. Sharp, L. B. Williams, and P. R. Christensen (2006), Emission spectroscopy of clay minerals and evidence for poorly crystalline aluminosilicates on Mars from Thermal Emission Spectrometer data, *Journal of Geophysical Research-Planets*, *111*(E3), E03004, doi:10.1029/2005je002438.

Michalski, J. R., and P. B. Niles (2010), Deep crustal carbonate rocks exposed by meteor impact on Mars, *Nat. Geosci.*, *3*(11), 751-755, doi:10.1038/NGEO971.

Michalski, J. R., F. Poulet, J. P. Bibring, and N. Mangold (2010), Analysis of phyllosilicate deposits in the Nili Fossae region of Mars: Comparison of TES and OMEGA data, *Icarus*, *206*(1), 269-289, doi:10.1016/j.icarus.2009.09.006.

Milliken, R. E., and D. L. Bish (2010), Sources and sinks of clay minerals on Mars, *Philos. Mag.*, *90*(17-18), 2293-2308, doi:10.1080/14786430903575132.

Milliken, R. E., J. P. Grotzinger, and B. J. Thomson (2010), Paleoclimate of Mars as captured by the stratigraphic record in Gale Crater, *Geophysical Research Letters*, *37*, 6, doi:10.1029/2009gl041870.

Moersch, J. E., and P. R. Christensen (1995), THERMAL EMISSION FROM PARTICULATE SURFACES - A COMPARISON OF SCATTERING MODELS WITH MEASURED SPECTRA, *Journal of Geophysical Research-Planets*, *100*(E4), 7465-7477, doi:10.1029/94je03330.

Moore, D. M., and R. C. Reynolds (1997), *X-ray Diffraction and the Identification and Analysis of Clay Minerals*, second ed., OXFORD UNIVERSITY PRESS, Oxford New York.

Murchie, S. L., J. F. Mustard, B. L. Ehlmann, R. E. Milliken, J. L. Bishop, N. K. McKeown, E. Z. Noe Dobrea, F. P. Seelos, D. L. Buczkowski, and S. M. Wiseman (2009), A synthesis of Martian aqueous mineralogy after 1 Mars year of observations from the Mars Reconnaissance Orbiter, *Journal of Geophysical Research: Planets 114*(E2), E00D06, doi:10.1029/2009JE003342.

Mustard, J. F., B. L. Ehlmann, S. L. Murchie, F. Poulet, N. Mangold, J. W. Head, J. P. Bibring, and L. H. Roach (2009), Composition, Morphology, and Stratigraphy of Noachian Crust around the Isidis basin, *Journal of Geophysical Research-Planets*, *114*, doi:10.1029/2009je003349.

Mustard, J. F., et al. (2008), Hydrated silicate minerals on mars observed by the Mars reconnaissance orbiter CRISM instrument, *Nature*, *454*(7202), 305-309, doi:10.1038/nature07097.

Mustard, J. F., and J. E. Hays (1997), Effects of hyperfine particles on reflectance spectra from 0.3 to 25 mu m, *Icarus*, *125*(1), 145-163, doi:10.1006/icar.1996.5583.

Pan, C., A. D. Rogers, and J. R. Michalski (2015), Thermal and near-infrared analyses of central peaks of Martian impact craters: Evidence for a heterogeneous Martian crust, *Journal of Geophysical Research-Planets*, *120*(4), 662-688, doi:10.1002/2014je004676.

Poulet, F., N. Mangold, D. Loizeau, J. P. Bibring, Y. Langevin, J. Michalski, and B. Gondet (2008), Abundance of minerals in the phyllosilicate-rich units on Mars, *Astron. Astrophys.*, *487*(2), L41-U193, doi:10.1051/0004-6361:200810150.

Ramsey, M. S., and P. R. Christensen (1998), Mineral abundance determination: Quantitative deconvolution of thermal emission spectra, *Journal of Geophysical Research-Solid Earth*, *103*(B1), 577-596, doi:10.1029/97JB02784.

Roach, L. H., J. F. Mustard, G. Swayze, R. E. Milliken, J. L. Bishop, S. L. Murchie, and K. Lichtenberg (2010), Hydrated mineral stratigraphy of Ius Chasma, Valles Marineris, *Icarus*, *206*(1), 253-268, doi:10.1016/j.icarus.2009.09.003.

Rogers, A. D., and O. Aharonson (2008), Mineralogical composition of sands in Meridiani Planum determined from Mars Exploration Rover data and comparison to orbital measurements, *Journal of Geophysical Research-Planets*, *113*(E6), E06S14, doi:10.1029/2007je002995.

Rogers, A. D., and P. R. Christensen (2007), Surface mineralogy of Martian low-albedo regions from MGS-TES data: Implications for upper crustal evolution and surface alteration, *Journal of Geophysical Research-Planets*, *112*(E1), E01003, doi:10.1029/2006je002727.

Rogers, A. D., O. Aharonson, and J. Bandfield (2009), Geologic context of in situ rocky exposures in Mare Serpentis, Mars: Implications for crust and regolith evolution in the cratered highlands, *Icarus*, *200*, 446-462, doi:10.1016/j.icarus.2008.11.026.

Rogers, A. D. (2011), Crustal compositions exposed by impact craters in the Tyrrhena Terra region of Mars: Considerations for Noachian environments, *Earth Planet. Sci. Lett.*, *301*(1-2), 353-364, doi:10.1016/j.epsl.2010.11.020.

Rogers, A. D., and R. L. Fergason (2011), Regional-scale stratigraphy of surface units in Tyrrhena and Iapygia Terrae, Mars: Insights into highland crustal evolution and alteration history, *Journal of Geophysical Research-Planets*, *116*, E08005, doi:E0800510.1029/2010je003772.

Ruff, S. W., and P. R. Christensen (2007), Basaltic andesite, altered basalt, and a TES-based search for smectite clay minerals on Mars, *Geophysical Research Letters*, *34*(10), L10204, doi:10.1029/2007GL029602.

Ruff, S. W., P. R. Christensen, P. W. Barbera, and D. L. Anderson (1997), Quantitative thermal emission spectroscopy of minerals: A laboratory technique for measurement and calibration, *Journal of Geophysical Research-Solid Earth*, *102*(B7), 14899-14913, doi:10.1029/97jb00593.

Ruff, S. W., P. R. Christensen, D. L. Blaney, W. H. Farrand, J. R. Johnson, J. R. Michalski, J. E. Moersch, S. P. Wright, and S. W. Squyres (2006), The rocks of Gusev Crater as viewed by the Mini-TES instrument, *Journal of Geophysical Research-Planets*, *111*(E12), doi:10.1029/2006je002747.

Ruff, S. W., et al. (2011), Characteristics, distribution, origin, and significance of opaline silica observed by the Spirit rover in Gusev crater, Mars, *Journal of Geophysical Research-Planets*, *116*, 48, doi:10.1029/2010je003767.

Salisbury, J. W., and J. W. Eastes (1985), THE EFFECT OF PARTICLE-SIZE AND POROSITY ON SPECTRAL CONTRAST IN THE MIDINFRARED, *Icarus*, *64*(3), 586-588, doi:10.1016/0019-1035(85)90078-8.

Salisbury, J. W., and A. Wald (1992), THE ROLE OF VOLUME SCATTERING IN REDUCING SPECTRAL CONTRAST OF RESTSTRAHLEN BANDS IN SPECTRA OF POWDERED MINERALS, *Icarus*, *96*(1), 121-128, doi:10.1016/0019-1035(92)90009-v.

Salisbury, J. W., L. S. Walter, and N. Vergo (1987), Mid-infrared (2.1–25 mm) spectra of minerals*Rep.*, U.S. Geological Survey, Reston, VA.

Salisbury, J. W., L. S. Walter, N. Vergo, and D. M. D'Aria (1991), *Infrared (2.1-25 µm) spectra of minerals*, The Johns Hopkins University Press, Baltimore.

Smith, M. D., J. L. Bandfield, and P. R. Christensen (2000), Separation of atmospheric and surface spectral features in Mars Global Surveyor Thermal Emission Spectrometer (TES) spectra, *Journal of Geophysical Research-Planets*, *105*(E4), 9589-9607, doi:10.1029/1999je001105.

Sperazza, M., J. N. Moore, and M. S. Hendrix (2004), High-resolution particle size analysis of naturally occurring very fine-grained sediment through laser diffractometry, Journal of Sedimentary Research, 74(5), 736-743, doi:10.1306/031104740736.

Squyres, S. W., et al. (2004), In situ evidence for an ancient aqueous environment at Meridiani Planum, Mars, *Science*, *306*(5702), 1709-1714, doi:10.1126/science.1104559.

Thorpe, M.T., A. D. Rogers, T. Bristow, and C. Pan (2015), Quantitative Compositional Analysis of Sedimentary Materials Using Thermal Emission Spectroscopy: 1. Application to Sedimentary Rocks, *Journal of Geophysical Research-Planets*, 2015JE004863R, in press..

Tornabene, L. L., J. E. Moersch, H. Y. McSween Jr, V. E. Hamilton, J. L. Piatek, and P. R. Christensen (2008), Surface and crater-exposed lithologic units of the Isidis Basin as mapped by coanalysis of

THEMIS and TES derived data products, *Journal of Geophysical Research, 113*(E10), E10001, doi:10.1029/2007JE002988.

Viviano, C. E., and J. E. Moersch (2013), Using THEMIS data to resolve the discrepancy between CRISM/OMEGA and TES modeled phyllosilicate abundance in Mawrth Vallis, *Icarus, 226*(1), 497-509, doi:10.1016/j.icarus.2013.06.005.

Wold, H. (1982), Soft modelling: the basic design and some extensions, *Systems under indirect observation, Part II*, 1-53.

Wold, S., M. Sjostrom, and L. Eriksson (2001), PLS-regression: a basic tool of chemometrics, *Chemometrics and Intelligent Laboratory Systems, 58*(2), 109-130, doi:10.1016/s0169-7439(01)00155-1.

Wray, J. J., B. L. Ehlmann, S. W. Squyres, J. F. Mustard, and R. L. Kirk (2008), Compositional stratigraphy of clay-bearing layered deposits at Mawrth Vallis, Mars, *Geophysical Research Letters, 35*(12), 6, doi:10.1029/2008gl034385.

Wray, J. J., et al. (2011), Columbus crater and other possible groundwater-fed paleolakes of Terra Sirenum, Mars, *Journal of Geophysical Research-Planets, 116*, 41, doi:10.1029/2010je003694.

Chapter 5 Conclusion and future work

Understanding the geologic evolution of Mars requires a detailed characterization of Martian surface compositions and their geologic settings. Because much of the Martian surface is covered with regolith or unconsolidated materials, in this work I focused on key locations in which to characterize Martian crustal materials, and assessed the degree of influence from physical sorting processes on measured surface compositions from orbit.

First, I identified and characterized 26 crater central peaks with distinctive spectral signatures from surrounding plains with thermal infrared and visible/near-infrared data, based on a global survey of Martian impact craters between 10-200 km diameter of 866 craters. The distribution of spectrally distinct central peaks (SDCPs) shows some degree of regional clustering, with most craters found in western Noachis Terra, Tyrrhena Terra, within the northern rim of Hellas Basin, and fewer in the northern lowlands, suggesting that subsurface diversity in crust-forming compositions, physical properties or alteration environments are present. The western Noachis Terra area is the only region where multiple THEMIS-defined spectral units are present in individual central peaks, suggesting crustal stratigraphies of igneous units, or ejected crustal materials, or impact melt from the Argyre Basin.

Detailed mapping for western Noachis Terra area is needed to further investigate the geologic history of this potentially unique region, as well as to understand its relationship to nearby Thaumasia Planum and outflow/chaos terrain. High resolution geomorphology and mineral distribution identification and mapping will help to understand the origin of the three distinct units detected in the crater central uplifts. The nearby Thaumasia highlands may have undergone a

distinct geologic evolution from western Noachis Terra [*Dohm et al.*, 2001]. In addition, there are multiple olivine-bearing units exposed in Ladon valles and Ares valles, which may share a similar origin with subsurface olivine units as in western Noachis Terra. By comparing these regions for compositional stratigraphy, geomorphology and physical properties, it will help reveal processes related to theevolution of the Tharsis rise and surroundings.

Second, I assessed the degree and occurrence of thermophysical and compositional heterogeneity for 42 dune fields and sand deposits within impact craters located between 0°N, 43°E to -14.3°N, 195°E on Mars. Among these, only four exhibit spatial heterogeneity in spectral properties and composition. Two of the four sites show a strong positive relationship between particle size and olivine abundance. This is similar to the observation in "El Dorado" dune field, which was investigated by the Mars Exploration Rover *Spirit*. However, this trend is opposite of what was observed for basaltic sediments on Earth. The rarity of compositional heterogeneity within dune fields may indicate phenocryst-poor source rocks; sorting within individual bedforms may be present but is below the resolution of available instruments. Alternatively, this could indicate that aeolian transport/processing is not a significant effect at the regional or global scale.

Lastly, I characterized the TIR spectral properties of compacted, very fine-grained mineral mixtures of oligoclase, augite, calcite, montmorillonite, and gypsum and then assessed the linearity of spectral combination using non-negative linear least squares minimization. I also applied a partial least squares model to thermal emission spectra of synthetic mixtures and natural mudstones to assess its applicability for retrieving mineral abundances from to fine-grained rocks. Non-linear relationships between known and modeled abundance are observed. However, using a partial least squares method, accurate mineral abundances can be recovered from TIR spectra of synthetic mixtures (within +/- 10% of known abundance for 78-90% of mixtures) and fine-grained rocks

(within ±10% for 85% of the mudstone samples).This method could potentially be applied to landed or orbital TIR observations, provided atmospheric components were first removed.

An improvement of the partial least squares model application would be two fold. First, non-negative partial least squares incorporated with constraints to output abundance to 0-100% will be applied to improve the accuracy and robustness. In addition, constraining the total abundance of minerals from single mixture to 100% will be added if it is needed. Second, the improved partial least squares algorithm will be applied to thermal infrared data orbiting on Martian surface. Starting with atmospheric corrected TES data, a comprehensive spectra library including rocks and minerals will be used as a training dataset. Much attention will be paid to areas with low-dust sedimentary deposits hosting phyllosilicates and the primary goal will be to look for detectable abundances of phyllosilicates through thermal infrared data.

Reference

Dohm, J. M., J. C. Ferris, V. R. Baker, R. C. Anderson, T. M. Hare, R. G. Strom, N. G. Barlow, K. L. Tanaka, J. E. Klemaszewski, and D. H. Scott (2001), Ancient drainage basin of the Tharsis region, Mars: Potential source for outflow channel systems and putative oceans or paleolakes, *J. Geophys. Res.-Planets*, *106*(E12), 32943-32958, doi:10.1029/2000je001468.

Bibliography

Aben, L. K. (2003), Extraterrestrial dunes: An introduction to the special issue on planetary dune systems, Arizona State University Tempe, Arizona.

Anderson, R. S., and K. L. Bunas (1993), Grain-size segregation and stratigraphy in aeolian ripples modeled with a cellular-automaton, *Nature*, *365*(6448), 740-743, doi:10.1038/365740a0.

Ansan, V., et al. (2011), Stratigraphy, mineralogy, and origin of layered deposits inside terby crater, mars, *Icarus*, *211*(1), 273-304, doi:10.1016/j.icarus.2010.09.011.

Baldridge, A. M., and P. R. Christensen (2009), A laboratory technique for thermal emission measurement of hydrated minerals, *Applied spectroscopy*, *63*(6), 678-688.

Baldridge, A. M., J. D. Farmer, and J. E. Moersch (2004), Mars remote-sensing analog studies in the badwater basin, death valley, california, *Journal of Geophysical Research-Planets*, *109*(E12), 18, doi:10.1029/2004je002315.

Bandfield, J. L. (2002), Global mineral distributions on mars, *Journal of Geophysical Research*, *107*(E6), 5042, doi:10.1029/2001JE001510.

Bandfield, J. L., P. R. Christensen, and M. D. Smith (2000), Spectral data set factor analysis and end-member recovery: Application to analysis of martian atmospheric particulates, *Journal of Geophysical Research-Planets*, *105*(E4), 9573-9587, doi:10.1029/1999je001094.

Bandfield, J. L., K. S. Edgett, and P. R. Christensen (2002), Spectroscopic study of the moses lake dune field, washington: Determination of compositional distributions and source lithologies, *Journal of Geophysical Research-Planets*, *107*(E11), doi:10.1029/2000je001469.

Bandfield, J. L., C. S. Edwards, D. R. Montgomery, and B. D. Brand (2013), The dual nature of the martian crust: Young lavas and old clastic materials, *Icarus*, *222*(1), 188-199, doi:10.1016/j.icarus.2012.10.023.

Bandfield, J. L., T. D. Glotch, and P. R. Christensen (2003), Spectroscopic identification of carbonate minerals in the martian dust, *Science*, *301*(5636), 1084-1087, doi:10.1126/science.1088054.

Bandfield, J. L., D. Rogers, M. D. Smith, and P. R. Christensen (2004a), Atmospheric correction and surface spectral unit mapping using thermal emission imaging system data, *Journal of Geophysical Research-Planets*, *109*(E10), E10008, doi:10.1029/2004je002289.

Bandfield, J. L., D. Rogers, M. D. Smith, and P. R. Christensen (2004b), Atmospheric correction and surface spectral unit mapping using thermal emission imaging system data, *Journal of Geophysical Research-Planets*, *109*(E10), doi:E1000810.1029/2004je002289.

Bandfield, J. L., and M. D. Smith (2003), Multiple emission angle surface-atmosphere separations of thermal emission spectrometer data, *Icarus*, *161*(1), 47-65, doi:10.1016/s0019-1035(02)00025-8.

Baratoux, D., P. Pinet, A. Gendrin, L. Kanner, J. Mustard, Y. Daydou, J. Vaucher, and J. P. Bibring (2007), Mineralogical structure of the subsurface of syrtis major from omega observations of lobate ejecta blankets, *Journal of Geophysical Research-Planets*, *112*(E8), doi:10.1029/2007je002890.

Baratoux, D., M. J. Toplis, M. Monnereau, and O. Gasnault (2011), Thermal history of mars inferred from orbital geochemistry of volcanic provinces, *Nature*, *472*(7343), 338-U235, doi:10.1038/nature09903.

Barlow, N., J. Boyce, F. Costard, R. Craddock, J. Garvin, S. Sakimoto, R. Kuzmin, D. Roddy, and L. Soderblom (2000), Standardizing the nomenclature of martian impact crater ejecta

morphologies, *Journal of Geophysical Research*, *105*(E11), 26733, doi:10.1029/2000JE001258.

Barlow, N. G., and C. B. Perez (2003), Martian impact crater ejecta morphologies as indicators of the distribution of subsurface volatiles, *Journal of Geophysical Research-Planets*, *108*(E8), doi:10.1029/2002je002036.

Barnhart, C. J., and F. Nimmo (2011), Role of impact excavation in distributing clays over noachian surfaces, *Journal of Geophysical Research-Planets*, *116*, 14, doi:10.1029/2010je003629.

Bell III, J. (2008), *The martian surface-composition, mineralogy, and physical properties*, Cambridge University Press, Cambridge, U. K.

Bibring, J. P., et al. (2005), Mars surface diversity as revealed by the omega/mars express observations, *Science*, *307*(5715), 1576-1581, doi:10.1126/science.1108806.

Bibring, J. P., et al. (2006), Global mineralogical and aqueous mars history derived from omega/mars express data, *Science*, *312*(5772), 400-404, doi:10.1126/science.1122659.

Blatt, H., G. Middleton, and R. Murray (1980), *Origiin of sedimentary rocks*, Prentice-Hall, Englewood Cliffs, New Jersey.

Boggs, S. (1995), *Principles of seimentology and stratigraphy*, Prentice Hall, Englewood Cliffs, New Jersey.

Boyce, J. M., and H. Garbeil (2007), Geometric relationships of pristine martian complex impact craters, and their implications to mars geologic history, *Geophysical Research Letters*, *34*(16), doi:10.1029/2007gl029731.

Boynton, W. V., et al. (2009), Evidence for calcium carbonate at the mars phoenix landing site, *Science*, *325*(5936), 61-64, doi:10.1126/science.1172768.

Bridges, N. T., P. E. Geissler, A. S. McEwen, B. J. Thomson, F. C. Chuang, K. E. Herkenhoff, L. P. Keszthelyi, and S. Martinez-Alonso (2007), Windy mars: A dynamic planet as seen by the hirise camera, *Geophysical Research Letters*, *34*(23), doi:10.1029/2007gl031445.

Bullock, M. A., and J. M. Moore (2007), Atmospheric conditions on early mars and the missing layered carbonates, *Geophysical Research Letters*, *34*(19), doi:10.1029/2007gl030688.

Cannon, K. M., J. F. Mustard, C. D. K. Herd, and J. Filiberto (2014), Melting mars with impacts: Proximal melt deposits and their compositions as determined by remote sensing, paper presented at Lunar and Planetary Institute Science Conference Abstracts, LPI, Houston, TX.

Carr, M. H., and J. W. Head, III (2010), Geologic history of mars, *Earth and Planetary Science Letters*, *294*(3-4), 185-203, doi:10.1016/j.epsl.2009.06.042.

Carter, J., and F. Poulet (2013), Ancient plutonic processes on mars inferred from the detection of possible anorthositic terrains, *Nature Geoscience*, *6*(12), 1008-1012, doi:10.1038/ngeo1995.

Carter, J., F. Poulet, J. P. Bibring, N. Mangold, and S. Murchie (2013), Hydrous minerals on mars as seen by the crism and omega imaging spectrometers: Updated global view, *Journal of Geophysical Research-Planets*, *118*(4), 831-858, doi:10.1029/2012je004145.

Carter, J., F. Poulet, J. P. Bibring, and S. Murchie (2010), Detection of hydrated silicates in crustal outcrops in the northern plains of mars, *Science*, *328*(5986), 1682, doi:10.1126/science.1189013.

Carter, L. M., B. A. Campbell, J. W. Holt, R. J. Phillips, N. E. Putzig, S. Mattei, R. Seu, C. H. Okubo, and A. F. Egan (2009), Dielectric properties of lava flows west of ascraeus mons, mars, *Geophysical Research Letters*, *36*, L23204, doi:10.1029/2009gl041234.

Caudill, C. M., L. L. Tornabene, A. S. McEwen, S. Byrne, L. Ojha, and S. Mattson (2012), Layered megablocks in the central uplifts of impact craters, *Icarus*, *221*(2), 710-720, doi:10.1016/j.icarus.2012.08.033.

Chojnacki, M., D. M. Burr, and J. E. Moersch (2014), Valles marineris dune fields as compared with other martian populations: Diversity of dune compositions, morphologies, and thermophysical properties, *Icarus*, *230*, 96-142, doi:10.1016/j.icarus.2013.08.018.

Chojnacki, M., D. M. Burr, J. E. Moersch, and T. I. Michaels (2011), Orbital observations of contemporary dune activity in endeavor crater, meridiani planum, mars, *Journal of Geophysical Research-Planets*, *116*, doi:10.1029/2010je003675.

Christensen, P. R., et al. (1992), Thermal emission spectrometer experiment: Mars observer mission, *Journal of Geophysical Research-Planets*, *97*(E5), 7719-7734, doi:10.1029/2000JE001370.

Christensen, P. R., et al. (2003), Morphology and composition of the surface of mars: Mars odyssey themis results, *Science*, *300*(5628), 2056-2061, doi:10.1126/science.1080885.

Christensen, P. R., et al. (2000a), Detection of crystalline hematite mineralization on mars by the thermal emission spectrometer: Evidence for near-surface water, *Journal of Geophysical Research-Planets*, *105*(E4), 9623-9642, doi:10.1029/1999je001093.

Christensen, P. R., et al. (2001), Mars global surveyor thermal emission spectrometer experiment: Investigation description and surface science results, *Journal of Geophysical Research-Planets*, *106*(E10), 23823-23871, doi:10.1029/2000JE001370.

Christensen, P. R., J. L. Bandfield, M. D. Smith, V. E. Hamilton, and R. N. Clark (2000b), Identification of a basaltic component on the martian surface from thermal emission spectrometer data, *Journal of Geophysical Research-Planets*, *105*(E4), 9609-9621, doi:10.1029/1999je001127.

Christensen, P. R., R. L. Fergason, C. S. Edwards, and J. Hill (2013), Themis-derived thermal inertia mosaic of mars: Product description and science results, paper presented at Lunar and Planetary Science Conference.

Christensen, P. R., et al. (2004a), The thermal emission imaging system (themis) for the mars 2001 odyssey mission, *Space Sci. Rev.*, *110*(1-2), 85-130, doi:10.1023/b:spac.0000021008.16305.94.

Christensen, P. R., et al. (2005), Evidence for magmatic evolution and diversity on mars from infrared observations, *Nature*, *436*(7052), 882-882, doi:10.1038/nature04075.

Christensen, P. R., and H. J. Moore (1992), The martian surface layer, in *Mars*, edited by H. H. Kieffer, Jakosky, B. M. ,Snyder, C. W.,Matthews, M. S., pp. 686-729, University of Arizona Press, Tucson.

Christensen, P. R., et al. (2004b), Initial results from the mini-tes experiment in gusev crater from the spirit rover, *Science*, *305*(5685), 837-842, doi:10.1126/science.1100564.

Christensen, P. R., et al. (2004c), Mineralogy at meridiani planum from the mini-tes experiment on the opportunity rover, *Science*, *306*(5702), 1733-1739, doi:10.1126/science.1104909.

Clancy, R. T., S. W. Lee, G. R. Gladstone, W. W. McMillan, and T. Rousch (1995), A new model for mars atmospheric dust based upon analysis of ultraviolet through infrared observations from mariner-9, viking, and phobos, *Journal of Geophysical Research-Planets*, *100*(E3), 5251-5263, doi:10.1029/94je01885.

Clark, R. N. (1999), Spectroscopy of rocks and minerals, and principles of spectroscopy, in *Manual of remote sensing, volume 3, remote sensing for the earth sciences*, edited by A. N. Rencz, pp. 3-58, John Wiley and Sons, New York.

Clark, R. N., and T. L. Roush (1984), Reflectance spectroscopy - quantitative-analysis techniques for remote-sensing applications, *Journal of Geophysical Research*, *89*(NB7), 6329-6340, doi:10.1029/JB089iB07p06329.

Clegg, S. M., E. Sklute, M. D. Dyar, J. E. Barefield, and R. C. Wiens (2009), Multivariate analysis of remote laser-induced breakdown spectroscopy spectra using partial least squares, principal component analysis, and related techniques, *Spectrochimica Acta Part B-Atomic Spectroscopy*, *64*(1), 79-88, doi:10.1016/j.sab.2008.10.045.

Clenet, H., P. Pinet, G. Ceuleneer, Y. Daydou, F. Heuripeau, C. Rosemberg, J. P. Bibring, G. Bellucci, F. Altieri, and B. Gondet (2013), A systematic mapping procedure based on the modified gaussian model to characterize magmatic units from olivine/pyroxenes mixtures: Application to the syrtis major volcanic shield on mars, *Journal of Geophysical Research-Planets*, *118*(8), 1632-1655, doi:10.1002/jgre.20112.

Clenet, H., P. Pinet, Y. Daydou, F. Heuripeau, C. Rosemberg, D. Baratoux, and S. Chevrel (2011), A new systematic approach using the modified gaussian model: Insight for the characterization of chemical composition of olivines, pyroxenes and olivine-pyroxene mixtures, *Icarus*, *213*(1), 404-422, doi:10.1016/j.icarus.2011.03.002.

Cloutis, E. A., P. M. Asher, and S. A. Mertzman (2002), Spectral reflectance properties of zeolites and remote sensing implications, *Journal of Geophysical Research-Planets*, *107*(E9), doi:10.1029/2000je001467.

Coblentz, W. W. (1906), *Investigations of infrared spectra*, Carnegie institution of Washington, Washington, D.C.

Cooper, C. D., and J. F. Mustard (2002), Spectroscopy of loose and cemented sulfate-bearing soils: Implications for duricrust on mars, *Icarus*, *158*(1), 42-55, doi:10.1006/icar.2002.6874.

Cornwall, C., J. L. Bandfield, T. N. Titus, B. C. Schreiber, and D. R. Montgomery (2015), Physical abrasion of mafic minerals and basalt grains: Application to martian aeolian deposits, *Icarus*, *256*, 13-21, doi:10.1016/j.icarus.2015.04.020.

Croft, S. K. (1985), The scaling of complex craters, *Journal of Geophysical Research: Solid Earth 90*(S02), C828-C842.

Cudahy, T. J., R. Hewson, J. F. Huntington, M. A. Quigley, P. S. Barry, and I. Ieee (2001), *The performance of the satellite-borne hyperion hyperspectral vnir-swir imaging system for mineral mapping at mount fitton, south australia*, 314-316 pp.

Dehouck, E., N. Mangold, S. Le Mouelic, V. Ansan, and F. Poulet (2010), Ismenius cavus, mars: A deep paleolake with phyllosilicate deposits, *Planet Space Sci.*, *58*(6), 941-946, doi:10.1016/j.pss.2010.02.005.

Diniega, S., S. Byrne, N. T. Bridges, C. M. Dundas, and A. S. McEwen (2010), Seasonality of present-day martian dune-gully activity, *Geology*, *38*(11), 1047-1050, doi:10.1130/g31287.1.

Dobrea, E. Z. N., et al. (2010), Mineralogy and stratigraphy of phyllosilicate-bearing and dark mantling units in the greater mawrth vallis/west arabia terra area: Constraints on geological origin, *Journal of Geophysical Research-Planets*, *115*, doi:10.1029/2009je003351.

Dohm, J. M., J. C. Ferris, V. R. Baker, R. C. Anderson, T. M. Hare, R. G. Strom, N. G. Barlow, K. L. Tanaka, J. E. Klemaszewski, and D. H. Scott (2001), Ancient drainage basin of the tharsis region, mars: Potential source for outflow channel systems and putative oceans or paleolakes, *Journal of Geophysical Research-Planets*, *106*(E12), 32943-32958, doi:10.1029/2000je001468.

Dyar, M. D., M. L. Carmosino, E. A. Breves, M. V. Ozanne, S. M. Clegg, and R. C. Wiens (2012), Comparison of partial least squares and lasso regression techniques as applied to laser-induced breakdown spectroscopy of geological samples, *Spectrochimica Acta Part B-Atomic Spectroscopy*, *70*, 51-67, doi:10.1016/j.sab.2012.04.011.

Edgett, K. S., and P. R. Christensen (1991), The particle-size of martian aeolian dunes, *Journal of Geophysical Research-Planets*, *96*(E5), 22765-22776, doi:10.1029/91je02412.

Edwards, C. S., J. L. Bandfield, P. R. Christensen, and R. L. Fergason (2009), Global distribution of bedrock exposures on mars using themis high-resolution thermal inertia, *Journal of Geophysical Research-Planets*, *114*, E11001, doi:10.1029/2009je003363.

Ehlmann, B. L., J. F. Mustard, C. I. Fassett, S. C. Schon, J. W. Head, D. J. D. Marais, J. A. Grant, and S. L. Murchie (2008a), Clay minerals in delta deposits and organic preservation potential on mars, *Nat. Geosci.*, *1*(6), 355-358, doi:10.1038/ngeo207.

Ehlmann, B. L., J. F. Mustard, S. L. Murchie, J.-P. Bibring, A. Meunier, A. A. Fraeman, and Y. Langevin (2011a), Subsurface water and clay mineral formation during the early history of mars, *Nature*, *479*(7371), 53-60, doi:10.1038/nature10582.

Ehlmann, B. L., J. F. Mustard, S. L. Murchie, J. P. Bibring, A. Meunier, A. A. Fraeman, and Y. Langevin (2011b), Subsurface water and clay mineral formation during the early history of mars, *Nature*, *479*(7371), 53-60, doi:10.1038/nature10582.

Ehlmann, B. L., et al. (2008b), Orbital identification of carbonate-bearing rocks on mars, *Science*, *322*(5909), 1828-1832, doi:10.1126/science.1164759.

Ehlmann, B. L., et al. (2009), Identification of hydrated silicate minerals on mars using mro-crism: Geologic context near nili fossae and implications for aqueous alteration, *Journal of Geophysical Research-Planets*, *114*, doi:10.1029/2009je003339.

Farmer, V. C. (1974), *Infrared spectra of minerals*, Mineralogical society.

Farquhar, J., M. H. Thiemens, and T. Jackson (1998), Atmosphere-surface interactions on mars: Delta o-17 measurements of carbonate from alh 84001, *Science*, *280*(5369), 1580-1582, doi:10.1126/science.280.5369.1580.

Fedo, C. M., I. O. McGlynn, and H. Y. McSween (2015), Grain size and hydrodynamic sorting controls on the composition of basaltic sediments: Implications for interpreting martian soils, *Earth and Planetary Science Letters*, *423*, 67-77, doi:10.1016/j.epsl.2015.03.052.

Feely, K. C., and P. R. Christensen (1999), Quantitative compositional analysis using thermal emission spectroscopy: Application to igneous and metamorphic rocks, *Journal of Geophysical Research-Planets*, *104*(E10), 24195-24210, doi:10.1029/1999JE001034.

Feldman, W. C., et al. (2002), Global distribution of neutrons from mars: Results from mars odyssey, *Science*, *297*(5578), 75-78, doi:10.1126/science.1073541.

Fenton, L. K. (2005), Potential sand sources for the dune fields in noachis terra, mars, *Journal of Geophysical Research-Planets*, *110*(E11), doi:10.1029/2005je002436.

Fenton, L. K., J. L. Bandfield, and A. W. Ward (2003), Aeolian processes in proctor crater on mars: Sedimentary history as analyzed from multiple data sets, *Journal of Geophysical Research-Planets*, *108*(E12), doi:10.1029/2002je002015.

Fenton, L. K., and R. K. Hayward (2010), Southern high latitude dune fields on mars: Morphology, aeolian inactivity, and climate change, *Geomorphology*, *121*(1-2), 98-121, doi:10.1016/j.geomorph.2009.11.006.

Fenton, L. K., and M. T. Mellon (2006), Thermal properties of sand from thermal emission spectrometer (tes) and thermal emission imaging system (themis): Spatial variations within

the proctor crater dune field on mars, *Journal of Geophysical Research-Planets*, *111*(E6), doi:10.1029/2004je002363.

Fergason, R. L., P. R. Christensen, J. F. Bell, M. P. Golombek, K. E. Herkenhoff, and H. H. Kieffer (2006), Physical properties of the mars exploration rover landing sites as inferred from mini-tes-derived thermal inertia, *Journal of Geophysical Research-Planets*, *111*(E2), doi:10.1029/2005je002583.

Filiberto, J., and R. Dasgupta (2011), Fe2+-mg partitioning between olivine and basaltic melts: Applications to genesis of olivine-phyric shergottites and conditions of melting in the martian interior, *Earth and Planetary Science Letters*, *304*(3-4), 527-537, doi:10.1016/j.epsl.2011.02.029.

French, B. (1998), Traces of catastrophe: A handbook of shock-metamorphic effects in terrestrial meteorite impact structures.

Gaffey, S. J., L. A. McFadden, D. B. Nash, and C. M. Pieters (1993), Ultraviolet, visible, and near-infrared reflectance spectroscopy: Laboratory spectra of geologica materials, in *Remote geochemical analysis: Elemental and mineralogical composition*, edited by C. M. Pieters and P. A. J. Englert, Cambridge University Press, Cambridge, UK.

Gardin, E., P. Allemand, C. Quantin, S. Silvestro, and C. Delacourt (2012), Dune fields on mars: Recorders of a climate change?, *Planetary and Space Science*, *60*(1), 314-321, doi:10.1016/j.pss.2011.10.004.

Geissler, P. E. (2005), Three decades of martian surface changes, *Journal of Geophysical Research-Planets*, *110*(E2), 23, doi:10.1029/2004je002345.

Gillespie, A. R. (1986), Lithologic mapping of silicate rocks using tims, paper presented at The TIMS Data User's Workshop., Jet Propulsion Laboratory, Jet Propulsion Laboratory, Pasadena, CA.

Gillespie, A. R., A. B. Kahle, and R. E. Walker (1986), Color enhancement of highly correlated images. 1. Decorrelaton and hsi contrast stretches, *Remote Sensing of Environment*, *20*(3), 209-235, doi:10.1016/0034-4257(86)90044-1.

Glotch, T. D., J. L. Bandfield, P. R. Christensen, W. M. Calvin, S. M. McLennan, B. C. Clark, A. D. Rogers, and S. W. Squyres (2006), Mineralogy of the light-toned outcrop at meridiani planum as seen by the miniature thermal emission spectrometer and implications for its formation, *Journal of Geophysical Research-Planets*, *111*(E12), 14, doi:10.1029/2005je002672.

Greeley, R., and J. Guest (1987), *Geologic map of the eastern equatorial region of mars*, Geological Survey (US).

Greeley, R., and A. R. Peterfreund (1981), Aeolian" megaripples" examples from mono craters, california and northern iceland [abs], paper presented at Geological Society of America, Abstracts with Programs.

Grotzinger, J. P., et al. (2005), Stratigraphy and sedimentology of a dry to wet eolian depositional system, burns formation, meridiani planum, mars, *Earth Planet. Sci. Lett.*, *240*(1), 11-72, doi:10.1016/j.epsl.2005.09.039.

Grotzinger, J. P., and R. E. Milliken (2012), The sedimentary rock record of mars: Distribution, origins, and global stratigraphy, in *Sedimentary geology of mars*, edited by J. P. Grotzinger and R. E. Milliken, pp. 1-48.

Grotzinger, J. P., et al. (2014), A habitable fluvio-lacustrine environment at yellowknife bay, gale crater, mars, *Science*, *343*(6169), 14, doi:10.1126/science.1242777.

Hamilton, V. E., and P. R. Christensen (2000), Determining the modal mineralogy of mafic and ultramafic igneous rocks using thermal emission spectroscopy, *Journal of Geophysical Research-Planets*, *105*(E4), 9717-9733, doi:10.1029/1999je001113.

Hamilton, V. E., and S. W. Ruff (2012), Distribution and characteristics of adirondack-class basalt as observed by mini-tes in gusev crater, mars and its possible volcanic source, *Icarus*, *218*(2), 917-949, doi:10.1016/j.icarus.2012.01.011.

Hapke, B. (1981), Bidirectional reflectance spectroscopy .1. Theory, *Journal of Geophysical Research*, *86*(NB4), 3039-3054, doi:10.1029/JB086iB04p03039.

Hapke, B. (1993a), *Introduction to the theory of reflectance and emittance spectroscopy*, Cambridge University Press, New York.

Hapke, B. W. (1993b), *Theory of reflectance and emittance spectroscopy*, Cambridge University Press, Cambridge, U.K.

Hausrath, E. M., A. K. Navarre-Sitchler, P. B. Sak, C. I. Steefel, and S. L. Brantley (2008), Basalt weathering rates on earth and the duration of liquid water on the plains of gusev crater, mars, *Geology*, *36*(1), 67-70, doi:10.1130/g24238a.1.

Hayward, R. K., L. K. Fenton, and T. N. Titus (2014), Mars global digital dune database (mgd(3)): Global dune distribution and wind pattern observations, *Icarus*, *230*, 38-46, doi:10.1016/j.icarus.2013.04.011.

Hayward, R. K., K. F. Mullins, L. K. Fenton, T. M. Hare, T. N. Titus, M. C. Bourke, A. Colaprete, and P. R. Christensen (2007), Mars global digital dune database and initial science results, *Journal of Geophysical Research-Planets*, *112*(E11), doi:10.1029/2007je002943.

Hecker, C., J. H. Dilles, M. van der Meijde, and F. D. van der Meer (2012), Thermal infrared spectroscopy and partial least squares regression to determine mineral modes of granitoid rocks, *Geochemistry Geophysics Geosystems*, *13*, doi:10.1029/2011gc004004.

Hook, S. J., J. E. Dmochowski, K. A. Howard, L. C. Rowan, K. E. Karlstrom, and J. M. Stock (2005a), Mapping variations in weight percent silica measured from multispectral thermal infrared imagery—examples from the hiller mountains, nevada, USA and tres virgenes-la reforma, baja california sur, mexico, *Remote sensing of environment*, *95*(3), 273-289, doi:10.1016/j.rse.2004.11.020.

Hook, S. J., J. E. Dmochowski, K. A. Howard, L. C. Rowan, K. E. Karlstrom, and J. M. Stock (2005b), Mapping variations in weight percent silica measured from multispectral thermal infrared imagery - examples from the hiller mountains, nevada, USA and tres virgenes-la reforma, baja california sur, mexico, *Remote Sensing of Environment*, *95*(3), 273-289, doi:10.1016/j.rse.2004.11.020.

Horgan, B., and J. F. Bell, III (2012), Widespread weathered glass on the surface of mars, *Geology*, *40*(5), 391-394, doi:10.1130/g32755.1.

Horgan, B., E. A. Cloutis, P. Mann, and J. F. Bell (2014), Near-infrared spectra of ferrous mineral mixtures and methods for their identification in planetary surface spectra, *Icarus*, *234*, 132-154, doi:10.1016/j.icarus.2014.02.031.

Horz, F., M. J. Cintala, T. H. See, F. Cardenas, and T. D. Thompson (1984), Grain-size evolution and fractionation trends in an experimental regolith, *Journal of Geophysical Research*, *89*, C183-C196, doi:10.1029/JB089iS01p0C183.

Huang, J., and L. Xiao (2014), Compositional evolution of lava plains in the syria-thaumasia block, mars, *Science China-Physics Mechanics & Astronomy*, *57*(5), 994-1000, doi:10.1007/s11433-014-5407-3.

Hunt, G. R., and L. M. Logan (1972), Variation of single-particle mid-infrared emission-spectrum with particle-size, *Appl. Optics*, *11*(1), 142-&, doi:10.1364/ao.11.000142.

Hunt, G. R., and R. K. Vincent (1968), The behavior of spectral features in the infrared emission from particulate surfaces of various grain sizes, *Journal of Geophysical Research*, *73*(18), 6039-6046, doi:10.1029/JB073i018p06039.

Hurowitz, J. A., S. M. McLennan, N. J. Tosca, R. E. Arvidson, J. R. Michalski, D. W. Ming, C. Schroder, and S. W. Squyres (2006), In situ and experimental evidence for acidic weathering of rocks and soils on mars, *Journal of Geophysical Research-Planets*, *111*(E2), doi:10.1029/2005je002515.

Jackson, M. L. (1967), Soil chemical analysis, edited, pp. 146-157, Prentice Hall of India, New Delhi, India.

Jaeger, W. L., L. P. Keszthelyi, A. S. McEwen, C. M. Dundas, and P. S. Russell (2007), Athabasca valles, mars: A lava-draped channel system, *Science*, *317*(5845), 1709-1711, doi:10.1126/science.1143315.

Jakosky, B. M. (1979), Effects of nonideal surfaces on the derived thermal-properties of mars, *Journal of Geophysical Research*, *84*, 8252-8262, doi:10.1029/JB084iB14p08252.

Jaumann, R., et al. (2005), Interior channels in martian valleys: Constraints on fluvial erosion by measurements of the mars express high resolution stereo camera, *Geophysical Research Letters*, *32*(16), doi:10.1029/2005gl023415.

Kahle, A. B., M. S. Shumate, and D. B. Nash (1984), Active airborne infrared-laser system for identification of surface rock and minerals, *Geophysical Research Letters*, *11*(11), 1149-1152, doi:10.1029/GL011i011p01149.

Keszthelyi, L., W. L. Jaeger, C. M. Dundas, S. Martinez-Alonso, A. S. McEwen, and M. P. Milazzo (2010), Hydrovolcanic features on mars: Preliminary observations from the first mars year of hirise imaging, *Icarus*, *205*(1), 211-229, doi:10.1016/j.icarus.2009.08.020.

Keszthelyi, L., S. Self, and T. Thordarson (2006), Flood lavas on earth, io and mars, *Journal of the Geological Society*, *163*, 253-264, doi:10.1144/0016-764904-503.

Kieffer, H. H., T. Martin, A. R. Peterfreund, B. M. Jakosky, E. D. Miner, and F. D. Palluconi (1977), Thermal and albedo mapping of mars during the viking primary mission, *Journal of Geophysical Research*, *82*(28), 4249-4291, doi:doi:10.1029/JS082i028p0424.

Kiminami, K., and K. Fujii (2007), The relationship between major element concentration and grain size within sandstones from four turbidite sequences in japan, *Sedimentary Geology*, *195*(3-4), 203-215, doi:10.1016/j.sedgeo.2006.08.002.

Knauth, L. P., D. M. Burt, and K. H. Wohletz (2005), Impact origin of sediments at the opportunity landing site on mars, *Nature*, *438*(7071), 1123-1128, doi:10.1038/nature04383.

Koeppen, W. C., and V. E. Hamilton (2008), Global distribution, composition, and abundance of olivine on the surface of mars from thermal infrared data, *Journal of Geophysical Research-Planets*, *113*(E5), E05001, doi:10.1029/2007je002984.

Korteniemi, J., V. P. Kostama, T. Törmänen, M. Aittola, T. Öhman, H. Lahtela, J. Raitala, and G. Neukum (2005), Complex geology of two large impact craters in tyrrhena terra, mars: Detailed analysis using mex hrsc camera data, *Journal of Geophysical Research: Planets* *110*(E12), E12S18, doi:10.1029/2005JE002427.

Kraft, M. D., J. R. Michalski, and T. G. Sharp (2003), Effects of pure silica coatings on thermal emission spectra of basaltic rocks: Considerations for martian surface mineralogy, *Geophysical Research Letters*, *30*(24), doi:10.1029/2003gl018848.

Kraft, M. D., M. Salvatore, C. Edwards, and P. Christensen (2014), Occurrence, distribution and implications of mafic igneous bedrock throughout the uzboi-ladon-margaritifer fluvial system, mars, paper presented at Lunar and Planetary Institute Science Conference Abstracts, LPI, Houston, TX.

Kruse, F., A. Lefkoff, J. Boardman, K. Heidebrecht, A. Shapiro, P. Barloon, and A. Goetz (1993), The spectral image processing system (sips)--interactive visualization and analysis of imaging spectrometer data, *Remote sensing of environment*, *44*(2-3), 145-163.

Lane, M. D., and P. R. Christensen (1998), Thermal infrared emission spectroscopy of salt minerals predicted for mars, *Icarus*, *135*(2), 528-536, doi:10.1006/icar.1998.5998.

Lane, M. D., and P. R. Christensen (2013), Determining olivine composition of basaltic dunes in gale crater, mars, from orbit: Awaiting ground truth from curiosity, *Geophys. Res. Lett.*, *40*(14), 3517-3521, doi:10.1002/grl.50621.

Lapotre, M., B. Ehlmann, F. Ayoub, S. Minson, N. Bridges, A. Fraeman, R. Arvidson, J. Eigenbrode, R. Ewing, and J. Johnson (2015), The bagnold dunes at gale crater---a key to reading the geologic record of mount sharp, paper presented at Lunar and Planetary Science Conference.

Lawson, C. L., and R. J. Hanson (1974), *Solving least squares problems*, Society for Industrial and Applied Mathematics (SIAM), doi:10.1137/1.9781611971217.

Leonard, G. L., and K. L. Tanaka (2001), *Geologic map of the hellas region of mars*, Geological Survey (US), Flagstaff, AZ.

Li, S., L. Li, R. Milliken, and K. Song (2012), Hybridization of partial least squares and neural network models for quantifying lunar surface minerals, *Icarus*, *221*(1), 208-225, doi:10.1016/j.icarus.2012.07.023.

Lucey, P. G. (2004), Mineral maps of the moon, *Geophysical Research Letters*, *31*(8), doi:10.1029/2003gl019406.

Lyon, R. (1965), Analysis of rocks by spectral infrared emission (8 to 25 microns), *Economic Geology*, *60*(4), 715-736.

Makse, H. A. (2000), Grain segregation mechanism in aeolian sand ripples, *European Physical Journal E*, *1*(2-3), 127-135, doi:10.1007/pl00014592.

Malin, M. C., et al. (2007), Context camera investigation on board the mars reconnaissance orbiter, *Journal of Geophysical Research-Planets*, *112*(E5), 25, doi:10.1029/2006je002808.

Malin, M. C., and K. S. Edgett (2000), Sedimentary rocks of early mars, *Science*, *290*(5498), 1927-1937, doi:10.1126/science.290.5498.1927.

Mangold, N. (2012), Fluvial landforms on fresh impact ejecta on mars, *Planetary and Space Science*, *62*(1), 69-85, doi:10.1016/j.pss.2011.12.009.

Mangold, N., S. Adeli, S. Conway, V. Ansan, and B. Langlais (2012), A chronology of early mars climatic evolution from impact crater degradation, *Journal of Geophysical Research-Planets*, *117*, 22, doi:10.1029/2011je004005.

Mangold, N., D. Baratoux, O. Arnalds, J. M. Bardintzeff, B. Platevoet, M. Gregoire, and P. Pinet (2011), Segregation of olivine grains in volcanic sands in iceland and implications for mars, *Earth and Planetary Science Letters*, *310*(3-4), 233-243, doi:10.1016/j.epsl.2011.07.025.

Mangold, N., A. Gendrin, B. Gondet, S. LeMouelic, C. Quantin, V. Ansan, J.-P. Bibring, Y. Langevin, P. Masson, and G. Neukum (2008), Spectral and geological study of the sulfate-rich region of west candor chasma, mars, *Icarus*, *194*(2), 519-543, doi:10.1016/j.icarus.2007.10.021.

Mangold, N., et al. (2007), Mineralogy of the nili fossae region with omega/mars express data: 2. Aqueous alteration of the crust, *Journal of Geophysical Research-Planets*, *112*(E8), doi:10.1029/2006je002835.

Marzo, G. A., A. F. Davila, L. L. Tornabene, J. M. Dohm, A. G. Fairen, C. Gross, T. Kneissl, J. L. Bishop, T. L. Roush, and C. P. McKay (2010), Evidence for hesperian impact-induced hydrothermalism on mars, *Icarus*, *208*(2), 667-683, doi:10.1016/j.icarus.2010.03.013.

Maxwell, A. E. (1977), *Multivariate analysis in behavioural research*, Chapman and Hall London, London, U. K.

McDowell, M. L., and V. E. Hamilton (2009), Seeking phyllosilicates in thermal infrared data: A laboratory and martian data case study, *Journal of Geophysical Research-Planets*, *114*, 21, doi:10.1029/2008je003317.

McEwen, A. S., et al. (2007), A closer look at water-related geologic activity on mars, *Science*, *317*(5845), 1706-1709, doi:10.1126/science.1143987.

McGlynn, I. O., C. M. Fedo, and H. Y. McSween (2011), Origin of basaltic soils at gusev crater, mars, by aeolian modification of impact-generated sediment, *Journal of Geophysical Research-Planets*, *116*, 15, doi:10.1029/2010je003712.

McGlynn, I. O., C. M. Fedo, and H. Y. McSween, Jr. (2012), Soil mineralogy at the mars exploration rover landing sites: An assessment of the competing roles of physical sorting and chemical weathering, *Journal of Geophysical Research-Planets*, *117*, doi:10.1029/2011je003861.

McLennan, S. M., et al. (2014), Elemental geochemistry of sedimentary rocks at yellowknife bay, gale crater, mars, *Science*, *343*(6169), 10, doi:10.1126/science.1244734.

McLennan, S. M., et al. (2005), Provenance and diagenesis of the evaporite-bearing burns formation, meridiani planum, mars, *Earth Planet. Sci. Lett.*, *240*(1), 95-121, doi:10.1016/j.epsl.2005.09.041.

McSween, H. Y., et al. (2006), Characterization and petrologic interpretation of olivine-rich basalts at gusev crater, mars, *Journal of Geophysical Research-Planets*, *111*(E2), doi:10.1029/2005je002477.

Melosh, H. J. (1989), *Impact cratering: A geologic process*, Oxford University Press, New York.

Melosh, H. J., and B. A. Ivanov (1999), Impact crater collapse, *Annual Review of Earth and Planetary Sciences*, *27*, 385-415, doi:10.1146/annurev.earth.27.1.385.

Mest, S. C., and D. A. Crown (2005), Millochau crater, mars: Infilling and erosion of an ancient highland impact crater, *Icarus*, *175*(2), 335-359, doi:10.1016/j.icarus.2004.12.008.

Michalski, J. R., J. Cuadros, P. B. Niles, J. Parnell, A. D. Rogers, and S. P. Wright (2013), Groundwater activity on mars and implications for a deep biosphere, *Nature Geoscience*, *6*(2), 133-138, doi:10.1038/NGEO1706.

Michalski, J. R., and R. L. Fergason (2009), Composition and thermal inertia of the mawrth vallis region of mars from tes and themis data, *Icarus*, *199*(1), 25-48, doi:10.1016/j.icarus.2008.08.016.

Michalski, J. R., M. D. Kraft, T. G. Sharp, L. B. Williams, and P. R. Christensen (2006a), Emission spectroscopy of clay minerals and evidence for poorly crystalline aluminosilicates on mars from thermal emission spectrometer data, *Journal of Geophysical Research-Planets*, *111*(E3), E03004, doi:10.1029/2005je002438.

Michalski, J. R., M. D. Kraft, T. G. Sharp, L. B. Williams, and P. R. Christensen (2006b), Emission spectroscopy of clay minerals and evidence for poorly crystalline aluminosilicates on mars

from thermal emission spectrometer data, *Journal of Geophysical Research-Planets*, *111*(E3), doi:10.1029/2005je002438.

Michalski, J. R., and P. B. Niles (2010), Deep crustal carbonate rocks exposed by meteor impact on mars, *Nature Geoscience*, *3*(11), 751-755, doi:10.1038/ngeo971.

Michalski, J. R., F. Poulet, J. P. Bibring, and N. Mangold (2010), Analysis of phyllosilicate deposits in the nili fossae region of mars: Comparison of tes and omega data, *Icarus*, *206*(1), 269-289, doi:10.1016/j.icarus.2009.09.006.

Milliken, R. E., and D. L. Bish (2010), Sources and sinks of clay minerals on mars, *Philos. Mag.*, *90*(17-18), 2293-2308, doi:10.1080/14786430903575132.

Milliken, R. E., J. P. Grotzinger, and B. J. Thomson (2010), Paleoclimate of mars as captured by the stratigraphic record in gale crater, *Geophysical Research Letters*, *37*, 6, doi:10.1029/2009gl041870.

Minitti, M. E., C. M. Weitz, M. D. Lane, and J. L. Bishop (2007a), Morphology, chemistry, and spectral properties of hawaiian rock coatings and implications for mars, *Journal of Geophysical Research-Planets*, *112*(E5), E05015, doi:10.1029/2006je002839.

Minitti, M. E., C. M. Weitz, M. D. Lane, and J. L. Bishop (2007b), Morphology, chemistry, and spectral properties of hawaiian rock coatings and implications for mars, *Journal of Geophysical Research-Planets*, *112*(E5), 24, doi:10.1029/2006je002839.

Moersch, J. E., and P. R. Christensen (1995), Thermal emission from particulate surfaces - a comparison of scattering models with measured spectra, *Journal of Geophysical Research-Planets*, *100*(E4), 7465-7477, doi:10.1029/94je03330.

Moore, D. M., and R. C. Reynolds (1997), *X-ray diffraction and the identification and analysis of clay minerals*, second ed., OXFORD UNIVERSITY PRESS, Oxford New York.

Moore, J. M., and A. D. Howard (2005), Large alluvial fans on mars, *Journal of Geophysical Research-Planets*, *110*(E4), E04005, doi:10.1029/2004je002352.

Moore, J. M., and D. E. Wilhelms (2001), Hellas as a possible site of ancient ice-covered lakes on mars, *Icarus*, *154*(2), 258-276, doi:10.1006/icar.2001.6736.

Morris, A. R., P. J. Mouginis-Mark, and H. Garbeil (2010), Possible impact melt and debris flows at tooting crater, mars, *Icarus*, *209*(2), 369-389, doi:10.1016/j.icarus.2010.05.029.

Murchie, S., et al. (2009a), Evidence for the origin of layered deposits in candor chasma, mars, from mineral composition and hydrologic modeling, *Journal of Geophysical Research-Planets*, *114*, doi:10.1029/2009je003343.

Murchie, S. L., et al. (2007), Compact reconnaissance imaging spectrometer for mars (crism) on mars reconnaissance orbiter (mro), *Journal of Geophysical Research-Planets*, *112*(E5), E05s03, doi:10.1029/2006je002682.

Murchie, S. L., et al. (2009b), A synthesis of martian aqueous mineralogy after 1 mars year of observations from the mars reconnaissance orbiter, *Journal of Geophysical Research-Planets*, *114*, 30, doi:10.1029/2009je003342.

Murchie, S. L., J. F. Mustard, B. L. Ehlmann, R. E. Milliken, J. L. Bishop, N. K. McKeown, E. Z. Noe Dobrea, F. P. Seelos, D. L. Buczkowski, and S. M. Wiseman (2009c), A synthesis of martian aqueous mineralogy after 1 mars year of observations from the mars reconnaissance orbiter, *Journal of Geophysical Research: Planets 114*(E2), E00D06, doi:10.1029/2009JE003342.

Mustard, J. F., C. D. Cooper, and M. K. Rifkin (2001), Evidence for recent climate change on mars from the identification of youthful near-surface ground ice, *Nature*, *412*(6845), 411-414, doi:10.1038/35086515.

Mustard, J. F., B. L. Ehlmann, S. L. Murchie, F. Poulet, N. Mangold, J. W. Head, J. P. Bibring, and L. H. Roach (2009), Composition, morphology, and stratigraphy of noachian crust around the isidis basin, *Journal of Geophysical Research-Planets*, *114*, doi:10.1029/2009je003349.

Mustard, J. F., and J. E. Hays (1997), Effects of hyperfine particles on reflectance spectra from 0.3 to 25 mu m, *Icarus*, *125*(1), 145-163, doi:10.1006/icar.1996.5583.

Mustard, J. F., et al. (2008), Hydrated silicate minerals on mars observed by the mars reconnaissance orbiter crism instrument, *Nature*, *454*(7202), 305-309, doi:10.1038/nature07097.

Mustard, J. F., and C. M. Pieters (1987), Quantitative abundance estimates from bidirectional reflectance measurements, *Journal of Geophysical Research-Solid Earth and Planets*, *92*(B4), E617-E626, doi:10.1029/JB092iB04p0E617.

Mustard, J. F., F. Poulet, A. Gendrin, J. P. Bibring, Y. Langevin, B. Gondet, N. Mangold, G. Bellucci, and F. Altieri (2005), Olivine and pyroxene, diversity in the crust of mars, *Science*, *307*(5715), 1594-1597, doi:10.1126/science.1109098.

Niles, P. B., D. C. Catling, G. Berger, E. Chassefiere, B. L. Ehlmann, J. R. Michalski, R. Morris, S. W. Ruff, and B. Sutter (2013), Geochemistry of carbonates on mars: Implications for climate history and nature of aqueous environments, *Space Science Reviews*, *174*(1-4), 301-328, doi:10.1007/s11214-012-9940-y.

Ody, A., F. Poulet, J. P. Bibring, D. Loizeau, J. Carter, B. Gondet, and Y. Langevin (2013), Global investigation of olivine on mars: Insights into crust and mantle compositions, *Journal of Geophysical Research-Planets*, *118*(2), 234-262, doi:10.1029/2012je004149.

Ojha, L., M. B. Wilhelm, S. L. Murchie, A. S. McEwen, J. J. Wray, J. Hanley, M. Massé, and M. Chojnacki (2015), Spectral evidence for hydrated salts in recurring slope lineae on mars, *Nature Geoscience*.

Osinski, G. R., et al. (2013), Impact-generated hydrothermal systems on earth and mars, *Icarus*, *224*(2), 347-363, doi:10.1016/j.icarus.2012.08.030.

Pan, C., A. D. Rogers, and J. R. Michalski (2015), Thermal and near-infrared analyses of central peaks of martian impact craters: Evidence for a heterogeneous martian crust, *Journal of Geophysical Research-Planets*, *120*(4), 662-688, doi:10.1002/2014je004676.

Pearson, K. (1901), On lines and planes of closest fit to systems of points in space, *Philosophical Magazine*, *2*(7-12), 559-572, doi:10.1080/14786440109462720.

Pelkey, S., J. Mustard, S. Murchie, R. Clancy, M. Wolff, M. Smith, R. Milliken, J. Bibring, A. Gendrin, and F. Poulet (2007), Crism multispectral summary products: Parameterizing mineral diversity on mars from reflectance, *J. Geophys. Res*, *112*(E8), E08S14, doi:10.1029/2006JE002831.

Peslier, A. H. (2010), A review of water contents of nominally anhydrous natural minerals in the mantles of earth, mars and the moon, *Journal of Volcanology and Geothermal Research*, *197*(1-4), 239-258, doi:10.1016/j.jvolgeores.2009.10.006.

Peterfreund, A. R. (1982), Formation of aeolian megaripples, mono craters, california [abs]: International congress on sedimentology, paper presented at Abstracts.

Pettijjohn, F. J., P. E. Potter, and R. Siever (1987), *Sand and sandstone*, Springer Science & Business Media, New York,US.

Pieters, C. M., and S. Tompkins (1999), Tsiolkovsky crater: A window into crustal processes on the lunar farside, *Journal of Geophysical Research-Planets*, *104*(E9), 21935-21949, doi:10.1029/1998je001010.

Pieters, C. M., S. Tompkins, J. W. Head, and P. C. Hess (1997), Mineralogy of the mafic anomaly in the south pole aitken basin: Implications for excavation of the lunar mantle, *Geophysical Research Letters*, *24*(15), 1903-1906, doi:10.1029/97gl01718.

Pinet, P., and S. Chevrel (1990), Spectral identification of geological units on the surface of mars related to the presence of silicates from earth-based near-infrared telescopic charge-coupled device imaging, *Journal of Geophysical Research-Solid Earth and Planets*, *95*(B9), 14435-14446, doi:10.1029/JB095iB09p14435.

Pinet, P., S. D. Chevrel, and P. Martin (1993), Copernicus - a regional probe of the lunar interior, *Science*, *260*(5109), 797-801, doi:10.1126/science.260.5109.797.

Plescia, J. B. (1990), Recent flood lavas in the elysium region of mars, *Icarus*, *88*(2), 465-490, doi:10.1016/0019-1035(90)90095-q.

Poulet, F., J. P. Bibring, J. F. Mustard, A. Gendrin, N. Mangold, Y. Langevin, R. E. Arvidson, B. Gondet, C. Gomez, and T. Omega (2005), Phyllosilicates on mars and implications for early martian climate, *Nature*, *438*(7068), 623-627, doi:10.1038/nature04274.

Poulet, F., and S. Erard (2004), Nonlinear spectral mixing: Quantitative analysis of laboratory mineral mixtures, *Journal of Geophysical Research-Planets*, *109*(E2), 12, doi:10.1029/2003je002179.

Poulet, F., C. Gomez, J. P. Bibring, Y. Langevin, B. Gondet, P. Pinet, G. Belluci, and J. Mustard (2007), Martian surface mineralogy from observatoire pour la mineralogie, l'eau, les glaces et l'activite on board the mars express spacecraft (omega/mex): Global mineral maps, *Journal of Geophysical Research-Planets*, *112*(E8), doi:10.1029/2006je002840.

Poulet, F., N. Mangold, D. Loizeau, J. P. Bibring, Y. Langevin, J. Michalski, and B. Gondet (2008), Abundance of minerals in the phyllosilicate-rich units on mars, *Astron. Astrophys.*, *487*(2), L41-U193, doi:10.1051/0004-6361:200810150.

Presley, M. A., and P. R. Christensen (1997), Thermal conductivity measurements of particulate materials .2. Results, *Journal of Geophysical Research-Planets*, *102*(E3), 6551-6566, doi:10.1029/96je03303.

Putzig, N. E., and M. T. Mellon (2007), Apparent thermal inertia and the surface heterogeneity of mars, *Icarus*, *191*(1), 68-94, doi:10.1016/j.icarus.2007.05.013.

Quantin, C., J. Flahaut, H. Clenet, P. Allemand, and P. Thomas (2012), Composition and structures of the subsurface in the vicinity of valles marineris as revealed by central uplifts of impact craters, *Icarus*, *221*(1), 436-452, doi:10.1016/j.icarus.2012.07.031.

Ramsey, M. S., and P. R. Christensen (1998), Mineral abundance determination: Quantitative deconvolution of thermal emission spectra, *Journal of Geophysical Research-Solid Earth*, *103*(B1), 577-596, doi:10.1029/97JB02784.

Realmuto, V. J. (1990), Separating the effects of temperature and emissivity: Emissivity spectrum normalization, in *Proceedings of the Second TIMS Workshop*, edited, pp. 23-27, JPL Publication, Pasadena, CA.

Roach, L. H., J. F. Mustard, G. Swayze, R. E. Milliken, J. L. Bishop, S. L. Murchie, and K. Lichtenberg (2010), Hydrated mineral stratigraphy of ius chasma, valles marineris, *Icarus*, *206*(1), 253-268, doi:10.1016/j.icarus.2009.09.003.

Robbins, S. J., and B. M. Hynek (2012a), A new global database of mars impact craters≥ 1 km: 1. Database creation, properties, and parameters, *Journal of Geophysical Research*, *117*(E5), E05004.

Robbins, S. J., and B. M. Hynek (2012b), A new global database of mars impact craters≥ 1 km: 2. Global crater properties and regional variations of the simple-to-complex transition diameter, *Journal of Geophysical Research: Planets (1991–2012)*, *117*(E6).

Rogers, A. D., and O. Aharonson (2008), Mineralogical composition of sands in meridiani planum determined from mars exploration rover data and comparison to orbital measurements, *Journal of Geophysical Research-Planets*, *113*(E6), E06S14, doi:10.1029/2007je002995.

Rogers, A. D., and J. L. Bandfield (2009), Mineralogical characterization of mars science laboratory candidate landing sites from themis and tes data, *Icarus*, *203*(2), 437-453, doi:10.1016/j.icarus.2009.04.020.

Rogers, A. D., and P. R. Christensen (2003), Age relationship of basaltic and andesitic surface compositions on mars: Analysis of high-resolution tes observations of the northern hemisphere, *Journal of Geophysical Research-Planets*, *108*(E4), doi:10.1029/2002je001913.

Rogers, A. D., and P. R. Christensen (2007a), Surface mineralogy of martian low-albedo regions from mgs-tes data: Implications for upper crustal evolution and surface alteration, *Journal of Geophysical Research-Planets*, *112*(E1), E01003, doi:10.1029/2006je002727.

Rogers, A. D., and P. R. Christensen (2007b), Surface mineralogy of martian low-albedo regions from mgs-tes data: Implications for upper crustal evolution and surface alteration, *Journal of Geophysical Research-Planets*, *112*(E1), doi:10.1029/2006je002727.

Rogers, A. D., P. R. Christensen, and J. L. Bandfield (2005), Compositional heterogeneity of the ancient martian crust: Analysis of ares vallis bedrock with themis and tes data, *Journal of Geophysical Research-Planets*, *110*(E5), E05010, doi:10.1029/2005je002399.

Rogers, A. D., and R. L. Fergason (2011a), Regional-scale stratigraphy of surface units in tyrrhena and iapygia terrae, mars: Insights into highland crustal evolution and alteration history, *Journal of Geophysical Research-Planets*, *116*, E08005, doi:E0800510.1029/2010je003772.

Rogers, A. D., and R. L. Fergason (2011b), Regional-scale stratigraphy of surface units in tyrrhena and iapygia terrae, mars: Insights into highland crustal evolution and alteration history, *Journal of Geophysical Research-Planets*, *116*, doi:10.1029/2010je003772.

Rogers, A. D., and V. E. Hamilton (2015), Compositional provinces of mars from statistical analyses of tes, grs, omega and crism data, *Journal of Geophysical Research-Planets*, *120*(1), 62-91, doi:10.1002/2014je004690.

Ruff, S. W., and P. R. Christensen (2002), Bright and dark regions on mars: Particle size and mineralogical characteristics based on thermal emission spectrometer data, *Journal of Geophysical Research-Planets*, *107*(E12), 22, doi:10.1029/2001je001580.

Ruff, S. W., and P. R. Christensen (2007), Basaltic andesite, altered basalt, and a tes-based search for smectite clay minerals on mars, *Geophysical Research Letters*, *34*(10), L10204, doi:10.1029/2007GL029602.

Ruff, S. W., P. R. Christensen, P. W. Barbera, and D. L. Anderson (1997), Quantitative thermal emission spectroscopy of minerals: A laboratory technique for measurement and calibration, *Journal of Geophysical Research-Solid Earth*, *102*(B7), 14899-14913, doi:10.1029/97jb00593.

Ruff, S. W., P. R. Christensen, D. L. Blaney, W. H. Farrand, J. R. Johnson, J. R. Michalski, J. E. Moersch, S. P. Wright, and S. W. Squyres (2006), The rocks of gusev crater as viewed by the mini-tes instrument, *Journal of Geophysical Research-Planets*, *111*(E12), doi:10.1029/2006je002747.

Ryan, A. J., and P. R. Christensen (2012), Coils and polygonal crust in the athabasca valles region, mars, as evidence for a volcanic history, *Science*, *336*(6080), 449-452, doi:10.1126/science.1219437.

Sabine, C., V. J. Realmuto, and J. V. Taranik (1994), Quantitative estimation of granitoid composition from thermal infrared multispectral scanner (tims) data, desolation wilderness, northern sierra nevada, california, *Journal of Geophysical Research: Solid Earth 99*(B3), 4261-4271, doi:10.1029/93JB03127.

Salisbury, J. W. (1993), Mid-infrared spectroscopy laboratory data, in *Remote geochemical analysis: Elemental and mineralogical composition*, edited by C. M. Pieters and P. A. Englert, pp. 79-98, Cambridge University Press, Cambridge, U.K.

Salisbury, J. W., and J. W. Eastes (1985), The effect of particle-size and porosity on spectral contrast in the midinfrared, *Icarus*, *64*(3), 586-588, doi:10.1016/0019-1035(85)90078-8.

Salisbury, J. W., and A. Wald (1992), The role of volume scattering in reducing spectral contrast of reststrahlen bands in spectra of powdered minerals, *Icarus*, *96*(1), 121-128, doi:10.1016/0019-1035(92)90009-v.

Salisbury, J. W., L. S. Walter, and N. Vergo (1987), Mid-infrared (2.1–25 mm) spectra of minerals*Rep.*, U.S. Geological Survey, Reston, VA.

Salvatore, M. R., J. F. Mustard, M. B. Wyatt, and S. L. Murchie (2010), Definitive evidence of hesperian basalt in acidalia and chryse planitiae, *Journal of Geophysical Research-Planets*, *115*, doi:10.1029/2009je003519.

Sautter, V., et al. (2014), Igneous mineralogy at bradbury rise: The first chemcam campaign at gale crater, *Journal of Geophysical Research-Planets*, *119*(1), 30-46, doi:10.1002/2013je004472.

Scott, D. H., and K. L. Tanaka (1986), *Geologic map of the western equatorial region of mars*, Geological Survey (US), Flagstaff, AZ.

Seelos, K. D., F. P. Seelos, C. E. Viviano-Beck, S. L. Murchie, R. E. Arvidson, B. L. Ehlmann, and A. A. Fraeman (2014), Mineralogy of the msl curiosity landing site in gale crater as observed by mro/crism, *Geophys. Res. Lett.*, *41*(14), 4880-4887, doi:10.1002/2014gl060310.

Sharpton, V. L. (2014), Constraints on crater growth mechanisms, ejecta thicknesses and excavation depths from target outcrops at fresh lunar craters, paper presented at Lunar and Planetary Institute Science Conference Abstracts, LPI, Houston, TX.

Shepherd, K. D., and M. G. Walsh (2002), Development of reflectance spectral libraries for characterization of soil properties, *Soil Science Society of America Journal*, *66*(3), 988-998.

Skok, J., J. Mustard, L. Tornabene, C. Pan, D. Rogers, and S. Murchie (2012a), A spectroscopic analysis of martian crater central peaks: Formation of the ancient crust, *Journal of Geophysical Research: Planets 117*(E11), E00J18, doi:10.1029/2012JE004148.

Skok, J. R., J. F. Mustard, L. L. Tornabene, C. Pan, D. Rogers, and S. L. Murchie (2012b), A spectroscopic analysis of martian crater central peaks: Formation of the ancient crust, *Journal of Geophysical Research-Planets*, *117*, doi:10.1029/2012je004148.

Smith, M. D., J. L. Bandfield, and P. R. Christensen (2000), Separation of atmospheric and surface spectral features in mars global surveyor thermal emission spectrometer (tes) spectra, *Journal of Geophysical Research-Planets*, *105*(E4), 9589-9607, doi:10.1029/1999je001105.

Smith, M. R., J. L. Bandfield, E. A. Cloutis, and M. S. Rice (2013), Hydrated silica on mars: Combined analysis with near-infrared and thermal-infrared spectroscopy, *Icarus*, *223*(2), 633-648, doi:10.1016/j.icarus.2013.01.024.

Squyres, S. W., et al. (2004), In situ evidence for an ancient aqueous environment at meridiani planum, mars, *Science*, *306*(5702), 1709-1714, doi:10.1126/science.1104559.

Stockstill-Cahill, K. R., F. S. Anderson, and V. E. Hamilton (2008), A study of low-albedo deposits within amazonis planitia craters: Evidence for locally derived ultramafic to mafic materials, *Journal of Geophysical Research-Planets*, *113*(E7), doi:10.1029/2007je003036.

Sullivan, R., et al. (2008), Wind-driven particle mobility on mars: Insights from mars exploration rover observations at "el dorado" and surroundings at gusev crater, *Journal of Geophysical Research-Planets*, *113*(E6), doi:10.1029/2008je003101.

Sun, V. Z., and R. E. Milliken (2014), The geology and mineralogy of ritchey crater, mars: Evidence for post-noachian clay formation, *Journal of Geophysical Research-Planets*, *119*(4), 810-836, doi:10.1002/2013je004602.

Tanaka, K. L., and G. J. Leonard (1995), Geology and landscape evolution of the hellas region of mars, *Journal of Geophysical Research-Planets*, *100*(E3), 5407-5432, doi:10.1029/94je02804.

Thorpe, M. T., A. D. Rogers, T. F. Bristow, and C. Pan (2015), Quantitative compositional analysis of sedimentary materials using thermal emission spectroscopy: 1. Application to sedimentary rocks, *Journal of Geophysical Research: Planets*, *120*(11), 1956-1983, doi:10.1002/2015JE004863.

Tirsch, D., R. Jaumann, A. Pacifici, and F. Poulet (2011), Dark aeolian sediments in martian craters: Composition and sources, *Journal of Geophysical Research-Planets*, *116*, doi:10.1029/2009je003562.

Tolosana-Delgado, R., and H. von Eynatten (2009), Grain-size control on petrographic composition of sediments: Compositional regression and rounded zeros, *Mathematical Geosciences*, *41*(8), 869-886, doi:10.1007/s11004-009-9216-6.

Tompkins, S., and C. M. Pieters (1999), Mineralogy of the lunar crust: Results from clementine, *Meteoritics & Planetary Science*, *34*(1), 25-41.

Tornabene, L. L., A. McEwen, C. Caudill, G. Osinski, J. Wray, G. Marzo, J. Mustard, J. Skok, J. Grant, and S. Mattson (2010), A crater-exposed bedrock database for mars with applications for determining the composition and structure of the upper crust, paper presented at Lunar and Planetary Science Conference.

Tornabene, L. L., J. E. Moersch, H. Y. McSween, V. E. Hamilton, J. L. Piatek, and P. R. Christensen (2008a), Surface and crater-exposed lithologic units of the isidis basin as mapped by coanalysis of themis and tes derived data products, *Journal of Geophysical Research-Planets*, *113*(E10), doi:10.1029/2007je002988.

Tornabene, L. L., J. E. Moersch, H. Y. McSween Jr, V. E. Hamilton, J. L. Piatek, and P. R. Christensen (2008b), Surface and crater-exposed lithologic units of the isidis basin as mapped by coanalysis of themis and tes derived data products, *Journal of Geophysical Research*, *113*(E10), E10001, doi:10.1029/2007JE002988.

Tornabene, L. L., J. E. Moersch, G. R. Osinski, P. Lee, and S. P. Wright (2005), Spaceborne visible and thermal infrared lithologic mapping of impact-exposed subsurface lithologies at the haughton impact structure, devon island, canadian high arctic: Applications to mars, *Meteoritics & Planetary Science*, *40*(12), 1835-1858, doi:10.1111/j.1945-5100.2005.tb00149.x.

Tornabene, L. L., G. R. Osinski, A. S. McEwen, V. Ling, C. M. Caudill, A. Nuhn, R. Hopkins, B. D. Aoust, and S. Mattson (2014), A global synthesis of the meter- to decameter-scale morphology and structure of complex crater central uplifts, *Eighth International Conference on Mars (2014)*.

Tornabene, L. L., G. R. Osinski, A. S. McEwen, J. J. Wray, M. A. Craig, H. M. Sapers, and P. R. Christensen (2013), An impact origin for hydrated silicates on mars: A synthesis, *Journal of Geophysical Research-Planets*, *118*(5), 994-1012, doi:10.1002/jgre.20082.

Tornabene, L. L., G. R. Osinski, A. S. McEwenb, J. M. Boyce, V. J. Bray, C. M. Caudill, J. A. Grant, C. W. Hamilton, S. Mattson, and P. J. Mouginis-Mark (2012), Widespread crater-related pitted materials on mars: Further evidence for the role of target volatiles during the impact process, *Icarus*, *220*(2), 348-368, doi:10.1016/j.icarus.2012.05.022.

Vincendon, M., J. Audouard, F. Altieri, and A. Ody (2015), Mars express measurements of surface albedo changes over 2004-2010, *Icarus*, *251*, 145-163, doi:10.1016/j.icarus.2014.10.029.

Vincent, R. K., and F. Thomson (1972), Spectral compositional imaging of silicate rocks, *Journal of Geophysical Research*, *17*(14), 2465-2473.

Viviano-Beck, C. E., et al. (2014), Revised crism spectral parameters and summary products based on the currently detected mineral diversity on mars, *Journal of Geophysical Research-Planets*, *119*(6), 1403-1431, doi:10.1002/2014je004627.

Viviano, C. E., and J. E. Moersch (2013), Using themis data to resolve the discrepancy between crism/omega and tes modeled phyllosilicate abundance in mawrth vallis, *Icarus*, *226*(1), 497-509, doi:10.1016/j.icarus.2013.06.005.

Weltje, G. J., and H. von Eynatten (2004), Quantitative provenance analysis of sediments: Review and outlook, *Sedimentary Geology*, *171*(1-4), 1-11, doi:10.1016/j.sedgeo.2004.05.007.

Wentworth, C. K. (1922), A scale of grade and class terms for clastic sediments, *Journal of Geology*, *30*(5), 377-392.

Williams, D. A., et al. (2009), The circum-hellas volcanic province, mars: Overview, *Planet Space Sci.*, *57*(8-9), 895-916, doi:10.1016/j.pss.2008.08.010.

Williams, D. A., R. Greeley, L. Manfredi, J. Raitala, G. Neukum, and H. C.-I. Team (2010), The circum-hellas volcanic province, mars: Assessment of wrinkle-ridged plains, *Earth and Planetary Science Letters*, *294*(3-4), 492-505, doi:10.1016/j.epsl.2009.10.007.

Wilson, J. H., and J. F. Mustard (2013), Exposures of olivine-rich rocks in the vicinity of ares vallis: Implications for noachian and hesperian volcanism, *Journal of Geophysical Research-Planets*, *118*(5), 916-929, doi:10.1002/jgre.20067.

Wilson, S. A., A. D. Howard, J. M. Moore, and J. A. Grant (2007), Geomorphic and stratigraphic analysis of crater terby and layered deposits north of hellas basin, mars, *Journal of Geophysical Research-Planets*, *112*(E8), E08009, doi:10.1029/2006je002830.

Wohler, C., A. Grumpe, A. Berezhnoy, M. U. Bhatt, and U. Mall (2014), Integrated topographic, photometric and spectral analysis of the lunar surface: Application to impact melt flows and ponds, *Icarus*, *235*, 86-122, doi:10.1016/j.icarus.2014.03.010.

Wold, H. (1982), Soft modelling: The basic design and some extensions, *Systems under indirect observation, Part II*, 1-53.

Wold, S., M. Sjostrom, and L. Eriksson (2001), Pls-regression: A basic tool of chemometrics, *Chemometrics and Intelligent Laboratory Systems*, *58*(2), 109-130, doi:10.1016/s0169-7439(01)00155-1.

Wray, J. J., B. L. Ehlmann, S. W. Squyres, J. F. Mustard, and R. L. Kirk (2008), Compositional stratigraphy of clay-bearing layered deposits at mawrth vallis, mars, *Geophysical Research Letters*, *35*(12), 6, doi:10.1029/2008gl034385.

Wray, J. J., S. T. Hansen, J. Dufek, G. A. Swayze, S. L. Murchie, F. P. Seelos, J. R. Skok, R. P. Irwin, III, and M. S. Ghiorso (2013), Prolonged magmatic activity on mars inferred from the detection of felsic rocks, *Nature Geoscience*, *6*(12), 1013-1017, doi:10.1038/ngeo1994.

Wray, J. J., et al. (2011), Columbus crater and other possible groundwater-fed paleolakes of terra sirenum, mars, *Journal of Geophysical Research-Planets*, *116*, 41, doi:10.1029/2010je003694.

Wulf, G., M. H. Poelchau, and T. Kenkmann (2012), Structural asymmetry in martian impact craters as an indicator for an impact trajectory, *Icarus*, *220*(1), 194-204, doi:10.1016/j.icarus.2012.04.025.

Wyatt, M. B., and H. Y. McSween (2002), Spectral evidence for weathered basalt as an alternative to andesite in the northern lowlands of mars, *Nature*, *417*(6886), 263-266, doi:10.1038/417263a.

Wyatt, M. B., H. Y. McSween, K. L. Tanaka, and J. W. Head (2004), Global geologic context for rock types and surface alteration on mars, *Geology*, *32*(8), 645-648, doi:10.1130/g20527.1.

Wyrick, D., D. A. Ferrill, A. P. Morris, S. L. Colton, and D. W. Sims (2004), Distribution, morphology, and origins of martian pit crater chains, *Journal of Geophysical Research-Planets*, *109*(E6), doi:10.1029/2004je002240.

Zolotov, M. Y., and M. V. Mironenko (2007), Timing of acid weathering on mars: A kinetic-thermodynamic assessment, *Journal of Geophysical Research-Planets*, *112*(E7), 20, doi:10.1029/2006je002882.